A systematic study of the explosion energy issue in core collapse supernova theory

June 2016

Yu YAMAMOTO

A systematic study of the explosion energy issue in core collapse supernova theory

June 2016

Waseda University
Graduate School of Advanced Science and Engineering
Department of Pure and Applied Physics, Research on Theoretical Astrophysics and Cosmology

Yu YAMAMOTO

Abstract

Massive stars with main sequence masses greater than 8 solar mass ($M_\odot$) the main target of CCSNe researches. According to initial mass function (IMF) they occupy about 15As a matter of fact, supernova theorists have failed to reproduce this energetic stellar explosion for about a half century because micro and macro physics are highly complex and are mutual influenced. The theoretical investigation of the explosion mechanism is based on numerical simulations, which will ultimately require computational sources of exsa scales. With recent remarkable developments both in hardware and software, however, more realistic physics are incorporated and research group are beginning to overcome the difficulties, reporting successful explosions in their numerical models. The successful is still partial, unfortunately, since in the most of the cases the explosion energy hardly reaches the typical value (10^{51}erg). What is worse other groups found no explosion for almost same setups. The robust explosion mechanism has not yet been ascertained and is still a remaining issue.

The purpose of this paper is to study how far our understanding of "neutrino heating mechanism" , the current paradigm, has reached, or put another way, to expose what kind of physics are still missing to explain observations , such as explosion energy and nickel mass. As already remarked the physics in CCSNe are quite complicated with extremely high Reynolds number, highly uncertain equation of state (EOS) at supra-nuclear densities , copious neutrinos not in thermal nor chemical equilibrium with matter normally. I believe that it is justified to devote a somewhat large number of pages to the introduction. It will be also helpful for understanding the motivation of this paper. Starting with evidence from supernova light curves I will then move to the basics idea of neutrino heating mechanism and summarize some recent developments in various micro and macro physics. Key factors in the theory of massive-star evolutions are also illuminated in the introduction. Other important ingredients that are not directly related with the thesis, such as numerical treatments of neutrino transport, are given in appendices.

To find the missing pieces of the current CCSNe theory, I employed an experimental way instead of running "realistic" simulations. In fact, I conducted experimental computations systematically so as to reveal (1) what is the necessary condition of the canonical explosion energy (2) what is the dominant contribution to the explosion energy (3) when the explosion energy is settled to the final value, and, finally, (4) features in pre-explosion structure of the progenitor are critical for the explosion energy. In this paper I paid particular attention to nuclear energies released in association with the production of various elements up to $A \sim 56$, which are likely to contribute to the energetics of CCSNe.

I performed multi-dimension hydrodynamic simulations that can also handle the evolution of elements in both nuclear statistical equilibrium (NSE) and non-equilibrium, taking particular care of transition from one to the other. We take a multi-step strategy: collapse, shock revival and the subsequent evolution until the settlement of explosion energy are treated separately and consecutively; the collapse phase is calculated under spherical symmetry to obtain mass accretion histories for different progenitors; in so doing, the inner

part of the core is removed and replaced with the artificial inner boundary; the second phase treats shock revival; we construct steady accretion flows through the stalled shock wave on to the proto neutron star; using these configurations as initial conditions for 1D and 2D simulations, we determine the critical neutrino luminosities for shock revival; the evolutions that follow the shock revival are computed in the last phase, with the mass accretion histories obtained in the first phase being taken into account.

In the first of two studies done for the thesis we used a single progenitor of $15M_{\odot}$ provided by a realistic stellar evolution calculation and studied the post-shock revival evolutions, changing the time of shock revival. We run seven 1D and five 2D models. In the second exploration, on the other hand, we pay attention to the progenitor dependence of the dynamics. Instead of using progenitor models from realistic stellar evolution calculations, I construct six pre-collapse models with different masses of Fe core and Si+S layer assuming entropy and electron fraction distributions and varying rather arbitrarily the parameters included. Unlike in the first study, we did not specify the shock revival time explicitly but gave the neutrino luminosity in this study. The explosion energy and nickel mass are calculated for eighteen 1D and eight 2D models, respectively.

The two studies demonstrate that early explosions are necessary for strong explosions. It is also found that nuclear recombination energy is a major contributor to the explosion energy which is settled to the final value in $\sim$500ms whereas the nickel mass needs much longer times to reach the final value, particularly in 2D. Since the nickel tends to be overproduced in early explosions, enhanced fallbacks in multi-dimensional hydrodynamics seem to be crucial to reproduce the observed values of nickel mass and explosion energy simultaneously. As for the progenitor dependence, we found that light cores with relatively high entropies seem to be favorable for reproducing the canonical explosion by the neutrino heating mechanism. It is interesting that the explosion energy is strongly correlated with the mass accretion rate at shock revival regardless of the spatial dimensions.

Contents

Chapter 1

Overview

Above our head countless stars are brightening in the sky and those beautiful lights are coming from mostly conversion of nuclear fusion energy of hydrogen into radiation energy. These stars are called main-sequence stars and last for almost 90% of its life (from 10 million to 10 billion years!!) until hydrogen inside the core is depleted. If stars are sufficiently massive, the advanced nuclear burning take place in their central core. These stars end their life with producing shock wave around the center which propagates toward the envelope and finally breaks out from stellar surface so that we may observe one of the brightest stellar explosion, luminosity $L \gtrsim 10^{9-12} L_{\odot}$erg/s, called "supernova (SN)" which is coined by Walter Baade and Fritz Zwicky in 1931. The absolute magnitude of single SN is almost comparable to its host galaxy and the diverse electro-magnetic signatures are found since their discovery.

It is well known from observations that the canonical explosion energy is 10^{51}erg and those gas ejected by SN propagate through interstellar matters by $\sim 2,000 - 30,000$km/s. There are mainly two categories for supernova which are attributed to different scenarios , one called thermo-nuclear supernova (SNIa) which is driven by carbon-oxygen ignition in relatively lower progenitor mass $M_{\rm ZAMS} \lesssim 8M_{\odot}$ and the other called core-collapse supernova (CCSN; SNII, Ib/c) which takea place in rather higher mass ($M_{\rm ZAMS} \gtrsim 8M_{\odot}$) and is concerned with this paper. For the massive star case, the nearest naked-eyed visible supernova event, i.e. SN1987A which is located in Large Magelanic Colud (LMC) 50kpc far from the earth, produces large number of neutrino flux (19 numbers of anti-electron type neutrino $\bar{\nu_e}$) at KamiokaNDE [175] and brought the important insight into the theoretical modeling. In general, CCSNe are thought to happen where the massive stars are born actively, e.g. in star forming regions in spiral and irregular galaxies, in spiral arms near HII region and never in elliptical galaxies [203, 146, 148, 147]. It is not easy, however, to detect since they are very rare phenomena (about single event per century in Milky Way; [428, 211, 61, 265, 247, 210, 34, 60] due to the small population of massive stars predicted by initial mass functions. In spite of those rareness, CCSNe are relevant to many stellar phenomena in the high energy astrophysical fields such as neutrino burst phenomena and gravitational waves due to its large gravitational source ($E \sim 3 \times 10^{53}$erg) and a short dynamical time scale of proto-neutron star (PNS). They are also associated with nucleosynthesis and galactic chemical evolutions, i.e. the one third of iron and all the α elements which are heavier than oxygen are made in the Galaxy by this type of supenova events [476, 437, 314, 218, 74]. After releasing the gigantic kinetic energy and amount of mass ejection, CCSN forms compact object such as neutron star (NS) or black hole (BH) which is thought to be the candidate of cosmic rays accelerator. Therefore, the theoretical

CCSNe modeling is quite mandatory for whole astrophysical fields.

In spite of its long history, none of CCSNe modelers have yet obtained feasible theoretical modeling so far due to quite complicated physics and also numerics. In fact, the theory has progressed in terms of the both aspects step-by-step and state-of-the art numerical simulations have enabled us to handle three-dimensional issues. It should be stressed that there are several non-negligible discrepancies, e.g. whether shock revival takes place or not, between the current realistic simulations which appear to be difficult to distinguish one method from another. As a consequence, the field is hardly followed, especially, by non-expert and enforces considerable effort to isolate physical and numerical issue. Furthermore, the relation between fundamental physics and CCSNe may not be completely clear. Hence, in this paper I decided to address some reviews as well as my main research, i.e. the experimental investigation of intrinsic properties of explosion. Although few important ingredients of CCSNe theory are chosen, the review part would be still helpful to understand state-of-the-art calculation results. In fact, the review parts are important not only for educational point of view but also for introducing the problems thoroughly in CCSNe theory which will shed light on my concern. The structure of this paper is depicted in Fig. 1.1. The numbers in the figure correspond to chapter number.

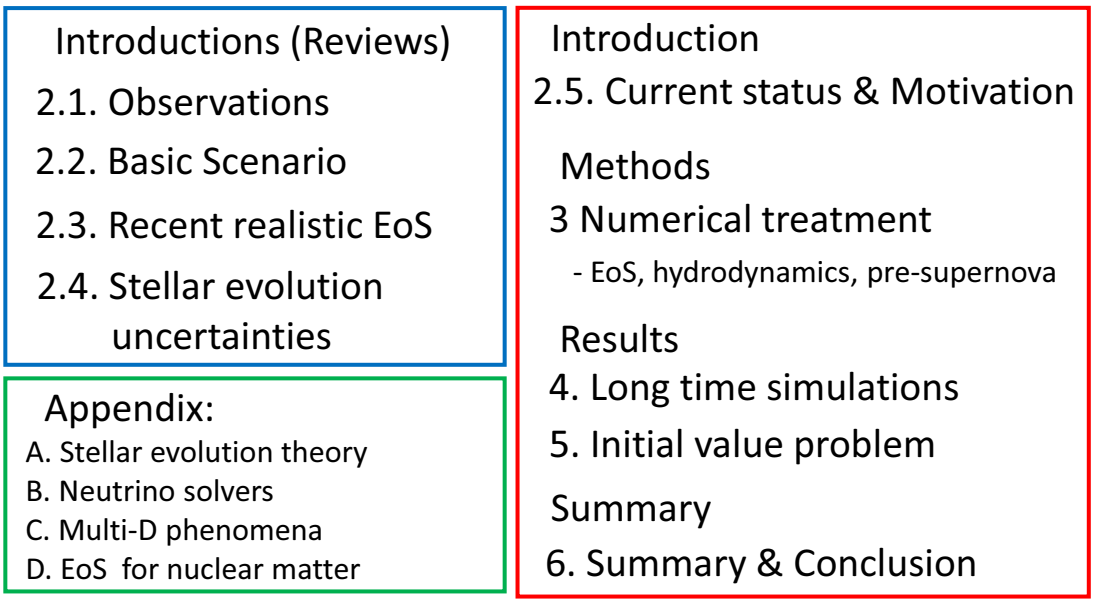

Figure 1.1: The roadmap of this paper. Chapters surrounded by blue and green lines are mostly consisted of review parts while those highlighted in red line address the main investigation parts in this paper.

First the observation evidences are chosen so as to illustrate how explosion energy and nickel mass are evaluated by observations and then, a brief discussion about the neutrino heating mechanism are addressed in the next chapter. The current reports of nuclear matter equation of state (EoS) is also high-lighted as well as theoretical uncertainties in stellar evolution fields in the middle part of the introduction. At the end of the introduction current numerical studies of CCSNe and stellar evolution are summarized which is directly associated with the motivation of this paper (section 2.5).

Since this study takes particular care of the nuclear abundance evolution incorporated in hydrodynamics simulation, the impact of equation of state and their numerical treatment

are not apparent and should be discussed carefully. Therefore, those two topics are in chapter 3. The subsequent chapters are devoted to the results of the first and second study as well as summary.

There are also supplementary materials in appendices for understanding subtle physics which is relevant to CCSNe thoery. The present numerical treatments of neutrino transport are also addressed in the appendix, since neutrino heating mechanism is regarded as essential pieces for robust explosion. As a consequence, the topics are rather vast so that one who is especially familiar with these theoretical topics should only follow section 2.3, section 2.4 and jump to chapters where is surrounded by the red line in Fig. 1.1.

Chapter 2

Introduction

2.1 Observation properties of supernova

2.1.1 Observations and Theoretical prediction

There are two historical discoveries of two explosion event, SN1987A and SN1993J. Since the distances of this two stellar objects are sufficiently near from earth, their bolometric and spectrum survey found multiple ring structures and indicate the imprint of aspherical morophology, binary interaction and even progenitor which is likely to be super blue giants (SGB). These explosion features provide the new insight for both CCSNe and stellar evolution studies. The binarity of SN1993J is well guaranteed by pre-explosion image detection.

As already mentioned, SN1987A has emitted huge number of neutrino which expose that the theoretical CCSNe model is linked to neutrino heating mechanism. Furthermore, the two aspherical explosions have indicated the necessity of multi-dimension simulation (see appendix C).

The question is what kind of stars produce SN1987A, SN1993J and other observed SNe. As mentioned already, CCSNe take place when the massive stars are in the last stage of its life. There are, however, large divergences in the path to the end of stage which affect the feature of explosion. For instance, Table 2.1 shows the evolution list of O stars which is taken from [279]. The mass difference by $10M_{\odot}$ in zero age main-sequence (ZAMS) provides the color divergence of star, i.e. the radius of star. In case of more than $30M_{\odot}$, if metalicity is non-zero serious mass-loss event take place, thus most of their hydrogen envelopes are stripped off. As a consequence, these astrophysical phenomena affect the spectra type of SN from Type II to Type I.

Moreover, since the massive stars preserve enormous binding energies during collapse, the compact remnants such as NS and BH are produced after the explosion. As a matter of fact, the one of issue is what kind of initial conditions will leave NS or end up BH. Heger et al.(2003) [161] suggests that the boarderline of CCSNe fate maybe lie between somewhere around $20-30M_{\odot}$ but the results are highly influenced by initial condition such as metalicity (see Fig. 2.1). The formation of BH is quite sensitive since not only direct stellar collapse but also the conversion from NS via strong matter fall back event is possible fate (see reviews, e.g. [125] and reference therein).

It should be noted that these predictions are based on stellar evolution calculations which possess a number of uncertainty, thus still under debate (see section 2.4 for further discussions). Difficulties in the prediction are also directly linked to the theoretical modeling

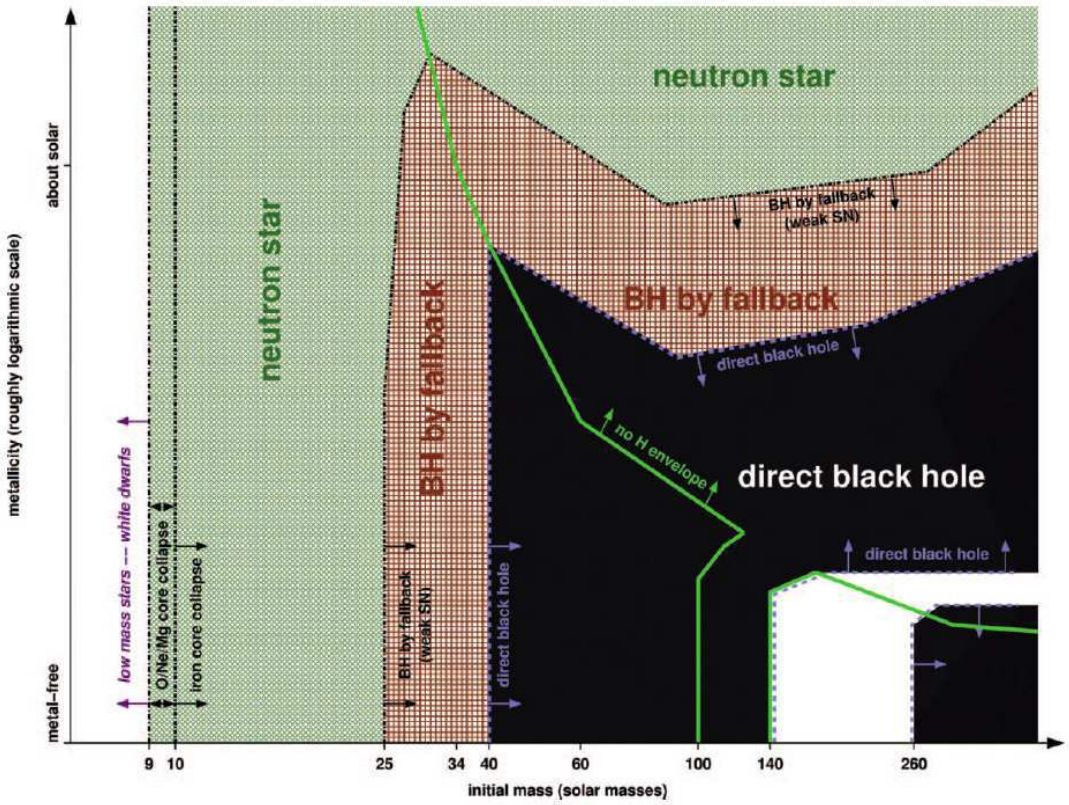

Figure 2.1: The theoretical prediction of massive star fates in initial and final mass map. The figure is taken from Heger et al.(2003) [161].

so that exploring the true picture of CCSNe is urgent and interior structure features are highly required. The central portion of star is, however, too opaque for photon to escape so that the electro-magnetic signals are not available to these probe. For massive stars, recently new astronomy observations have been paid attention instead so as to extract the stellar structure properties around PNS. Gravitational waves and neutrino emissions, which result from energy conversion of gravitational energy, can carry informations of very central portion of massive stars and be expected as the strong candidates of next astrophysical observation eras (see [260, 1, 24, 93, 188, 267, 380, 422, 221, 127, 220, 327, 89, 329, 223]). These signals have a potential to distinguish which theoretical EoS represent the true nature (see section. 2.3 for further discussions).

As a matter of fact, since the strengths of interaction with matter are extremely weak, the explosion objects need to be quite close enough (100-1,000pc) so as to be detected and there are no observation, except for SN1987A, by these new challenges yet. Hence, the importance of the electro-magnetic signals has remained unchanged since the observation takes advantage of a number of observations and also investigating physical supernova characters, e.g. eject mass, explosion energy and nickel mass. Furthermore, new satellite missions, e.g. Gaia, have provided fresh and/or precise properties of supernovae [9]. In this section I focus on the optical photon signals, especially light curve, and address how the supernova properties are extracted.

Table 2.1: Schematic illustration for evolution scenarios of "single" massive O type stars taken from [279].

progenitor mass	Evolution sequences
$M > 90M_\odot$:	O-Of-WNL-(WNE)-WCL-WCE-SN(Ibc/BH/SNIIn)
	or (PCSN/Hypernova low Z) ?
$60 - 90M_\odot$:	O - Of/WNL $\Leftrightarrow$ LBV - WNL(H poor)- WCL-E - SN(SNIbc/BH/SNIIn)?
$40 - 60M_\odot$:	O - BSG - LBV $\Leftrightarrow$ WNL -(WNE) - WCL-E - SN(SNIb)
	- WCL-E - WO SN (SNIc)
$30 - 40M_\odot$:	O - BSG - RSG - WNE - WCE - SN(SNIb)
	OH/IR $\Leftrightarrow$ LBV
$20 - 30M_\odot$:	O -(BSG)- RSG - BSG (blue loop) - RSG - SN(SNIIb, SNIIL)
$10 - 20M_\odot$:	O - RSG - (Cepheid loop, $M < M_\odot$) RSG - SN (SNIIP)

Note: O stars start their life as first main sequence and then swell by more than $10^2 R_\odot$ during red supergiant (RSG) or blue supergiant (BSG). Stars with less than $\sim 30M_\odot$ go through only small amount of mass loss while more massive stars come to Wolf-Rayet stars (WR) due to large mass loss rate and severe eruption events. WR stars can be divided into WN (nitrogen emission line) and WC (carbon and oxygen emission line). The last letters "E" and "L" in WR stars mean the hotter "early"-type and cooler "late"-type objects, respectively. Transition between two stages back and force is expressed as the sign $\Leftrightarrow$. See discussions in [279].

2.1.2 SN spectrum and light curve categories

Firstly, spectra types of supernovae are one of the typical characterizations [113, 446]. The core-collapse induced explosion are divided into three major types; one called Type II which shows hydrogen absorption line, another called Type Ib which provide no hydrogen but rich helium absorption lines and the last called Type Ic in which neither H nor He absorption line appear. These lines result from doppler shift; bluer absorption demonstrates ejected matters are moving towards the observers while redder absorption indicates the opposite matter motion. Hence, they are usually regarded as good measurement of velocity. In addition, the difference of spectrum can be interpreted as the imprints of the different mass transformation scenario in the outer envelope. Hence, SN Ib/c occur when hydrogen envelopes of progenitor are completely stripped off before their late evolution stage, whereas copious hydrogen envelope still retain in case of SN II. There is also SN Ia explosion which is relatively bright and widely used for the distance measurement (see Fig. 2.2). In this paper, however, since the explosion is not originate from huge gravitational energy release but explosive carbon-oxgen burning, the further discussion about SNIa is frequently skipped so far.

There is an interesting observation probes demonstrated in Smith (2015) [392]. The author summarized the relation between spectral types and progenitor properties such as shown in table 2.2. From the figure spectral types seem to contain the progenitor mass and color information and also the amount of mass loss. Together with table 2.1, it is interesting that the relatively massive stars produce the relatively small mass in their pre-supernova stages which implies that supenovae theory involves the complex initial condition problem. The detail of this initial problem is repeated again section 2.5 and 2.4. It is noteworthy that attention has been paid to massive stars with relatively high mass loss rate in present

Table 2.2: Mapping of SN types to their likely progenitor star properties. The original table is seen in Smith et al.(2015) [392].

SN	Progenitor Star[a]	M_{ZAMS}	$\dot{M}^b$	V_∞
...	...	($M_\odot$)	($M_\odot$ yr^{-1})	(km s^{-1})
II-P	RSG	8–20	10^{-6}–10^{-5}	10-20
II-L	RSG/YSG	20–30 (?)	10^{-5}–10^{-4}	20-40
II-pec	BSG (b)	15–25	10^{-6}–10^{-4}	100-300
IIb	YSG (b)	10–25	10^{-5}–10^{-4}	20-100
Ib	He star (b)	15–25 (?)	10^{-7}–10^{-4}	100-1000
Ic	He star (b)/WR	25–?	10^{-7}–10^{-4}	1000
Ic-BL	He star (b)/WR	25–?	10^{-6}–10^{-5}	1000
IIn (SL)	LBV	30–?	(1–10)	50-600
IIn	LBV/B[e] (b)	25–?	(0.01-1)	50-600
IIn	RSG/YHG	25–40	10^{-4}–10^{-3}	30-100
IIn-P	super-AGB	8–10	0.01-1	10-600
Ibn	WR/LBV	40–?	10^{-3}–0.1	1000
Ia/IIn	WD (b)	5-8 (?)	0.01-1	50-100

[a]Most likely progenitor star type. Some of the symbols are same in table 2.1. In addition YSG, AGB and LBV denots yellow super giant, asymptotic giant branch and luminous blue variables, respectively. "(b)" indicates that a binary channel is probably key.
[b]Mass-loss rates for pre-SN eruptions are listed in parentheses, corresponding roughly to the total mass ejected in the few years immediately preceding core-collapse. The mass-loss rates may be lower but still substantial at larger radii traced by the expanding SN shock at late times.

since the strong eruption may be the plausible candidate of SNIIn whose spectrum show narrow H_α line as well as blue continuum which result from HII region and high density CSM. The mass-loss rate in massive star is, however, one of the most uncertainty properties which influence seriously the stellar evolution field.

There is also important signal from CCSNe called light curve, i.e. the time evolution of photon luminosity. The typical CCSNe light curves are depicted in Fig. 2.3. It is apparent that there are roughly two common features among all types, one is "hill" shape appearing at the beginning and the other is "tail" part continuing until the end. Meanwhile, other distinguishable shape properties, e.g. plateau feature, reflect substantial differences which will be discussed later so that these dispersions are also treated as different families (see II-P and II-L in the figure).

The relative supernova rate is illustrated in table 2.3. It is apparent that about 70% of light curves is occupied by Type II supernovae and 80% of those possess the "plateau" behavior in light curves shape (see also [10, 148]). This major type of SN is called SN II-P whose spectrum is dominated by Balmer lines of Hydrogen. The typical time variations of luminosities are illustrated in Fig. 2.3. Comparing with other spectra types SNIIP is quite distinguishable. As a matter of fact, SN II-P is one of the most difficult object to determine the explosion properties due to its large uncertainty of rich hydrogen envelopes. In next section this most major population of light curve is especially focused for explaining the connection between its shapes and physical properties of SN ejecta.

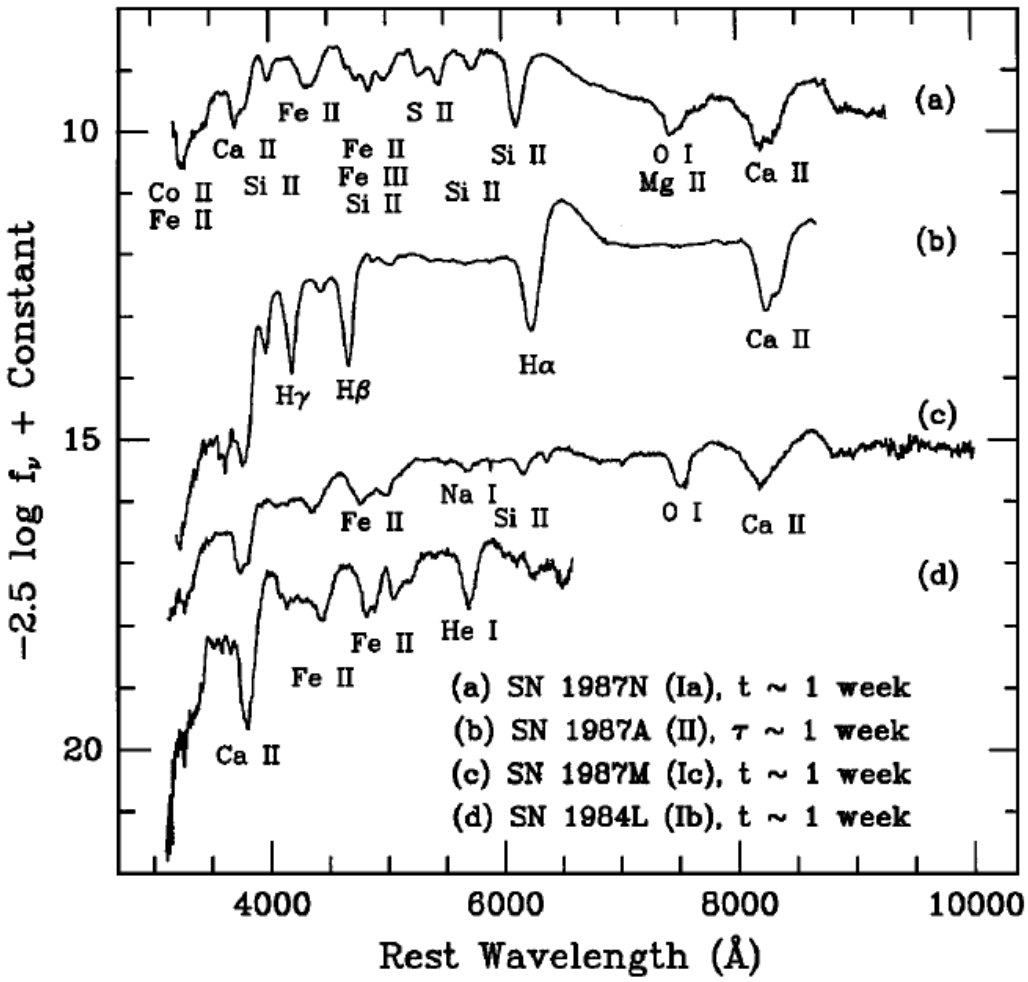

Figure 2.2: The typical supernova spectrum quoted from Filippenko et al.(1997) [113].

2.1.3 Shapes and Evolution stages

The purpose here is to see the correlation between light curve shapes and physical properties in SNe II-P. At first, it should be mentioned that the important fact which is common for all types of SN luminosities originate from shocked bulk fluids which are radiation dominated and also gamma-rays produced via radioactive decay chain from ^{56}Ni to ^{56}Fe. After shock breakout, the matters of envelope is transparent enough for photons so that radiation is able to escape from the bulk fluids.

As depicted in Fig. 2.3 the light curve feature of SNe II-P can be seperated into three epoches, (1) shock breakout,(2) peak and (3) tail phase in order. Firstly, the light curve depicts sharp spike, the maximum value is almost 10^{45}erg/s in UV band, and drops to 10^{42}erg/s soon after the shock breakout. The shock wave eruption heats the envelope up to 200,000K for about 2,000s which become responsible for radiation emission and declines to 30,000K after one day. There are only two observations for TypeIIP (SNLS-04D2dc, SNLS-06D1jd; [138]) and only one for Type Ib (SN2008D; [396]) in UV band. The direct observation of this shock breakout will aid to evaluate massive star radius in super giant phase which is barely determined via theoretical light curve modelings. It should be mentioned that the radio-active decay of ^{56}Ni and other heavy elements are also non-negligible contributions to increase the magnitude of light curves.

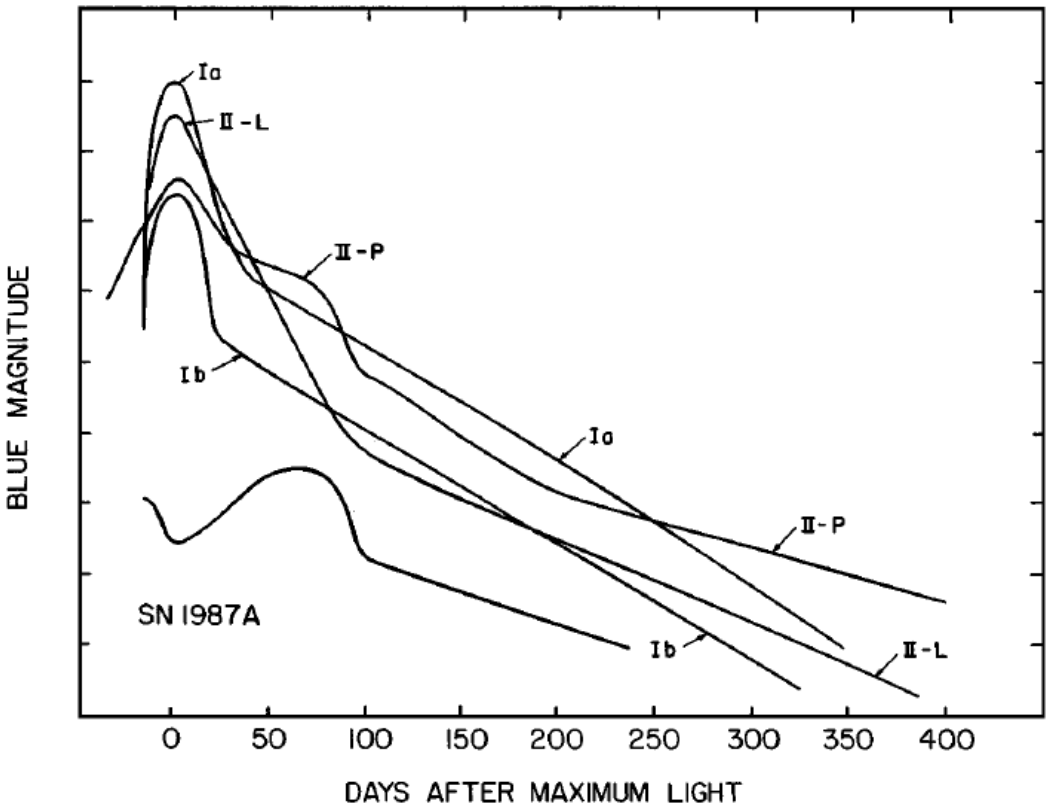

Figure 2.3: The typical supernova light curves quoted from Filippenko et al.(1997) [113].

Since the shock still heats up and ionizes the envelope matter immediately, the electrons make the shocked matter opaque so that the radiation can be approximated as the diffusive process. However, the shock expansion drives adiabtic cooling which dominates the photosphere position in early epoch so that the dynamical time scale is shorter than the diffusion time scale at first. This competetion of shock dynamics and radiation diffusive process determines the properties of peak shape appeared in light curve. The time scale of peak is about ten days which can be estimated easily by taking harmonic average of the dynamical times scale and diffusive process [172, 12, 94]. Furthermore, if a large amount of nickel mass is yielded the radio active decay provides non-negligible increase for the magnitude of light curve. The reason is because the first decay reaction

$$^{56}\mathrm{Ni} + e^- \rightarrow {}^{56}\mathrm{Co} + \nu_e + \gamma \qquad 1.7183\ [\mathrm{MeV}], \tag{2.1}$$

where the life times are $\tau_{1/2}$=6.075 days, is comparable to the width of peak time. After this peak epoch, the luminosity gradually decays and directly shows tail feature in SNIb/c cases.

In case of SNe IIP, their spectrum is blue which means high temperature ($\gtrsim 12,000$K) soon after peak. Ejecta still has more than 6,000K which is high enought for bound electron to escape from hydrogen atom during the passage of envelopes and atmosphere. This recombination front moves into the expanding envelope and last until temperature become too low to make this ionization.

The internal energy deposited by the shock is converted almost entirely to kinetic energy. Due to the ionization, luminosity is suppressed so that adiabatic expansion is good approximation. If shock is radiation dominant, the simple estimation of the internal energy

density of ejected matter, ε [erg/g], as a function of radius R can be derived when density is uniformly distributed, i.e. $\rho \propto \left(\frac{R}{R_0}\right)^{-3}$;

$$T \propto \left(\frac{R}{R_0}\right)^{-1}, \tag{2.2}$$

$$\varepsilon \propto \left(\frac{R}{R_0}\right)^{-1}, \tag{2.3}$$

where R_0 is the shock radius at the onset of explosion. Hence as long as no mass transfer take place the total internal energy is scaled with R^{-1}. Since the radius expands until about 10^{15}cm, i.e. factor of 100 for RSG and 1000 for BSG due to its smaller inital radius, the total internal energy left only $E_{\rm opt} \sim 10^{49}$erg and 10^{48}erg for RSG and BSG(e.g. SN1987A), respectively and most of them converted to kinetic energy.

As well as the first decay reaction given in eq. (2.1) whose life time is about 6.1day, the tail part of light curves are caused by high energy electron thermalized by γ -rays emitted from its daughter nucleus,

$$^{56}\mathrm{Co} \rightarrow {}^{56}\mathrm{Fe} + e^+ + \bar{\nu_e} + \gamma \qquad 3.72[\mathrm{MeV}] \tag{2.4}$$

where the life time is $\tau_{1/2}$=77.23 days and positron carries away 0.1159MeV per decay. Since the later life time is rather long, the light curve is still powered and decay gradually as tail shape for several years. The total energy release from these reaction chains are 2×10^{49}erg when the nickel ejecta mass is assumed as $M_{^{56}\mathrm{Ni}} \sim 0.1 M_\odot$. It is well known that these gamma-ray sources explain the tail profile well and are frequently used for the nickel yield. The emitted γ-rays, however, no longer fulfill the local energy depostion with matter since they can escape from the system well long after the maximum bright. It should be stressed that the light curve shape and spectrum depend on the spatial distribution of nickel mass.

It is noteworthy that the tail part of light curve results from other radio-active energy deposition, e.g ^{44}Ti, ^{57}Ni and ^{60}Co which possess further longer half life-time than ^{56}Ni. For instance, there is the youngest-known supernova remnant in Cassiopeia A (Cas A) which is located in our galaxy and emites strong γ- and X-ray signals from ^{44}Ti. Since the life-time is predicted more than 50 years, it is difficult to perform accurate experiments for radio-active decay rate in earth so that Cas A observation is frequently utilized. An abundance of titanium has been also investigated by many researchers [430, 490, 264] and the observed yield will be expected to give a clue to reaction rate of ^{40}Ca $(\alpha, \gamma)^{44}$ Ti [179]. Futhermore, since the shocked bulk fluid becomes more transparent than more than 25 years ago, several recent studies have revisited SN1987A for evaluating abundance and inner distribution of the remnant [200, 143, 381, 32].

2.1.4 Supernova parameters

As discussed in the previous section, the light curve is naively characterized by the competition of dynamical and diffusion time scales as well as nickel mass. Hence, the estimations of explosion energy, nickel mass and expansion velocity are important properties to understand the theoretical modeling for explosion mechanism and are usually extracted by light curve studies. It should be stressed that there are two major methods: semi-analytic and simulated light curve approachs. The former are obtained by decoupling the gas dynamics

Table 2.3: The relative frequency of core-collapse SN types discovered between 1998-2012.25 (14.25 yrs) in galaxies with recessional velocities less than 2000 kms^{-1}, quoted from [98].

SN Type	Number	Relative rate (per cent)	LOSS (per cent)
IIP	55 (70.5)	55.5 ± 6.6	$48.2\ ^{+5.7}_{-5.6}$
IIL	3 (3.8)	3.0 ± 1.5	$6.4\ ^{+2.9}_{-2.5}$
IIn	3 (3)	2.4 ± 1.4	$8.8\ ^{+3.3}_{-2.9}$
IIb	12 (15.4)	12.1 ± 3.0	$10.6\ ^{+3.6}_{-3.1}$
IIpec (87A-like)	1 (1.3)	1.0 ± 0.9	...
Ib	9 (11.4)	9.0 ± 2.7	$8.4\ ^{+3.1}_{-2.6}$
Ic	17 (21.6)	17.0 ± 3.7	$17.6\ ^{+4.2}_{-3.8}$
Total	100 (127)		

with radiation so as to separate spatial and temporal term in the internal energy of expanding matters while the latter uses density and temperature values from hydrodynamical calculation results.

In spite of its simplicity, physical modelings for reproducing light curve properties have successfully attempted by Arnett et al.(1980) [14] and Popov et al.(1993) [353] in semi-analytical ways. The typical observables, i.e. which are luminosity, $L_{\rm sn}$, light curve duration, $t_{\rm lc}$, and expansion velocity, $V_{\rm ej}$, are characterized by the explosion energy, $E_{\rm exp}$, total eject mass, $M_{\rm ej}$, presupernova radius, R_0, and opacity κ. from the scaling relations in those studies. Furthermore, Kasen et al.(2009) [205] found that from three fundamental assumptions: (1) homologous expansion (2) adiabatic evolution for ρ and T in radiation dominant system and (3) purely diffusion radiation process, i.e. expansion radius is equivalent to diffusion scale; the scaling relations for $t_{\rm lc}$ and $L_{\rm sn}$ are given by

$$\begin{aligned} t_{\rm lc} &\propto E_{\rm exp}^{-1/4}/M_{\rm ej}^{3/4}/\kappa^{1/2} \\ L_{\rm sn} &\propto E_{\rm exp}/M_{\rm ej}^{-1}R_0\ \kappa^{-1}, \end{aligned} \tag{2.5}$$

where κ is the opacity. This formulation is exactly same as those in the results of Arnett and surprisingly suitable for SNe Ib/c light curves.

On the other hand, when the spectra type is SN IIP the equations should take into acount the ionization of hydrogen and equation (2.5) may lead wrong scaling. Kasen proposed that it will be useful to put two additional conditions; firstly,

$$L_{\rm sn} = 4\pi R_{\rm I}^2 \sigma_{\rm SB} T_{\rm I}^4, \tag{2.6}$$

where $\sigma_{\rm SB}$ is the Stefan-Boltzmann constant, $R_{\rm I}$ and $T_{\rm I}$ are hydrogen ionized radius and temperature, respectively and, secondly, assuming the diffusion system size is as large as $R_{\rm I}$. These two conditions modifies the equations as follows;

$$\begin{aligned} t_{\rm lc} &\propto E_{\rm exp}^{-1/6} M_{\rm ej}^{1/2} R_0^{1/6} \kappa^{1/6} T_{\rm I}^{-2/3}, \\ L_{\rm sn} &\propto E_{\rm exp}^{5/6} M_{\rm ej}^{-1/2} R_0^{2/3} \kappa^{-1/3} T_{\rm I}^{4/3}. \end{aligned} \tag{2.7}$$

These scaling realtions are identical with those obtained by Popov and helpful to understand the dominant process of light curve formation and crude estimation of the important supernova properties (see more detail discussion in the original paper [205]).

Meanwhile, the simulated light curve method is based on using empirical relation ship between three light curve characters, the magnitude, velocity at the middle of plateau phase and plateau duration, and $E_{\rm exp}$, $M_{\rm ej}$, and R_0. Each properties is visualized in Fig. 2.4.

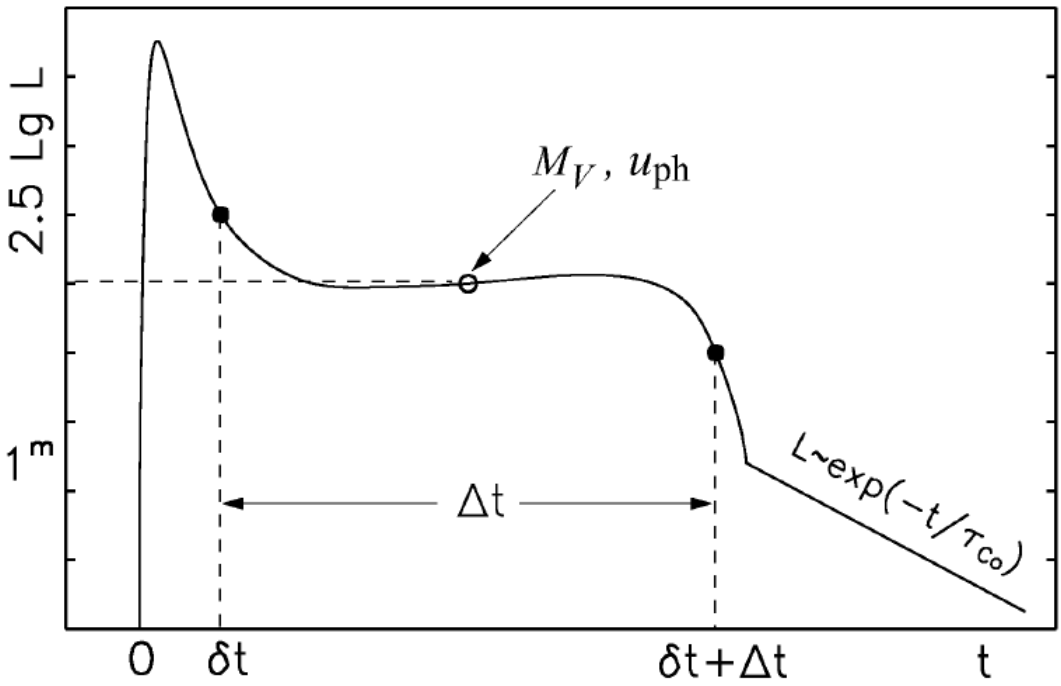

Figure 2.4: The schematic picture of typical SNIIP light curve shape and its characters. The illustration is taken from Nadyozhin et al.(2003) [300].

For instance, conducting the artificial explosion calculatons, Litvinova & Nodyozhin (1983) [254] found that the formulation of light curve shapes to the supernova parameters can be represented as follows:

$$\begin{aligned}
\log_{10} E_{\rm exp} &= 0.058V + 2.26\log_{10}\delta t + 2.79\log_{10} U_{\rm ph} - 4.275, \\
\log_{10} M_{\rm ej} &= 0.188V + 2.84\log_{10}\delta t + 1.73\log_{10} U_{\rm ph} - 2.412, \\
\log_{10} R_0 &= -0.596V - 0.911\log_{10}\delta t - 2.80\log_{10} U_{\rm ph} - 4.061,
\end{aligned}$$

where V, U_{ph} and δt denote the absolute magnitude, velocity and the width of plateau shape in light curve, respectively (see Fig. 2.4). This useful formulations are widely applied to other studies [151, 451] and the canonical explosion energy is determined in nearly 10^{51} erg.

The nickel mass amount of SN1987A is evaluted as nearly $0.08M_\odot$ which is slightly lower to $0.1M_\odot$. The eject nickel mass of SNII is usually in the range from 0.01 to $0.3M_\odot$ (Hamuy) with much larger scatters as well as kinetic energy comparing with other SNe types (see Fig. 2.5 and also [492, 313]) because of the large uncertainty of H envelope mass. Therefore massive stars which go through RSG are quite difficult to predict those fates. It should be stressed that the determination of eject mass is hardly predicted by this method since the plateau shape is also yielded by the radio-active decay of nickel so that the ambiguity of progenitor mass is still the outstanding issue especially in case of SNe IIP and (see [205] Bersten2010). Recently, there is interesting comparison of SN parameter determinations between these two methods in [343] (one may also need to refer to Pejcha2012 for following their methods). Figure 2.6 illlustrates the explosion energy and nickel mass distribution from the two introduced caribulations. It is interesting that the evaluation from semi-analytical approach gives smaller energy with similar amount of nickel while the observation errors are still larger than those differences.

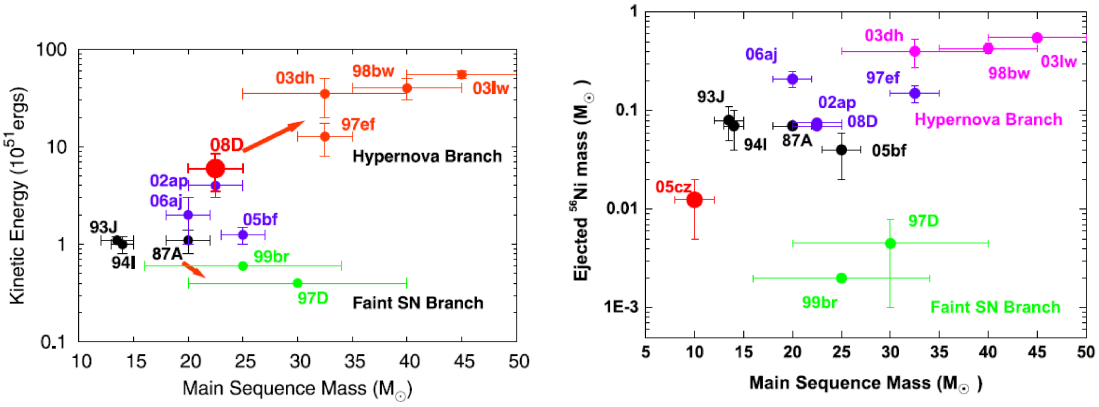

Figure 2.5: Progenitor mass distribution of observed explosion properties taken from [313]. The left and right panel show the explosion energy and nickel mass, respectively.

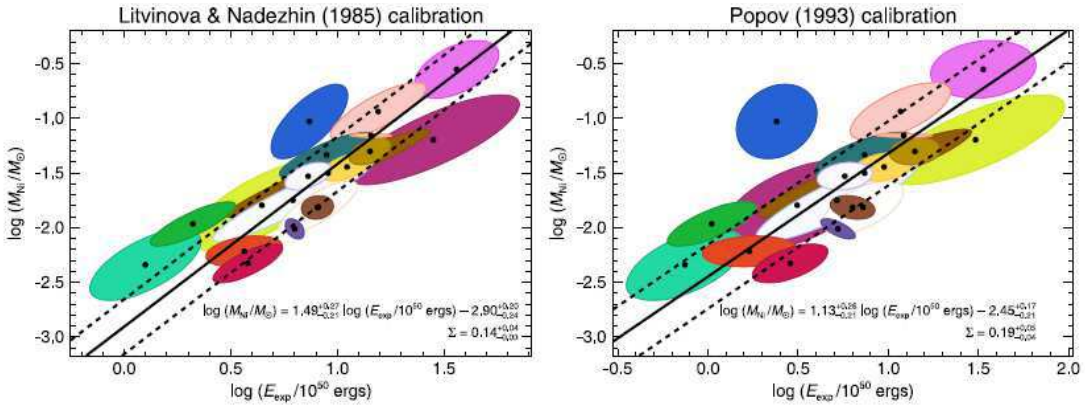

Figure 2.6: The observed explosion energy and nickel mass map with two different calibrations taken from [343]. The two explosion characters are estimated by [254] (left) and [353] (right), respectively and each black dot represent individual SNII. Colored elipsoids correspond to statistical errors attributing to distance and extinction uncertainties.

In fact, since the matter will become transparent much later after the maximum magnitude, the radation cannot be regarded as isotropic any more so that the diffusive process is no longer accurate. Instead, radiation transfer solver should be used to treat proper radiation characters. Furthermore, the photon radiations exchange momentum and energy with matters so that the basic equations of hydrodynamics is also influenced on the escaping radiations.

It is well known that there are two standard methods for numerical schemes: the Boltzmann solver which usually computes moment equations or stochastic process by Monte carlo method. There are several open-source for treating supernova light curves, e.g. CMFGEN [85] and SN (stellarcollapse.org) for the former. It is noteworthy that the latter numerical radiation transfer method is also adopted by various open sources, for instance, TORUS code [157] which is applied to massive star formation.

Here, CMFGEN is selected for introducing the difference between supernova and other radiation phenomena. CMFGEN, developed by Hillier, is originally in the concept of multipurpose atmospheric code for analyzing stellar wind spectrum and determine fundamental stellar parameters. The code has been applicable to O stars, WR stars, LBVs and even

A and B supergiants [174]. CMFGEN is extended to be available Type I/II supernovae [85, 86, 87, 173] as well as novae with few modifications such as

- photosphere dynamics,
- the correction of v/c,
- non-LTE ionization states with the complicated multi-lines due to the rich metal and
- the presence of γ-rays.

These components can be safely neglected in the wind profiles since they are sufficiently slower than light speed, associated with smaller size of nuclear set and absence of γ-rays.

The supernovae ejecta are also time dependent while winds are usually stationary. The time derivative term can be usually neglected when the matter velocity is considerable small compared with the light speed and optical depth, τ, is relatively small, i.e.

$$\frac{t_{\rm ph}}{t_{\rm dyn}} = \frac{\tau \delta R/c}{R/v} \ll 1$$

where $t_{\rm hyd} = R/v$ and $t_{\rm ph} = \delta R/c$ are expansion time scale of star and typical propagation time of photon, respectively. This effect should be, however, implemented if optical depth of system become sufficiently large. Then, the ratio of two time scales become almost unity so that it can be no longer neglect time derivative term and the fully time-dependent transfer equation is required. Moreover, even the matter velocity is small, supernova spectra are strongly influenced by this time-dependent terms (see [347, 172]). It is noteworthy that using this code, explosion energy stems from photospheric velocity and the velocity at the outer edge of oxygen-rich shell give constraints on progenitor mass. Moreover, the dependence of the stellar evolution parameters is explored in Dessart et al.(2013) [88] by studying SN1999em light curve.

On the other hand, monte carlo radiation transfer (MCRT) method are widely used in the current astrophysical phenomena. It is first applied by Avery & House (1968) and Caroff et al.(1972) [19, 64] to investigate radiation in stellar wind and . This approach allows one more easily to obtain spectrum and polarization information as well as luminosity which are the imprint of velocity and morophology, respectively, if statistical noises are adquently suppressed.

The basic ideas and techniques are reported by the series of Lucy's papers [255, 2, 256, 257, 258, 259] and the reference therein. Recently, the time-dependent multi-dimension radiation hydrodynamic simulations have been developed by many groups since the computational progresses are considerable. As a result, this powerful numerical tool is expected to yield more precise match with observation probes.

Neutrino should be evaluated properly via radiation transfer calculations as well as photon, so that the detail introduction of numereical implement is addressed in appendix B.

2.1.5 Progentior mass determination

In general, one of the most challenging astrophysical issue is a determination of progenitor mass. For last several years, however, observations allow us to know the initial condition of some supernova explosions. Smartt et al.(2009) [390] have examined progenitor candidates of type IIP supernova over 10.5 years period in limited volume (28 Mpc). They utilize direct pre-explosion images in order to determine progenitor masses for 20 events of SNeII-P in which 5 cases had clear red supergiants (RSG) images (see also [270, 10]). They run stellar evolutionally code STARS (Eldridge et al.(2004) [99];http://www.ast.cam.ac.uk/ stars) to find equivalent luminosities at end point of helium burning or before begining of neon burning stages to each data. As a result, their computation showed that progenitor masses are in range of $8M_{\odot} \lesssim M \lesssim 17M_{\odot}$, thus no progenitor heavier than $20M_{\odot}$ was found. This fact conflicts with the expected population suggested from initial mass function (IMF) but is coincide with Kochanek et al.(2008) [219] and is called the "RSG problems" and recent observation can not find the relatively heavy main sequence stars [389]. Another scenario is the missing mass range stars explode not as type-IIP but as type-IIL or -Ib [98].

According to Hamuy et al.(2003) [151], they examined several numbers of type II-P and concluded that some possess large progenitor mass up to $\sim 50M_{\odot}$. On the other hand, Kasen et al.(2009) [205] pointed out that the effect of radioacive decay ^{56}Ni sustain plateau duration longer and the progenitor with copious hydrogen envelope mass predicted by [151] would not be neccessary.

Recently, there are some groups who use color magnitude diagram (CMD) to determine progenitor masses ([294, 465]: originally, [142, 20, 71]) since it is a good indicator of steller object ages. For instance, Murphy et al.(2011) [294] determined a progenitor mass of SN 2011dh which located in M51 galaxy. Investigating star formation rate (SFH), They found that the most recent star formation burst occured in 17 Myrs ago and the progenitor of SN 2011dh may be likely to be born in this age. Therefore, they concluded that the progenitor mass in zero age main sequence (ZAMS) is $M_{\rm ZAMS} \sim 13M_{\odot}$ by running stellar evolution code "Padova". It is noteworthy that Williams et al.(2014) [465] revisited 17 historical SN progenitor and determine 11 additional masses precisely. They infer that no massive star more than $20M_{\odot}$ is present which is coincide with the previous studies.

However, these analyses completely rely on a single stellar evolution outcomes which are quite sensitive to its initial condition as well as numerical treatment. Furthermore, the presence of the fast rotation or strong overshooting inside massive stars make the helium core mass larger and hydrogen envelope much smaller which predicts rather small progenitor mass. Hence, it may takes longer time for much more precise progenitor mass determination so that one should wait for further numerical development.

2.2 Scenario

Historically the first numerical study of CCSNe is started by Colgate & White (1966) [73] and confirmed that the enourmous gravitational energy $E_g \sim 10^{53}$ erg is tapped by the sudden implosion, core collapse, and immediately converted to neutrino energy by almost 99% in the end of massive stars. The rest of energy is expected to become "kinetic" energy of ejecta when the shock, produced by core bounce, reaches towards the stellar envelope with leaving nascent neutron stars or black holes. Unfortunately, no study has established the complete theory of CCSNe owing to not only entanglement of micro and macro physics but also highly accurate numerical treatment so as to resolve such 1% energy residue.

There are plenties of scenarios which attempt to provide CCSNe explosions. One of the most promising scenario for CCSN is neutrino heating mechanism proposed by Bethe & Wilson (1985) [27]. Since its emission is confirmed from SN1987A, the neutrino is thought to play a key role in accelarating blast wave. On the other hand, magneto-rotation (see [221] and reference therein) and acoustic mechanisms [55] are the other candidates for the theory which are based on the energy conversion from roataion and magenetic field to kinetic and g-mode excitation of PNS powering stalled shock via acoustic wave, respectively. There are, however, several problems in these two scenarios. The former require unrealsitic initial conditions such as miliseconds rotation period, extremely large magnitude of magnetic field and also relies sensitively on the configuration of the magnetic field. Meantime, the latter is confirmed by only few numerical studies whose hydrodynamics code is similar to [55]. Furthermore, the excitation takes relatively long time which is another reason of missing the instability due to the limitation of computational source. Therefore, the neutrino heating mechanism is still employed in this paper.

The present SNe modelings have remarkably improved since Wilson's calculation and showed the importance of neutrino reactions, neutrino transport, equation of states (EoS) of nuclear density, multi-dimensional fluid mechanics and general relativity.

Due to such physical and numerical properties, however, one may encounter several difficulties in understanding the theory and hardly follow the difference and improvement of state-of-the-art modelings. Therfore, it might be helpful to start from a brief review of neutrino driven mechanism before moving to the current sophisticated numerical simulations. One who has already known the basic ideas of the mechanism should skip this section and is recommended to read the next section.

The outline of this section is depicted in Fig. 2.7 which is taken from Janka et al.(2007) [198]. The figure illustrates the series of snapshots from the onset of collapse to several seconds after explosion with enclosed mass in horizontal direction and radius in vertical direction for the each panels. The explanations are mainly consisted of following three parts:

(a) from the onset of core collapse to the standing accretion shock which correspond to the series of panels from No.1 to No.4 in Fig.2.7,

(b) shock heating period (the bottom left panel, No.5, in Fig. 2.7) and

(c) the shock ejection epoch (the bottom right panel, No.6, in Fig. 2.7).

For more detailed discussion, there are also excellent reviews [223, 196, 49] and reference therein.

2.2.1 From collapse to stalled shock

Massive stars with more than about $10M_\odot$ have relatively short life time ($\lesssim 10^{6-7}$ years), proceed to late nuclear burning stages beyond carbon-oxygen burning in which neutrino process becomes important and finally reach sufficiently high central temperature so that silicon burning takes place and produce iron group elements. After the formation of a iron core, they no longer continue the subsequent burning since iron groups have maximum nuclear binding energy. As a consequence, the massive stars halt to create heavier nuclei and lose the aid of heating resource which compete with huge central gravitational force. Therefore, after the silicon depletion the core is supported by only degenerate electron pressure. Meanwhile, the core gradually loses its energy by weak interaction, mainly electron capture toward neutron rich heavy elements, e.g. isotopes of Ni, Co, Fe, Mn [164]. As a result, the reduction of electron number induces the onset of core contraction (see the top left panel in Fig. 2.7). In this period weak interactions such as pair and plasmon process are still taking place as main cooling sources. As a result, the slow contraction of core increase the central density and temperature. As contraction proceed for several hours, central temperature raise more than 5×10^9K and the heavy iron groups commence to capture e^- more rapidly. Hence, the adiabtic index $\gamma_{\rm ad}$ becomes less than $\frac{4}{3}$ which is likely to violate hydrostatic and induces the serious accelaration of core contraction. This phenomena is so called core collapse and numerical simulations usually start from this pre-supernova stage (the top left panel of Fig. 2.7).

The infalling matters are highly compressed and undergo photodissociations,

$$^{56}Fe + \gamma \longrightarrow 13\alpha + 4n - 124.4\text{MeV}, \tag{2.8}$$

$$\alpha + \gamma \longrightarrow 2p + 2n - 7.4\text{MeV} \tag{2.9}$$

when temperature reaches $T \gtrsim 7.0 \times 10^9$K. This endothermic reaction also exhausts thermal energy and lead to further runaway falling toward the center of star.

It should be noted that electron capture reaction generate the electron type neutrinos from following process;

$$e^- + A \longrightarrow \nu_e + A', \tag{2.10}$$

$$e^- + p \longrightarrow \nu_e + n. \tag{2.11}$$

As the central density exceed around $10^{11} - 10^{12}\,\mathrm{g\,cm^{-3}}$, these electron type neutrinos begin to be trapped inside the core (see the top right panel in Fig. 2.7). The reason why this neutrino trapping occurs is because the presence of coherent scattering with nucleus (neutral current process), especially isoenergetic scattering process with nuclei, starts to dominate the weak interaction process. The cross section of the coherent scattering $\sigma_{\rm sc}$ is propotional to the square of the mass number of nuclei, A, hence,

$$\sigma_{\rm sc} \propto A^2. \tag{2.12}$$

The mean free path, $\lambda_{\rm sc}$, becomes shorter than the core radius, $R_{\rm c}$, so that the neutrino rarley escape from the iron core [375]. Moreover, when one compare the dynamical timescale, $t_{\rm dyn}$, with the neutrino diffusion timescale, $t_{\rm diff}$, these two satisfy $t_{\rm dyn} < t_{\rm diff}$ so that neutirnos are confined inside the infalling matters. There are further discussion about this neutrno trapping [375, 221].

During this collapse phase the matter demonstrates two trends of infall velocity; one is homologous collapse ($v_{\rm ic} \propto r$) which occur at the most central portion of core and the other is quasi-free fall ($v_{\rm oc} \propto (M_r/r)^{-1/2}$) for the outer core [478]. These two inner and

outer core region are roughly characterized as subsonic and supersonic, respectively, which implies important meaning in terms of hydrodynamics, i.e. the shock formation.

The neutrino trapping continues until the central density reached nuclear density ($3.0 \times 10^{14}\,\mathrm{g\,cm^{-3}}$ or $0.16\mathrm{fm}^{-3}$). At this density nuclear repulsive force starts to work against the supersonic infall matter, forms strong discontinuity between inner and outer core and launchs a shock wave outward. This phenomena is called bounce and commonly occur near Chandrasekhar mass,

$$M_{\rm ic} \approx 1.456(Y_l/0.50)^2 \approx 0.5 M_\odot\,, \tag{2.13}$$

where average lepton number fraction, Y_l, in central part of core, is roughly 0.35. The core is, thus, essentially divided into inner core and outer core by the bounce position. While the blast wave propagates against the outer core accretion, infalling matters, i.e. heavy nuclei, are immediately heated and melted into nucleon. When shock pass through the neutrino sphere surface, opacity reduce significantly low so that trapped neutrinos escape from the inner core. This causes huge neutrino luminosity $L_\nu \gtrsim 10^{53}$ erg/s, named neutronization burst, and sustains about few times 100ms which will be strong observational signal.

In early 80's this energetic shock , $E_{sh} \sim 10^{52} \left(\frac{M_{ic}}{0.5M_\odot}\right)^2 \left(\frac{R_{ic}}{10\mathrm{km}}\right)^{-1}$, succeed in penetrating the entire outer core [23, 21]. This simple scenario is well known as "prompt explosion mechanism". After the report of this prompt explosion, more realistic physics are incorporated in the subsequent numerical simulations since these previous studies employed

1. small iron core size ($M_{\rm Fe} \sim 1.1 M_\odot$) for pre-supernova stage,
2. too soft equation of state (EoS) which usually adopted incompressibilty $K = 180$MeV and
3. neglecting neutrino-electron scattering process which enhances the energy loss of blast wave [38, 39].

Since the rest of iron core still keeps on falling towards the blast wave, even more accretion matters go through photo-dissociation and dissolve into nucleon after which consume large amount of energy behind the shock front. Furthermore, the dynamics is also impeded by strong ram pressure of infalling matter and neutrino inelastic process ([282]; see table 2.4) so that it finally ends up with standing accretion shock. It should be noted that higher incompressibility yields smaller gravitional potential well which makes the situation even worse. Therefore, larger iron core, stiffer equation of state and the additional neutrino process lead serious negative effect for the successful shock breakout and many previous studies followed this failure of "prompt explosion mechanism" [171, 31, 452, 54, 38, 299, 22, 418].

Fortunately, Bethe & Wilson (1985) [27] and Wilson (1985) [466] have proposed the shock revival possibility which is known as neutrino heating mechanism and thought to be the most promising theory at present. The concept of this mechanism is the nergy exchange between the nucleon below the shock front and neutrinos emitted from proto-neutron star surface. The main process to activate the stagnant shock wave are neutrino-nucleon reactions presented below;

$$\nu_e + n \;\longleftrightarrow\; p + e^-\,, \tag{2.14}$$
$$\bar{\nu}_e + p \;\longleftrightarrow\; n + e^+\,, \tag{2.15}$$

where the right and left directions infer heating and cooling reactions, repectively. Between PNS surface and the stagnent shock wave, it is well known that there are positive net

heating area so called gain region which aid to push the stagnant shock and its presence is guaranteed by means of analytical method (see more detail discussions in the next section or in [195]).

2.2.2 Failure 1D neutrino driven simulations

After this successful shock heating scenario, supernova modelers started to concern with more exact treatment of neutrino since the matter between PNS and shock is semi-transparent so that their propagation is neither diffusive nor free streaming. Hence, the distribution function of neutrino should be properly computed by solving radiation transport. In those days the spacial dimension of transport was, however, limited to only 1D since the distribution function should depend on also momentum spaces as well as time. Therefore, if one tries to carry out nwutrino transport solver in 3D, the total number of independent variables is seven which is too expensive in terms of numerical aspects (see appendix B).

Although the complexity is relaxed by spherical symmetry, it is still challenging and the gradual development has been conducted so far. For instance, neutrino distrbution function is extended from averaged monochromatic dependence, which is obtained by gray (or grey) transport [51, 168, 53, 416, 417, 124, 128], to multi-group energy bins which provide even more problematic in the practical calculation (see appendix B). In addition, the number of reaction processes are increased which directly affect collision terms in Boltzmann equation. The velocity corrections to advection part of Boltzmann equaiton has been also included so as to approximately take into account either SR or GR.

Thanks to the considerable endevore, the numerical treatment for neutrino transport has undergone various development and finally reached the fully GR neutrino transport coupled with GR hydrodyanamics in spherical symmetry. For instance, a new numerical code of general relativistic-radiation hydrodynamics under spherical symmetry has been developed by Yamada (1997) [479] and Yamada et al.(1999) [480] for supernova simulations. The code solves a set of equations of hydrodynamics and neutrino transfer simultaneously in the implicit way, which enables us to have substantially longer time steps than explicit methods. This is advantageous for the study of long-term behaviors after core bounce.

The implicit method has been also adopted by Liebendörfer et al.(2004) [248] in their general relativistic-radiation hydrodynamics code. They have taken an operator splitting method so that hydrodynamics and neutrino transfer could be treated separately. The further details about recent transport development are shown in appendix B.

It should be noted that, because of its complexity, simple alternative approaches are also invented, e.g. leakage scheme [103] and light bulb approximation [199]. The former calculates neutrino energy loss and is usually applied during the collapse phase while the latter enables to handle "heating" reactions regarding the luminosities and average energies which is irrespective of radius. Furthermore, anlaytical heating and cooling neutrino source terms are also employed by many researches. These approximations are still used even in present simulations due to the convienent expressions.

Among those early realistic calculations there are several discoveries which are not present in the prompt explosion calculations. The one of the important discoveries is that the neutrino luminosity is emitted not only from the PNS cooling but also from the mass accretion on PNS surface. The contribution is called the accretion luminosity, $L_{\rm acc}$ and this additional energy release of gravity can be estimated as

$$L_{\rm acc} \sim G\frac{M_{\rm PNS}\dot{M}}{R_{\rm PNS}} \tag{2.16}$$

which increase the heating rate and often provide non-negligible contributions [250, 48, 322].

The equation of state (EoS) has been improved from the parametric approach [421] to more realisitic equation of states. At present they are well known as Lattimer-Swesty EoS [241] and Shen EoS [385] and often identified as soft EoS for the former and stiff EoS for the latter. The realisitic 1D simulation has demonstrated that the application of "soft" equation is much favorable for the shock revival which is carefully discussed in section. 2.3.

Moreover, general relativity has been expected to provide deeper potential well which also affect the initial strength of blast wave and generate higher neutrino energies due to compact and hotter proto-neutron star surface. As a result, GR is likely to increase the likelyhood of shock revival and this predection is now well confirmed by various researches [359, 47, 245]. On the other hand, neutrino electron-scattering process also drastically impacts shock dynamics (see table 2.4). The implement of more appropriate neutrino reaction process, precise numerical transport scheme and further realisitic equation of state than those in Wilson's computation ends up with preventing the successful explosion.

Although the profound comprehension has been obtained by these realization, many studies confirmed no explosion in spherical symmetry [284, 360, 433, 248, 411] except for the progenitor with oxygen, neon and magnesium (ONeMg) core whose explosion energy is smaller by an order than that from typical observation [216].

The reason why the early Wilson numerical computations succeeded in shock revival is because they applied artificial convection around neutrino sphere which enhance neutrino luminosity and also help escaping higher neutrino average energies confined inside opaque regime which is expected as a multi-dimension effect. Although Keil et al.(1996) [208] and Bruenn et al.(2004) [42] pointed out the possibility of chemical gradient driven instablity known as neutron fingers, no large-scale overturn around PNS surface is confirmed by the more realsitic calculation [84] (see also section. 2.4).

In addition, it should be noteworthy that in Wilson's calculation the evolution of mean neutrino energies or luminosity after 1sec from bounce is implausible because these neutrino properties usually increases via PNS core contraction. The neutrino luminosity also should gradually declines which is not seen in their result.

2.2.3 Neutrino contribution to shock revival

Before introducing the developments after the spherical symmetry computation failure, the question whether gain region exists or not should be discussed. Fortunately, the answer is likely to be "yes" from simplified analytic formulation provided by [195]. Their remarkable discussion proceed as follows.

First of all, the neutrino absorption rates for nucleon $1/\lambda_\nu$ is function of neutrino energy, ϵ, and given as following formulation:

$$\frac{1}{\lambda_\nu(\epsilon)} = \sigma_0 \eta_\pm \frac{3g_A^2 + g_V^2}{4} \left(1 - f_{\rm FD}(\epsilon \pm \Delta,\ \pm\mu_e)\right) \frac{(\epsilon \pm \Delta)^2}{m_e^2 c^4} \tag{2.17}$$

$$\times \left(1 - \frac{m_e^2 c^4}{(\epsilon \pm \Delta)^2}\right)^{\frac{1}{2}} \Theta\left(\epsilon \pm \Delta - m_e c^2\right) \tag{2.18}$$

$$\eta_\pm = \int \frac{2d^3p}{(2\pi)^3} F_n \left(1 - F_p\right) \tag{2.19}$$

where σ_0 is typical cross section of neutrino nucleon cross section, $1.76 \times 10^{44}{\rm cm}^2$, g_V and g_A are vector and axial vector coupling constants and Δ is the mass difference, thus $\Delta = m_n c^2 -$

$m_p c^2$, respectively. Moreover, the terms $\Theta(x)$, $f_{\rm FD}(\epsilon,\mu)$ and $\eta_\pm$ indicate Heaviside function, the Fermi-Dirac distribution and the degeneracy factor, respectively. Furthermore, the subscript signs are represented as electron type neutrino and anti-neutrino, respectively.

As a consequence, the heating rate as function of neutrino energy, ϵ, is evaluated as following:

$$Q^+_{\nu_i} = \frac{3g_A^2+g_V^2}{4}\frac{\sigma_0 c\, n_j}{(m_e c^2)^2}\int_0^\infty d\epsilon_\nu \frac{2\pi}{(hc)^3}\epsilon_\nu^2 \int_{-1}^{+1} {\rm d}\mu\, f_{\nu_i}(\epsilon_\nu,\mu)\,\epsilon_\nu^3 [{\rm erg/cm^3/s}]\,, \tag{2.20}$$

where subscript i denotes the type of neutrino, $\nu_i = \nu_e$, $\bar{\nu_e}$, and j is for nucleon. The expression of $Q^+_{\nu_i}$ can be rewritten by using luminosity L_{ν_i}, average neutrino energy $\langle\epsilon^2_{\nu_i}\rangle$ and averaged flux factor $\langle\mu_{\nu_i}\rangle$;

$$Q^+_{\nu_i} = \frac{3g_A^2+g_V^2}{4}\,\sigma_0\, n_j\,\frac{\langle\epsilon^2_{\nu_i}\rangle}{(m_e c^2)^2}\frac{L_{\nu_i}}{4\pi r^2\langle\mu_{\nu_i}\rangle}[{\rm erg/cm^3/s}]\,, \tag{2.21}$$

where n_p and n_n are proton and neutron number densities, respectively, or

$$q^+_{\nu_i} = \frac{3g_A^2+g_V^2}{4}\,\sigma_0\, Y_j\,\frac{\langle\epsilon^2_{\nu_i}\rangle}{(m_e c^2)^2}\frac{L_{\nu_i}}{4\pi r^2\langle\mu_{\nu_i}\rangle}[{\rm MeV/nuc/s}]\,, \tag{2.22}$$

Thus the total heating rate $q^+_\nu = q^+_{\nu_e} + q^+_{\bar{\nu_e}}$ is

$$q^+_\nu \approx 110\left(\frac{L_{\nu_e,52}}{r_7^2\langle\mu_{\nu_e}\rangle}\langle\epsilon^2_{\nu_e,15}\rangle Y_n + \frac{L_{\bar{\nu_e},52}}{r_7^2\langle\mu_{\bar{\nu_e}}\rangle}\langle\epsilon^2_{\bar{\nu}_e,15}\rangle Y_p\right)[{\rm MeV/nuc/s}]\,. \tag{2.23}$$

On the other hand, the cooling rate at each radius is given as follows;

$$Q^-_\nu = \frac{3g_A^2+g_V^2}{8}\frac{\sigma_0\, c}{(m_e c^2)^2}\int_0^\infty {\rm d}\epsilon\,\epsilon^3\left(n_p\frac{{\rm d}n_{e^-}}{{\rm d}\epsilon}+n_n\frac{{\rm d}n_{e^+}}{{\rm d}\epsilon}\right), \tag{2.24}$$

$$= (3g_A^2+g_V^2)\,\frac{\pi\ \sigma_0\, c\ (kT)^6}{(hc)^3(m_e c^2)^2}\,\frac{\rho}{m_{\rm u}}\times[Y_p\mathcal{F}_5(\eta_e)+Y_n\mathcal{F}_5(-\eta_e)] \tag{2.25}$$

where the distributions of relativistic electrons and positrons are given by

$$\frac{{\rm d}n_{e^\pm}}{{\rm d}\epsilon} = \frac{8\pi}{(hc)^3}\frac{\epsilon^2}{1+\exp(\epsilon/kT-\eta_{e^\pm})}\,. \tag{2.26}$$

and $T = T(r)$ is the local gas temperature and $\eta_{e^\pm}$ the degeneracy parameter of electrons or positrons, defined as the ratio of the chemical potential to the temperature. Equation (2.25) can be rewritten as

$$q^-_\nu \approx 145\,\frac{\rho}{m_{\rm u}}\left(\frac{kT}{2\,{\rm MeV}}\right)^6\ \ [{\rm MeV/nuc/s}] \tag{2.27}$$

hence, q^-_ν is proportion to T^6 which is equivalent to $q^-_\nu \propto r^{-6}$.

Much simpler interpretation is possible for the cooling rate as function of radius [27]. Assuming isotropic black body radiation, energy exchange between matter consisted of N_b number of nucleon and neutrino can be expressed as $q \sim \sigma_e F_{\rm bb}/N_b$ MeV per nucleon per

sec, where $F_{\rm bb}$ is the expected radiation flux of neutrino and cross section σ_e is interpreted as the probability of conversion from matter to neutrino. Using this relation, one can obtain

$$\sigma_e \propto \epsilon^2 \propto T^2 \tag{2.28}$$

$$q_\nu^- \sim \sigma_e acT^4 \frac{1}{N_b} \propto T^6 \tag{2.29}$$

Since temperature profile holds following relation: $T \propto r^{-1}$, one obtains the same radius scaling relation for the cooling rates.

Hence, eq. (2.23) and (2.27) represent that the cooling rate has much steeper power-law profile than the heating rate. As a result, there is a gain radius where the neutrino heating overcomes the cooling below the shock front [195].

The temperature near the PNS surface where pressure is matter dominant keeps relatively high value whereas those near the shock is sufficiently low due to the radiation dominant state so that there is a certain transition point where the net heating rate changes from negatiave to positive value. From this evidence, the neutrino heating mechanism has been thought to be one of the most promising candidate to revive the stagnent shock and produce the canonical explosion.

Equation (2.23) is really convenient to understand the essential part of neutrino heating process. First, the heating rate q_ν^+ drops by r^{-2} because of simple neutrino flux conservation with modification of inverse flux factor $1/\langle\mu_\nu\rangle$. The other point of view is that equation (2.23) visualize three important component, namely, the luminosities L_ν, flux factor $\langle\mu_\nu\rangle$ and rms energy $\langle\epsilon_\nu^2\rangle$.

Most of researchers who engage in developing the neutrino solver are looking forward to achieving the correct picture of neutrino interactions for CCSNe modeling. They pay attention to how these physics alter from the simple description such as leakage and light bulb approximation and which ingredients in eq. (2.23) provides the advantage of explosion when the dimension is extended. Moreover, the different solvers often encounter contradictions with each other (see appendix B) so that further numerical studies are also necessary.

2.2.4 The discoveries after the realistic 1D calculations

As shown in the previous section, the main problem of neutrino heating mechanism is the competition between mass accretion and neutrino heating effeciency from the PNS which is drawn in the schematic picture of the situation in Fig. 2.8. The failures under spherical symmetry have shown that the neutrino heating efficiency is not sufficient to overcome the strong ram pressure, i.e. high mass accretion rate $\dot{M}$, at any time after core bounce. As a matter of fact, the open question is now turned out to be whether neutrino heating mechanism is the most likely candidate or not. If still so, it is crucial to evaluate how much heating rate is required to reactivate the stalled shock.

An one great insight is provided by Burrows & Goshy (1993) [52] who performed the parametric research of the mass accretion rate $\dot{M}$ and the neutrino luminosity L_ν.
Assuming simplified spherical steady shock flow between the shock face and PNS surface, the basic equations are simplied in the series of ODE. They found that in $\dot{M}$-L_ν plane, there is a certain boundary curve which isolates parameter spaces where the solution is present from absent. This curve is so called neutrino critical luminosity curve, or only critical curve (see the left panel of Fig. 2.9). It should be noted carefully that the non-solution region corresponds to explosion since those neutrino luminosity is present above critical curve. Hence, it is natural to assume that the stagnent shock revives if the parameters pair ($\dot{M}$, L_ν) once lie above this peculiar curve.

The studies concerned with critical curve yield the expectation of success in shock revival via neutrino heating mechanism since CCSNe nature seem to require only slight enhancement of neutrino luminosity, several times 10% (see O'Connor et al.2011 [321] for instance), or reduction of flux factor in the same extent.

The further studies are performed via linear analysis for both radial and non-radial perturbations [481, 121, 344, 108]. These studies have infered that the perturbations induce hydrodynamical instabilities such as convection or the new shock instability, standing accretion shock instability (SASI), which is discovered by Blondin et al.(2003) [30] and reduce the value of critical curves, thus support the shock revival [325, 291, 193, 131, 77, 152]. The reason why the multi-dimensional flow is preferred can be explained by the simple discussion about the ratio of advection time scale, $\tau_{\rm adv}$, and heating time scale, $\tau_{\rm heat}$, in the gain region, thus $\tau_{\rm heat}/\tau_{\rm adv} \lesssim 1$. The multi-dimensional flow patterns could enhance the residual time scale inside the gain region and the failure in spherical symmetry is attribute to short advection time scale. The instabilities lead to high entropy bubble and may expedite pushing shock outward. If one adopt relatively light progenitor mass, there are simulations which showed shock revival but much smaller explosion energy ($E_{exp} \sim 10^{49}$ erg) [266, 412, 426]. It is interesting that, although SASI and/or convection help matter heating compared with 1D, there are some discrepancy between 2D and 3D in outcomes [317, 153]. Furthermore, the presence of SASI is also doubted by some recent numerical results (see more detailed discussion in appendix C).

In terms of mechanism, however, the question about which instability is dominant for the revival is still in the debate (see the detailed discussion in appendix C and also section. 2.5).

It should be stressed that these semi-analytical researches are based on not realistic transport but simpler neutrino treatment, for instance, the light bulb approximation which usually assume Fermi-Dirac neutrino distribution and free streaming propagation [325, 193, 291, 153, 108, 75, 152]. The simple heating and cooling rate as functions of radius which is derived in the previous section, is also handful method in the investigation of instability characters. These methodology not only save the computational resource but also can control the way of heating which can isolate the influence from other complicated physical ingredients. The light bulb approximation or other analytical neutrino heating and cooling formula , hence, are suitable for studying this generic trends of critical curve.

For the luminosity enhancement there are several ideas suggested by previous studies; the presence of accretion luminosity which is a contribution from accretion matter on neutrino sphere, PNS surface convection which dredges up the hotter interior matter, GR effect which makes gravitational potential well deeper.

Furthermore, the realistic calculations in 1D demonstrate important insights for the individual effect of neutrino process. In addition to the reaction of nucleon absorption and emission, one of the important process in supernova modeling is inelastic scattering with free electron and positrons [282]. Both electron type neutrino and anti-neutrino obtain energy from $e^{\pm}$, so that the total cooling rate increases which is unfavorable for the explosion.

In contrast, nucleon bremsstrahlung [415, 57, 155] and flavor changing reactions [45, 48] slightly enhance neutrino luminosity as well as nucleon-neutrino scattering, though not suffecient for the shock revival. According to Yamada et al.(1999) [480], nucleon correlation [376, 187, 357, 358, 209, 199], nucleon recoil and blocking [379] and nuclear interaction effects in neutrino process [354, 364] also reduce opacities.

Some neutrino processes and their impact are summarized in table 2.4. One can easily see that each process has competed and the net effect is quite unpredicable. In addition, the

active electron capture on heavy elements reduce the total lepton number inside the core. This phenomena makes the size of inner core smaller which are unfavorable for obtaining successful explosion.

2.2.5 Short summary for neutrino heating mechanism

Here the short summary is presented for the stalled shock phase. After the rejection of prompt mechanism the neutrino driven mechanism turns out to be the most promising scenario for CCSNe explosion. In early 00's sophisticated numerical simulations has been carried out in order to carefully examine the physical ingredient, such as neutrino transport and reaction processes, supra-nuclear density EoS and also the effect of general relativity in spherical geometry.

Further extension of spacial dimensions also has exposed the new hydrodynamical instability, though there are few cases which succeed in explosion without any artifact in neutrino transport.

At the same time, the runaway condition has been investigated by semi-analytical approach and critical curve has been utilized as good indicator of explosion. The accurate physical condition for shock revival, however, is still challenging issue. Among recent studies there are other possibilities of criterion for run away condition ([344, 292]; see also section. 2.5).

There may be three improvement from 1D case;

1. enhancing the duration of heating time
2. larger efficiency of heating rate
3. stronger and more energetic initial shock wave for the less additional internal energy to relaunch the stalled shock

Fortunately, the first idea has been confirmed from the many experimental researches that the critical luminosity is reduced by multi-dimensional fluid motion. The reason of this reduction is mainly owing to non-radial motion increasing residual time in the gain region. However, there are two typical instabilities in CCSNe and which instability dominantly aids the explosion has still remained uncertain. Further discussion is illustrated in appendix C.

If one recalls eq. (2.23), the second idea is identical to enhancement of luminosity or/and average energy ϵ_ν or reduction of flux factor μ_ν. Since EoS impacts the proto-neutron star evolution, it is frequently reported that soft EoS produce rather strong heating. This property is attributed to higher L_ν and $\langle\epsilon_\nu\rangle$ than those in stiffer EoS (see more discussion in section 2.3).

The importance of multi-dimensional effect orignates from more complex dynamical flow patterns and this aspherical morophology should also affect neutrino emissions so far. Furthermore, convection under PNS surface may produce non-uniform distribution of neutrino properties in angular direction which require the dimensional extension. This is why the current numerical development of neutrino transport is quite active. It is noteworthy that, in accordance with Melson et al.(2015), the modification of coupling constants for nucleon-neutrino scattering increase both L_ν and $\langle\epsilon_\nu\rangle$.

Finally, the concept of the third idea is to obtain the more energetic shock at the beginning of stalled state for relaxing the amount of necessary neutrino heating contribution. There may be two ways to achieve above objective; one is enhancing the initial shock energy at the bounce time by deeper gravitational potential well while the other is reducing

Table 2.4: Lists of neutrino reaction process incorporated in state-of-the-art simulations (see [196, 56] for more details). N means either n or p, $\nu = \nu_e, \bar{\nu}_e, \nu_\mu, \bar{\nu}_\mu, \nu_\tau, \bar{\nu}_\tau$, and $\nu_x = \nu_\mu, \bar{\nu}_\mu, \nu_\tau, \bar{\nu}_\tau$.

Process	References	favorable (◯) or unfavorable (×)
Beta-Processes		
$\nu_e + n \rightleftharpoons e^- + p$	Burrows et al.(1998) [57]†	(-)
$\bar{\nu}_e + p \rightleftharpoons e^+ + n$	Burrows et al.(1998) [57]†	(-)
$\nu_e + (A, Z) \rightleftharpoons e^- + (A, Z+1)$	Langanke et al.(2003) [232]	× (smaller Y_e)
Scattering Reactions		
$\nu + (A, Z) \rightleftharpoons \nu' + (A, Z)$	Horwitz et al.(1997) [184] (ion-ion correlations)	×
	Langanke et al.(2003) [232] (inelastic contribution)	×
$\nu + N \rightleftharpoons \nu' + N$	Burrows et al.(1998) [57]†	◯
$\nu + e^\pm \rightleftharpoons \nu' + e^\pm$	Mezzacappa et al.(1993) [282]	×
("Thermal") Pair Production		
$\nu + \bar{\nu} \rightleftharpoons e^- + e^+$	Bruenn et al.(1985), Pons et al.(1998)[37, 350]	◯
Nucleon-Nucleon Bremsstrahlung		
$\nu + \bar{\nu} + N + N \rightleftharpoons N + N$	Hannestad et al.(1998) [155]	◯
Reactions between Neutrinos		
$\nu_{\mu,\tau} + \bar{\nu}_{\mu,\tau} \rightleftharpoons \nu_e + \bar{\nu}_e$	Buras et al.(2003)[47]	◯ (L_ν electron and anti-electron type enhance)
$\nu_x + \{\nu_e, \bar{\nu}_e\} \rightleftharpoons \nu'_x + \{\nu'_e, \bar{\nu}'_e\}$	Buras et a.(2003) [47]	◯

the outer core mass in order to avoid the amount of photodissociation. Both are tightly associated with nuclear density equation of state (EoS) and pre-supernova structure which have large uncertainty. The recent development for high density EoS is mentioned in section 2.3. In addition, the brief description of problems in stellear evolution calculations is pointed out in section 2.4.

2.2.6 Shock expansion epoch

In right bottom panel of Fig. 2.7, the last picture of senario, the successful shock revival yield not only bright electro-magnetic signals but also extremely heavy nuclei. As shown in section. 2.1, the blast wave carries a large amount of energy, typically 10^{51}erg, and engulfs the statically bound envelopes. During the propagation through massive star, the conversion from the huge internal energy to kinetic energy mainly starts from the passage of C/He interface and gradually proceed even after shock breakout.

Although it has been repeated that the neutrino driven mechanism has yet produced the roburst explosion, there are several reports which obtained the shock revival without any apparent artifact owing to the currect high perfomance computational resources. These reports are, however, still under debate since the result from one group are contradictory to those from other (see section 2.5 for concrete comparision). Moreover, it is too time consuming for the realisitic simulations to follow the whole shock evolution until the shock breakout due to strict CFL conditions. Those numerical restriction is caused by extremly short timescale of proto-neutron star so that the simulations are usually limited at most one second after bounce.

As a matter of fact, there are several alternative way to follow subsequent shock evolutions and one of the most standard ways are known as piston model and thermal bomb which are both spherical hydrodynamics and solve nuclear evolution. These approachs start from presupernova stage and induce the artificial explosions by either strong mechanical force or internal energy injection instead of solving core-collapse and neutrino heating.

Thanks to this simplicity, nucleosynthesis has been calculated for wide initial parameter spaces, e.g. progenitor mass, metalicity, rotation period, mass loss rate and so on, as well as explosion properties such as kinetic energy, eject mass, shock velocity and the location of mass cut. These methods succeed in reproducing EM signals and understanding qualitative explosion characters for both type I and II . These simplified calculations are, however, not triggered by realistic way, i.e. neutrino heating, and very few calculation take into acount the formation of PNS. Moreover, the computations are mainly carried out in 1D so that they cannot reproduce observed aspherical moropholgy observed.

In contrast, there are multi-dimension simulations which are reflecting the neturino driven mechanism. These calculations employ grey neutrino transfer with calibrating neutrino luminosity at the inner boundary so that one can rather easily obtain various explosions as well as light bulb approximation or anlytical heating source [378]. In this sense, the results are multi-dimension based on neutrino heating and demonstrate various morophology patterns which is sensitive to initial perturbation and even resolutions. It is well known that when shock penetrate contact discontunities, the interface where chemical distribution change sharply, Rayleigh-Taylor (RT) instability take place so that the spatial distribution of nucleosynthesis yields is similar to that in in SN1987A. It should be noted that H/He layer interface is most likely site for RT instability since the density profile steeply declines [213, 126, 150, 472].

It is noteworthy that CCSNe has been expected to be the candidate of heavy nuclei

factory which produces the 2nd and 3rd peak elements probed in solar abundance and play key role in galactic chemical evolution [78, 106, 224, 225, 314, 355, 395, 460]. As illustrated in the last panel of Fig. 2.7, The hot neutron-rich matters in PNS are expected to be ejected by the rarefaction wave and acceralated by neutrino interaction. This phenomena is called neutrino driven wind and traditionally considered as one of the candidate of rapid neutron capture process sites which is well known as r-process and create metal whose mass number is larger than 100 [122, 123, 229, 278, 326, 356, 424, 429, 432, 433, 459, 458, 477, 486, 11, 55, 107, 126, 198, 336, 11, 55, 107, 126, 198, 336]. From "waiting point" approximation the favorable condition of r-process are either small ratio of Fe-group seed to free neutron, hot high entropy ejecta or long time wind duration. Since many studies have exhibited slight neutron-rich, rather low entropy and short expansion time scale, current CCSNe theory have failed in explaining either the second or third peak heavy nuclei whereas compact binary mergers have demonstrated suitable enviroments for r-process. Nevertheless, according to Roberts (2012) [366], the CCSNe site has not been completely ruled out yet [457]. See Thielemann et al.(2011) [431] for short review.

Since the discussions about explosion energy and nickel mass yield are our main purpose of this thesis, they are described in section 2.5.

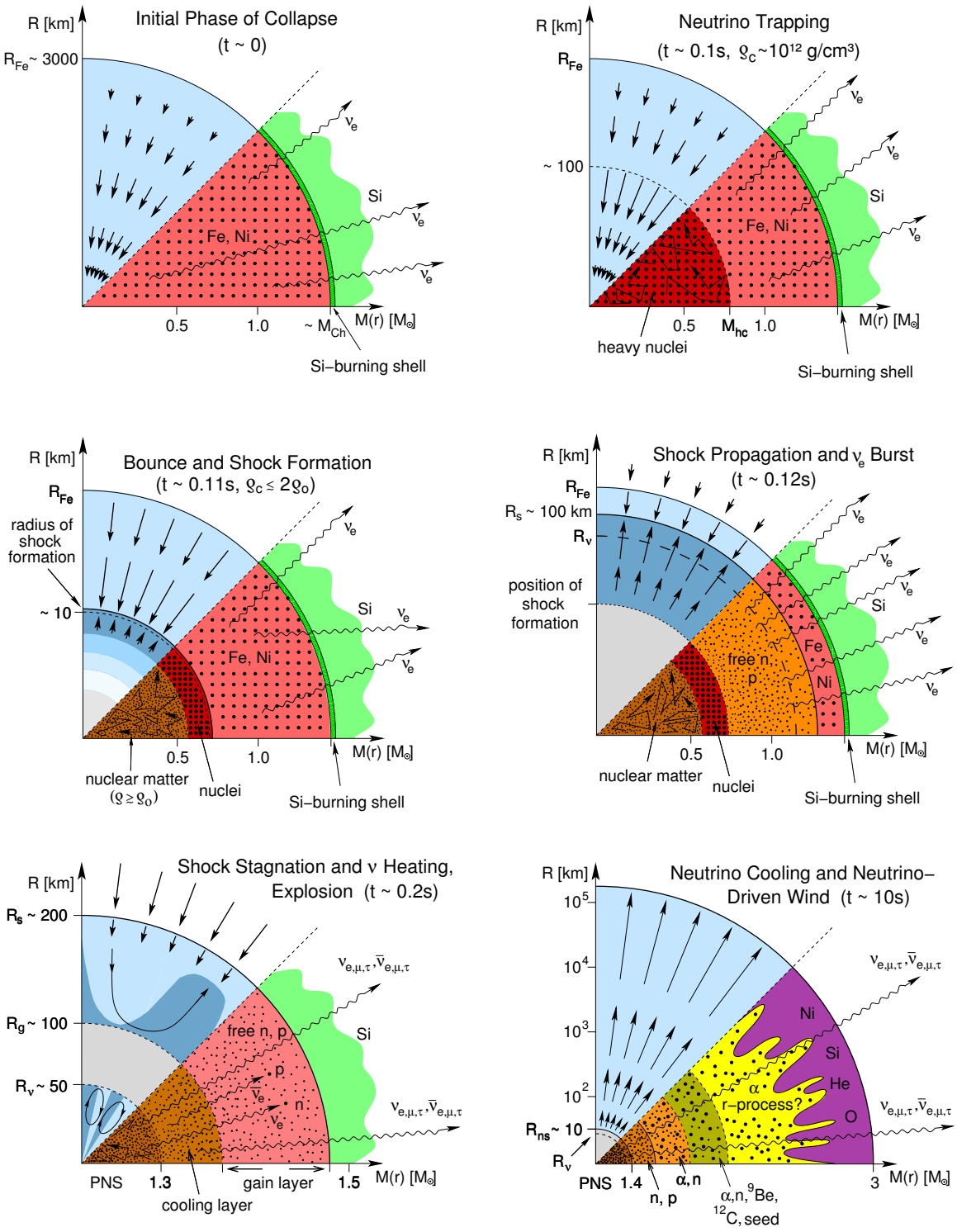

Figure 2.7: Schematic picture of the neutrino heating scenario taken from Janka et al.(2007). The sequence pictures illustrate 1. the onset of collapse (top left), 2. neutrino trapping (top right), 3. bounce and shock formation (middle left), 4. shock energy loss during propagation through the outer core (middle right), 5. stalled and revived shock due to neutrino driven mechanism (bottom left) and 6. evolution after onset of the explosion (bottom right), respectively. The solid arrows illustrate the fluid particle motion while wavy arrows denote the free streaming neutrino emisson in the overall stages.

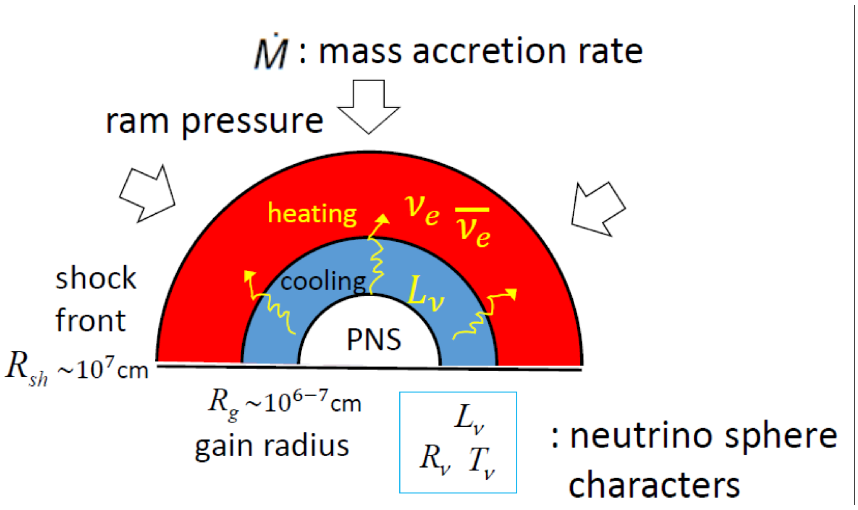

Figure 2.8: The balance of mass accretion and neutrino heating during the stalled shock phase.

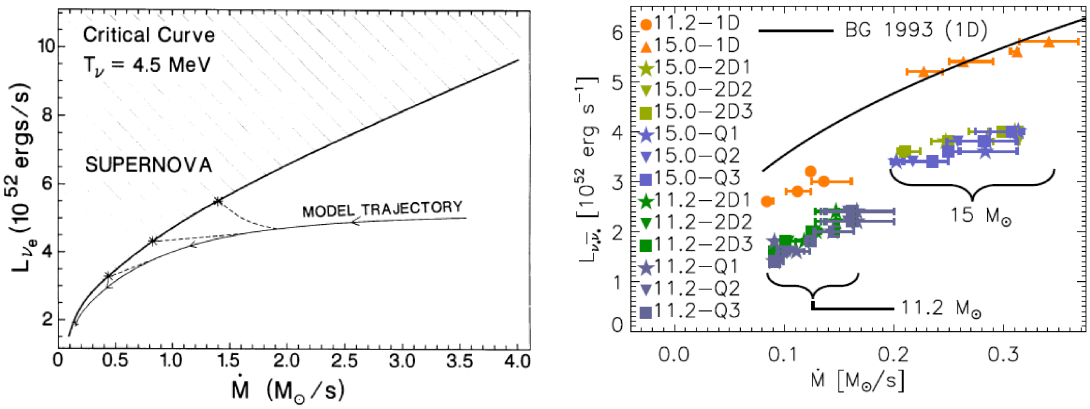

Figure 2.9: Critical curve in $\dot{M}$-L_ν map taken from Burrows & Goshy (1993) [52] (left) and Murphy et al.(2008) [291] (right).

2.3 Equations of State

CCSNe theory requires extremely wide range of density (from 10^{-8} to $10^{15.5}\,\mathrm{g\,cm^{-3}}$) in order to treat simulations correctly from core collapse to a shock breakout take place. The different EoS in high density regime significantly affect the location of bounce. Furthermore, the dynamical CCSNe calculation is in need of extension in EoS to finite temperature because the peak temperature increase $T_c \gtrsim 30$MeV after bounce. The difficulty of making finite temperature EoS is attributed to the presence of excited states and modification in distribution function. EoS is also responsible for time evolution of neutrino luminosity and neutrino average energies and neutrino opacity as well as core contraction dynamics and strength of shock. In addition, the properties of EoS around nuclear density dramatically influence not only dynamics in supernova but also black hole formation and neutrino signals [307, 305, 410].

However, physical properties in such an extremely high density regime still remains outstanding problem and it is not easy to probe it only by the earth experiments. Therefore, the observation of compact objects, especially neutron stars, are mandatory to assess the correctness of the present nuclear theories. Demorest et al.(2010) [79] updated mass-radius relation of neutron stars from observing Shapiro delay and reported the new record of maximum neutron star mass $1.97M_\odot$ which strongly restrict the EoS modeling. Bayesian analysis of six NS observation also give mass-radius relation constraint [399]. From these observations, equations of state are starting to be restricted. Nevertheless, due to its complicated background knowledge, it is quite difficult to follow what kind of equations of state are present, what is the difference between those modelings and what part of properties are updated from previous studies. This section is consisted of brief current EoS development and its application. Naive physical interpretations of nuclear matter equations of state are displayed in appendix D.

It should be warned that the whole discussion does not stepped into the detail of nuclear physics. For further reviews one should see, for instance, Lattimer (2012) [240].

2.3.1 Recent development

The equation of state also crucially depends on the appearence of the exotic matters which is commpletely neglected in the two widely used EoSs. The additional components modify the stiffness and the chemical mixture which would affect shock dynamics and also neutrino emission properties. The exotic matters usually emerge when the chemical potential of nucleon or electron exceeds the rest mass of them which may likely take place in hot dense PNS interior.

It is noteworthy that Sagert et al.(2009)[372] found that the transition from hadron matter to quark matter trigger the second blast wave after bounce and yield successful shock revival. Furthermore, according to Melson et al.(2015) [275], the modification of axial coupling constant by strange-quark contribution ([185]) also produce the crucial supprot for 3D successful explosion. There are a number of EoS research with extremely high density region which include kaon, quark, muon, hyperon and/or meson. For instance, Nakazato et al. (2008) and Ishizuka et al.(2008) [308, 192] take into account thermal pion and adopt MIT bag models. They demonstrated that the generation of pion and quark and soften EoS when the bag constant is given as particulerly small values. Moreover, the presence of hyperon at relatively high density drastically makes the EoS soft. Hence, for the inclusion of hyperons additional strong repulsive potentials such as three body effect

or YN interactions, are required to explain the maximum mass of neutron star.

Meanwhile, Oertel and coauthers [323, 324] extended LS EoS with including pions and hyperons at finite tempearture. They performed numerical simulations of the collapse from NS to BH for $T = 0$MeV and confirmed that pressure, internal energy and sound speed are affected by the additional bosons as well as STOS.

It should be noted that the transition from hadron phase to exotic matter phase does not suddenly happen [354]. There are two types of phase transition conditions, one is Maxwell construction [435, 354] and the other is Gibbs rules [140, 141, 351, 352]. Maxwell construction is based on a single chemical potential for one phase and local charge neutrality, e.g. the 1st order transition of water, produces sharp transition while Gibbs rule utilize different chemical potentials for transition phase regime and imposes global charge neutrality. As a consequence, the Gibbs rule usually provides more continous transition in coexistent phase and rather smaller surface tension (see more details in [7, 332, **?**, 463, 484]).

Furthermore, not only supra-saturation density regime, there is room for further improvement sub-nuclear density compositions. The two classical EoSs assume a single nuclei approximation, which is regarded as ensemble of alpha particles, and neglect shell effects which characterize the magic number. There are several EoSs which have improved multi-component heavy elements in inhomogeneous nuclear matter. Hempel et al.(2010) [167] (hereafter HS) have constructed RMF uniform nuclear matter with "TMA" parameter and extended to multi-component, the mixture of nuclei and interacting nucleons, under NSE condition for inhomogeneous nuclear matter. All nuclei are treated as separate particle species based on the experimental mass tables. This means that shell effects are incorporated and not only heavy nuclei but also light nuclei are taken into account which is important to estimate nucleon abundance more accurately. Moreover, nuclei are assumed as hard uniform sphere so that unbound nucleons only appear outside the nuclei. This excluded volume effect enable to make smooth transition to uniform nuclear matter. Thanks to including multi-component nuclei, HS connects NSE with non-NSE states in better way. Furthermore, Hempel et al.(2012) [166] has provided other various nuclear parameter sets, e.g. TM1, TMA and FSUgold, for homogeneous RMF nuclear matter and performed spherical GR CCSNe simulations in order to carry out systematic comparisions with LS and STOS in neutrino signals. During the collapse, the evolution of Y_e in the inner core is lower than STOS since they give smaller average heavy nuclei than STOS. They also found that HS causes less electron capture in the lower number fraction of free proton and cautioned the importance of the nuclear composition in dynamics. In addition, the mass difference of nucleon also reduce the electron capture. After bounce, the difference of non-uniform matter produces more compact PNS compared to STOS since the presence of light nuclei and smaller heavy nuclei is responsible for lower Y_e. Hence, the neutrino luminosities and mean energies are also larger than STOS. However, the difference from LS180 is larger than that from STOS. It is noteworthy that shock energy is also affected by the new treatment of inhomogeneous matter but hardly distinguishable after the shock halt.

There are more comparisons of various RMF parameters in Mattias Hempel's own homepage and the part of them is reproduced in table 2.5. The table also depict the solution of TOV equation for cold neutron star ($T = 0$MeV). It is apparent that high values of K and L produce larger maximum mass and radius which is qualitatively important and discussed in also appendix D. Moreover, the $M - R$ relations for these RMF parameters are shown with the observation data in Fig. 2.10.

At the almost same time, Furusawa et al.(2011; FYSS) [133] constructed their own

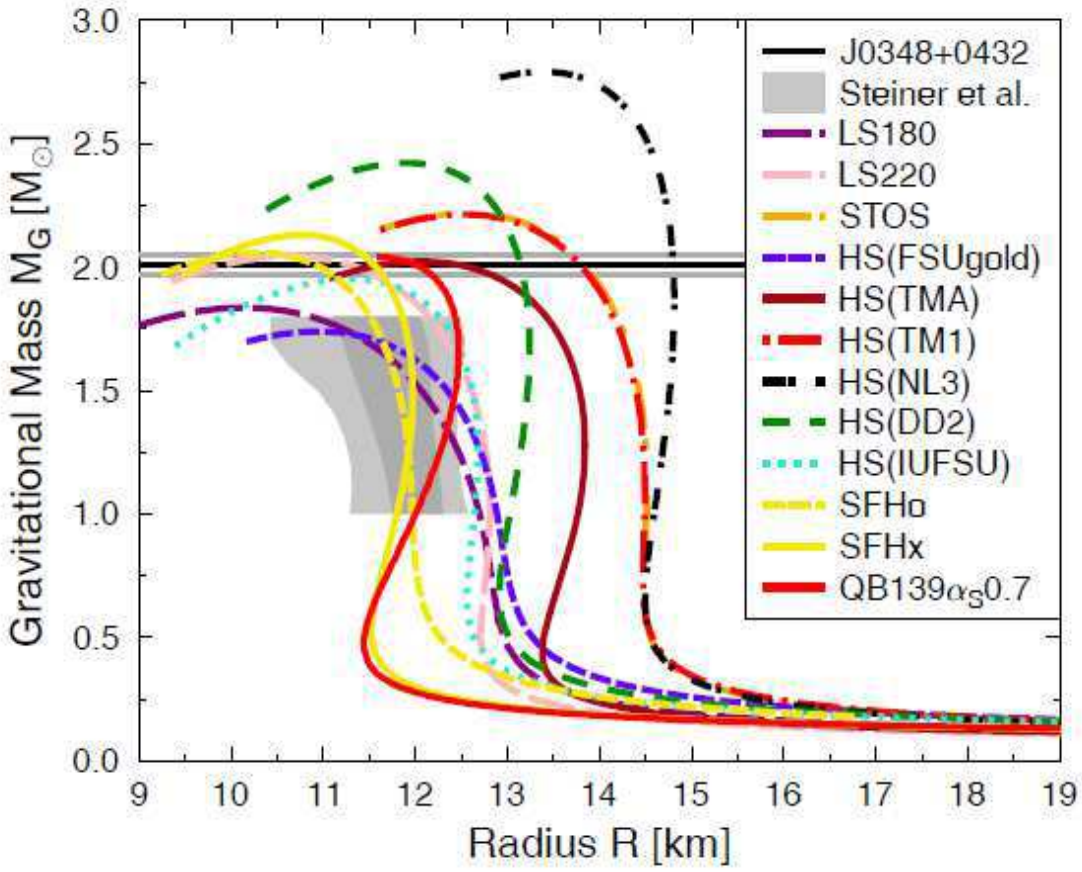

Figure 2.10: Mass - Radius relation of cold NS with various nuclear matter parameter sets. The figure is taken from Fischer et al.(2014) [114].

tabular EoS based on RMF with TM1 parameter for nuclear matter and applied liquid drop model for inhomogenous matters. While STOS discards nuclear shell effect in their Thomas-Fermi approximation, FYSS uses the mass formula based on experimetal data which contain the nuclear shell effect. As a consequence, their approach make a continous transition to the EOS for supranuclear density. According to previous studies [375, 433], the rate of coherent scatterings of neutrinos on nuclei is propotional to A^2 as long as the wavelength of neutrino is much larger than the nuclear size. Thus, it is expected that the coherant scattering rate will be reduced in core-collapse simulations if required heavy nuclei is absent. From this point of view, FYSS includes extremely heavy nuclei for $\rho \gtrsim 10^{13}$ [g/cm^3] which are neglected in HS.

They also updated their EoS [132] as follows:

1. to avoid unphysical jumps in the isotope distributions between the nuclei with and without experimental data,

2. bulk energies become temperature dependent,

3. nuclear shell effect is extended to nuclei whose experimental mass data is absent by adopting an empirical formula,

4. the appropriate modifications have an impact on the electron capture rate and coherent scattering on nuclei,

Table 2.5: Properties of nuclear matter with diffrent parameters.

	$n_{\rm b}^{(0)}$ [fm $^{-3}$]	BE/A [MeV]	K [MeV]	$K^{'}$ [MeV $\cdot$ fm^{-3}]	J [MeV]	L [MeV $\cdot$ fm^{-3}]	m_n^*/m_n	m_p^*/m_p	$R_{1.4}$ [km]	M_{max} [$M_\odot$]
TM1	0.1455	-16.31	281.6	-286.5	36.95	110.99	0.6343	0.6338	14.47	2.21
TMA	0.1472	-16.03	318.2	-572.2	30.66	90.14	0.6352	0.6347	13.85	2.02
FSUgold	0.1482	-16.27	229.5	-523.9	32.56	60.43	0.6107	0.6102	12.55	1.74
NL3	0.1482	-16.24	271.5	202.6	37.39	118.49	0.5954	0.5949	14.77	2.79
DD2	0.1491	-16.02	242.7	168.7	31.67	55.03	0.5628	0.5622	13.22	2.42
LS180	0.1550	-16.00	180.0	-450.7	28.61	73.82	1	1	12.16	1.84
LS220	0.1550	-16.00	220.0	-411.2	28.61	73.82	1	1	12.67	2.06

The table is taken from Hempel's personal homepage http://phys-merger.physik.unibas.ch/ hempel/eos.html.
Listed are the saturation density n_B^0, binding energy BE/A, incompressibility K, skewness coefficient K', symmetry energy J, symmetry energy slope coefficient L, the neutron and proton effective masses $m_{n,p}^*$, the radius of a 1.4 $M_\odot$ neutron star $R_{1.4}$ and the maximum mass M_{max} of a cold neutron star.
See the details in his homepage and also reference [114, 400].

5. Pauli- and self-energy shift are taken into account for light nuclei, $A < 6$, which affect nucleon abundance inside gain region in the CCSNe simulation.

Estimation of density and temperature dependence from the mass data is extracted by using following relations,

$$E_{\rm bulk} = M_{\rm data} - [E_S]_{\rm vac} - [E_C]_{\rm vac} \tag{2.30}$$

where $[E_S]_{\rm vac}$ and $[E_C]_{\rm vac}$ are the surface and Coulomb energy with the absence of free nucleon and leptons. In order to take into the account the temperature and density dependence of E_S and E_C on the binding energy, the two corrections will be represented as $\Delta E_S = E_S - [E_S]_{\rm vac}$ and $\Delta E_C = E_C - [E_C]_{\rm vac}$. By so doing, they obtain more accurate properties especially in the light nuclei.

The impact of the light nuclei, e.g. deuteron, on the shock heating dynamics is non-negligble when the shock expand sufficiently large radii ($\sim r_{\rm sh} = 400$km), although this situation is only satisfied near the threshold of critical luminosity value.

Even FYSS and HS are based on the same RMF parameter set and employing multi-nuclei, there are some differences between the two EoS at following points; Coulomb energy effect is added and modification of Pauli repulsive force and self-energy shift are also incorporated in light nuclei while the shell effect and nuclear pasta phase [363, 330, 306] are taken into acount even for very heavy nuclei ($Z \gtrsim 100$). Note that the shell effect is in need of reproducing the magic number and the nuclear pasta shape is usually determined by the balance between surface energy and Coulomb energy in sub-nuclear density. For clearer and more detailed comparison, the difference between multi- and single- nuclei equations of state is summarized in table 2.6.

G. Shen also has made two alternative tabular equations of state, NL3 [230] and FSUgold [438], which have fine grids assuring the first law of thermodynamics. NL3 is reltaively stiff RMF interaction which provides cold NS with ($M_{\rm max}$ [$M_\odot$], $R_{\rm NS}$ [km]) = (2.77, 13.3) while FSUgold whose maximum neutron star mass is only $1.7M_\odot$ is compatable with experimental

Table 2.6: The EoS comparision of multi-component nuclei with single approximation nuclei.

Modelers	FYSS	HS	LS	STOS
interaction	RMF [a]	RMF	Skyrme	RMF
heavy nuclei	multi ($Z < 100$), mass data [b] + LDM [c]	multi ($Z < 100$), mass data	Single, LDM	Single, TF [d]
light nuclei	multi Quantum	multi mass data	α only	α only
Shell effect	◯	◯	×	×
Nuclear Shape	Droplet $\leftrightarrow$[e] bubble	Droplet only	Droplet +bubble	Droplet only
$E_{\rm bulk}(\rho, T)$, $E_{\rm surf}(\rho, T)$	◯	×	◯	◯

[a] Relativistic mean field theory.
[b] Atomic mass data.
[c] Liquid drop model.
[d] Thomas-Fermi method.
[e] $\leftrightarrow$ illustrates a smooth interpolation between two phase.

constraints, e.g. large scattering length and heavy ion collision. For FSUgold they modified the extra-density dependent term so as to support the compact star up to $2.1 M_\odot$ [384, 383].

In low density regime they applied virial expansion of the grand partition function for dilute gas consisted of nucleon, α and thousands heavy nuclei components: for example, neutron matter number density is represented as follows

$$n = \frac{2}{\lambda^3 (z + 2z^2 b^{(2)} + 3z^3 b^{(3)} + O(z^4))}, \tag{2.31}$$

where z is fugacity $z = e^{\frac{\mu}{k_B T}}$ and λ is thermal wave length. The second order term in eq.2.31 is related to the two-body scattering phase shift [186] and those coeffecients in each particles are determined by the scattering theory. This treatment possess advantages in taking into account not only bound states but also scattering resonances. It should be stressed that the equation is valid when no phase transition occur.

Recent studies have highlighted an impact of symmetry energy which is associated with the mixture of compositions [39]. As one may have seen in eq. (D.3) and eq. (D.5), symmetry energy J is defined by the deviation of bulk energy from between asymetric and symetric matter at the saturation point and slop parameter L is directly related to pressure, thus stiffness. As a consequence, symmetry energy crucially influence neutron star radii. Lattimer et al.(2012) [240] have inferred that the symmetry energy constraints from convergence of observation, experiment and theory also exclude the classical parameter sets, e.g. "TM1", "TMA" and "NL3" [403, 441, 230] as well as soft EoSs. According to their investigation "DD2", proposed by [447] and constructed by the density dependent coupling constants, is feasible to account for the NS observation (see their discussion and reference).

Fischer et al.(2014) [114] compared DD2 with the two classical EoS, LS220 and STOS. This new EoS has shown intermediate behavior between the two classical EoS in time evolution of electron type neutrino and anti-neutrino luminosities, density, temperature and Y_e. They also found that symmetry energy is related to deleptonization during core collapse. After neutrino trapping lepton number fraction Y_l changes no longer and the

amount of Y_e strongly depends on symmetry energy. If J is large Y_e becomes large. Heavy nuclei compositions of DD2 are more similar to LS220, thus Y_l and Y_e distribution inside the core take closer values in the soft EoS than those in STOS. In contrast, symmetry energy is less important in post bounce evolution since asymmetric part of baryon pressure is dominated only at near saturation points.

In fact, these EoSs are based on the effective parameters, e.g. mass and coupling constant of virtual mesons, so that it is called "phenomenological" nuclear models. One may already notice that there is also ab initio theory which adopt the "bare" NN interaction potential and physical values which explain experimental scattering cross section.

For instance, Togashi [439, 440] has constructed his original EoS from bare nuclear force and carried out cluster variational method for 2 body nuclear potential (Argonne v18; AV18 [6]) and 3 body nuclear potential (Urbana IX; UIX potential [467]). Their EoS demonstrate that its application to cold NS strucure well explain the NS observation restriction in $M-R$ relation. The presence of condensed matter, however, yield contradiction to the observation [440]. They also performed spherical core-collapse calculation and found that the results are similar to LS rather than STOS which indicate soft EoS which result in the larger initial shock energy than STOS. Their EoS also showed that similiar lepten number fraction Y_l with STOS but smaller Y_e in the hot central core. This is attributed to the smaller symmetry energy.

Alternative ways have been developed, e.g. relativistic Dirac Bruckner Hartree-Fock (DBHF) and chiral effective field theory (EFT). DBHF incorporates Lambda hyperon effect while EFT takes into account all pion exchange but whose application is limited up to $n \lesssim 2 \times n_0$. See further discussions in [332, 160, 398, 181, 442, **?**, 310, 182, 102, 373].

2.3.2 Application of tabular EoS to numerical simulation

In the last part of this section I want to comment few words about practical application of EoS. Thanks to great effort, there are several open sources; EoS provided by LS, STOS, Hempel, G.Shen, Typel and Sagart are available and displayed in either tabular or subroutine style (see the web site"https://stellarcollapse.org"). As a consequence, nuclear field and astrophysics researchers have frequently carried out many cooperations and discussion, the EoS studies for CCSN simulation have become more and more activated in recent 10 years. In terms of EoS usage, especially tabulated case, however, one should be aware of some particular issues which may emerge in practical numerical computations. EoS table is usually first constructed by taking ρ, T and $Y_{\rm p}$ as independent variables and has more than hundred mega-byte due to the necessarity of covering wide physical ranges in CCSNe nature. It should be noted that CCSNe modelers have designed EoS tables by converting the independent variable from T to e, the internal energy density,for the numerical convienece; the hydrodynamical simulation often evloves not temperature itself but the internal energy density.

One of the important issues for the practical application is how to interpolate data points in EoS table because all possible states in CCSNe cannot be covered only by a finite number of grid point. The way of this interpolation result in different outcomes even the same EoS are employed. The coarse table often induces numerical errors especially in the phase transition regime so that finer resolution should be prepared instead.

Unless some kind of remedy is attempted to the lower resolution table, this coarseness seriously affects construction of neutrino distribution function computed by transport solver and also artificial wave produciton in fluid dynamics. Furthermore, one of the most

serious problem is generation of entropy by the artifact since CCSNe simulation needs the highnumerical accuracy to obtain the plausible explosion energy. Hence, especially for GR, collapse calculation in a single grid should be good check for confirming whether computation working correctly or not. Furthermore, the importance of the constrained parameters from NS probe is quite uncertain for CCSNe since the system of CCSNe is rather symmetric matter. The quantitative impact of K, J, L and other EoS parameters on CCSNe are, therfore, not straight forward as it seems to be and further EoS studies should be continued.

2.4 Stellar evolution

The results from stellar evolution are widely used in astrophysical fields. There is no doubt that the structure in pre-supernova stage plays crucial role in CCSNe modeling and these outcomes are yielded by 1D stellar evolution calculations. Furthermore, as mentioned in section. 2.1, the products of stellar evolution are commonly utilized to determine progenitor mass, explosion energies and nucleosynthesis yield and compared with observations. Inspite of its difficulty, many groups have done great effort and provided the last buring stage of massive stars. As a matter of fact, there are several discrepancies between each group even simulations start with the same simple initial conditions, such as same zero-age main-sequence mass, $M_{\rm ZAMS}$, zero metallicity and no rotation. This fact is owing to not only the difference in physical process, e.g. convection, but also numerical treatment and many researchers wish to know how and how much these factor influence pre-supernova stages.

The main purpose of this section is to understand what kind of uncertaintities exist, what kind of calculations are applied to the major steller evolution codes, how the physics ingredients affect the interior structure of last buring stage. A further introduction of the effort toward the multi-dimension calculations is addressed in section 2.5.

It may be useful to see the brief review of assumptions adopted in stellar evolutions. As well as physical assumptions, the difference in numerical treatment is also addressed in this paper. To understand these difference clearly, the basic equation, mixing length theory (MLT) and fundamental numerical technique, so called Henyey method, are described in appendix A.

2.4.1 The generic features of one dimensional convections

Convection will give crucial impact on where the opacity is high, especially Kramers opacity and ratio of L/M_r is high which are often seen in CNO cycle and also other concentrated energy release in massive stars. The main difficulty is how to include the effect of the mixing between different layers inside the stellar structure. Because of the large gap of time scale between time scale of convection overturn and nuclear burning, the time evolution of chemical abundances would be treated as diffusion process. The diffusion coefficient $D_{\rm mix}$ is based on MLT and show large divergence in different stellar evolution groups. Furthermore, $D_{\rm mix}$ is corrected by the presence of semi-convection, overshooting and other mixing process.

Semiconvection

When the part of stellar interior is unstable for Schwarzschild criterion but stable for Ledoux criterion, the mixing is suppressed by the difference of chemical components (see section A.2) and the diffusion coeffcient $D_{\rm semi}$ tend to be given smaller value than that for Schwardschild. (see the choice of $D_{\rm semi}$ in [474] and references therein). However, if the timescale of mixing is longer than the thermal timescale, the difference between Schwarzschild and Ledoux is quite small, e.g. the massive H core evolution during main-sequence [235]. The effect of semiconvection is important for stellar objects, such as low-mass stars and AGB phase [180, 189, 190]. In this paper, however, I mainly fouse on the massive stars in further discussions.

Usually being very slow convection process, semiconvection does not influence the energy transport but the chemical elements mixing. For massive star, it takes place in (1) outside of He core after the hydrogen depletion, (2) convective He core and (3) Si burning phase. In

the first case, the early epoch mixing makes the gravitaional potential deeper which leads to less mixing and lower temperature, i.e. redder giant star. This impacts the appearence of blue loops and the population rate of BSG to RSG [235].

During the convective He core phase, the treatment of semiconvection is complicated due to a numerical instability which originates from atomic weight barrier at the edge of core where Schwarzshild criterion is satisfied. If there is no mixing the fresh fuels are not supplied to the hot core so that C/O core tends to be smaller. The size of C/O core correlate with that of iron core which is definitely crucial to CCSNe theory. WHW2002 found that taking larger diffusion coffecient, thus faster semiconvection, evades the numerical instability. As a result, their massive stellar models tend to hold larger C/O core [339, 201].

Similar to the other advanced stage, pair and plasma neutrino process are dominant in the silicon burning stage, and carry the energy outside the core so that entropy tend to be minimum value at the center. This implies that the entropy is monotonic function of radius, thus $dS/dr < 0$. On the other hand, electron capture on heavy nuclei also starts to play important role and produce a Y_e discontinuity whose gradient become mostly positive at the edge of convective zone. Under this situation, employing Ledoux critreion restrict the mixing inside the convective shell which interrupt with growing Fe core size.

Overshooting

Owing to non-zero velocity at the edge of covectively unstable zone, overshooting is the type of mixing which penetrates the convectively stable region, therefore it takes place between convective and radiative region. As a result, the width of convective region is expected to be spread and the extent of expansion relies on the convective velocity, the entropy and chemical inhomogenity barriers. This additional mixing process brings the unburned material to the active shell burning layer or core so that the size of convection regions becomes larger if it is taken into account. As a result, overshooting yields higher luminosities after leaving MS, produces larger helium cores and makes its lifetime longer. Determining how much overshooting occurs is also one of the important problems and only a few implication is given by the observation, e.g. the presence of blue loops requires not too large degree of overshooting in hydrogen and helium burning stages. Roxburgh (1978;1989) [369, 370] suggested that this mixing process is completely global phenomena and the range of convetice zone can be represented by the simple integral form called "Roxburgh criterion" which is only valid under a negligible viscous dissipation. Vandenberg et al.(2006) [453] developed this integration formula by using observation calibration. However, the most of the stellar evolution calculations for massive star neglect this overshooting or take it into acount as the modification of diffusion coeffecient considering the scale height (see [70] and reference therin).

There are another problem that the remaining inertial behavior of overshooting turn out to be turbulent motion which is usually omitted in current 1D stellar evolution code. Recently there have been several multi-dimension hydrodynamical simulations which may give the clue to this problem. The current development is illustrated in section 2.5.2.

Thermohaline

Thermohaline mixing, which is also well known as salt finger instability or doubly diffusive instability, occurs when stellar interior is unstable to Ledoux criterion but stable to Schwarzchild criterion such that heavier chemical element attempt to drive instability.

Thermohaline convection rarely happens in single massive stars because heavy elements are produced by nuclear burning at the center or deeper part of shells in general. Therefore, the molecular weight usually stabilize the thermohaline convection. When it comes to a massive star among a binary system, the helium rich matter from the secondary star accreted onto the primary star so that thermohalne mixing is likely to happen during Roche-Lobe overflow.

Note that thermohaline mixing is also expected in the context of proto-neutron star convection for CCSNe theory, which is called neutron finger instead, if ,lepton number gradient becomes negative. The condition of unstable convection eq. (A.7) is modified in the following way

$$\left(\frac{\partial \rho}{\partial S}\right)_{P,Y_l} \frac{dS}{dr} + \left(\frac{\partial \rho}{\partial Y_l}\right)_{P,S} \frac{dY_l}{dr} > 0, \tag{2.32}$$

due to the presence of leptons which is responsible for dynamics rather than ions. Inside the proto neutron star $\frac{dS}{dr}$ tend to be positive or almost 0 so that the neturon finger convection take place if $\frac{dY_l}{dr} < 0$.

Wilson & Mayle(1988) suggested the neutron finger instability is likely to drive higher neutrino luminosity and/or mean energy. Several researches [168, 208, 40, 42] reported that no matter whether Schwarzchild criterion is stable or not, the unstable large overturn convection may bring the hot inner matter and lepton outter region and reach the PNS surface, i.e. enhance the neutrino luminosity. Dessart et al.(2006) [84], however, carried out two dimensional simulations and has found no doubly diffusive instability around neutrino sphere surface whereas the convection overturns are present inside PNS which is located too deep to penetrate the neutrino sphere. Hence, no ν_e luminosity shows increase while slight enhancement appears in $\bar{\nu_e}$ and ν_x by 10-15%. These outcomes agree with other simulation results, e.g. [48].

From above brief review, the various convective conditions result from MLT which directly influence the evolution of stars. There are, however, several different ways in formulation, assumption and hidden parameters between different stellar codes, and it is not obvious to evaluate appropriate physics of convection by just comparing the mixing length parameter. Furthermore, there are fundamental deficits in MLT; first it is local theory so that no overshooting from convective boundaries, ignores presence of chemical gradients, thus semi-convection (slow mixing on diffusive timescale), applies time independent instantaneous adjustment which become serious problem if other time scales (pulsation, nuclear burning) get short and takes into acount only one length scale which discards spectrum of turbulance eddies.

To carry out computation of convective region carefully in massive star, one has to make sure that interior matters are highly turbulent, three dimensional and global motion in compressible medium on dynamical timescales. The multi-dimensional calculations are limited to illustrative cases and dynamical models are too complicated for stellar evolutions so that operations such as proper averages and/or simplifications are still highly required. In spite of these difficulties, some current progresses have been done by several studies which is mentioned in chapter 2.5.

2.4.2 Other physical uncertainties

There are also uncertainties in other physics as well as convection which are relevant to evolve massive stars. Firstly, rotation is one of the most essential ingredient since it deform

stellar structure due to additional centrifugal force and also induce meridional circulation motion because of angular momentum transport.

In CCSNe the important factor named "compactness parameter" [321] is tightly relavant to the size of CO core [407] which is mentioned in section 2.5. Next several uncertain nuclear reaction rates and reaction process itself, e.g. α processes, produce the large difference in outcomes of the last burning stage. In addition, since neutrino emission becomes dominant instead of radiation, weak interaction process is rather important in advanced burning stage. Meanwhile, mass loss rate is also crucial to the evolution of massive stars. This ingredient is also well known as highly uncertain component since it demonstrate considerable sensitivity to rotation period, metallicity value and whether stellar system is single or multiple.

Rotation

In general observations have shown that massive stars, such as OB stars, rotate rapidly and this rapid rotation also affect the interior structure and chemical distribution of massive stars. The rapid rotation is likely to generate strong mass loss and produce Wolf-Rayet stars which are strong progenitor candidate of SNIb/c.

Centrifugal force in rotating star leads to a reduction of the stellar luminosity and central temperature. Moreover, since the centrifugal force distore the spherical geometry, the rapid rotators are brighter and hotter at their poles while dimmer and cooler at their equators.

The presence of rotation also induces meridional circulation (Eddington-Sweet circulation) due to the local angular momentum conservation which takes place in both radiative and convective region. This motion carries angular momentum and increase the gradient of angular velocity which drive the shear instability. In addition, it also smoothens temperature distribution and drives global chemical mixing. As a consequence, the structure of rapid rotating star is completely different from that for non-rotating star, e.g. it produces the larger He core, thus the more massive C/O core, in general. Interestingly, Eddington-Sweet circulation as well as convection tends to enforce rigid rotation on main sequence so that the initial angular moment distribution is not much important.

For shellular (differential) rotation, stellar structure can be regarded as baroclinic instead of barotropic. In this case, Solberg-Hoiland instability is related to Coriolis force and shear instabilities also play important roles in the evolution of stars. Fortunetly, these additional instabilities remedy the difference between the Schwartzchild and Ledoux criterion [333].

In terms of numerical simulations, there are mainly two ways to incorporate the rotational effects in 1D stellar evolution codes, one is proposed by Endal & Sofia(1978) [100, 346] and the other by Zahn et al.(1992) [491, 263, 269]. The first one regards the rotation effect as diffusion process which means that all the instabilities are taken into account as diffusion coeffecient in angluar momentum and chemical evolution equations. This treatment is much easier to implement in computation, however, neglect the advection term of Eddington-Sweet circulation. The methodology is employed by KEPLER, STERN, Padova, MESA , Modified Paczynski [163, 485, **?**, 340, 80].

On contrary, the treatment of angular momentum transport incorporates meridional flow advection, internal gravity wave and diffusion process in the second family; Geneva, STAREVOL, FRANEC [95, 334, 67] follow this method. Although the computation is more complicated, the formalism seems to be less artificial. Hence, the treatment of advective property of meridional flow is different while both method give only slight difference when

the turbulent instabilities ruled the angular momentum transport. Note that in both approach the rigid-body rotation is assumed for the convective zone.

Compared to observations, 1D rotational stellar evolution models succeed to explain several astrophysical phenomena such as the surface chemical abundance of Wolf-Rayet stars. There are, however, certain problem of angular momentum transport for massive stars such that central core reachs rotation threshold where the centrifugal force balances with gravitational force during the formation iron core. This implies that the meridional circulation and the shear instability does not carry sufficient angular momentum to outside the core. Several researchs [263, 163, 176] infer that the effect of mean molecular weight barrier enhances the angular momentum transport, nevertheless, it is still too large to explain the slow spin young neutron stars an white dwarfs. Therefore, additional angular momentum transport mechanisms are needed, e.g. magnetic torques. The numerical treatment of rotation still remains as challenging problem (see more details in [333] and reference therin)

Chemical reactions during advanced burning stages

The entropy at all stages show correlation with progenitor mass as well as the core size and the most amount of entropy contained inside the core is lost during carbon burning in general. Hence, the structure of C/O core, e.g. its mass and the abundance ratio of carbon to oxygen, is indispensible to the iron core mass [176, 450, 407]. Moreover, according to Sukhbold et al.(2014) [407], the size of C/O core also seriously affect the compactness parameter, the indicator of explodabilty [321].

Firstly, C/O ratio is highly influenced by the reaction rate of $^{12}\mathrm{C}(\alpha,\gamma)^{16}\mathrm{O}$, however, there are large uncertainty left for this reaction rate and competition with triple α reaction determines C/O abundance ratio, thus change final iron core masses [44, 473]. This reaction process is relevant to temperature and the amount of α so that the high entropy, thus the high progenitor mass, reduce the C/O ratio and the presence of overshooting also give same effect for the central core. It is noteworthy that these uncertainty of reaction rates influences also nucleosynthesis [445, 464]. In addition, the implementation of some alpha-chain reactions, e.g. $^{22}\mathrm{Ne} \rightarrow^{25,\,26}$ Mg, produce non-negligible effect on nucleosynthesis (see [361]). Furthermore, the presence of those chain reactions also change temporal structure evolutions which results in the difference in C/O core size (also refer [201] for instance).

Therefore, the C/O core mass is sensitive to the mixing process. A Slow inefficient mixing which originate from Ledoux criterion [234] inhibits the growth of the core size wheras a fast mixing due to Schwarzshild criterion [262] bring the larger CO mass [201]. It is interesting that even one employs Ledoux criterion, fast semiconvection produce also larger core mass which leads to stellar evolution theory more subtle [474]. Turning attention to weak interaction process, neutrino pair creation (and also plasmon) process also affect C/O size. The neutrino cooling process becomes more significant than the radiative transport in the advanced nuclear burning stages (see appendix A). The neutrino carries not only energy but also entropy which generate the large discontinuities between one shell and another. Since entropy is almost increase function of radius, this discontinuity impedes the overshooting to adjacent radiative layers and/or convection zone. Furthermore, during the oxygen and silicon burning, the nuclear reaction timescales become comparable to the convection timescale, thus the mixing process is hardly expressed by MLT and multi-dimension or, strictly speaking, 3D simulations are demanded for the handling of accurate energy and chemical transport [16].

As a result, a smaller C/O abundance ratio inside the core results in less neutrino loss and thus stronger convective C burning after He burning stage which makes the entropy inside iron core larger as well as mass [450, 449]. Even after the end of Si burning, neutrino play a key role in collapse period. The electron capture rates on heavy nuclei in Fe core have been improved by [233, 177] They taken into acount Gamow-Teller transition of $N > 40$ which is ignored in Fuller et al.(1980) (FFN;[130]). However, this results produce an unpleasant fate in the supernova theory. The increment of the electron capture rates decreases the lepton number inside the core, thus inner core turns out to be smaller and shock wave ends up with stagnant discontinuity because of large energy drain during propagation inside the outer core (see also section 2.3).

Mass loss and interactions

Mass loss takes place in the relatively massive rotating star ($M_{ZAMS} \gtrsim 30M_{\odot}$) [**?**]. The gravitational energy loss alters the life time and luminosity, thus evolutionary path, so that the strong mass loss seriously affects the final stage of structure. More than $20M_{\odot}$ stars dramatically change those C/O and final core masses. Since the large opacity obtain more momentum from the radiation, it is apparent that stellar mass transformation is sensitive to metallicity. In the theoretical point of view, however, the treatment of mass loss is the challenging matter due to complex non-LTE multi-line absorptions and scattering process [66, 456, 227] in case of continous wind and also sudden non-negligible eruption events ($\dot{M} \gtrsim 10^{-3}\mathrm{M}_{\odot}/\mathrm{yrs}$), e.g. Type-IIn and LBV. The problem has still remained unsolved. For single massive stars, the major choice of $\dot{M}$ has only three types, i.e.

1. mass-loss rate based on observations from $T_{eff} \lesssim 15,000\mathrm{K}$ [309],
2. theoretical wind driven model for OB star with $T_{eff} \gtrsim 15,000\mathrm{K}$ [226],
3. empirical mass-loss rate adjusted to WR star [149].

Energy generation and initial H/He abundance are influenced as well as opacities by metallicity.

Furthermore, it should be stressed that all the discussions above are based on single star evolution. Most of massive stars such as OB stars, however, usually form binary system [374] so that serious mass transfers occur between parent and donor stars as one may easily imagine. Recalling the discussion of convection, Ledoux criterion support the mass transfer due to its liklihood of forming RSG whose envelope expand larger than BSG. Podsiadlowski et al.(1992) [348] suggest that mass transfer occurs when donor star is in main sequence (Case.A), He core burning (Case.B) and after He depletion (Case.C). In fact, most binary massive stars have gone through Case.B and .C without forming the common envelope so that their fates tend to be SNeIb or SNeII with very low hydrogen mass. SN1993J, one of best known supernovae, is categorized as Case.C (or .B) and the rapid mass transfer commence not during late C burning by Roche-Lobe overflow but during early He burning by wind. Owing to the large mass loss of hydrogen envelope, He core of donor is inhibited to grow large and ends up with small convective core. This influence the supplement of fresh α in shell layers to the central core so that the reaction process $^{12}\mathrm{C}(\alpha,\gamma)^{12}\mathrm{O}$ rarely take place. Hence, the binary interaction causes the high ratio of C/O which results in low iron core and is likely to leave nacent neutron star after explosion.

For binary system theory, there are more interesting and less understood phenomena , e.g. angular momentum transport and particulerly common envelope.

In contrast to steady mass transfer events, Smith (2015) [392] reviewed the episodic eruption and especially paid attention to SNIIn eruptive mass loss which should also be explained in the steller evolution theory.

2.4.3 Comparison of methodology

In general, stellar evolution codes assume 1D spherical symmetry for simplicity and solve their basic equations by implicit scheme because of the unaffordable timescale difference between each physical process. Therefore, there are several differences in numerical techniques between stellar evolution modelers. First of all, Kepler code, which is developed and improved by Woosley and his co-authors [461, 476, 474, 163, 473], should be introduced since their results are the most commonly used for the initial condition of countless supernova simulations. Their code is based on the implicit hydrodynamical scheme which is quite different from other stellar evolution groups. One of the great advantage of their code is that all equations are treated in time dependent forms so that they can handle with the acceralation and discontinuities more easily than other groups. Hence, they can calculate massive star evolutions until collapse and also nucleosynthesis yielded by explosive burnings. The chemical abundances are mixed not by the flow advection. Instead, they assume that the secular mixing effect is approximated as diffusive process during the evolution. The code can handle even magnetic field as well as rotation which modifies the dimension of basic equations from 1 to "1.5". Meanwhile, turning attention to the Tokyo group [312, 487, 450, 423] and Geneva group (GENEREC; [281, 176, 95]), numerical methods of the two groups is similiar to the traditional Henyey method. Slightly different approach is, however, employed by Tokyo group in the advanced burning stages. Both groups solve structure, burning and diffusive mixing separately and for GENEREC the mixing is assumed to take place instantaneously up to Oxygen. The two groups also can handle the rapid rotations by applying the different approachs; one is Zahn's method adopted by Tokyo and the other is Endal's method by Geneva. Moreover, the accelaration term is included at the very beginning of collapse in Tokyo group while GENEREC code does not.

Turning attention to Bonn group [237, 236, 162], their STERN code included the nuclear burning effect into the Henyey method, i.e. the nuclear abundances are added to the independent variables so that the nuclear burning energy and composition change are simulataneously taken into account. In addition, they applied their Heney method to the atmosphere of stars where other groups usually solved by Runge-Kutta method [238].

FRANEC code, which is developed by Limongi and his co-authors [68, 252, 253], also employed the combination of nuclear evolution with Henyey method and the convection treatment is assumed as instantenous mixing in every time steps instead of the usual diffusive process. They use a tabular EoS and electron fraction is treated as function of density and temperature in their calculation. Their group recently increase the size of nuclear network from 100 to 300 species and it is only this group who afford to treat such a considerable size of matrix.

On the other hand, thanks to great talent and considerable effort of Bill Paxton, the new open source called MESA has been developed. Not only low, medium and high mass single stars which other groups also can handle, the code is applicable to large variety of astrophysical stellar evolution such as pre main-sequence, compact remnants, such as WD and NS, and even planet evolutions. Furthermore, mass transfer event, i.e. either mass loss or accretion, and also binary interactions are implemented as well as rotation and many

types of convective mixing can be chosen as an option. MESA are based on following codes: EV [96], EVOL [169], EZ [338], FLASH-the-tortoise [246], GARSTEC [462], NOVA [397], TITAN [136], and TYCHO [488]. It employs Henyey style method as well as many groups but additionally incorporates automatic mesh refinement, analytic Jacobians, and coupled solution of the structure and composition equations. It is surprising that the code is neither splitting the large matrix into small section nor decoupling space part and time part. See more details in [339, 340, 341]

Recently some detailed difference in numerical treatments are summarized in Martines et al.(2013) and Jones et al.(2015). The senesitivity to mass loss rate and the resolution are yet discussed as well as the presence of rotation and binary interactions in those work which are often well known for the origins of stochastic trends in stellar evolution structure. Furthermore, no verification has been done for the treatment of numerics in 1D steller evolutions, e.g. the selection of β's (eq. (A.36)) as well as those of convection criterion and mixing parameters. What is still more complicated is that the non-trivial modification is conducted in the original numerical scheme so that uncertainties is present even in the same group.

Although many success are provided by these calculation, it should be emphasized that none of them extend their calculation to the multi-dimension. This extension should be necessary to handle "realistic" convection, rotation, mass transfer and other important physics which would be indispensible to the massive star evolution.

2.5 Current status & Motivation of this work

2.5.1 Recent discoveries in CCSNe

Thanks to progress of computational resource, multi-dimension calculations up to three dimension has started to be available. It is well known that Nordhaus et al.(2010) [317] show the lower critical luminosity in 3D than 2D while Hanke et al.(2012) [153] obtain completely opposite results (see also appendix C). This conflict is based on the presence of large scale buoyant bubbles which appear in [317] but dissipated to much smaller scales in [153]. In addition several simulations cannot affirm the sloshing mode of SASI in 3D [193, 50, 77, 194] and doubted that this mode is produced by artificial restriction in geometry [49]. Hence, whether SASI plays key role in explosion or not is the current open question.

As mentioned in section. 2.2 (and also appendixand C), the runaway condition for neutrino-driven explosion is one of the most challenging issues for CCSNe modelers. It is well known that critical luminosity curve and time scales ratio, $\tau_{\rm adv}/\tau_{\rm heat}$ are the most successful indicators to quickly understand the qualitative aspect of shock revival. There are, however, still in debate for their quantitativity and only few discussion about relations between one and the other.

Pejcha & Thompson (2012) [344] proposed that not the time scales ratio but other physical condition, so called "antesonic condition", should be rather precise. In their paper the simple Bondi accretion flow is first discussed in order to show that there is certain transition point where solutions change from accretion shock flow to wind shock flow. This transition happens when isothermal sound speed, c_T satisfies the antesonic condition, which $c_T^2/v_{\rm esc}^2$ is larger than 3/16 where $v_{\rm esc}$ is the escape velocity. They solved 1D steady stalled shock solution as well as Yamasaki & Yamada(2005) [481], but modified the condition by replacing c_T on c_S and checked whether this condition is valid. The main difference in methodolgy from [481] is the treatment of neutrino transport, i.e. they take into account the accretion luminosity by solving gray neutrino transport. The accretion luminosity support by about 30% at shock radius. They concluded that this antesonic condition, $c_s^2/v_{\rm esc}^2 > 0.19$, yield no steady solution and is even more appropriate than the time scale comparison. Meanwhile, the multi-dimension calculation demonstarted that although the condition worked well in spherical symmetry the threshold value should change from 0.19 to about 0.30 [289, 90]. Furthermore, this condition is determined only after the onset of explosion happen as well as the time scale ratio case and seems to be unadequate to be used in the prediction. They have improved the Burrows' work incorporating the accretion luminosity and associated the critical luminosity $L_\nu^{(c)}$ with the other physical values, e.g. $\dot{M}$, M_{PNS}, r_ν,

$$L_\nu^{(c)} \propto M^{1.23}\dot{M}^{0.482}r_\nu^{-0.41} \tag{2.33}$$

which is compatible with previous researches [196, 288].

These semi-analytical studies suggested that the spherical simulations failed because the $\dot{M}$-L_ν trajectories for all models have never touched the critical curves and only passed under them. Therefore, it has been urgent to explore what kind of physics would decrease the critical luminosity and how the multi-dimensionality contributes to the CCSNe simulation.

Revisiting these runaway conditions, Murphy & Dolence (2015) proposed the new integral condition. Instead of providing the traditional steady "stalled"-shock solution, they search family of steady shock solutions by changing the shock radius. By so doing, imposing the simple condition, $v_{\rm sh} > 0$ where $v_{\rm sh}$ denotes shock velocity, they explored that a single dimensionless quantity Ψ which is associated with the integraded value of not the

energy but momentum equation from PNS surface to shock seems to be the plausible candidate of the explosion assessment. They confirmed that the dynamical simulation based on Murphy et al.(2013) [293] produce the shock revival when Ψ become positive value and discover that the explosion happen when the minimum value of Ψ, $\Psi_{\rm min}$, among the all shock radius fulfill $\Psi_{\rm min} > 0$ which infers that all steady solutions have $v_{\rm sh} > 0$.

There are several advantages of employing this new conditions rather than other conditions. Fixing other quantities, R_ν, $M_{\rm PNS}$ and T_ν, they can easily reproduce the same critical curve with Burrows & Goshy(1993) [52] which means the condition are more general. Moreover, the criterion $\Psi_{\rm min} > 0$ is more accurate than other previous conditions and more useful since the integral condition predict either success or failure in explosion. The other previous conditions have shortage of this aspect. The validity of this integral condition is, however, still uncertain as well as Pejcha & Thompson(2012) [344] when the system break spherical symmetry and further studies are awaited.

Recently, there is also great discovery of bridging progenitor structure and explosion. O'Connor & Ott (2011) [321] found the useful tool for the explosion named compactness parameter:

$$\xi_{M_R} = \frac{M_R}{R_{1{,}000{\rm km}}}$$

where M_R is enclosed mass at the radius R and $R_{1{,}000{\rm km}}$ is the normalized value of R by 1,000km. This new value is estimated at the bounce. They developed and performed GR 1D hydrodynamic calculation (O'Connor et al. 2010 [320]) incorporating various EoS and employing artficial enhancement in heating effeciency since the spherical symmetry disfavors the shock revival. They have explored that $\xi_{2.5}$ is valid to diagnose the fate of massive star and the progenitors with higher compactness possess larger iron cores which tends to form BH. It is interesting that this tendecy holds for almost all progenitor models with regardless of which stellar evolution group privide. Therfore the compactness parameter is regarded as powerful measurment for the prediction of CCSNe remnants.

For more than 100 single evoluted progenitors, Ugliano et al.(2012) [448] performed 1D simulation with grey transport and subsequent shock evolutions after revival until fall back is completed and demonstrated a wide range of blast energies ($0.1-2.0\times10^{51}$) by adjusting their simulation setups, e.g. neutrino luminosities at the inner boundary, to obtain the comparable explosion features to SN1987A with $19.8M_\odot$. Imposing this calibration, they found that the explosion properties and remnant mass are highly non-monotonic feature in progentior mass. NS and BH mass gap [25] are also seen in their calculation.

Further study is performed by Ertl et al.(2016) [105] They extended number of progenitior models to more than 600; not only solar but also other metallicity models with different convection and much finer mass resolution and also including Nomoto models which is also used for one of the additinal calibration. The absence of $16M_\odot \lesssim M \lesssim 25M_\odot$ progenitor for SNeIIP in observation [219, 390] seem to be consistent with this compactness argument (see also discussions in [183]). Confirming the validity of compactness, they insisted that non-monotonic varitation of compact star formations have yet explained by any single structure parameter. Therefore, they attempt to reveal what kind of multi-parameters enable to classify the families of fate by introducing $M_{S=4}$ and $\mu_{S=4}$ which denote enclosed mass where entropy per nucleon is equal to 4 and the mass deratives around the same point, respectively. They suggested that the combinaiton of two parameters, x=$\mu_{S=4}$ and y=$\mu_{S=4}M_{S=4}$, is directly linked to mass accretion rate, $\dot{M}$, and accretion luminosity, i.e. critical curve. As a consequence, the fate of progenitors can be discussed in this two parameters map and they find the presence of similar boundary 'lines' which are quite accurate to

separate explosion and non-explosion regime for the same calibration explosions. There are several outliers among 621 progentiors, $1-3\%$, which reflect the different composition-shell structure in Si-O layers. This new proposal seems to be also good alternative indicator for the prediction of compact remnant formation. There are, however, several questions in their quantitativity; how much dependence on the way of calibration there is, why the boarders can be described as lines and how $\mu_{S=4}M_{S=4}$ and the true luminosity are related quantitatively. The further discussion should be waited carefully. Covering also nucleosynthesis and light curve profiles, Sukhbold et al.(2015)[406] also performed similiar systematic study but more complete sets of progenitor.

Turning attention to "the first principle calculation", the situations become still more confusing since every research groups who perform multi-dimensional simulation obtain their own results which is frequently incompative with the others even the same initial condition, for instance, state-of-the-art simulations frequently have yielded no explosion or weaken explosion by more than an order while some studies show large explosion energy in realtively heavy progenitor masses.

At first one of the earliest stat-of-the-art simulation, Marek & Janka (2009) [266] showed a weaker explosion ($\sim 10^{49} - 3 \times 10^{50}$erg) by calculating two-dimensional newtonian calculation with variable Eddington factor scheme in neutrino solver (see appendix B). Similar results are explored by [289] who incorprated general relativity effect and employed 8.1 and $27M_{\odot}$. They terminate their simulation few hundred milliseconds after shock revival in which explosion energy is still small but showing sharp increase. They expect the neutrino driven wind may remarkably increase the explosion energy and overcome the strong gravitational binding. However, this is quite optimistic [337] and longer simulations are necessary to confirm exact termination time and total internal energy contribution of neutrino wind.

Müller et al.(2015) [288] revisted $11M_{\odot}$ with PROMETHEUS-VERTEX code in two and three dimensions and found that the higher dimension can trigger faster shock revival and stronger explosion comparable to $t_{pb} \sim 400$ms. Although some of the calculations are followed for more than seconds which is surprisingly long, the explosion almost converged at most 3×10^{50}erg in 2D.

As mentioned in section. 2.3, using the same code, Melson et al.(2015) [275] carried out three dimension simulations with $20M_{\odot}$ progenitor mass and found that changing 10% level of axial coupling constant of strangeness contribution in nucleon-neutrino scattering turn from failure to succesful explosion. This is due to the reduction of opacity of neutral-current scattering process for neutron so that luminosity and mean energies for all species are enhanced sufficiently.

Suwa et al.(2016) [414] investigated the mass accretion rate histories and the explosion energies in a wide range of progenitor masses and suggested that plotting trajectories in mass accretion rate - luminosity plane will be useful way to comprehend different groups outcomes. They obtained some explosions with light progenitors in 2D with IDSA neutrino solver which indicated only 0.1 Bethe, where Bethe is identified as 10^{51}erg.

Nakamura et al.(2015) [303] demonstrated two-dimensional hydrodynamic calculation which incorporate isotropic diffusion source approximation (IDSA) for neutrino transfer scheme using 101 progentitors and obtained few explosion models. It is interesting that large compactness $\xi_{2.5} \gtrsim 0.35$ indicated relatively large explosion energies (more than 0.4 Bethe). However, these explosions leave more than $2.0M_{\odot}$ remnant which seem to be large compared with observation and in their overall explosions, average explosion energy is about ~ 0.3Bethe.

Takiwaki et al.(2012) [426] who conducted the first realistic simulation in 3D confirmed

that the light progenitor ($M = 11.2M_{\odot}$) with relatively soft EoS (LS [241]; K=180 MeV) produce weaker explosion in 3D than in 2D. In this case, the higher dimension makes the situation worse. Takiwaki et al.(2014) [427] also warned that lower resolutions delay the onset of blast.

On the contrary, Bruenn et al.(2014) [41] reported surprising outcomes. They carried out two-dimensional calculation with multi group flux limited diffusion (MGFLD) approximation and obtained viable explosion energies and nickel masses comparing with observations [151], though their nickel amount seems to be slightly overproduced in relatively weak explosion models. Furthermore, Pan et al.(2016) [335] carried out 2D FLASH hydrodynamic simulation which implement IDSA transport and employs two EoS, i.e. DD2 and LS220. They obtained fast ($t_{\rm pb} \sim 100 - 300$ms) and strong diagnostic explosion ($0.1 < E_{\rm exp} < 0.5$) which are measured at $t_{\rm exp} \sim 300$ms. Among these results, $20M_{\odot}$ presupernova progenitor showed explosions which is incompatible with [304]. The reason why there are so many explosion models in their calculation is that multi-dimensional extension is implemented in IDSA instead of ray-by-ray. Their neutrino treatment generate prompt convection above PNS and supports faster shock expansion. They also found that DD2 yields faster shock expansion than LS220.

Even though there are some grateful results, we have to be careful to rush into conclusion that theory has been completed because many CCSNe groups failed in explaining the canonical explosion with the same progenitor models, for instance 15, 20, 25 and/or $27M_{\odot}$ progenitors in [474]. Many problems still remain unsolved and it is urgent to explore the lack of canonical energy as long as the explosion is guaranteed by neutrino driven mechanisms.

The recent simulations have demonstrated that the physics in supernova is not evident. One improvement show favorable aspects by several percents whereas another bring same degree of disadvantages.

The observations [151, 314, 451] are indicating that something crucial maybe still missing in our comprehension. Many failure of the first principle simulations suggest that further improvement in extending dimension for neutrino transport scheme, more realistic treatment in either supra- and sub-nuclear density for equations of state and more accurate GR hydrodynamic solver. It seems that there is no "most" important piece; every single physical element plays significant role in either positive or negative effect for producing explosion.

Turning attention to another aspect, however, it may be more likely that the initial condition is prior to the other problems because crude approximations and numerical artifacts are included so as to save compuational resources (see the previous section) which may be also responsible for the failure of shock revival. Furthermore, the weak explosion energies obtained by some studies are caused by remarkably low mass accretion rate on the stagnant shock owing to presupernova structure, one of the main conclusion of this paper, which is demonstrated in section. 5. Although there are long history in the stellar evolution fields, the distinctive difference in timescales hinder carrying out the evolution in adequate way so that many simplification is applied. In fact, there is no way to verify those physical and numerical approximations and this leads to wide variations in stellar evolution code development.

In the last part of this section, the recent status of stellar evolution is briefly summarized and the whole introduction is closed.

2.5.2 Progresses in stellar evolution

As seen in the previous section, the CCSNe issue still keep on providing troubles to theoretical modelers. What kind of realism is left for the next?

As mentioned before, it is well known that even in same masses and metallicities there are large divergence due to different physical input and numerical method , e.g. MESA code [339] , KEPLER code [461, 476, 474, 163, 473] , Tokyo group code [312, 487, 423] , GENEREC (Geneva) code [261, 95, 97] , FRANEC code [69, 252, 253]. For instance, the iron core masses vary in the range of $1.3 \lesssim M_{Fe} \lesssim 1.5$ which result from $15M_{\odot}$ progenitor models perfomed by 5 different codes (see Table.13 in [339]). The results also change even in same group by modest difference in input physics. As a consequence, mass accretion and luminosity histories are completely affected by subtle difference of stellar evolution [46, 414]. Hence, it is important to understand why the difference appear and how different between each group and which structure properties play key roles in CCSNe thoery.

Thanks to the great invention, MESA code would accelerate the much more qualitative systematic studies for the dependence of traditional parameter options such as convection type and parameter values and spatial resolution check. Recent studies have attempted to reveal the outcome difference by comparing raditation properties and precollapse structures. Martins et al.(2013) [268] investigate surface properties of stars from plots in HR diagrams for three different stellar evolution codes until the He depletion. They find that after main sequence (MS) overshooting makes the difference in MS width between low and high mass star in Hertzsprung-Russell (HR) diagram. Sukhbold et al.(2014) [407] performed a systematic study of compactness for 15-65$M_{\odot}$ provided by both KEPLER and MESA. They confirmed that carbon-oxygen core reflects the core structure better than ZAMS mass though there is still open question which is also discussion in Hirschi et al.(2004) [176]. The range of bare C/O core mass from 3 to $12M_{\odot}$ roughly correspond to those of main sequence mass from 15-30$M_{\odot}$ and observed similar non-monotonic compactness distribution even with different convective parameter choices. The variation of compactness is attributed to that of carbon and oxygen shell burning, e.g, CO core mass and they confirmed not only the treatment of convection but also the reaction rate of $^{12}\mathrm{C}(\alpha,\gamma)^{16}\mathrm{O}$ process is important for the size of CO core. They infered that this feature indicate the robustness of explodability which is apparently seen in 8-20$M_{\odot}$ and 25-30$M_{\odot}$ which is compatible with other compact remenant studies. It is noteworthy that the location of the compactness peaks and valleys are sensitive to semi-convection and overshooting treatment. In addition, since the net binding energy outside of iron core almost monotonicaly increase along with compactness values, higher compactness also impede explosion also for higher net binding energy outside of iron core.

Furthermore, Jones et al.(2015) [201] conduct detailed comparison of three stellar evolution codes with different input physics. They evolved the same ZAMS masses until the end of helium burning and investigated C+O cores. They found the key physics for core size and life time are the types of convection criterion and selection of overshooting or semiconvection. C/O ratio is also affected by the choice of nuclear network channels.

On the other hand, as mentioned in section 2.4, the treatment of the convection is one of the most important ingredient for evolutionary path of massive star. Recently the importance of 3D turbulence has been confirmed [273] and the research activity of how to incorporate 3D phenomena to 1D stellar evolution codes has been increased [16, 58, 15].

Usually the stellar evolution code assumes spherically symmetry, so that the mixing process is approximated by MLT which is first suggested by Böhm-Vitense(1958) [33]. Substituting mixing process for diffusing process is, however, only valid when the convective

scale is much smaller than scale height which is not true in the stellar object (Daly & Halo 1970). In addition, present 1D stellar evolution codes adopt diffusion process instead of turbulence process to take into account mixing of chemical elements. Smith & Arnett (2014) [393] warned that this alternative approach leads to incorrect answers at mathmatical and physical standpoints. The correct turbulence physics influence the late stages in massive stars.

Woosley & Weaver (1988) [475] has also shown that the iron core structure is very sensitive to how mixing is handeled at convective boundaries where turbulence and internal waves play important role.

Hence, strictly speaking, the calculation should be treated as three dimenosional, global and highly turbulent. Although 3D simulations are limited to illustrative cases, there are important implication from state-of-the-art calculation , for instance, performed by Herwig et al.(2006), Meakin & Arnett (2007), Arnett & Meakin (2011) and Mocak et al.(2011) [170, 273, 16, 287]. In multi-dimension the wave generation and mass entrainment are indispensible to the dynamical behavior of stable stratified layers adjacent to the convection layers. According to Meakin & Arnett (2007) [273], Richardson number, Ri_B, is represented as the ratio of braking (buonyoncy) energy to turbulence energy which are measures of the "stiffness" of the boundary and the strength of turbulance, respectively. If Ri_B is small ($\lesssim$ 1/4; [280]), the convective region is rapidly expanded because the gravitational force of from convection motion. Hence, Richardson number is good indicator of convection boundary penetration. On the contrary, if Ri_B becomes larger than certain criterion number [206], the entrainment process ceases and the evolution of convective boundary is ruled by molecular diffusive process.

Moreover, in later burning stages, convective layer near the core has superadiabatic profile $\nabla_{\rm sim} \lesssim \nabla_{\rm ad} + 10^{-3}$ and $\nabla_{\rm ad} < \nabla_{\rm sim} < \nabla_{\rm Led}$. Note that superadiabatic profile show large deviation from $\nabla_{\rm ad}$ at the boundaries between convective stable and unstable regions where convective enthalpy flux turn out to be negative [271]. In stable region, g-mode is induced by velocity fluctuations excited by turbulent motion lying below the stratified layer. The velocity fluctuations seem to be stronger by a factor 2 in 2D than in 3D. There are interesting mode trends in velocity fluctuations. Considering Fourier space of the fluctuations, lower wave number $k \lesssim 10$ corresponds to p-mode (pressure mode), g-mode (gravity mode) is lower frequency $\omega \lesssim 0.1$ and f-mode (surface mode) lies between p- and g-mode where both k and ω are small values. Inside the convective layer p-mode is suppressed, whereas g-mode becomes dominant even in stable region above upper boundary layer due to entrainment process of the turbulent motion. Similar discussion is also inferred in [170] whose pupose was exploring convective He burning. The physical process of entrainment phenomena is similar to those of semiconvective mixing but what distinguish these two are time scales, i.e. dynamical and thermal timescales. The axisymmetry calculation seems much better than sphrecal cases, however, Arnett et al.(2011) [16] have pointed out that it is still incomplete since power law spectrum for turbulence is not equivalent to that in 3D.

Moreover, 3D simulation is neccesary because typical flow patterns in 2D are torn apart and go through the turbulant cascade. This damping may affect the amplitude of velocity fluctuation by nearly 50% [271] inside convectively unstable layer . Although axisymmetry simulation give important clue to convection motion patterns, the bridging gap between three dimension and spherical symmetry is strongly required in developing correct stellar evolution [13, 16].

As a matter of fact, dynamical modeling are unaffordable for stellar evolutions unless one needs to invent appropriate averaging method and simplifications. This is why

MLT is employed in major stellar evoution groups, although several significant deficits is contentained in the theory. As repeated many times, MLT is local theory, neglects overshooting from convective boundaries and discards chemical gradients, e.g. semiconvection (see Appendix A). It is also based on the time independent instantaneous adjustment and only one length scale. The former assumption is seriously violated if other timescales such as pulsation or nuclear burning get short while the latter may be too crude to handle stellar turbulance which is subjected to Kolmogorov spectrum [59]. So far, there are various difference in formulation, assumption and hidden parameters between different stellar evolution codes and it is not apparent to evaluate convection properties by just comparing the mixing length parameter.

Several studies have attempted to take turbulence effect into account for one-dimensional stellar evolution. For instance, Arnett et al.(2011) [16] found that kinetic turbulence burst act as fluctuation in Lorentz attractor model of non-linear convective rolls caused by interation between temperature gradient and convection velocity (see also [393]). In order to distinguish large eddy scale (Lorentz roll) and small dissipative scale (Kolmogrov law), they proposed the turbulent vortex approximation which compensate the acceralation term dropped in MLT. However, the time scale problem is not resolved yet in this approach and numerical breakthrough is needed.

Furthermore, Renolds-averaged Navier-Stokes (RANS) is the one of useful turbulence representation which decompose velocity into an average part and a flucturation part in Navier-Stokes equations. The separation of the two quantities is avialable to explore sophiscated turbulance physics. However, the additional term forces to introduce higher order moment which means that the equation is not closed. Canuto et al.(2011) [58] proposed a third order closure equation called Renolds stress models (RSM) which are usually used in geophysics field. Considering that MLT only treats the equation of second moments, one would think that it seems rather suitable for the stellar evolution calculations. Nevertheless, RSM has not been widely applied due to its numerical difficulty. Numerical simulation conducted by [455] confirmed validity of the RANS approach, therefore RSM may also handle improved convection model in stllear evolution [18]. It should be noted that RSM is inadequate under strong magnetic field because it is based on neutral fluid dynamics Furthermore, multi-dimensional hydrodynamic code, such as anelastic solver ([228]), low-mach solver ([8], [493], [315], [139], [316]) and time implicit method ([454], [455], [212]), allow to take 10-100 times larger time interval which is still not applicable to steller evolution.

It is worth while to pointing out that explosive oxygen burning is also induced by violent turbulent motion. In addition, although silicon burning suppress the explosive excursion (acoustic pulsation with high frequency) due to alpha and nucleon creation from endothermic reactions, the turbulence is expected to make burning active and distort the Si layer [16]. These non-linear spacial distributions may also play key role in support to triggering supernova explosion (see appendix C).

2.5.3 Motivation of this thesis

As mentioned previously, the remarkable progress in computational resources has enabled to treat the sophisticated micro and macro physics in numerical simulations in neutrino heating mechanism, i.e. the first principle calculation.

As a matter of fact, we know that the explosion energy of CCSNe is $\sim 10^{51}$erg canonically but most of these computations were not yet successful to obtain the number ([266, 290, 427, 303, 414] but see also [41]). Ni yields are another important observation, since

they decay radiatively and brighten the supernova ejecta later.

As discussed in section 2.1, we can infer the mass of synthesized Ni which is typically $\lesssim 0.1 M_\odot$ [151, 314, 451, 219, 390] from the exponential decay observed in the light curve over hundreds of days after the initial brightening. It is not clear whether the most advanced theoretical models can indeed reproduce this quantity, since it takes many seconds for the mass of Ni in the ejecta to be settled. In fact, most of the successful simulations cited above were not able to extend their computations much beyond a second because the CPU time would be simply unaffordable or some physical processes that are important in the late phase were not incorporated in their models.

In this paper, we are interested in what will happen after the stagnated shock wave is successfully relaunched by the neutrino heating. In particular we discuss (1) when the explosion energy is determined, (2) which processes contribute to the explosion in what proportions, (3) how the explosion energy and neutron star mass are dependent on the timing of shock revival, and (4) how multi-dimensionality affects all of these issues. For these purposes, we have done a couple of numerical experiments in 1D (spherical symmetry) and 2D (axisymmetry). In real massive stars, the trajectory in $\dot{M}$-L_ν plane evolves from large to small accretion rate and hits the critical curve where the shock begins to relaunch outward. Controlling neutrino luminosities under the light bulb approximation, we have induced shock revival from different points on the critical curve (the critical luminosity as a function of the mass accretion rate) and computed the following evolutions of matter flows outside the proto neutron star long enough for the energy of ejecta to become constant.

In so doing we have chosen first a single $15 M_\odot$ progenitor and taken into account nuclear reactions in a manner consistent with the EOS employed. The results are illustrated in chapter 4. The feedback from the reactions to hydrodynamics is fully incorporated. These consistencies were lacked in previous works [266, 112, 448, 302].

Our another concern is what kind of modification is needed in pre-supernova stage to obtain the canonical explosion. As the first principle calculations of CCSNe imply the presence of initial value problem, something important may be missing in current precollapse structures to explain the canonical explosion unless the neutrino heating mechanism is not the correct picture of nature. In addition, I also want to confirm the compactness is the precise measure of explodability. Though there are some excellent success in explaining observations, we are afraid that relying too much on this indicator may lead to the possibility of dropping the essential part of massive star evolution. Therefore, this paper is the first step to reveal dependence of supernova characters on different groups progenitor model with same ZAMS mass as shown in [414] in experimental way.

In order to study their systematics, i.e., how they depend on, e.g., the progenitor structure, inner boundary condition, and so on, I adopted multiple progenitor models and try different boundary conditions at the inner boundary in section 5. It is well known in fact that the structures of massive progenitors are very sensitive to small differences in mass as well as the numerical treatment of some physical processes such as convections in the stellar evolution calculations [474, 473, 235, 407]. It is hence mandatory to see how robust our findings are when we change progenitors and this is exactly what we aim to clarify. In so doing, we did not use the progenitor models provided by stellar evolution calculations. Instead we constructed toy models of progenitors, in which non-rotating, hydrostatic configurations with an iron core in NSE, a Si+S mantle in QSE as well as other outer envelopes are calculated by employing parametrized distributions of entropy and electron fraction as a function of density. By so doing, we can vary the masses of these different layers rather arbitrarily. We are also able to obtain the abundance of various

elements so that we could use them later for the network calculations.

These models are better suited for the systematic studies conducted in this paper than more realistic models. As mentioned above, the structures of the realistic models change in a complicated way as a function of mass [407], which makes it difficult to interpret which features in the progenitor have what consequences. It is not helpful either that the progenitor models provided by different groups are sometimes very different [252, 97, 339, 487, 201] and the structures of massive stars are likely to be very sensitive intrinsically to some input physics as well as to numerical resolutions [407]. As shown later, adopting an appropriate entropy distribution and paying a proper attention to the transition condition at the layer boundary, we can capture the essential features in the massive progenitors.

Before demonstrating the results, the treatment of EoS and numerical strategies are presented in the next chapter.

Chapter 3

Numerical method

3.1 Multi-component EoS

As already discussed in section **??**, appropriate chemical element distribution is indispensible since it affects not only mean molecular weight but also the internal energy magnitude via the nuclear binding energy release which is usually non-negligible in CCSNe simulation.

After core collapse, it is well known that the iron core can be regarded as nuclear statistical equilibrium (herafter NSE) state. As a matter of fact, when the central density reaches sub-nuclear density, strong interaction starts to dominate hamiltonian of nuclei and affecrt thermodynamic variables as well as the nuclear binding energy. Moreover, all nuclei become uniform and undistinguishable at the saturation point. As a consequence, one has to pay attention carfully to the difference between current realisitic and an simple ideal NSE equation of state in inhomogenous matter case since the binding energy provided by the experimental data does not take into account either (ρ, T, Y_e) dependence or presence of other nuclei.

As a matter of fact, NSE is only ensured where temperature is sufficiently high, for instance $T \gtrsim 0.5$MeV. The chemical evolution should be taken into account for non-equilibrium process, e.g. explosion Si burning and recombinaiton chain reactions. Due to the chain nuclear reactions, the members of nuclei supposed to be selected from continous series of neutron and/or proton number, especially for neutron-rich nuclei yield, in the ordinary nuclear reaction network (NRN) calculation. Hence, the large number size of nuclear set is unavoidable unless one employs physical approximations, quasi-statistical equilibrium (QSE) and/or steady flow approximation. The application of large number size of NRN leads to unfeasible computational resources in terms of memory and CPU.

Furthermore, the transition between realisitic and non-NSE EoS is one of the most difficult but important issue since the binding energy supposed to be given one with expermental values in non-NSE case. In fact, there is almost no study which succeed in transiting the two different state consistently so far.

The main topic of this section is to address what kind of EoS is employed in this entire study. At first, the properties of NSE EoS with 297 nuclei are discussed by demonstrating deviations from other ideal gas cases and FYSS which takes into account multi-species equation of state in tabular form (see section 2.3). Next, I have suggested which density-temperature regime is proper to transit from the ideal EoS to FYSS. The suggestion is applied to the CCSNe simulations in the second study (chapter 5). There is also an illustration about numerical treatment of NRN.

3.1.1 Chemical elements reaction and equilibrium

The nuclear fusions, e.g. p-p chain, triple-α, CNO cycle, as well as dissociations, are sensitive to the enviroment states, especially temperature. The balance between thermal energy and Coulomb barriers determine which reactions dominate and how much daughter nuclei produced. There are, however, many reaction chains, about ten times larger than considering nuclei set size, and every chemical element abundance Y_i are tightly relied on several other components. The time evolution of Y_i is, therfore, given as follow;

$$\begin{aligned}
\dot{Y}_i &= f_i\left(\rho, T, Y_k\right) \\
&= \sum_{r_a \in \mathcal{R}} f_{r_a,i}\left(\rho, T, Y_k\right) \\
&= \sum_{r_1 \in \mathcal{R}_1} \lambda_{r_1} Y_j + \sum_{r_2 \in \mathcal{R}_2} \mathcal{N}_{j,k} \rho N_A \langle \sigma_{r_2} \rangle Y_j Y_k \\
&+ \sum_{r_3 \in \mathcal{R}_3} \mathcal{N}_{j,k,l} \rho^2 N_A^2 \langle \sigma_{r_3} \rangle Y_j Y_k Y_l \\
&- \text{(counter terms)}
\end{aligned} \tag{3.1}$$

where the six sums are reactions which produce (terms linked to "+") or destroy (terms linked to "-") a nucleus of species i with j, k, l reactant nuclei, respectively. The labeled reaction r_1, r_2 and r_3 represent

1. decay or photodissociation r_1 :
   $j \to i$, $j \longrightarrow i + k$ or $j \longrightarrow i + k + l$

2. two body fusion or exchange or others r_2:
   $j + k \longrightarrow i$, $j + k \longrightarrow i + l$ or $j + k \longrightarrow i + l + m(+n)$

3. three body fusion r_2:
   $j + k + l \longrightarrow i$ or $j + k + l \longrightarrow i + m$

The $\mathcal{N}$ s provide for proper accounting of numbers of nuclei which avoid double counting of the number of reactions when identical particles react with each other (for example in the ^{12}C + ^{12}C or the triple-α reactions).

On the other hand, NSE state appears in very late stage of burning, namely, after silicon burning depletion, during collapse or shock dissociation. The reason why the chemical equilibrium is only fulfilled under these circumstance is because all the nuclear particle need to overcome the binding energy barrier, mainly Coulomb barrier, thus the system is required to raise sufficiently high temperature to achieve the balance between creation and destruction number flux in right hand side of chemical evolutions eq. (3.1). This implies that all the chemical elements are equlibrium with nucleon so that the following relations are satisfied:

$$\mu_i = Z\mu_p + N\mu_n \ . \tag{3.2}$$

where μ is chemical potential including rest mass energy and subscripts p and n denote proton and neutron, respectively. The element i is composed of Z proton and $N = (A - Z)$ proton, respectively. Hence, a number fraction of i component, Y_i, can be represented as a following formulation;

$$Y_i = \frac{G_i}{2^A} \left(\frac{\rho N_A}{\theta} \right)^{A-1} A^{\frac{3}{2}} \exp\left(\frac{B_i}{k_B T} \right) Y_n^N Y_p^Z, \tag{3.3}$$

$$\theta = \left(m_b k_B T / 2\pi\hbar^2 \right), \tag{3.4}$$

where G_i and B_i are partition function and nuclear binding energy of i.

3.1.2 Comparision of NSE EoS for practical simulation

Nuclear elements dependence

Before carrying out comparison with FYSS, firstly I will investigate the properties of the ideal EoS carefully. In this paper NRN is the most time-consuming part in the entire calculation so that 28 nuclei are employed. In order to figure out the generic properties of the ideal EoS, the comparison is performed between the smaller number set NSE (28 species) which is smoothely connected to netwrok and the larger number one (297 species) which contains much more neutron-rich nuclei. For convinence, density ρ, temperature T and electron fraction Y_e is chosen as the independent variables for two equation of states and matter is consisted of free ions, electron, positron and photon. It should be warned that Coulomb term in Wigner-Zeit approximation is also included for evaluating internal energy density and pressure, respectively in spite of the word "ideal" in this paper.

Firstly, the deviation of pressure is discussed since it directly influence dynamics in supernova. The pressure differences, ΔP, for six Y_e is depicted as function of denesity, ρ, and temperature, T, in Fig. 3.1. The discrepancy ΔP is defined as measurment from the larger number set of nuclei, $\Delta P = P_{\mathrm{N_{nuc}=28}} - P_{\mathrm{N_{nuc}=297}}$. Paying attention to top left parts of all six panels, the differences demonstrate almost 0 since the all nuclei are melted to nucleon and the elements are safely assumed as identical. The top left panel of the figure, Y_e=0.50, demonstrate less than 0.5% difference in most of the map , however, the transion region from heavy nuclei to nucleon is not equivalent (see the yellow-red region) and $P_{\mathrm{N_{nuc}=28}}$ differs by at most 3%. It is worth while to pointing out that the larger number size model more easily dissociates into α and retains the state longer than 28 nuclei EoS as well as $Ye = 0.48$ in smaller number size.

In meantime, when it comes to more neutron-rich cases, not only the transition boundaries but also both low ρ and T regimes start to show non-negligible deviations up to 30% since the most neutron excess nuclei among the smaller set is ^{54}Fe ($Z/A = 26/54$) and free neutron starts to remedy the charge neutrality. As a result, the application of 28 nuclei is limited in $Ye \gtrsim 0.48$.

Furthermore, similar trends are seen in Fig. 3.2 which represent the mean molecular weight difference. It is apparent that the tendency can be understood by the presence of neutron. Due to less neutron-rich heavy elements, neutron become more responsible for satisfying charge neutrality in low electron fraction cases. Hence, the average mass numbers take lower value and pressures enhance rapidly below $Y_e = 0.48$ which is still larger than those at pre-collapse in the most of iron core. Showing 20-30% deviations in both low ρ and T, the smaller number size of nuclei leads to serious effect in core collapse dynamics. This is the main reason why the extended number size is applied for NSE region instead.

Tabular EoS and ideal gas EoS

Next the differences between $N_{\mathrm{nuc}} = 297$ and FYSS are assessed. As well as the previous section, the dependence of density, temperature and electron fraction on thermodynamical variables is discussed and paid particular attention where nuclear chemical transition, e.g. from iron to α, drastically happens.

Before carrying out the comparison we should define the internal energy density, e_{int}[erg/g], which is substantial for computing hydrodynamics. The internal energy density is given by

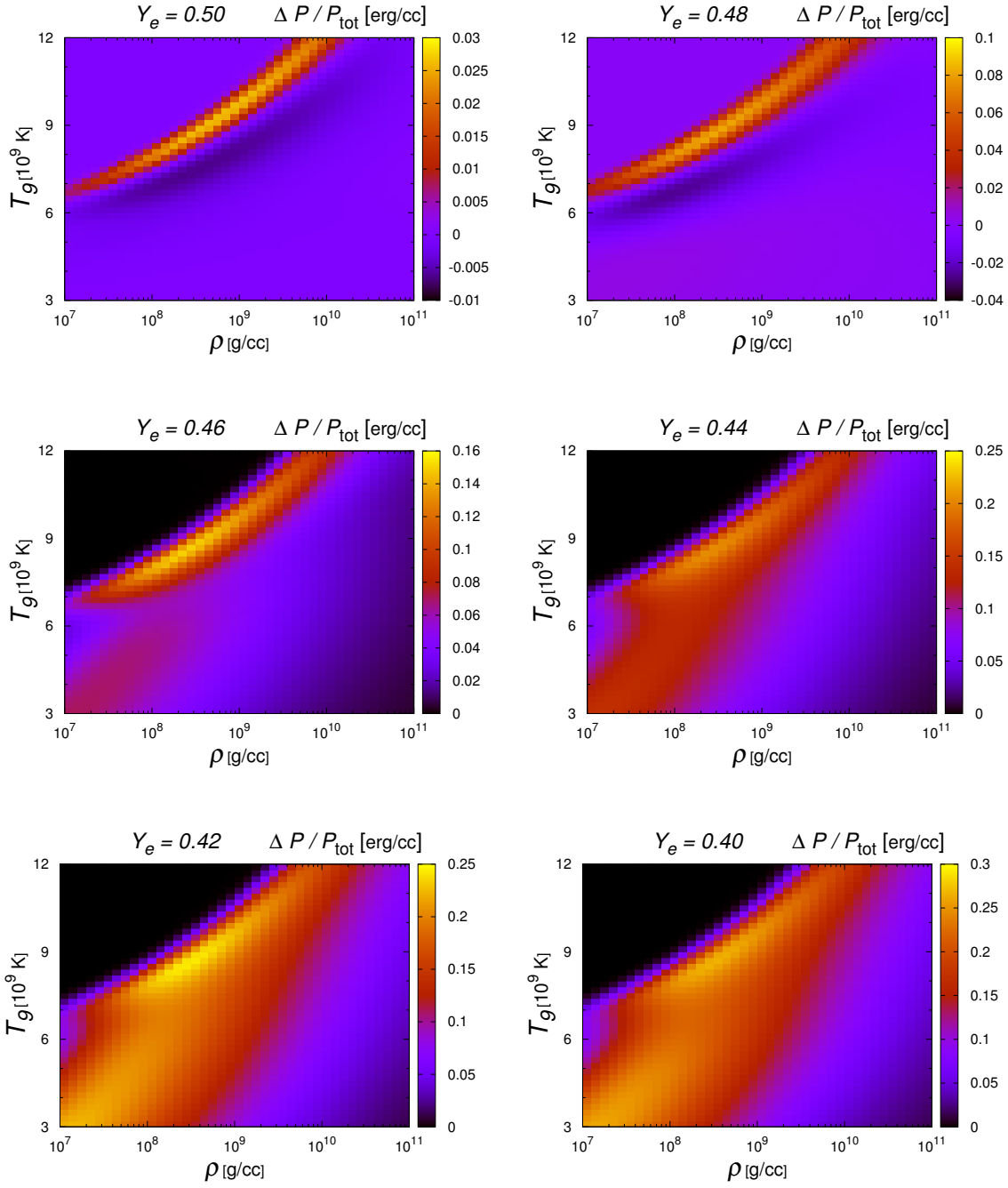

Figure 3.1: Pressure difference between large(297) and small(28) number NSE EoS in density-temperature map. The six panels are plots with different Y_e: Y_e=0.50(top left), 0.48(top middle), 0.46(top right), 0.44(bottom left), 0.42(bottom middle) and 0.40(bottom right), respectively. Note that the color origins are not always identical with each panels.

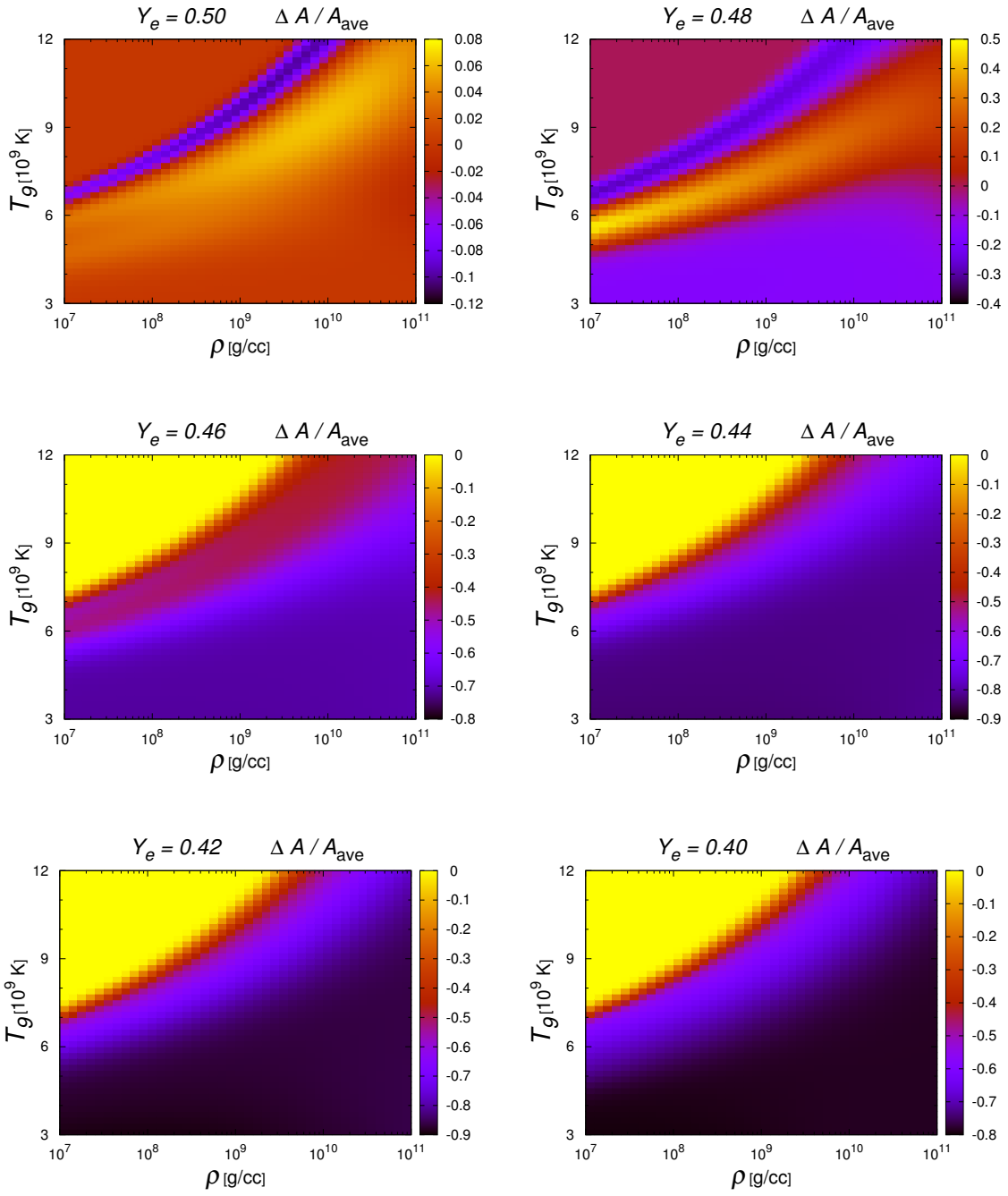

Figure 3.2: Same as Fig. 3.1 but the average mass number, or mean molecular weight in other words, is represented.

following form;

$$
\begin{aligned}
e_{\rm int} &= e_{\rm ion} + e_{\rm epr}, \\
e_{\rm ion} &= \sum_i \left(e_i^{\rm (rm)} + e_i^{\rm (th)} \right), \\
e_i^{\rm (rm)} &= A_i \cdot (M_{\rm b} - M_{\rm off}) - E_{{\rm bind},\, i}
\end{aligned}
$$

where $e_{\rm epr}$ is total energy density of e^-, e^+ ([28]) and γ. The contribution of ion, $e_{\rm ion}$ is represented as the sum of rest masses, $e_i^{\rm (rm)}$, and thermal energy, $e_i^{\rm (th)}$ which includes Coulomb correction effect under Wigner-Seitz approximation; subscript i denotes the label of nuclear species so that A_i and $E_{{\rm bind},\, i}$ correspond to mass number and nuclear binding energy for the i-th nuclei, respectively. In this paper, the baryon rest mass, $M_{\rm b}$, and the offset energy per nucleon, $M_{\rm off}$, are chosen as 938.0MeV and 931.49432MeV respectively, which are also adopted in FYSS. The offset energy is required for assuring the hydrodynamical simulation accuracy since the thermal energy is different from the rest mass by 2-3 orders. It should be noted that the ideal eos is constructed under no correction term in experimental binding energy.

In Fig. 3.3 - 3.5, the deviation of $e_{\rm int}$ between FYSS from 297 NSE EoS, $\Delta e_{\rm int}$ (left top), are investigated as well as ΔP (right top), ΔX_h (left bottom) and ΔA_h (right bottom) are represented where X_h and A_h are total mass fraction and averaged mass number of heavy elements, respectiely. All variables are measured from those of FYSS. One should be careful of a difference in normalization between $\Delta e_{\rm int}$ and ΔP. For ΔP the total pressure is given as a denominator whereas $e_{\rm epr}$ is selected in $\Delta e_{\rm int}$ since the nuclear binding energy frequently leads negative value in fotal energy.

The lines plotted in the figures are the outcomes of spherical core-collapse calculation incorporated Sn neutrino transport solver and FYSS EoS which is calculated by H. Nagakura. The line types indicate the different time when the central density reached 10^{10}[g/cm^3] (solid line), 10^{11}[g/cm^3] (thick dashed line) and 10^{12}[g/cm^3] (thin dashed line) whereas the colors represent the different electron fraction sets, $0.45 \leq Y_e \leq 0.50$ (aqua) and $0.35 \leq Y_e < 0.45$ (green), respectively.

From the top left panels in Fig. 3.3, the most of area in ρ-T map with Y_e=0.50 shows good agreement except for the transition region whose shape is "valley" in the internal energy density discrepancy (black area in the top left panel) and whose depth is up to 5%. Paying attention to the other left panels, ΔX_h, in Fig. 3.3 - 3.5, the relatively large discrepancies appear in almost same regime which implies that the energy density differences originate from the heavy nuceli abundance. The heavy elements state stay more stable in FYSS than in the ideal EoS. It should be noted that the differences result from not the number of size whose impact has been already demonstrated in the previous section but the treatment of nuclear binding energy, especially the bulk energy part.

In the top right panel of the figure, however, the pressure difference is less than the internal energy. This fact indicates that the leptons are crucial for dynamics in this regime and the binding energy difference produce the valley strcuture in ρ-T plane. It is interesting that the trajectries of the simulation on ρ-T map evolve parallel along the EoS valley/mountain while the aqua lines (relatively larger Y_e)), unfortunately, pass nearby this large discrepancy regime. Similarly, when electron fraction is reduced to 0.45, the good agreement between two EoS still holds except for the transition region, however, the black valley region in the top left panel move to the lower density direction. As a result, the paths of core-collapse simulation lie on the edge of the valley (see Fig. 3.4). There are, however, another large

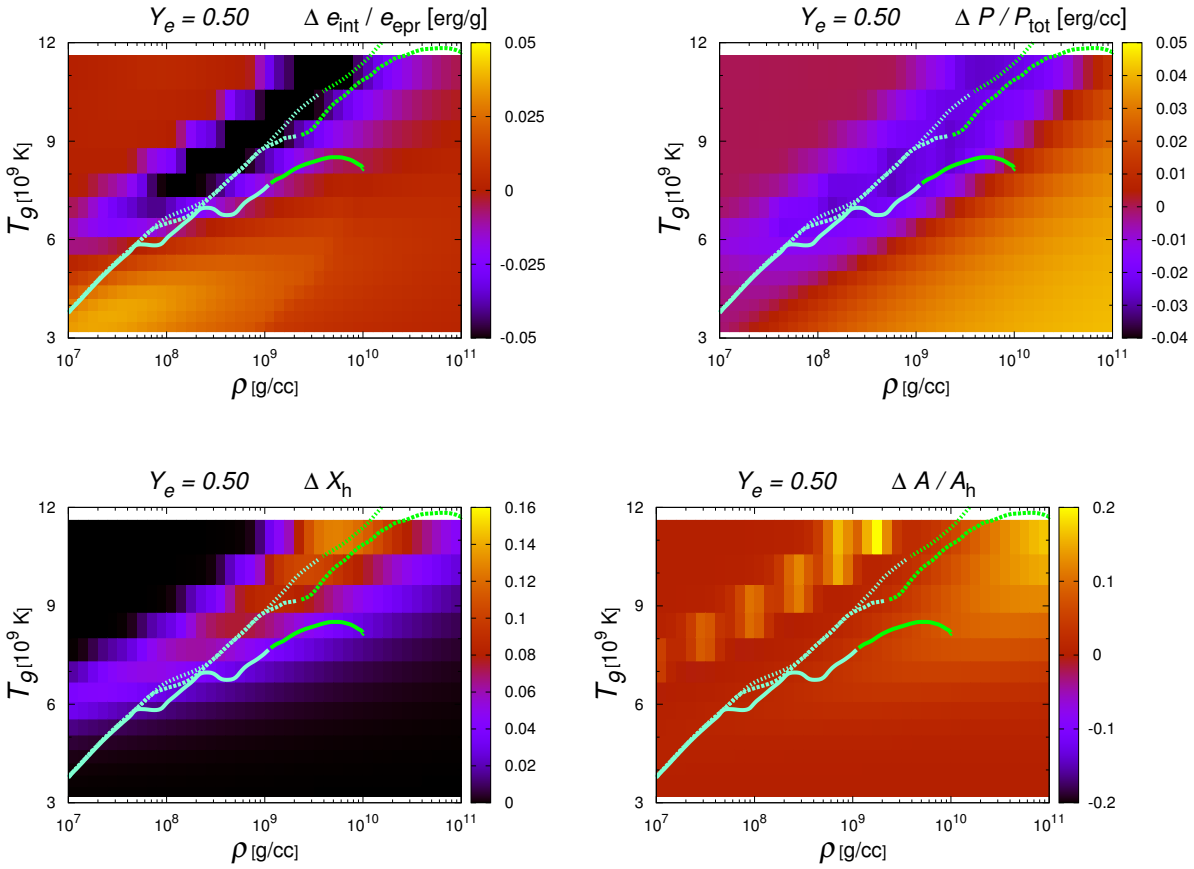

Figure 3.3: The physical properties deviation of FYSS from the 297 nuclei eos projected on density-temperature map. The internal energy density (left top), pressure (right top), heavy nuclei mass fraction (left bottom) and average heavy nuclei mass number (right bottom) are illustrated, respectively. Electron fraction Y_e is chosen as 0.50. The three line types depict trajectories of realisitic 1D simulation during core collapse phase when central densities reach 10^{10} (solid), 10^{11} (thick dotted) and 10^{12}[g/cm^3] (thin dotted), respectively. The line colors illustrate different electron fraction set, $0.45 \leq Y_e \leq 0.50$ (aqua) and $0.35 \leq Y_e \leq 0.45$ (green).

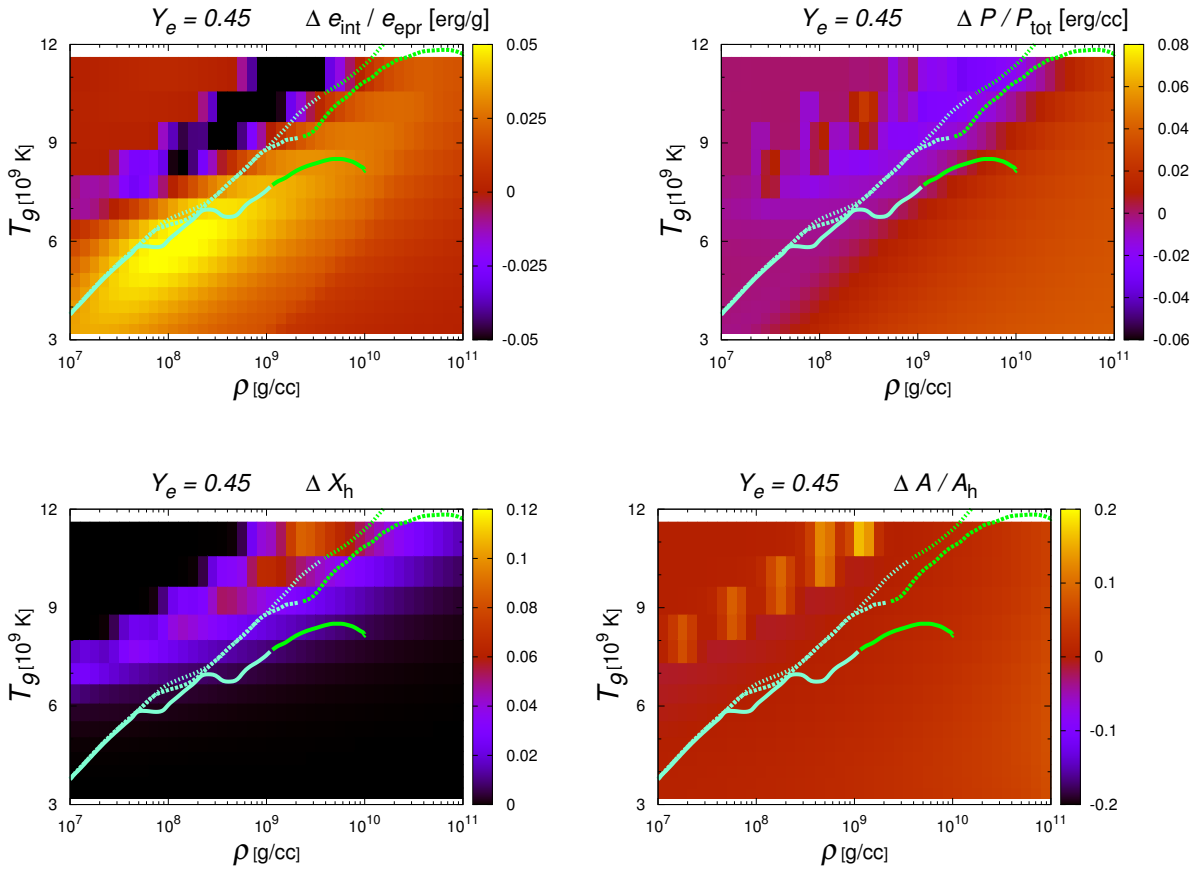

Figure 3.4: Same as Fig. 3.3 but Y_e=0.45.

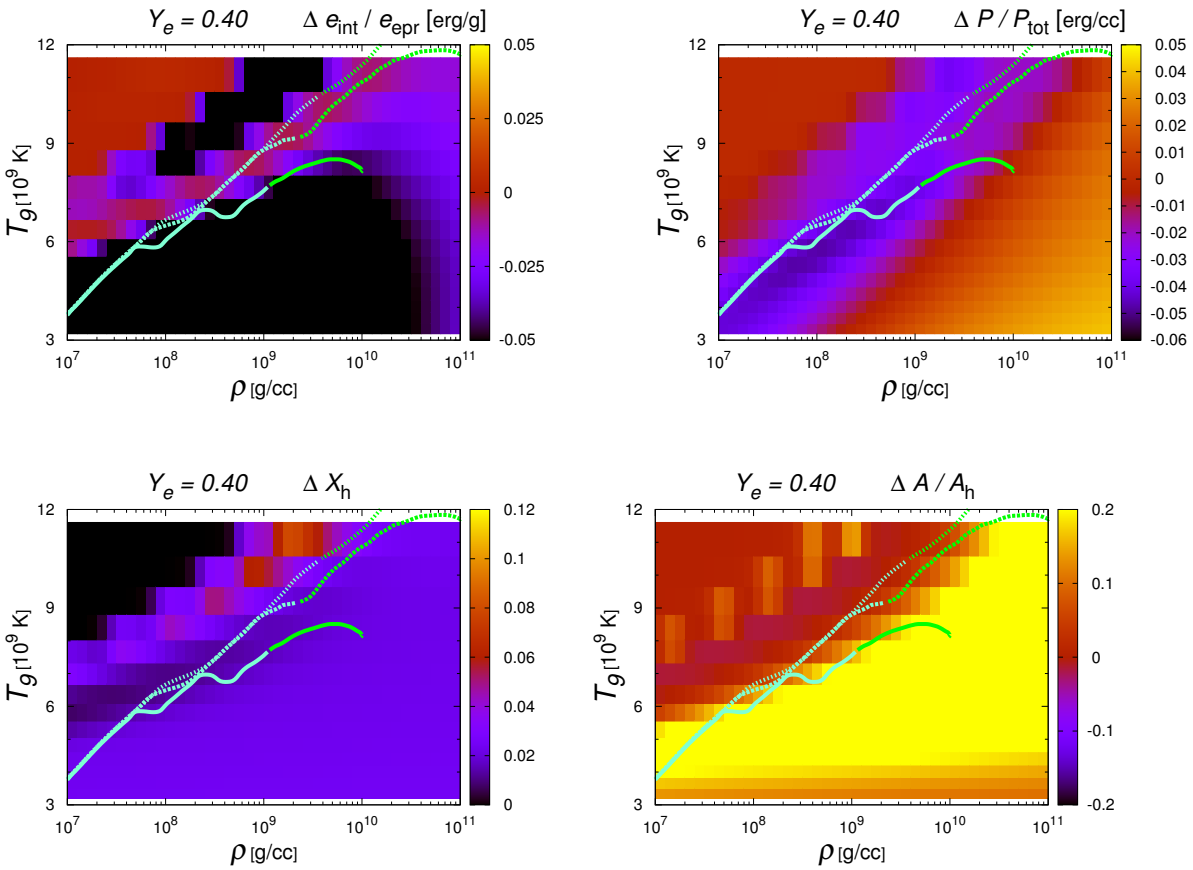

Figure 3.5: Same as Fig. 3.3 but Y_e=0.40.

deviation in the internal energy density where both eos are governed by heavy elements with almost the same A_h. This yellow colored "mountain" in $\Delta e_{\rm int}$ means that FYSS has larger internal energy than 297 nuclei EoS under the same thermodynamical inputs. The dynamical evolution paths are partly on this yellow mountain instead of black valley. The internal deviation problem seems to appear around the chemical transition regions.

In Fig. 3.5, on the contrary, there are large gap between the two EoS so that the tendecy commonly seen in $Ye = 0.50$ and 0.45 is violated. The reason of this violation is, however, quite apparent since the similar phenomena has been already demonstrated in Fig. 3.1-3.2. It is expected that the difference should be relaxed if one prepare larger size of nuclear sets which contains adequant numbers of neutron-rich nuclei.

Finally I increase the size of nuclei set up to 683 so as to investigate how the deviation of two EoS alter. In this case the nuclear set almost cover the same chemical species with $A \leq 78$ in FYSS. Fig. 3.6 - 3.8 demonstrate the difference in internal energy density, $e_{\rm int}$[erg/g], pressure, P[erg/cm^3], mass fraction of heavy nuclei ($Z > 6$), X_h and average mass number of heavy nuclei, A_h, with 3 different Y_e, which are exactly same as the previous comparison.

Comparing Fig. 3.6 and 3.7 with Fig. 3.3 and 3.4, respectively, it is apparent that the results of $N_{\rm nuc} = 682$ show identical features with those of $N_{\rm nuc} = 297$ in Y_e=0.50 and 0.45. This fact implies that the latter smaller number sets of nuclei is responsible for

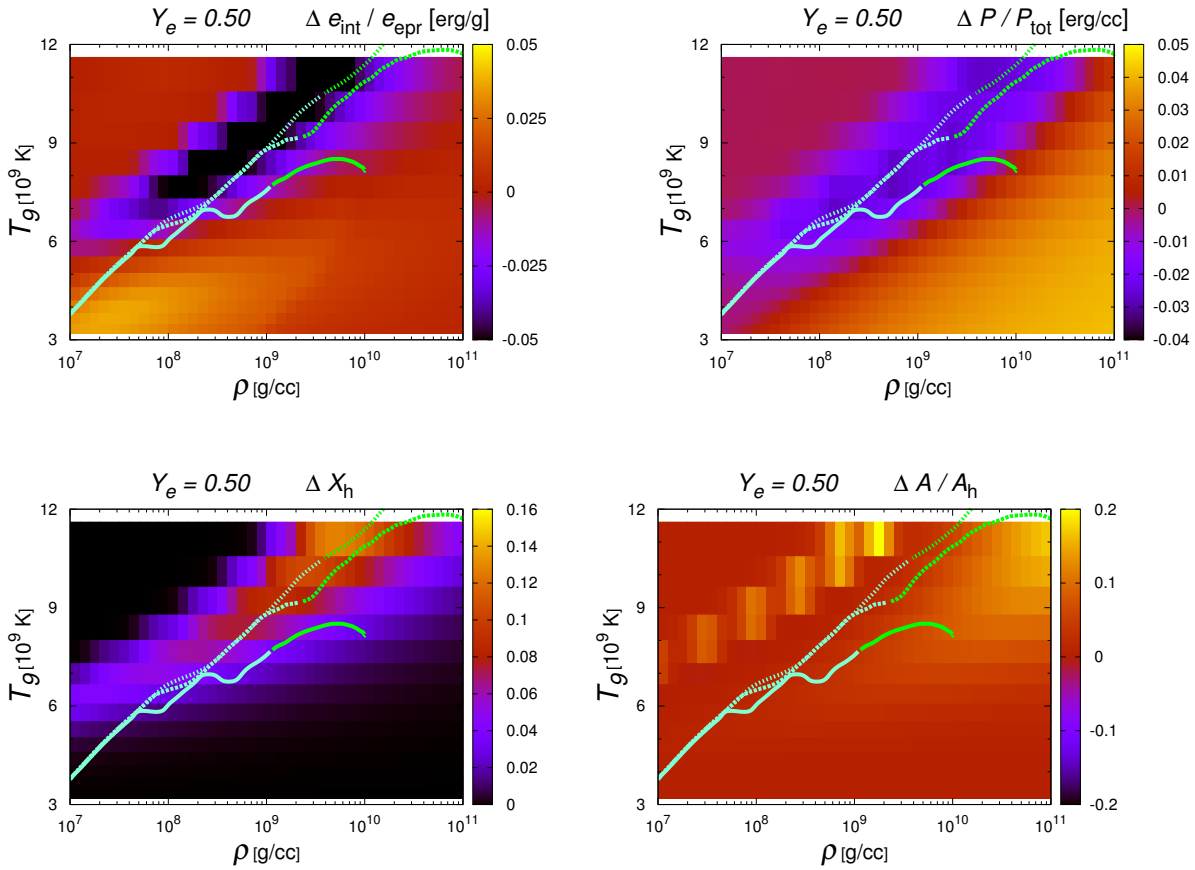

Figure 3.6: Same as Fig. 3.3 but the total number of nuclei is 683, instead.

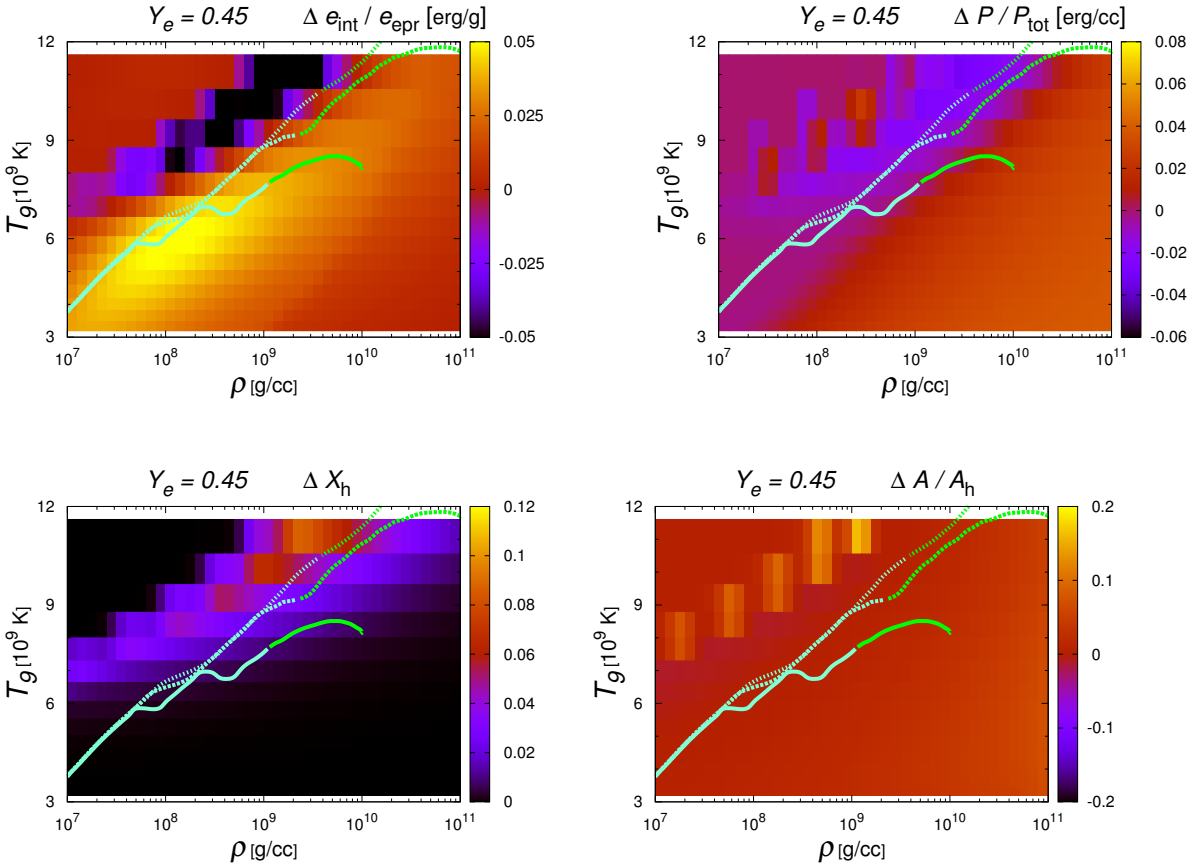

Figure 3.7: Same as Fig. 3.4 but $N_{\rm nuc} = 683$.

internal energy density, pressure and other thermal quantities. Increasing the total number of nuclei does not help to remedy the difference from FYSS so that the alternative approach is required.

Meanwhile, in Fig. 3.8, i.e. the case of Y_e=0.40, $N_{\rm nuc} = 682$ EoS provide great improvement to match FYSS due to the additional neutron-rich nuclei. As a consequence, the common properties are shown in the latest three figures and not only the black "valley" but also the "yellow" mountain also move as electron fraction changes. It seems that the slight difference in A_h leads to about 5% discrepancy in internal energy due to the binding energy difference. The issue is pinned down to which correction term or terms of binding energy is important. The modification of nuclear binding energy is investigated in the next section. In this paper, I choose $\rho_{\rm min} \leq \rho \leq \rho_{\rm max}$ for two EoS buffering connection region where $\rho_{\rm min} = 10^9 [{\rm g/cm^3}]$ and $\rho_{\rm max} = 10^{10} [{\rm g/cm^3}]$ and offset value $\delta M_{\rm off} = 0.06 {\rm MeV}$.

The binding energy correction

As already mentioned in the beginning of the two eos comparisoion, the information of internal energy density plays crucial role for dynamical calculations. The less deviation in $e_{\rm int}$ is preferred for two different equation of states connenction. From Fig. 3.6 to 3.8 the postive and negative discrepancies seems to rely on electron fraction so that nuclear

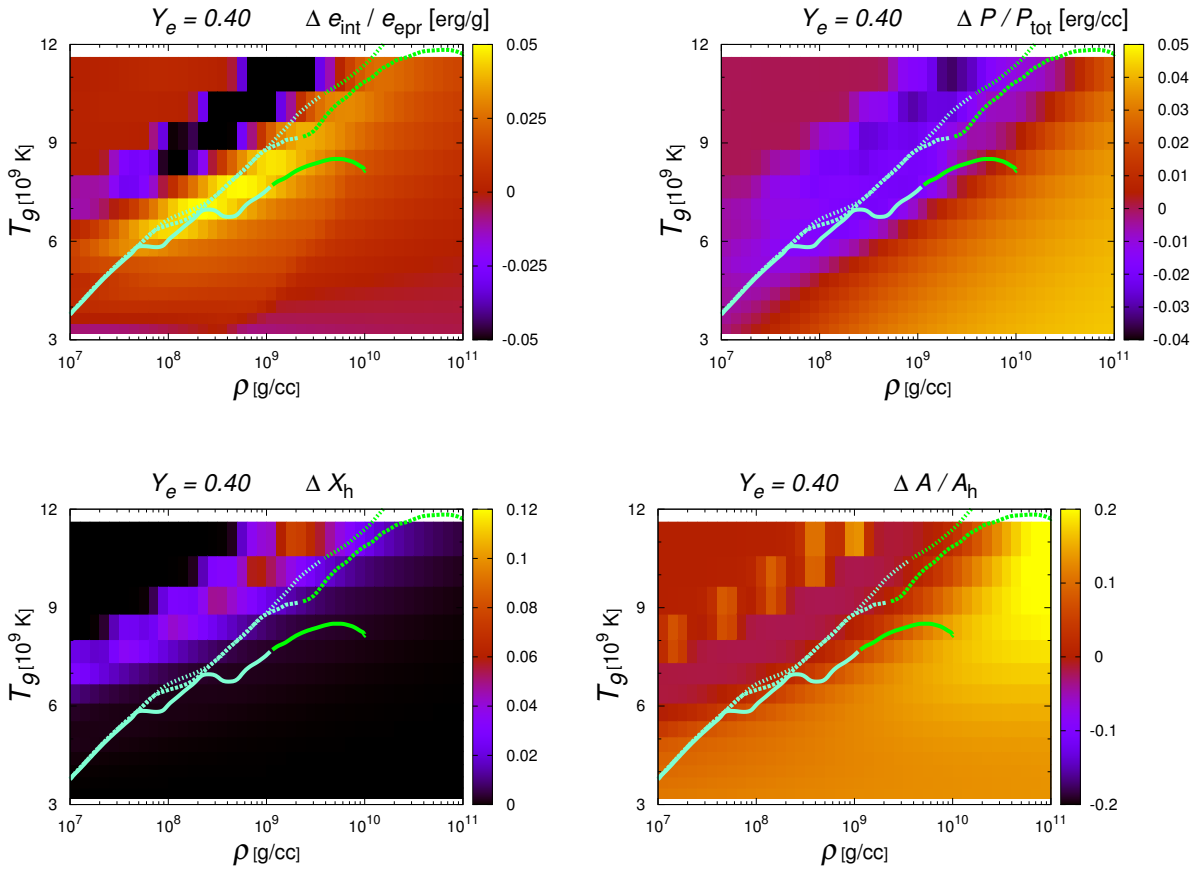

Figure 3.8: Same as Fig. 3.5 but $N_{\rm nuc} = 683$.

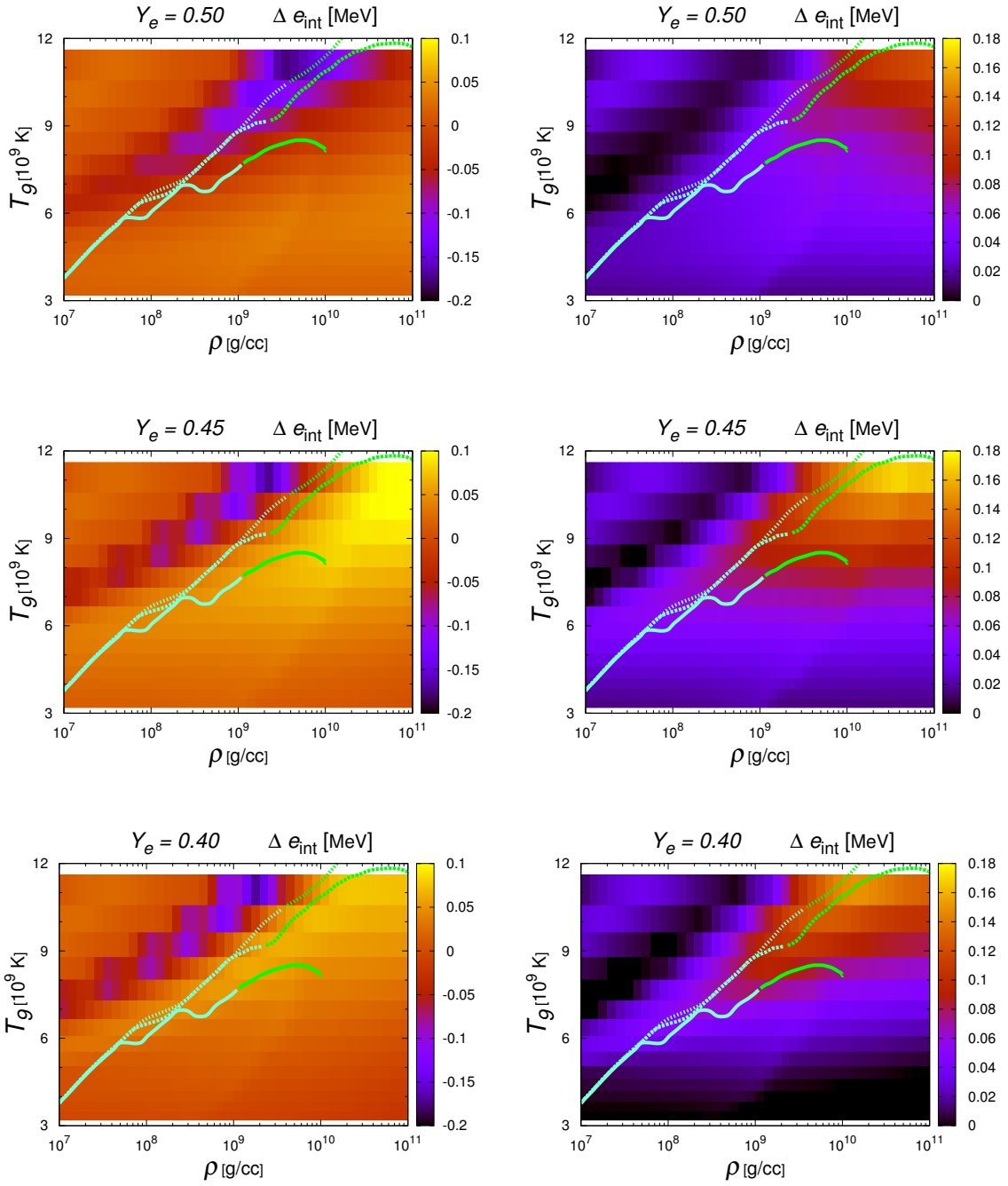

Figure 3.9: The difference in internal energy density in MeV per nucleon unit between FYSS and the ideal EoS. The Coulomb term in nuclear binding energies derived from Wigner-Zeit approximation is neglected in the left panels while it is incorporated in the right panels.

interactions associated with asymmetry or charge may be responsible. Being incorporated in pressure and internal energy density, the effect is not taken into account for chemical potential. For this reason, the nuclear binding energies is modified by adding Coulomb correction term, $E^{(C)}_{\rm bind}$, to confirm how much the deviation of $e_{\rm int}$ is relaxed. As well as in internal energy density, the formulation of Coulomb energy between an ion and electron is given as following relation;

$$E^{(C)}_{\rm bind} = -\frac{3}{5}\frac{Z^2e^2}{r_{\rm A}}\left(\frac{3}{2}\frac{r_{\rm A}}{r_{\rm WS}} - \frac{1}{2}\left(\frac{r_{\rm A}}{r_{\rm WS}}\right)^3\right)$$

where A, Z, $r_{\rm A} = (4\pi n_0/3A)^{-1/3}$ and $r_{\rm WS} = (4\pi n_e/3Z)^{-1/3}$ are mass number, proton number, radius of nucleus and Wigner-Zeit cell, respectively (see also [242, 167, 134]).

Figure 3.9 illustrates $\Delta e_{\rm int}$ in MeV per nucleon unit for no correction cases (left panels) and correction included cases (the right panels). Thanks to the modification of nuclear binding energy, the range of errors turn out to be smaller value and only the mountain structures emerge where $e_{\rm int}$ of FYSS is larger in ρ-T plane. This is because the chemical phase transition take place almost simultaneously so that the valley structure vanish from the map. In terms of physics, this can be interpreted that the Coulomb effect usually increase binding energy so that it tends to prefer the state with heavy elements to those with nucleon. Recalling that the binding energy per nuclon for heavy elements is about 8.8MeV, the deviations are suppressed in the extent of only 1-2% for the Coulomb correction and the remarkable agreement is shown in Y_e =0.50.

Although the corrected binding energy of $N_{\rm nuc} = 682$ seem to converge to the FYSS binding energy better, the magnitude of $\Delta e_{\rm int}$ still remain non-neglegible compared with $e_{\rm epr}$ especially when Y_e <0.50, the asymmetry matter cases. This fact may be suggesting that the treatment of symmetry energy which is one of the bulk energy term should be another origin of difference between the two equation of states. The further study is, however, beyond this work and will be done in the forthcoming paper.

3.1.3 Nuclear reaction network

Nuclear reaction network (NRN) is utilized in wide astrophysical fields where temperature is not considerably high and chemical elements evolution is substantial, e.g. steller evolution and nucleosynthesis. In this paper I compute NRN to investigate nuclear recombinations, the explosive Si/O burning and α-rich freeze-out so as to understand how these reactions contribute to explosion energy and nickel mass. Since NSE EoSs tend to overestimate the heavy nuclei abundance and recombination energy, NRN is necessary for these explosion properties study. In this chapter, EoS and non-NSE are both important ingredients so that physics, numerical treatments and implementation to hydrodynamics are discussed.

Numerical treatment

It is helpful for readers to follow previous studies, e.g. [178], [436], and the excellent lecture notes provided by Frank Timmes (cococubed.asu.edu/) together with this section. Since independent variables are only chemical potentials of nucleon, NSE can easily (but carefully) computed under mass and charge constraints by Newton-Raphson method.

On the other hand, NRN is more complicated. The nuclear timescale for each i-th nuclear element is evaluated as

$$\tau_{nuc,\,i} \equiv \frac{Y_i}{\dot{Y}_i} \tag{3.5}$$

and usually different by several order of magnitude. Hence, the ODEs of nuclear reaction network are "stiff " which implies numerical instability and requires extremely small time steps to evolve safely. In such a case, it is more favorable to choose implicit method to time evolution of nuclear elements.

Adopting implicit method, the discretization of eq. (3.1) is given by

$$\frac{Y_i^{(\mathrm{n}+1)} - Y_i^{(\mathrm{n})}}{\Delta t} = f_i\left(\rho, T, Y_k^{(\mathrm{n}+1)}\right) \tag{3.6}$$

where superscript (n) denote the n-th time steps and the right hand side of Y_i take the next time step values. However, the set of $Y^{(\mathrm{n}+1)}$ is still unknown, eq. (3.6) should be linearized and expressed as

$$\left(\frac{\delta_{ij}}{\Delta t} - \frac{\partial f_k}{\partial Y_j}\right) \cdot \Delta\widetilde{Y}_j^{(\mathrm{it})} = f_i\left(\rho, T, \widetilde{Y}_k^{(\mathrm{it})}\right) - \frac{\widetilde{Y}_i^{(\mathrm{it})} - Y_i^{(\mathrm{n})}}{\Delta t} \tag{3.7}$$

$$Y_i^{(\mathrm{n}+1)} = \widetilde{Y}_i^{(\mathrm{it})} + \Delta\widetilde{Y}_i^{(\mathrm{it})} \tag{3.8}$$

where chemical abundance guess $\widetilde{Y}_i^{(\mathrm{it})}$ and the number of iteration (it) are introduced.

Solving $\Delta\widetilde{Y}_i^{(\mathrm{it})}$, the next guess is obtained by

$$\widetilde{Y}_i^{(\mathrm{it}+1)} = \widetilde{Y}_i^{(\mathrm{it})} + \Delta\widetilde{Y}_i^{(\mathrm{it})} \tag{3.9}$$

and iterations last until $\Delta\widetilde{Y}_i \sim 0$. In my calculation, the nuclear calculation is assumed to be converged if $\frac{\Delta\widetilde{Y}_i}{\widetilde{Y}_i} < 10^{-6}$ for all dominant abundance of nuclei. The time interval relies on the accuracy of nuclei abundance. It should be noted that it is usually difficult to give Δt as hydrodynamic time step in eulerian based code since $Y_i^{(n)}$ is temporary affected by advection flow. Therefore, time interval values, i.e. $Y_i^{(\mathrm{int})}$ and $\Delta t^{(\mathrm{int})}$, are prepared in order to obtain $Y_i^{(n+1)}$ during dynamical computation.

It should be noted that the main computational cost in this implicit method is solving the inverse matrix of $A_{ij} = \frac{\delta_{ij}}{\Delta t} - \left(\frac{\partial f}{\partial Y}\right)_{ij}$, thus sensitively depend on the size of the matrix A_{ij}. Moreover, usually the matrix is "sparse" which means the most of its elements are 0 and holds no symmetry in its structure. Timmes (1999) [436] demonstrates how the matrix solver subroutines are time consuming and which solvers are the most efficent. They also propose semi-implicit method for retaining accuracy with larger time intervals.

Due to using an Eulerian hydrodynamical code, the compositions in each grids are altered by advection flow from their adjacent grids. This cause numerically unstable behavior at the first several subsize time-step of nuclear network calculations. I employed semi-implicit method for the first two substeps in order to avoid wasteful computation above $T_9 > 3.0$. Semi-implicit method is also utilized for all steps when temperature T_9 are between 3.0 and 1.5.

We deploy 28 nuclei: n, p, D, T, ^{3}He, ^{4}He and 12 α-nuclei, i.e., ^{12}C, ^{16}O, ^{20}Ne, ^{24}Mg, ^{28}Si, ^{32}S, ^{36}Ar, ^{40}Ca, ^{44}Ti, ^{48}Cr, ^{52}Fe, ^{56}Ni, and 9 their neutron-rich neighbors, or ^{27}Al, ^{31}P, ^{35}Cl, ^{39}K, ^{43}Sc, ^{47}V, ^{51}Mn, ^{53}Fe, and ^{55}Co. We take into account emissions of a nucleon and α particle as one-body interactions as well as three-body reactions such as $3\alpha \rightarrow$ C in addition to the main reactions: (α, γ), (α, p), (p, γ) and their inverses. The reaction rates are taken from REACLIB [362] as well as nuclear binding energies, spin values and partition functions. As demonstrated later, the employment of this rather small network is validated by the re-computations of nuclear yields with a larger network including 463 nuclei, from n, p, and α up to ^{94}Kr (Fujimoto et al.2004) for the densities and temperatures obtained by the simulations as a post-process.

3.2 Implement of hydrodynamics simulaiton

To implement the accurate chemical abundance evolution, I designed EoS programs so as to combine it with hydrodynamical simulations. The bulk fluid is consisted of ion gas, $e^{\pm}$ and photon. The estimation of electron and positron contributions is based on Blinnikov et al.(1996) [28]. In addition to the ideal part, Coulomb correction is also calculated for ion gases under either Wigner-Zeit approximation or fitting formula from Ichimaru et al.(1982) [191]. The strategy is shown in Fig. 3.10. I classify three temperature region as freeze-out ($T_9 \leq 1.5$), NRN ($1.5 \leq T_9 < 7.0$) and NSE ($7.0 \leq T_9$). For the computations, one needs to prepare ρ, $e_{\rm int}$, Y_e and $T^{(0)}$, the initial guess of temeprature, for all three divisions and carried out Newton-Raphson or bi-section method to obtain the given internal energy $e_{\rm int}$. Firstly, in case of freeze-out, the nuclear time scale is rather larger than dynamical one so that Y_k is unchanged from the input. Secondly, NRN is computed to determine the correct T under evolving Y_k, i.e. the variation of $e_{\rm m}$. If T is sufficiently high, chemical elements are in NSE. Since NSE region contains the high density region where strong interaction should be take into account, I connect my 'ideal' EoS to FYSS carefully where the two EoS show smaller difference in $0.45 \leq Y_e \leq 0.50$. From the previous section, the density range from 10^8[g/cm^3] to 10^{10}[g/cm^3]seems to be preferable and it would be safe to employ ρ between $\rho_{\rm min} = 10^9\,{\rm g\,cm^{-3}}$ and $\rho_{\rm max} = 10^{10}\,{\rm g\,cm^{-3}}$ for the buffer region where two EoS are blended

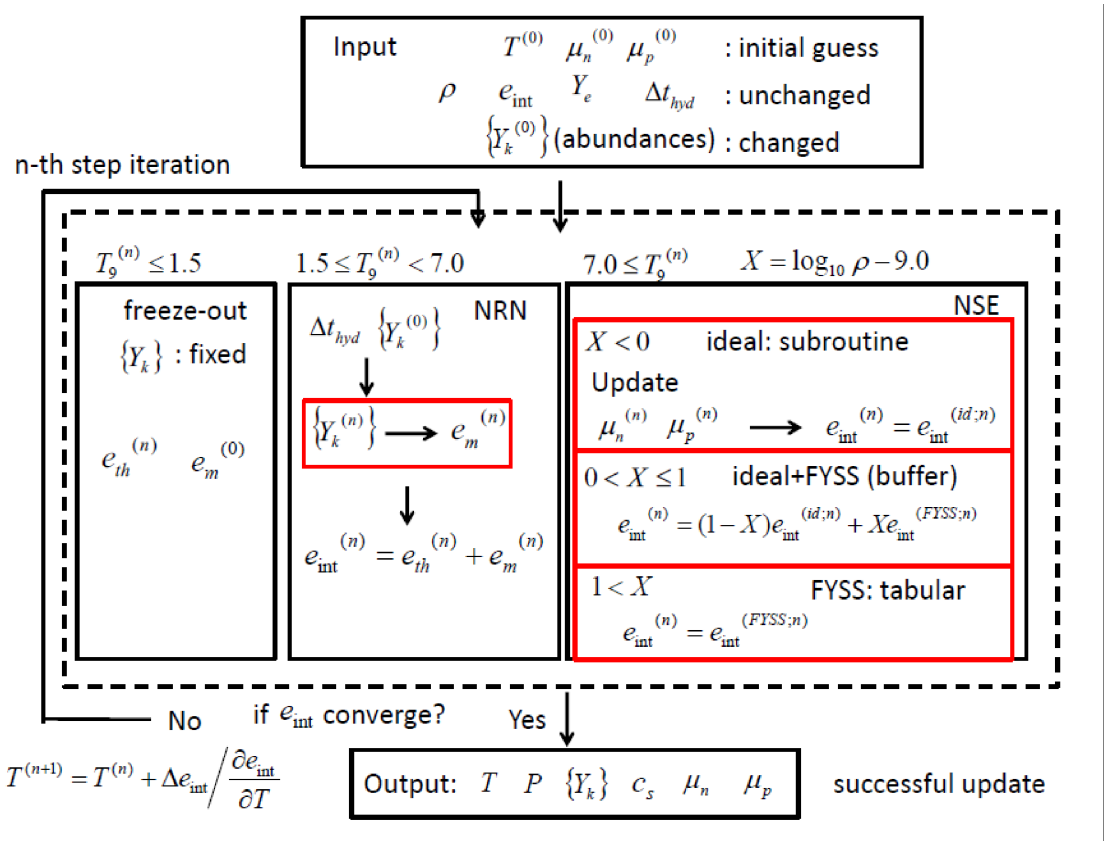

Figure 3.10: Numerical procedure of determining EoS together with hydrodynamical code.

in following way:

$$\left(\frac{\partial e_{\rm int}}{\partial T}\right)_{\rho,Y_e} = X\left(\frac{\partial e_{\rm int}^{\rm (FYSS)}}{\partial T}\right)_{\rho,Y_e} + (1-X)\left(\frac{\partial e_{\rm int}^{(id)}}{\partial T}\right)_{\rho,Y_e} \tag{3.10}$$

$$X = \frac{\ln\rho - \ln\rho_{\rm min}}{\ln\rho_{\rm max} - \ln\rho_{\rm min}}. \tag{3.11}$$

3.3 Steady shock solution

As mentioned in section 2.2, the propagation of shock launched from inner core is halted by serious photo-dissociation and neutrino emission. If dynamical timescale is much shorter than the typical evolution timescale inside the shock front, e.g. PNS mass, the system may be safely represented by steady shock solution. Due to supersonic flow velocity, the pre-shock region is independent of inner boundary condition and relies on only the history of outside the shock. If one impose steady flow under spherical symmetry, the upstream flow state corresponds to the past history of downflow state. The physical variables, e.g. density, velocity, internal energy and pressure, behind shock are associated with the preshock region

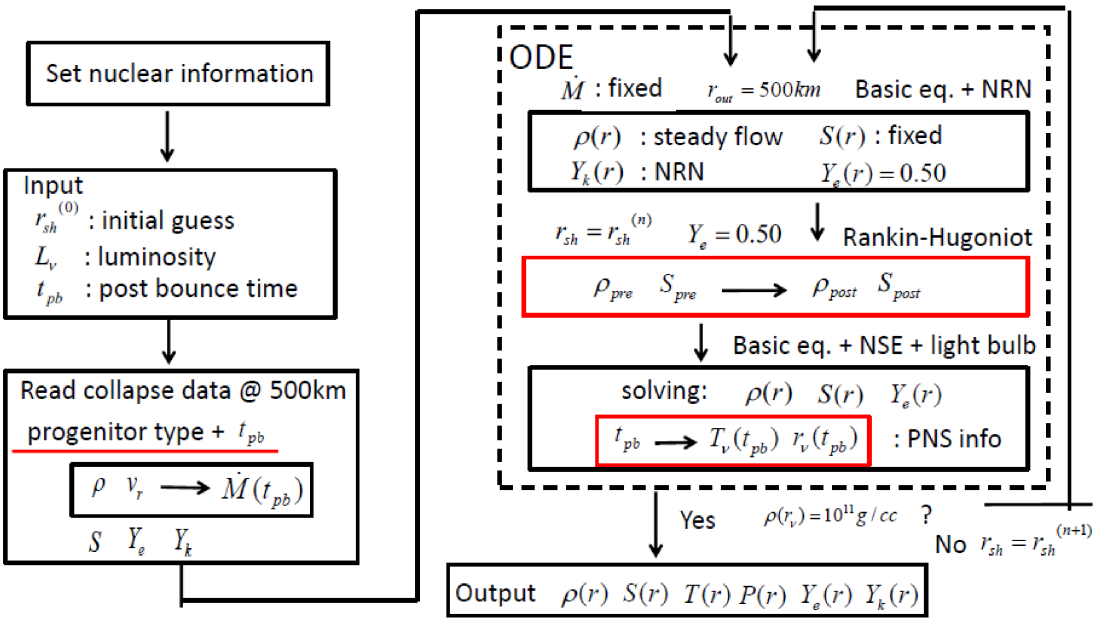

Figure 3.11: An illustration of numerical treatment for steady shock solution.

and satisfy Rankin-Hugoniot jump conditions;

$$\rho_{\rm post} v_{\rm post} = \rho_{\rm pre} v_{\rm pre} \tag{3.12}$$

$$\rho_{\rm post} v_{\rm post}^2 + P_{\rm post} = \rho_{\rm pre} v_{\rm pre}^2 + P_{\rm pre} \tag{3.13}$$

$$v_{\rm post}\left(\rho_{\rm post}\frac{v_{\rm post}^2}{2} + h_{\rm post}\right) = v_{\rm pre}\left(\rho_{\rm pre}\frac{v_{\rm pre}^2}{2} + h_{\rm pre}\right) \tag{3.14}$$

where ρ, v, P and h are density, radial velocity, pressure and enthalpy, respectively while the suffixes "post" and "pre" indicate the position of variables. Here, the shock velocity is identified as 0 since it is assumed as stalled shock.

In order to construct the steady shock solution, we assume mass accretion rate $\dot{M}$ and neutrino luminosity L_ν as two parameters and have first started compuatation from outer boundary region (radius, $r \sim 500 - 1,000$km) where the mass accretion rate is given and are almost constant up to neutrino sphere. The equations are given as following relations (see [482]);

$$4\pi r^2 \rho v_r = \dot{M}, \tag{3.15}$$

$$\frac{dM_r}{dr} = 4\pi r^2 \rho, \tag{3.16}$$

$$v_r \frac{dv_r}{dr} + \frac{1}{\rho}\frac{dp}{dr} + \frac{GM}{r^2} = 0, \tag{3.17}$$

$$v_r \rho T \frac{dS}{dr} = \dot{q}, \tag{3.18}$$

$$v_r n \frac{dY_e}{dr} = \lambda, \tag{3.19}$$

$$v_r \frac{dY_i}{dr} = f_i(\rho, T, Y_k) \tag{3.20}$$

where r, v_r, ρ, P, S, Y_e and n denote the radius, radial velocity, density, pressure, entropy per unit mass, electron fraction and baryon number density, respectively; $\dot{M}$, G and M_r are

the mass accretion rate, gravitational constant and mass enclosed in the sphere of radius r, respectively; $\dot{q}$ and λ are the heating and reaction rates due to the reactions with neutrinos, respectively.

If $r \leq r_{\rm sh}$, the heating and reaction number rates can be decomposed accordingly as

$$\dot{q} = \dot{q}_{\rm ep} - \dot{q}_{\nu \rm n} + \dot{q}_{\rm e^+n} - \dot{q}_{\bar{\nu}\rm p}, \tag{3.21}$$

$$\lambda = -\lambda_{\rm ep} + \lambda_{\nu \rm n} + \lambda_{\rm e^+n} - \lambda_{\bar{\nu}\rm p}. \tag{3.22}$$

otherwise q and λ are zero. The subscripts represent the left hand side of neutrino-nucleon reactions (see the next section). The neutrino is emitted from the inner boundary where PNS surface is located and the condition $\rho = 10^{11}$g/cc is imposed. The subscripts denote parent elements of weak interaction reaction.

The basic equations from eq. (3.15) to (3.20) correspond to mass, momentum and energy conservations, electron fraction and nuclear abundance evolutions, respectively. One of our improvment from previous research [481] is the proper treatment of chemical component, the last line of above equation set, above the stalled shock front. The abundances change gradually until they reach $r \sim 200 - 300$km and suddenly transform to iron or ^{4}He which has been already seen in our core collapse calculaitons. It should be noted that the neutrino reactions are turned off in this pre-shock region due to the absence of nucleon.

After solving the super sonic regime, the physical properties right behind the shock front is determined by Rankin-Hugoniot equations (see eq. 3.12-3.14) and, because of its high tempearature ($T \gtrsim 10^{10}$K), nuclear reaction are completely chemical equilibrium, i.e. NSE approximation is assured. The basic equations are slightly changed in energy conservation (eq. 3.14) due to the presence of neutrino heating and cooling and chemical abundance evolutions are neglected.

The electron and anti-electron type neutrino sphere radius, $r_{\nu_e,\,\bar{\nu_e}}$ and temperature, $T_{\nu_e,\,\bar{\nu_e}}$ are given as parameters and choosen to reproduce those obtained from realisitic simulation [411, 304]. As a result, the evolution of neutrino sphere properties, r_ν and T_ν, is related to $\dot{M}$ since we characterized the mass accretion rate as function of post bounce time.

To obtain the steady shock solution for the given parameter set ($\dot{M}$, L_ν), we first give the initial guess of shock radius, $r_{\rm sh}^{(i)}$, and carry out the computations until density at the inner boundary satisfies $\rho = 10^{11}\,{\rm g/cm^3}$.

The procedure of steady shock solution construction is drawn in Fig. 3.11. First, set nuclear properties such as mass, charge and neutron number, binding energy, spin and partition function for selected species. Next, choose luminosity, L_ν, and post bounce time, $t_{\rm pb}$, as well as initial guess of shock radius $r_{\rm sh}^{(0)}$ which is usually given as 100km. The collapse profile for selected progenitor models at $t_{\rm pb}$ provide density, velocity, entropy, electron fraction and chemical abundances at $r = 500$km. Since the flow is steady, mass accretion rate is easily calculated from ρ and v_r. In order to solve the ODEs, three steps are carried out. Starting from $r_{\rm out} = 500$km, initial values are known so that the basic equaitons are immediately solved toward the shock position under no neutrino interaction, i.e. entropy and Y_e are unchanged during this upstream flow, since there are neither proton nor neutron outside the stagnent shock. It should be noted that self-gravity is included in gravitational field. When the radius reached $r = r_{sh}$, one has to obtain the discontinuous values, e.g. $\rho_{\rm post}$, $S_{\rm post}$ and $Y_{e,\,\rm post}$ from Rankin-Jugoniot relation (eq. 3.12-3.14). Already knowing the complete preshock states, $v_{\rm sh} = 0$ and

$$v_{\rm post} = \frac{\rho_{\rm pre}}{\rho_{\rm post}} v_{\rm pre}, \tag{3.23}$$

one only need to solve $\rho_{\rm post}$ and $S_{\rm post}$. The two postshock variables are updated until the mometum and energy conservation are accurately fulfilled. After solving Rankin-Jugoniot, same procedure as those in preshock region carried out except for the presence of neutrino interaction. The postion and temperature (mean energy) of neutrino are function of post bounce time.

ODEs are solved until density reaches $\rho(r) = 3.0 \times 10^{11}{\rm g/cm^3}$. If the neutrino sphere density is not matched accurately with the condition, $r_{\rm sh}$ is updated to

$$r_{\rm sh}^{(n+1)} = r_{\rm sh}^{(n)} + \frac{dr_{\rm sh}}{d\rho_{\rm in}}\Delta\rho_{\rm in} \tag{3.24}$$

and repeat the calculation until they converge.

3.4 Light bulb approximation for neutrino heating

The realistic treatment of neutrino is extremely delicate (as one may has already seen in appendix B) and apparently uncontrolable. Furthermore, since other physics are also tightly entangled, the neutrino transportsolver doesn't suit for carrying out experimental researchs of physical properties in some cases. By alternative approaches, the light bulb approximation or analytic neutrino source terms, $q^+ \propto r^{-2}$ and $q^+ \propto r^{-6}$, are rather simple and convienent so that shock revival can easily obtained [481, 121, 325, 291, 193, 344, 108, 131, 77, 152].

In this paper, I employed the light bulb approximation which is established on the assumptions that neutrino obeys Fermi-Dirac distribution and travels through matters as free streaming emisson from PNS. In this case, the average neutrino energy and flux factor are given by hand. As for the neutrino reactions, we take into account only the emission and absorption on free nucleons;

$$p + e^- \rightleftharpoons \nu_e + n, \tag{3.25}$$

$$n + e^+ \rightleftharpoons \bar{\nu}_e + p. \tag{3.26}$$

The chemical potentials are assumed to be zero for simplicity. In evaluating the heating and cooling of matter by neutrino absorptions and emissions, we employ the local distribution function of neutrino given by the following expression:

$$f(r, \varepsilon) = \frac{C(r)}{1 + \exp(\epsilon/k_B T_\nu)}, \tag{3.27}$$

where k_B is the Boltzmann's constant and the normalization factor, $C(r)$, is determined so that the local number density of neutrino, $n_\nu(r)$, is given by the following relation:

$$L_\nu = 4\pi r^2\, n_\nu(r) \cdot \langle \varepsilon_\nu \rangle \cdot \langle \mu(r) \rangle, \tag{3.28}$$

where the last factor, $\langle \mu(r) \rangle$, is the flux factor that accounts for how quickly the angular distribution becomes forward-peaked. We again employ the fitting formula given in [378] for the radial dependence of the flux factor.

The neutrino reaction rates are calculated in almost same way in Ohnishi et al.(2006) [325] but the flux factor, $\mu(r)$, is modified in the way proposed by Scheck et al.(2006) [378]. We should also stress that the effect of neutrino sphere evolution is considered in this paper and fitted by the formulae described in [199, 195] (see the next two chapters for detailed expressions).

3.5 Dynamical calculation using ZEUS2D

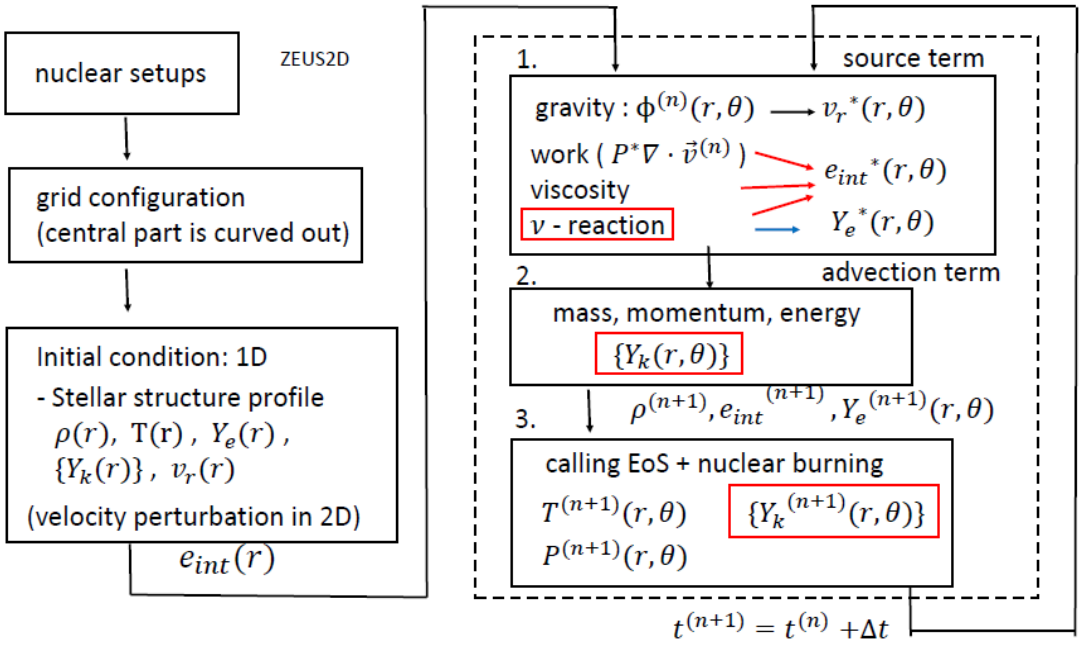

Figure 3.12: The strategy of calculating hydrodynamics via ZEUS2D [402].

Throughout this paper I replace the time evolution inner boundary instead of solving PNS interior and employ Newtonian equations of motion (see the later chapters). Not only for the post-relaunch evolutions but also for the preparations of the initial conditions we solve the following equations:

$$\frac{D\rho}{Dt} + \rho\nabla\cdot\mathbf{v} = 0, \tag{3.29}$$

$$\rho\frac{D\mathbf{v}}{Dt} = -\nabla P - \rho\nabla(\Phi + \Phi_c), \tag{3.30}$$

$$\rho\frac{D}{Dt}\left(\frac{e}{\rho}\right) = -P\nabla\cdot\mathbf{v} + \dot{q}, \tag{3.31}$$

$$\frac{DY_e}{Dt} = \frac{\lambda}{\rho N_A}, \tag{3.32}$$

$$\frac{DY_i}{Dt} = f_i\,(\rho, e, \{Y_k\}), \tag{3.33}$$

where ρ, P, $\mathbf{v}$, e, Y_e, Y_i and N_A are mass density, pressure fluid velocity, energy density, electron fraction, number fraction of nucleus i and Avogadro's number, respectively. We denote the Lagrange derivative as D/Dt. Note that the energy density in Eq. (3.31) includes the rest mass energy and the energy production by nuclear reactions are thus taken into account.

In Eq. (3.30), it is expressed explicitly that the gravitational potential has two contributions, Φ from the accreting matter and Φ_c from a central object, whose mass, $M_{\rm in}$, is

a function of time and calculated by the integration of mass accretion rates at the inner boundary of computational domain. They satisfy the following equations:

$$\triangle\Phi = 4\pi G\rho, \tag{3.34}$$

and

$$\Phi_c = -\frac{GM_{\rm in}}{r}, \tag{3.35}$$

where G is the gravitational constant.

To handle these equations, an open source code called ZEUS2D [402, 159] is utlized for calculating hydrodynamical calculations which employ staggered grids and the operetar splitting method, i.e. the source term and advection term is decoupled. Since the precise methodology is written in the original papers, I only highlight the modification from the original code in this study. The flow chart of numerical treatment is illustrated in Fig. 3.12. Firstly, MICCG method is employed Poission solver which is developed by H. Nagakura [301]. Next, neutrino contribution is added as well as calculating pressure work and viscosty in the source term so as to evolve $e_{\rm int}$ and Y_e. The advection of electron fraction and chemical abundances are also taken into account. Finally, nuclear burning is implicitly included in EoS and calculated in the last part of each intermediate time evolutions. The way of EoS computation is addressed in section 3.1.3.

3.6 Presupernova model construction

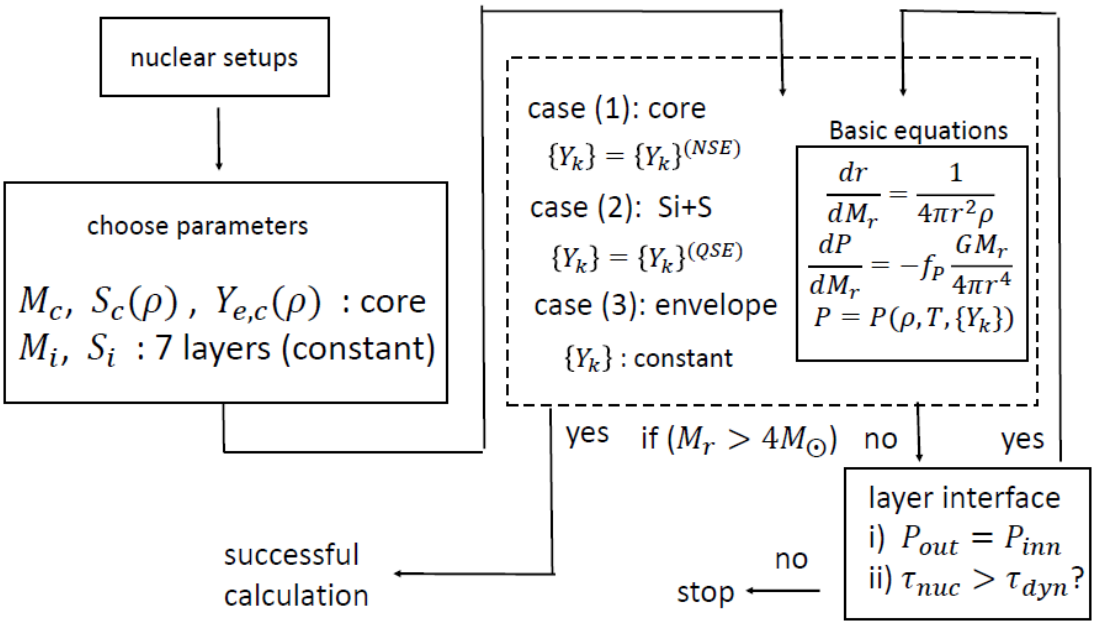

Figure 3.13: The precedures of constructing "toy" pre-supernova.

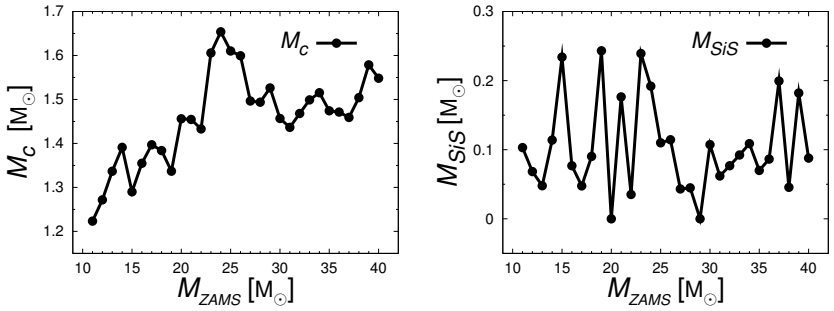

Figure 3.14: The masses of Fe core and Si+S layer for the pre-supernova models with $11-40\mathrm{M}_\odot$ by WHW2002. The left panel displays the Fe core masses, M_c, which have non-monotonic changes between $1.2\mathrm{M}_\odot$ and $1.7\mathrm{M}_\odot$, whereas the right panel gives the masses of Si+S layer, M_{SiS}, which also show large fluctuations between $0\mathrm{M}_\odot$ and $0.25\mathrm{M}_\odot$.

As highlighted in chapter 2.4 and 2.5, progenitor dependence turns out to be one of the most crucial ingredient in CCSNe theory. Numerical resolution also provide the wide variations of progenitor fate in practical stellar evolution computation as well as physical uncertainties. For instance, it is well known that the masses of Fe core and Si+S layer are critically important for shock revival [46, 414] because both of them affect one way or another the neutrino luminosity and mass accretion rate, the main controlling parameters of the stagnant shock wave. They are notoriously stochastic as a function of the stellar mass, though. Fig. 3.14 illustrates this, showing the masses of Fe core and Si+S layer for various pre-supernova models with $11-40\mathrm{M}_\odot$ taken from Woosley et al.(2002) [474] (here

after WHW2002). It is evident that neither the iron core mass, M_c, nor the Si+S mass, $M_{\rm SiS}$, is a monotonic function of the progenitor mass.

If we pay attention, however, to the entropy, S, and electron fraction, Y_e as a function of density inside the Fe core, which is defined hereafter to be the central region in NSE, those apparently diverse progenitors can be nicely categorized into three groups as demonstrated for the same pre-supernova models in Fig. 3.15. The first group is characterized by the

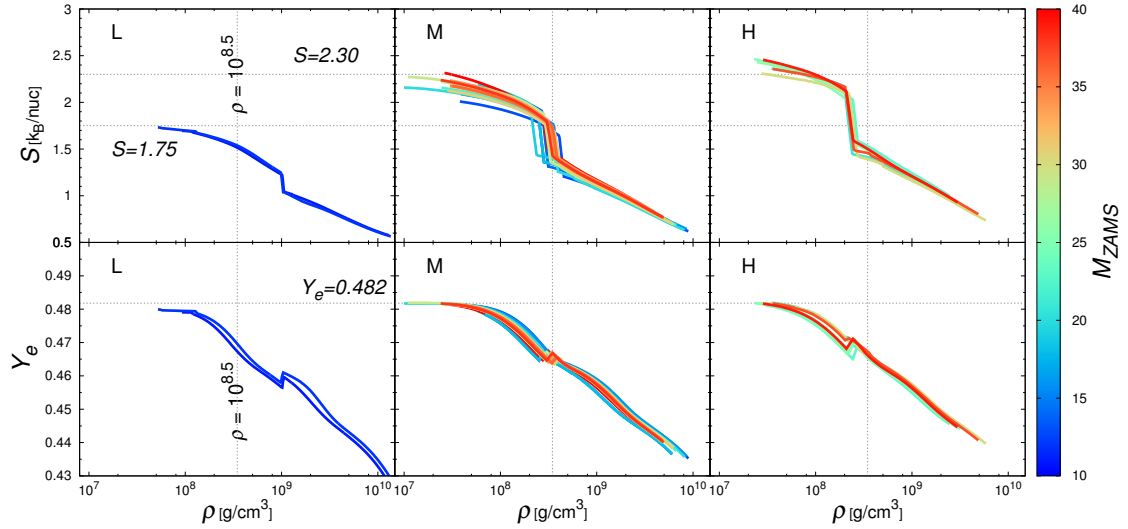

Figure 3.15: The entropy and electron fraction inside the core as density functions for 11-40 $M_\odot$ pre-supernova stages from WHW2002 models. The left panel shows the low entropy group (only 2 progenitor) labeled "L". Here k_B is the Boltzmann's constant. On the other hand, the right panel shows the high entropy group (8 progenitor) labeled "R". The rest of the progenitors are labeled as medium entropy group, "M". The color contour illustrates the zero-age main sequence mass of each model.

relatively low entropies, i.e., $S < 1.75 k_B$ at the edge of the Fe core and is plotted in the left panel with the label "L". Here k_B is the Boltzmann's constant. On the other hand, the right panel shows the models, which have rather high entropies, $2.3 k_B < S$ at the edge and are referred to the label "H". In between fall most of the pre-supernova models as demonstrated in the middle panel labeled with "M". They are conveniently characterized by the moderate entropies of $1.75 k_B \leq S \leq 2.3 k_B$ at the edge of Fe core. The important thing is that the members of each group seem to obey approximately the same $\rho - S$ and $\rho - Y_e$ relations irrespective of their Fe core masses. One may complain that the boundary between groups "M" and "H" is rather blurred as long as the value of the entropy at the edge of Fe core is concerned. Note, however, the different locations of the jump in the entropy distributions between the two groups: it occurs at a lower density for group "H" than for group "M". It is also mentioned that the members of group "H" have larger compactness $\xi_{2.5}$ [321, 407] and may form a black hole instead of a neutron star.

It is found from Fig. 3.15 that S and Y_e as functions of ρ have some features in common among these groups: plotted as in the figure, they are almost linearly increasing from the central point of star corresponding to the right ends of lines until a certain point, where the S and Y_e jump nearly discontinuously; the positions of the latter points are different

among the three groups as mentioned already and mark the locations, at which the shell Si burning once took place. It induced violent convection outside the shell and produced almost homogeneous entropy and Y_e distributions there, which were later bent downwards at smaller radii by electron captures on nuclei during the subsequent phase. The resultant distributions of S and Y_e are approximated by parabolic functions quite well. Inside the Si-burning shell, on the other hand, matter stratification is stable against convection mainly due to efficient neutrino cooling in the central region. As a result the linear distributions just mentioned are obtained there for S and Y_e. These functional relations are later used to build the toy model.

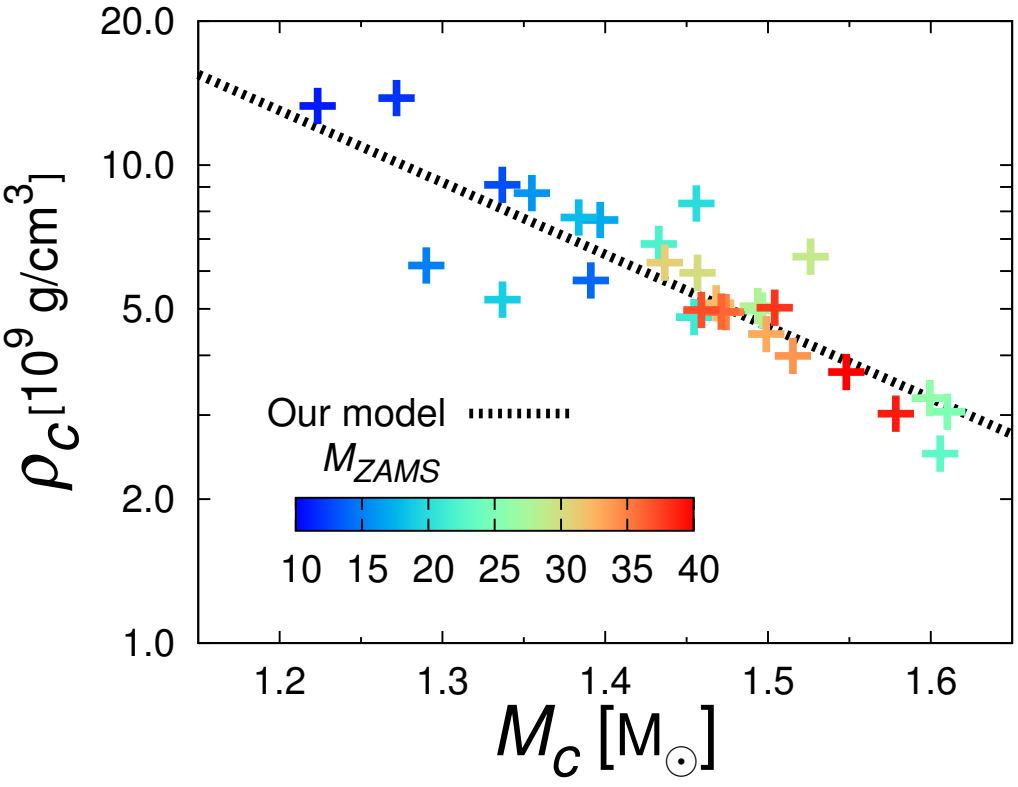

Figure 3.16: The central density distribution among the various core masses in 11-40 $M_\odot$. Although there are several scatters, the strong correlation is shown in the relation between the two, The color contour represents zero-age main sequence (ZAMS) mass. The black dotted line represents the central density as the function of iron core mass employed in this paper (see eq. 5.1).

We also point out the correlation between the central density and the mass of Fe core as shown in Fig. 3.16 although there are some scatters: massive cores tend to have smaller central densities just prior to collapse. This is mainly because of the generic trend that the more massive the core is, the higher the entropy becomes due to the shorter life time and, as a consequence, the less efficient neutrino cooling. We will use this correlation in

the following when we construct the toy model.

It is stressed again that the purpose of the toy model is to reproduce key features commonly observed in the massive star structures just prior to collapse, simultaneously leaving some degree of freedom to modify them rather arbitrarily for systematic studies. We might thus be able to suggest a feature or features that may be essential to robust shock revival but may have somehow eluded the current stellar evolution theory. In this series of papers, we will study the effects on shock revival of various features in the massive star structures reproduced by the toy model one after another. In this first paper, we pay particular attention to the masses of the iron core, M_c, and of the Si+S layer, $M_{\rm SiS}$, which certainly play major roles in the neutrino heating mechanism, dictating the neutrino luminosity and accretion rate, the two key parameters in the mechanism. Other features may be equally or more important and will be investigated in the forthcoming paper.

Among three groups we focus on group M in this paper, since it is the largest group, to which most of the progenitor models we show in Fig. 3.15 belong, and it is hence supposed to represent the canonical progenitor of CCSNe. We then use the following parametrization for the entropy S and electron fraction Y_e as functions of ρ:

$$S(\rho) = \begin{cases} \dfrac{(S_1 - S_0)}{(\log\rho_1 - \log\rho_0)} \cdot (\log\rho - \log\rho_0) + S_0 & (\rho \geq \rho_1), \\ \dfrac{(S_2 - S_3)}{(\log\rho_2 - \log\rho_3)^2} \cdot (\log\rho - \log\rho_3)^2 + S_3 & (\rho \leq \rho_2), \end{cases} \tag{3.36}$$

$$Y_e(\rho) = \begin{cases} \dfrac{(Y_{e1} - Y_{e0})}{(\log\rho_1 - \log\rho_0)} \cdot (\log\rho - \log\rho_0) + Y_{e0} & (\rho \geq \rho_1), \\ \dfrac{(Y_{e2} - Y_{e3})}{(\log\rho_2 - \log\rho_3)^2} \cdot (\log\rho - \log\rho_3)^2 + Y_{e3} & (\rho \leq \rho_2), \end{cases} \tag{3.37}$$

in which $\rho_1 = 10^{8.5}$g/cm^3 and $\rho_2 = 10^{8.4}$g/cm^3 specify the region, where the jump occurs, whereas other parameters determine the shapes of the functions and their values are set to $\rho_0 = 10^{9.8}$g/cm^3, $\rho_3 = 10^{7.1}$g/cm^3, $S_0 = 0.70{\rm k_B}$, $S_1 = 1.50{\rm k_B}$, $S_2 = 2.00{\rm k_B}$, $S_3 = 2.30{\rm k_B}$ and $Y_{e0} = 0.435$, $Y_{e1} = 0.467$, $Y_{e2} = 0.465$, $Y_{e3} = 0.482$. In the transition region between ρ_1 and ρ_2, S and Y_e are interpolated linearly in $\log\rho$. Fig. 3.17 displays the resultant relations (black dotted lines) between S and ρ in the left panel and between Y_e and ρ in the right panel together with the 30 pre-supernova models from WHW2002 (colored solid line), which consist of group "M". It is clear that the essential features of the group are well reproduced.

Next we shift our attention to outer layers. We begin with the Si+S layer that neighbors the Fe core. The important feature of this layer is that nuclei are no longer in NSE but the temperature is still high enough to maintain the so-called quasi-statistical equilibrium (QSE) [178], in which the Fe group, Si group and another group of lighter elements separately establish chemical equilibrium among the elements belonging to each group. We hence have the following relations among the chemical potentials of various elements:

$$\mu_{i_{\rm Fe}} = \mu_{Ni} + (N_{i_{\rm Fe}} - 28)\,\mu_n + (Z_{i_{\rm Fe}} - 28)\,\mu_p, \tag{3.38}$$

$$\mu_{j_{\rm Si}} = \mu_{Si} + (N_{j_{\rm Si}} - 14)\,\mu_n + (Z_{j_{\rm Si}} - 14)\,\mu_p, \tag{3.39}$$

$$\mu_{k_{\rm L}} = N_{k_{\rm L}}\,\mu_n + Z_{k_{\rm L}}\,\mu_p, \tag{3.40}$$

where μ, N, Z denote the chemical potential, neutron number and proton number of the nuclei specified by the subscript: $i_{\rm Fe}$, $j_{\rm Si}$ and $k_{\rm L}$ specify the member of the Fe, Si and

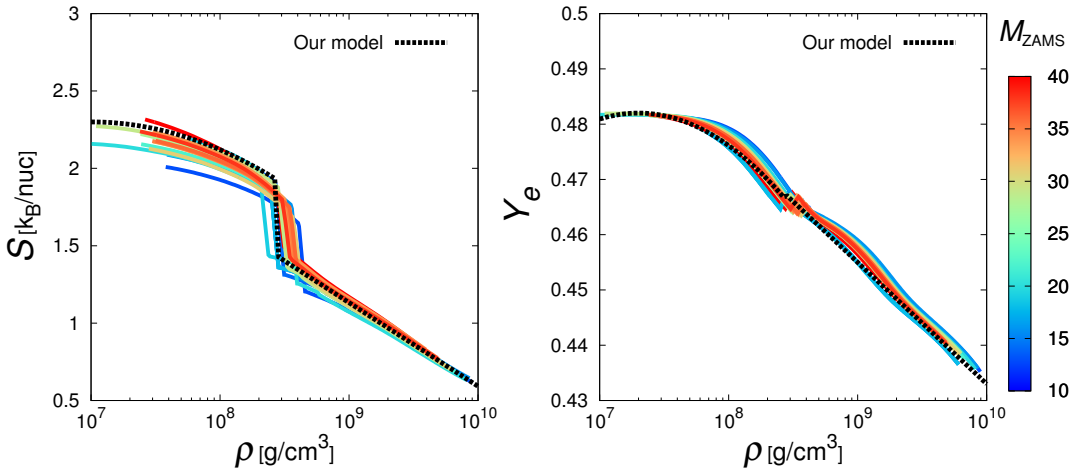

Figure 3.17: Same as Fig.3.15 but selecting only the group "M" adding our model profiles. The black dashed lines in two panels are analytical functions employed in the current paper (see eq.3.36, 3.37 and details in the text).

light-element groups, respectively, whereas p and n stand for the free proton and neutron, respectively. Note that only the chemical potentials of ^{56}Ni, ^{28}Si, neutron and proton are independent, which is analogous to NSE, in which the chemical potentials of nucleons are sufficient to give the entire chemical abundance. These four independent chemical potentials are determined by specifying the baryon density, total proton proton fraction as well as the mass fraction of the silicon group, $X_{\rm Si-G}$, and the proton fraction in the silicon group, which is set to 0.5 as a good approximation. In this paper $X_{\rm Si-G}$ is assumed to be expressed as a simple linear function of temperature as follows:

$$X_{\rm Si-G} = \begin{cases} \epsilon_0 & (4.5 \leq T_9), \\ 1-\epsilon_0-(1-2\epsilon_0)\cdot(T_9-3.5) & (3.5 \leq T_9 \leq 4.5), \\ 1-\epsilon_0 & (T_9 \leq 3.5), \end{cases} \tag{3.41}$$

where $T_9 = T/10^9$K and $\epsilon_0 = 2.0 \times 10^{-3}$. We also assume that the charge fraction in each group is 0.5. We adopt constant entropy and electron fraction distributions in this layer for simplicity.

The treatment of other outer envelopes, in which no chemical equilibrium is established even approximately, are simplified further: homogeneous distributions of entropy, electron fraction and chemical abundance are assumed in each of these layers. This is not so bad an approximation, though, since convection once prevailed in most of these layers, making the entropy and chemical abundance uniform there. We take the typical values from WHW2002 (see Table 3.1).

As explained shortly, since we solve the hydrostatic equations to build the toy models, we assume the continuity of pressure at their boundaries. The parameter values we choose are further constrained if one were to calculate the evolutions of chemical abundances later, since the time scale of nuclear reactions, $\tau_{\rm nuc} = \max_k Y_k/\dot{Y}_k$, should be longer than the

dynamical time scale, $\tau_{\rm ff} = \sqrt{r^3/GM_r}$ in every layer. Note that $\tau_{\rm nuc}$ may be shorter than the typical time for the consumption of nuclear fuel owing to the rises of density by core contraction, especially in silicon and oxygen-neon-magnesium layers.

As already mentioned repeatedly, the toy models are obtained by solving the hydrostatic equations for non-rotating, spherically symmetric stars. We do not solve the equation for energy generation and transport, which normally determines the temperature profile in the stellar interior. Instead the functional relations described above are employed in the Fe core and the constant S and Y_e distributions are adopted in the outer layers. As for the chemical abundances, NSE and QSE are assumed in the Fe core and Si+S layer, respectively. Further outside, uniform distributions of various elements are assumed. Then the basic equations for the NSE core are given as

$$\frac{dr}{dM_r} = \frac{1}{4\pi r^2 \rho}, \tag{3.42}$$

$$\frac{d\rho}{dM_r} = -(1-f_P)\cdot\frac{GM_r}{4\pi r^4} \Big/ \left(\left(\frac{\partial P}{\partial \rho}\right)_{S,Y_e} + \left(\frac{\partial P}{\partial S}\right)_{\rho,Y_e}\frac{dS}{d\rho} + \left(\frac{\partial P}{\partial Y_e}\right)_{\rho,S}\frac{dY_e}{d\rho}\right), \tag{3.43}$$

where r, M_r, P are radius, mass coordinate, pressure, respectively. f_P is a parameter to allow for some deviation from the complete hydrostatic equilibrium, which is commonly the case for realistic progenitor models provided by stellar evolution calculations, in which gravitational contraction has already sets in. It is assumed to be given by the following form

$$f_P = 0.05\exp\left(-0.5\left(\log(\rho)-7.2\right)^2\right), \tag{3.44}$$

which is found to fit the realistic progenitor models of different masses that have entered the collapse phase. As for the outer envelopes, the basic equations are essentially the same except the piecewise constant S, Y_e and element distributions as well as $f_p = 0$. Since the layer boundaries are contact surfaces, pressure is assumed to be continuous there.

Table 3.1: Parameter sets used in toy presupernova stage construction.

	core	QSE	Si+S+O	O+Mg+Si	O+Ne+Mg	C+O	C+O+He	He
M [$M_\odot$]	M_c	$M_{\rm SiS}$	0.36-$M_{\rm SiS}$	0.09	2.21-M_c	0.15	$\gtrsim$ 0.10	$\lesssim$1.10
S [k_B/nuc]	eq.3.36	3.3	4.0	5.0	5.9	6.5	7.6	12.0
chemical abundance X_k	NSE	QSE	$X_{Si}=0.45$, $X_S=0.35$, X_O=0.20	$X_O=0.80$, $X_{Mg}=0.15$, $X_{Si}=0.05$	$X_O=0.70$, $X_{Ne}=0.25$, $X_{Mg}=0.05$	$X_C=0.20$, $X_O=0.80$	$X_C=0.30$, $X_O=0.60$, $X_{He}=0.10$	$X_{He}=1.00$

Note: In this paper we pay attention mainly to the core mass, $M_c = 1.3, 1.4, 1.5{\rm M}_\odot$ and Si+S layer mass, $M_{\rm SiS} = 0.09, 0.18{\rm M}_\odot$.

Chapter 4

Post-shock-revival evolutions in the neutrino-heating mechanism of core-collapse supernovae

4.1 Setup

4.1.1 Outline

Before going into the details of our model building, we give a brief description of what we are going to do, emphasizing the underlying ideas.

We are interested in what happens after the relaunch of the stalled shock wave. The investigations in this paper are of experimental nature. We assume that the neutrino heating mechanism works successfully, which implies that the neutrino luminosity and accretion rate should be located on the critical curve just at the shock revival. Exactly at which point on the curve the shock is relaunched is still uncertain as mentioned earlier, however. We hence take the neutrino luminosity (or equivalently the accretion rate) at the shock revival as a free parameter and vary it arbitrarily to see how the ensuing physical processes are affected. We prepare a couple of initial conditions, which correspond to the points for different neutrino luminosities on the critical curve. We then solve the hydrodynamical equations together with nuclear reactions in 1D (spherical symmetry) and 2D (axial symmetry) to obtain the ensuing evolutions. See Section 4.1.3 for more details on how to trigger the shock revival.

We do not solve the evolution of the central high-density region, in which a proto-neutron star sits, but replace it by appropriate inner boundary conditions. The temporal variation of mass accretion rate is obtained by the computation of the infall of a realistic stellar envelope after the loss of pressure support at the inner boundary and is employed for the preparation of the initial states and subsequent hydrodynamical simulations. This also enables us to use the mass accretion rate as a clock. We follow the post-revival evolutions long enough so that the so-called diagnostic explosion energy is settled to the terminal value. Integrating the heating rates both by neutrino absorptions and nuclear reactions, we also obtain each contribution to the explosion energy. The nuclear reactions are divided into the recombinations of free nucleons to heavy nuclei and the explosive nuclear burnings and we estimate their contributions separately. We further distinguish the recombinations that occur in the nuclear statistical equilibrium (NSE) and those out of equilibrium. By so doing, we can pin down what contributes to the explosion energy in what proportions.

We can also find the dependence of the results on the timing of shock relaunch as well as the dimensionality of dynamics.

In the following we give the details of our modeling. The basic equations, input physics and numerical methods are described first. Then the preparation of the initial conditions, which requires multiple steps to avoid full computations of the collapse to bounce to shock stagnations, will then be presented in detail.

As already mentioned, in this entire paper we concentrate on this canonical model. The dependence of the results on the progenitor structures and the details of our modeling will be reported elsewhere. Note that according to the recent observations [391, 388, 394] of core-collapse supernovae as well as their progenitors, the $15M_\odot$ star may be a typical progenitor of Type-II supernovae. Hence, we first adopt a $15M_\odot$ progenitor model computed by Woosley & Heger(2007) [473]. The profile just prior to collapse is shown in Fig. 4.1.

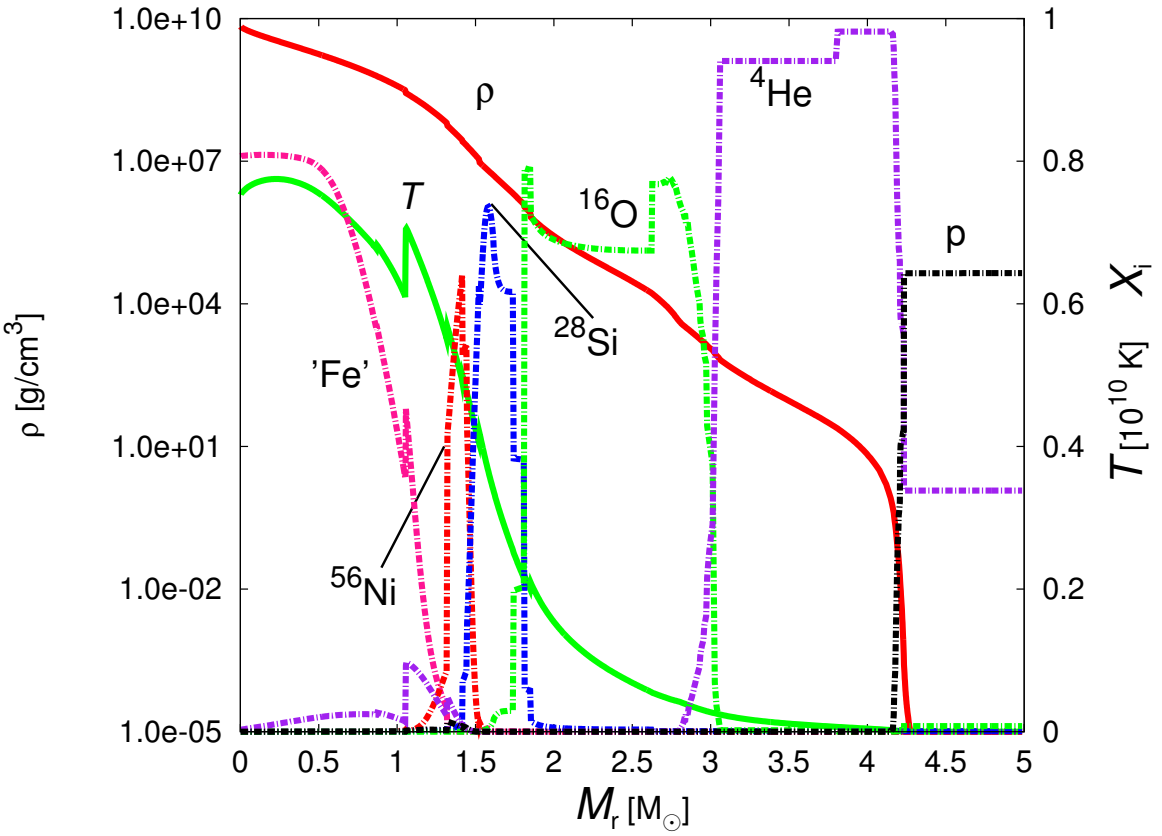

Figure 4.1: The initial profile of the $15M_\odot$ progenitor with the iron core of $M_{Fe} = 1.4M_\odot$. The density (red solid line) and temperature (green solid line) as well as mass fractions of some representative nuclei (solid dotted lines) are shown.

4.1.2 Step 1: 1D simulation of the infall of envelope

We now proceed to the description of the first step in the preparation of initial models. The aim of this step is to sample the mass accretion rates as a function of time together with the changes in the structure and composition of the envelope. For this purpose we perform a 1D simulation of the spherically symmetric implosion of the stellar envelope. We excise the interior of $r = 60$km and replace it with the inner boundary, at which we impose the free inflow condition. Since no bounce occurs in this simulation, no shock wave emerges. Note that what we need is the accretion rate and the structure outside the stalled shock wave, which would be produced and stalled somewhere inside the core in reality and that they are unaffected by what happens inside the shock wave, since they are causally disconnected. The location of the inner boundary is chosen so that they would always reside inside the shock wave.

We deploy 500 grid points to cover the region extending up to $r = 2 \times 10^5$km. This is large enough to ensure that matter outside the outer boundary does not move essentially for $\sim$ a second during this stage. The weak interactions are turned off for this computation, since the they are indeed negligible in the infalling envelope. Note again that the computational results for the region that would be engulfed by the shock wave in reality are irrelevant and do not have any consequence on the results outside. Hence the neglect of neutrino heating and cooling is completely justified. The nuclear reactions for the 28 nuclei, on the other hand, are computed for the region with $T < 7 \times 10^9$K to follow the change in chemical composition and take account of its influence on the hydrodynamics during the implosion. The NSE composition is calculated for higher temperatures.

We show the results in Fig. 4.2. In the upper panel we show the mass accretion rate, $\dot{M} = 4\pi r^2 \rho v_r$, as a function of radius for different t_e, which is the elapsed time from the beginning of collapse. It is seen that the rarefaction wave generated by the inflow at the inner boundary propagates outward, triggering the infall of matter at large radii. After $t_e \sim 300$ms the accretion rates at $r \lesssim 500$km become independent of radius. This implies that the flows in this region can be approximated by steady accretions. The region is actually expanded outward gradually. The lower panel shows the accretion rates at three different radii as a function of time. As pointed out right now, they coincide with each other after $t_e \sim 300$ms. Before this time, on the other hand, the accretion rate is higher at smaller radii. There appears a peak at $t_e \sim 180$ms , which is rather insensitive to the radius. From a comparison with realistic simulations [198], we find that this time roughly corresponds to the core bounce. We hence refer to as the time elapsed from this point as the post-bounce time hereafter, i.e, $t_{pb} \equiv t_e - t_{e(p)}$, where $t_{e(p)}$ denotes as the time of peak accretion rate. In the same panel we also show the mass that has flown into the inner boundary by the given time, to which we refer as the proto-neutron star (PNS) mass (M_{PNS}). In the bottom panel we present the time evolution in the plain of mass accretion rate and PNS mass.

The evolutions of the chemical composition together with the density, velocity and temperature are displayed in Fig. 4.3. In the left column the density and velocity are shown for three different post-bounce times (t_{pb}). As the time passes, the density at a fixed radius decreases monotonically whereas the inflow velocity gets larger. The outward propagation of the rarefaction wave is also recognized in the figure, which is exactly how the implosion of envelope proceeds. In the right column, the chemical composition and temperature are presented for the same t_{pb}. The temperature at a fixed radius is in general a decreasing function of time. It is observed that heavy elements are advected inward. In addition, the changes in composition by nuclear burnings are also taken into account in

this figure.

We employ these results not only at the next step in the preparation of initial conditions, which we will describe in the next section, but also for the simulations of the post-relaunch evolutions, the results of which will be presented in § 5.3.

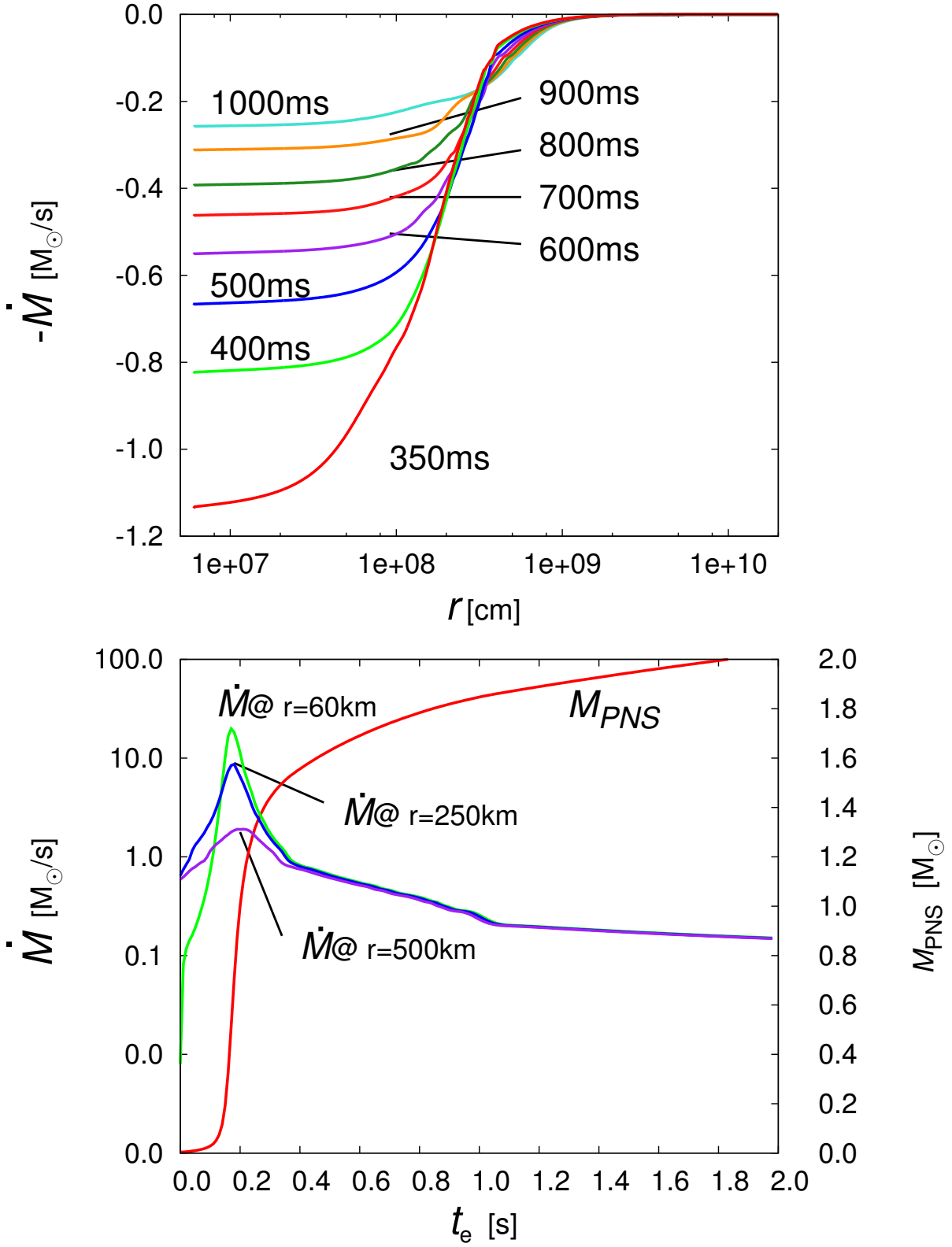

Figure 4.2: The characters of the mass accretion rates. The upper panel shows the radial profiles of $\dot{M}$ for different elapsed times, t_e. The lower panel displays the time evolutions of $\dot{M}$ at 3 different radii together with the proto-neutron star mass, M_{PNS}.

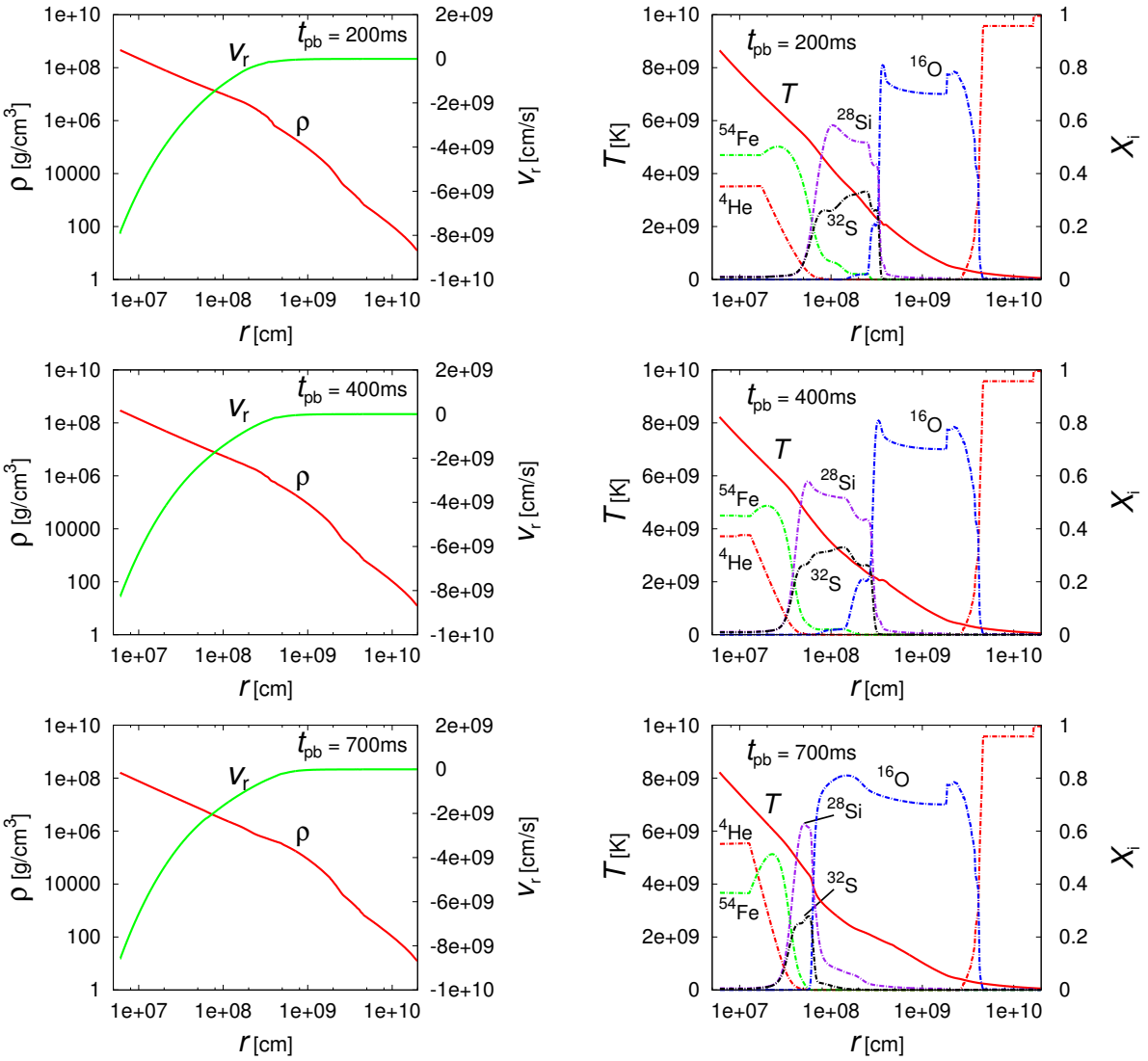

Figure 4.3: The evolutions of the chemical composition as well as density, velocity and temperature. In the left column the density (red line) and velocity (green line) are displayed for three different times, $t_{pb} = 200$, 400 and 700ms, respectively. In the right column, the abundances of some representative nuclei (solid dotted lines) are shown with the temperature (solid line) for the same three times.

4.1.3 Step 2: search of critical luminosities

The aim of this step is to construct the critical steady accretion flows with a standing shock wave for the mass accretion rates obtained in step 1. It is important here to define unambiguously the critical point for a given accretion rate, since in this paper it is not meant for the flow with the luminosity, above which no steady accretion flow exists [52]. Instead we define it to be the flow, in which the stalled shock wave is actually relaunched within a certain time. This is because the shock revival normally occurs owing to hydrodynamical instabilities even in 1D before the luminosity, above which no steady accretion is possible, is reached. Hence we determine the critical point hydrodynamically by following the growths of the instabilities for initially spherically symmetric and steady accretion flows.

We hence adopt a two-step procedure. In the first step, we construct a sequence of spherically symmetric and steady accretion flows with a standing shock wave for a given mass accretion rate. We solve Eqs. (3.29)-(3.33) in 1D, dropping the Eulerian time derivatives. At the shock wave, we impose the Rankine-Hugoniot jump conditions. The nuclear reactions and weak interactions that are described in chapter 3 are fully taken into account. The outer boundary of the computational domain is set to 500km and the values of various quantities are taken from the results of Step 1 at the times that correspond to the given mass accretion rates (see the bottom panel of Fig. 4.2). As already mentioned in section 8.4, we impose the two condition for inner boundary which is regarded as neutrino sphere surface; one is that the density fulfill $\rho = 10^{11}\mathrm{g/cm}^3$ and the other is the location of sphere contract toward center. Therefore, the radius of neutrino sphere is a function of time and is assumed in this paper to be given as follows [378]:

$$R_\nu(t) = \frac{R_{\nu,i}}{1 + (1 - \exp(-t/t_c))(R_{\nu,i}/R_{\nu,f} - 1)}, \tag{4.1}$$

where $R_{\nu,i}$ and $R_{\nu,f}$ are the initial and final values, respectively, and t_c is the characteristic time scale. They are set to be $R_{\nu,i} = 58$km for ν_e, 52km for $\bar{\nu}_e$, $R_{\nu,f} = 15$km and $t_c = 800$ms. The temperatures, T_ν, in the Fermi-Dirac distributions for the electron-type neutrino and anti-neutrino are chosen so that their average energies would be $\langle \varepsilon_{\nu_e} \rangle = 20 - 8.0 \times (1/2)^{t/200\mathrm{ms}}$MeV and $\langle \varepsilon_{\bar{\nu}_e} \rangle = 23 - 8.0 \times (1/2)^{t/200\mathrm{ms}}$MeV [411].

We cover the computational region with 300 grid points. As the neutrino luminosity is increased, the location of the standing shock wave is shifted outwards and at some point the steady solution ceases to exist. As mentioned already, however, we do not need to search that point, since the shock revival occurs earlier owing to the hydrodynamical instabilities. We do need to identify this point, to which we refer the critical point in this paper, in the second step.

The hydrodynamical simulations are performed both in 1D and in 2D in the second step. As mentioned just now, these computations are used to judge whether the spherically symmetric, steady accretion flows, which are obtained in the first step, induce shock revival by the hydrodynamical instabilities. The nature of the instabilities are different between 1D and 2D: in 1D radial oscillations become over-stabilized at some luminosity, which is lower than the one, at which the steady flow ceases to exist [325, 108]; in 2D, on the other hand, the non-radial instability called SASI occurs even earlier on [483]. Hence in reality the latter will be more important. We think that 1D models are still useful to understand the physical processes that occur after the shock relaunch as well as to elucidate the differences caused by the dimensionality of hydrodynamics.

We solve numerically Eqs. (3.29) - (3.33) with all the time derivatives turned on. Both the input physics and radial grid are identical to those employed in the first step, in which

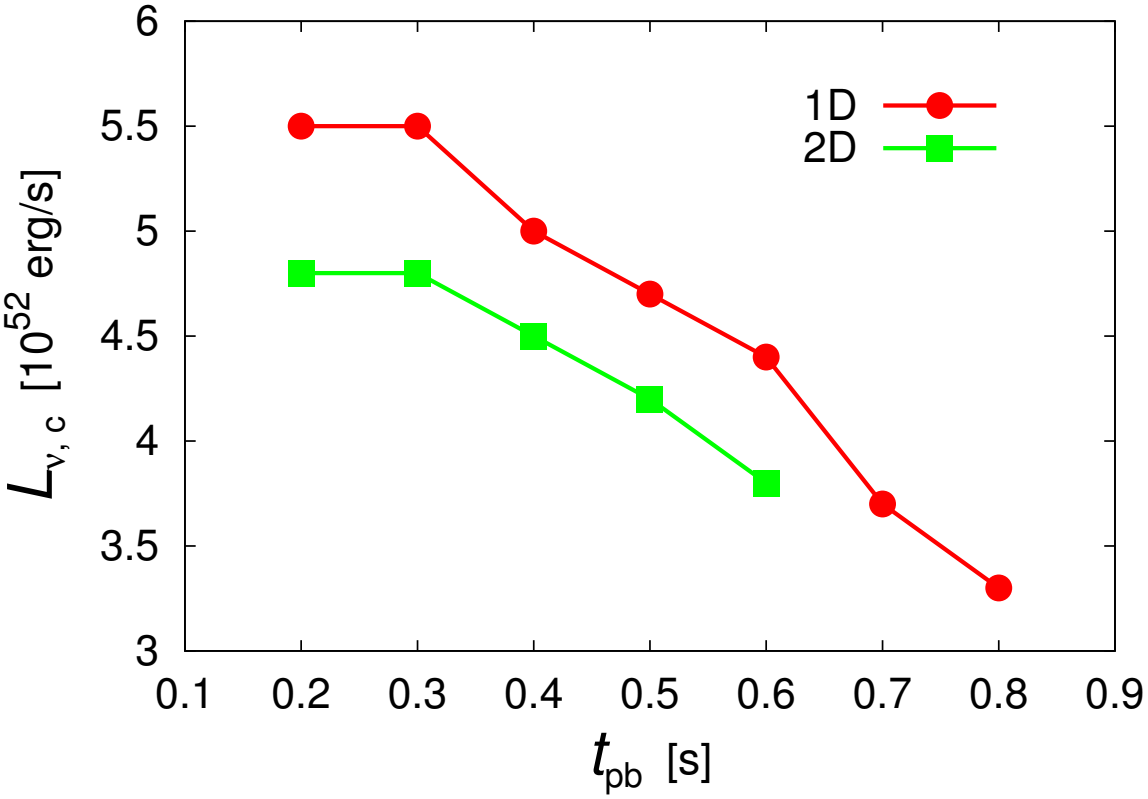

Figure 4.4: The critical neutrino luminosities in 1D and 2D as a function of the post-bounce time.

the steady accretion flows are calculated. In 2D simulations we deploy 60 grid points in the $\theta-$direction to cover 180° and add random 1% perturbations to the radial velocity to induce SASI. In these simulations we fix both the outer and inner boundary conditions and follow the evolution for 200ms. If the shock wave reaches the outer boundary located at $r = 500$km within this period, we judge that the shock is successfully revived. The reason why we fix the boundary conditions is that if the shock revival occurs at a certain time, the instabilities should have reached the nonlinear stage by that time but the growth of the instabilities takes some time. For each mass accretion rate we determine the minimum luminosity for the successful shock revival within a few percent and refer to it as the critical luminosity. In 1D the shock relaunch is preceded by the growth of radial oscillations (not shown in the figure) whereas the non-radial modes with $\ell = 1, 2$ are followed by the shock revival in 2D. Here ℓ stands for the index of spherical harmonics in the expansion of unstable modes. In Fig. 4.4 the critical luminosities are presented both for 1D and 2D as a function of mass accretion rate. It is evident that the critical luminosity is decreasing function of mass accretion rate and it is reduced in 2D, both of which are well known [325, 291].

4.1.4 Step 3: computations of post-relaunch evolutions

In this section we give some details of the 1D and 2D hydrodynamical simulations of post-shock-revival evolutions. We continue the computations of step 2 for the models with the critical luminosities. We first map the results to a larger mesh that covers the region extending from the neutrino sphere to the radius of $r = 2 \times 10^5$km. In all 1D models we computed the post-revival evolutions for $\sim$ 2s, which is found to be long enough to estimate the explosion energy. In fact, we follow the evolutions for two 1D models until the shock reaches the stellar surface, which is located at $r = 5 \times 10^8$km. In those simulations we expand the mesh twice as the shock propagates outward. The inner boundary is also shifted to larger radii, to $r = 10^3$km for the first re-griding and to 10^4km for the second expansion, so that we could avoid too severe CFL conditions on the time step. We confirmed that these shift of the inner boundary do not violate the energy conservation in ejecta by more than 0.1%. We also performed long simulations in the similar way (see section 4.2.4) for three 2D models in order to determine the asymptotic ejecta mass accurately. In all simulations we employ non-uniform 650 radial grid points in 1D and 500 points in 2D. In 2D simulations, 60 grid points are distributed uniformly in the $\theta-$direction to cover the entire meridian section.

The outer boundary condition poses no problem this time, since it is located at a very large radius. We just impose the free in-flow/out-flow condition there. The inner boundary conditions are a bit more difficult. We assume the time evolution of neutrino luminosity is given by

$$L_\nu(t_{exp}) = L_{\nu,c} \cdot \exp(-t_{exp}/800\text{ms}), \tag{4.2}$$

where t_{exp} is the time elapsed from the shock relaunch and $L_{\nu,c}$ is the critical luminosity obtained in Step 2. We fix the density, pressure and velocity at the ghost mesh point at the inner boundary when matter is flowing inward. When matter begins to flow outward, i.e. the transition to the neutrino wind phase occurs, those quantities are extrapolated from the innermost active mesh point to the ghost mesh point except when the entropy per baryon tends to be too high, in which case we put the upper bound of $s = 100k_B$ to the entropy per baryon and the density is adjusted. These prescriptions are applied to each angular grid point at the inner boundary for 2D simulations.

We investigate seven 1D models, for which the stalled shock is relaunched at $t_{pb} = 200$, 300, 400, 500, 600, 700 and 800ms. Note that t_{pb} has a one to one correspondence with the mass accretion rate, which is shown in Fig. 4.2. Five 2D simulations are performed, in which the shock revival is assumed to occur at $t_{pb} = 200$, 300, 400, 500 and 600ms. See Fig. 4.4 for the critical luminosities in these models. The input physics, such as nuclear and weak interactions, are the same as those employed in the second step of Step 2. The results of all the computations in this step will be presented in the next section first for the 1D models and then for the 2D cases.

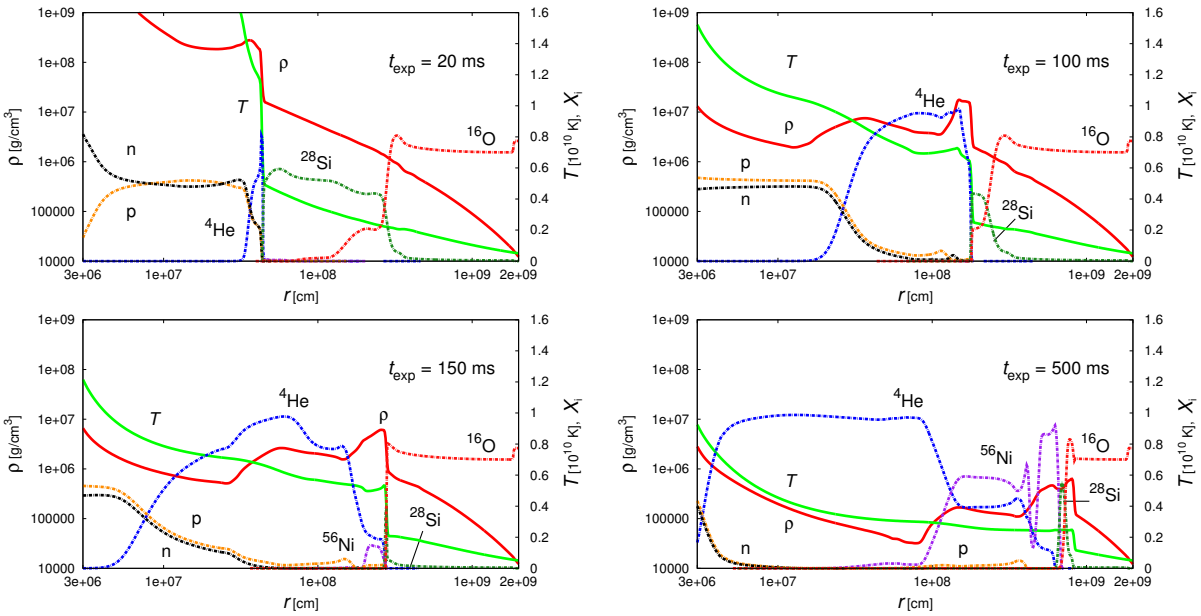

Figure 4.5: The density (red solid line), temperature (green solid line) and mass fractions of representative nuclei (solid dotted lines) for the 1D fiducial model as a function of radius at four different post-relaunch times, t_{exp} =20, 100, 150 and 500ms, respectively. The last snapshots show ^{56}Ni production (purple) and α-rich freeze-out (blue). One can also see in the last panel the ^{28}Si production (dark green) by the O-burning (magenda).

4.2 Results

4.2.1 Spherically symmetric 1D models

The evolution of the fiducial model

We first describe in detail the evolution of the 1D model, in which the shock relaunch is assumed to occur at $t_{pb} = 400$ms. This corresponds to the time, at which the mass accretion rate is $0.53 M_\odot$/s. The critical luminosity in 1D is 5×10^{52}erg/s.

In Fig. 4.5 we show the density, temperature and mass fractions of representative nuclei as a function of radius for four different times. In the upper left panel the profile at $t_{exp} =$ 20ms after the shock relaunch is displayed. The shock is still located around $r = 500$km. The post-shock temperature is $T \gtrsim 1$MeV, so high that the nuclei, mainly ^{28}Si, flowing into the shock are decomposed to α particles, which are further disintegrated into nucleons immediately. The post shock composition is perfectly described by NSE. At $t_{exp} = 100$ms the shock reaches $r \sim 2,000$km but is still inside the Si layer as seen in the upper right panel. The post-shock matter is mainly composed of α particles, which are not disintegrated any more owing to the lower temperature, $T \sim 7 \times 10^9$K. Another 50ms later, the shock enters the Oxygen layer (see the lower left panel). Now ^{56}Ni emerges just behind the shock wave. This is mainly due to the recombination of α particles, which will be evident shortly. The post-shock temperature is $T \sim 5 \times 10^9$K and matter is beginning to be out of NSE. In the lower right panel we present the profile at $t_{exp} = 500$ms. At this time, the temperature is

$T \sim 2 \times 10^9$K and matter is completely out of NSE and the nuclear reactions yield mainly ^{28}Si. Much behind the shock wave some α particles are recombined to ^{56}Ni. Slightly later all nuclear reactions are terminated behind the shock wave, since the temperature does not rise to high enough values by shock heating.

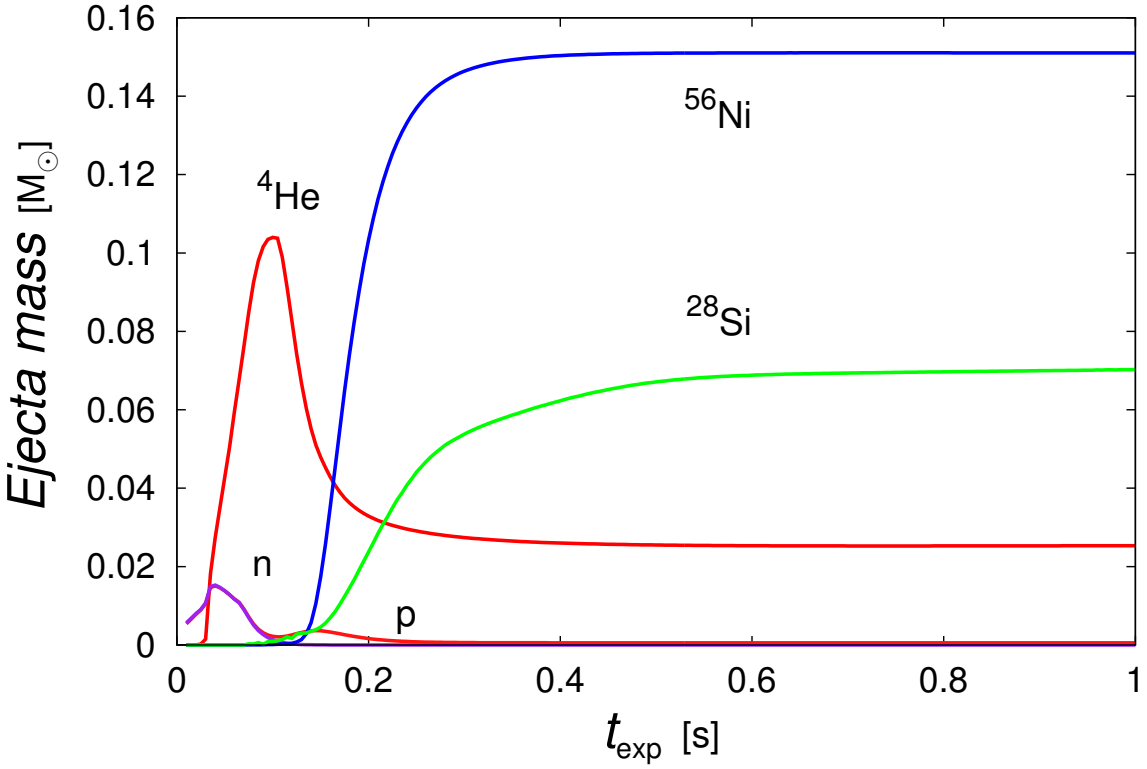

Figure 4.6: The ejecta masses of proton (dark red line) , neutron (purple line), α (red line) , ^{28}Si (green line) and ^{56}Ni (blue line) integrated over the post-shock region are displayed as a function of the elapsed time, t_{exp}, for the 1D fiducial model. No fall back occurs and the masses of ^{56}Ni and ^{28}Si are determined as early as $t_{exp} \sim 500$ms.

In Fig. 4.6 we show the masses of proton, neutron, α, ^{28}Si and ^{56}Ni integrated over the region inside the shock wave as a function of t_{exp} for the 1D fiducial model. In accord with the description in the previous paragraph, α particles are the main yield of nuclear reactions up to $t_{exp} \sim 100$ms. The depletion of neutrons after $t_{exp} \sim 50$ms implies that the nucleons are recombined to α particles during this period. From $t_{exp} \sim 100$ms to $t_{exp} \sim 150$ms, on the other hand, α particles are diminished while ^{56}Ni is increase, which means that the former is recombined to the latter. After $t_{exp} \sim 150$ms α particles cease to recombine any more and are frozen, and ^{56}Ni and later ^{28}Si are produced by nuclear burnings. These results are obtained with the nuclear network with 28 nuclei (see chapter 3). In order to confirm that it is large enough, we conduct a larger network with 463 nuclei as a post-processing calculation, employing the time evolutions of density, temperature and electron fraction obtained by the simulation with the original network. The nickel and silicon masses are 0.140M$_\odot$ and 0.068M$_\odot$ for the larger network, whereas they are 0.151M$_\odot$

and $0.071 M_\odot$ for the standard case. Further more, the difference in the total mass of heavy nuclei with A $\geq$ 48 is only $2.0 \times 1.0^{-3} M_\odot$ and the additional energy release from these difference is estimated to be less than 1.0×10^{49}erg. These results imply that the original network is appropriate.

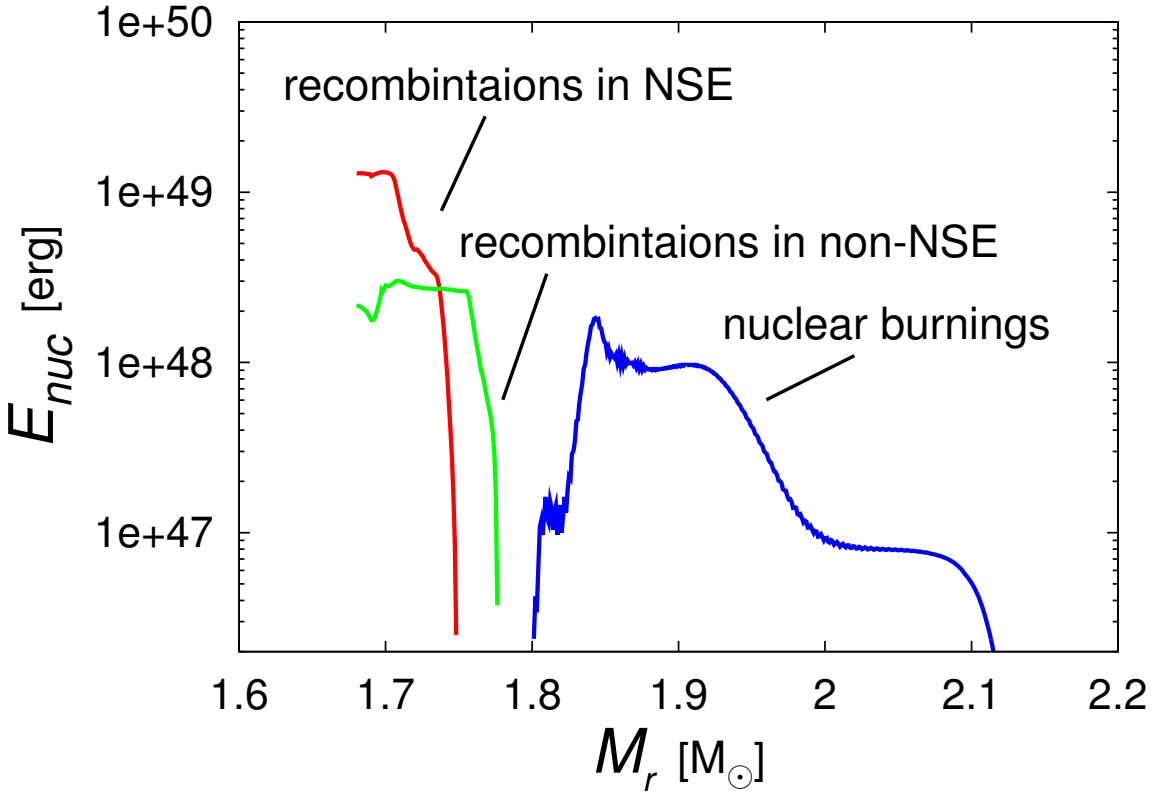

Figure 4.7: Total energy release by nuclear reactions as a function of mass coordinates. The size of mass bin is $1.0 \times 10^{-3} M_\odot$. The energy production rate is given by integrating over the entire evolution. mass bins being taken as Three contributions, i.e., recombinations in NSE (red line), those in non-NSE (green line) and nuclear burnings (blue line), are distinguished.

The energy release by these nuclear reactions is presented in Fig. 4.7. We time-integrate the energy production rate over the entire evolution as a function of mass coordinates. In so doing, we distinguish the contributions of the recombinations from those of the nuclear burnings. Moreover, the former is divided into two pieces, one of which comes from the recombinations in NSE and the other from those in non-NSE. In the interior ($\lesssim 1.75 M_\odot$) the recombinations start in NSE and end in non-NSE and there are hence two contributions. In the slightly outer layer up to $\sim 1.8 M_\odot$, on the other hand, the recombinations occur in non-NSE conditions. Further outside ($\gtrsim 1.8 M_\odot$) the nuclear burnings take their places. In fact, the densities and temperatures that the matter in this region expansions are inside the O-burning regime (see Fig.1 in Hix & Thielemann(1999) [178]). It is evident that the largest energy release comes from the recombinations that occur in NSE and the contributions of

the nuclear burnings are rather minor even after the integrated over the mass coordinate for this particular model. This is a generic trend as will be shown later. There is a gap between $\sim 1.75 M_\odot$ and $\sim 1.8 M_\odot$. This is a region, in which energy is not released but absorbed. The main reaction in this region is the burning of ^{28}Si to ^{56}Ni. Some fractions of ^{28}Si are disintegrated to α particles, however. Although the latter is minor, the mass difference between α and ^{28}Si is much greater than that between ^{28}Si and ^{56}Ni. As a results the energy suck by the decomposition overwhelms the energy release by the burning.

4.2.2 The evolution of diagnostic explosion energy

Understanding the evolutions of density, temperature, chemical composition as well as the energy generations by nuclear reactions, we now turn our attention to the explosion energy. Following the conventional practice, we define the diagnostic explosion energy of provisional ejecta. At each grid point the total energy density, e_{tot}, is given by

$$e_{tot} = e_{kin} + e_{int} + e_{grav}, \tag{4.3}$$

where $e_{kin} = 1/2\rho v^2$ is the kinetic energy density, e_{int} denotes the internal energy density and $e_{grav} = \rho(\Phi + \Phi_c)$ stands for the gravitational potential energy density. We judge that the mass element at a certain grid point will be ejected if the total energy density is positive, $e_{tot} > 0$, and if the radial velocity is positive ($v_r > 0$) at a given time. Then the diagnostic explosion energy is defined as a function of time to be the sum of the total energy density times volume over the ejecta, which is just determined.

The diagnostic explosion energy changes in time indeed. In the early phase of shock revival, the neutrino heating is the main source of the diagnostic explosion energy. As the shock propagates outward, the neutrino heating becomes inefficient, since the matter to be heated is also shifted to larger radii, where the neutrino flux is lower, and the luminosity itself becomes smaller as the time passes. It is also important that nucleons, which are mainly responsible for the heating, are depleted as they recombine to α particles and heavier nuclei as the temperature decreases. After the neutrino heating subsides, the nuclear reactions are the main energy source. As described in the previous section, the recombination of nucleons occurs at first and the nuclear burnings take their place later. After all nuclear reactions are terminated owing to low temperatures, the diagnostic explosion energy decreases slowly since matter, which is gravitationally bound and hence has negative specific energy, is swallowed by the shock wave. As the shock wave proceeds outwards, this contribution becomes smaller and the diagnostic explosion energy approaches its asymptotic value, the actual explosion energy.

Figure 4.8 shows the time evolution of the diagnostic explosion energy for the 1D fiducial model, in which the shock is relaunched at $t_{pb} = 400$ms. The horizontal axis in the figure is the time elapsed from the shock relaunch, t_{exp}. The diagnostic explosion energy increases for the first ~ 200ms. Then it decreases gradually and becomes almost constant at $t_{exp} \sim 1$s. Also displayed in the figure are the individual contributions to the diagnostic explosion energy from the neutrino heating and nuclear reactions. As described in the previous paragraph, the neutrino heating is dominant over the nuclear reactions initially up to $t_{exp} \sim 120$ms. Then the nuclear reactions become more important and raise the diagnostic explosion energy to $\sim 10^{51}$erg at by the time $t_{exp} \sim 200$ms in this particular case. As indicated by the colored shades in the figure, the nuclear reactions are mainly the recombinations until $t_{exp} \sim 150$ms. The nuclear burnings follow until $t_{exp} \sim 300$ms. The asymptotic value of the diagnostic explosion energy is approached from above owing to the engulfing of matter with negative energy by the outgoing shock wave.

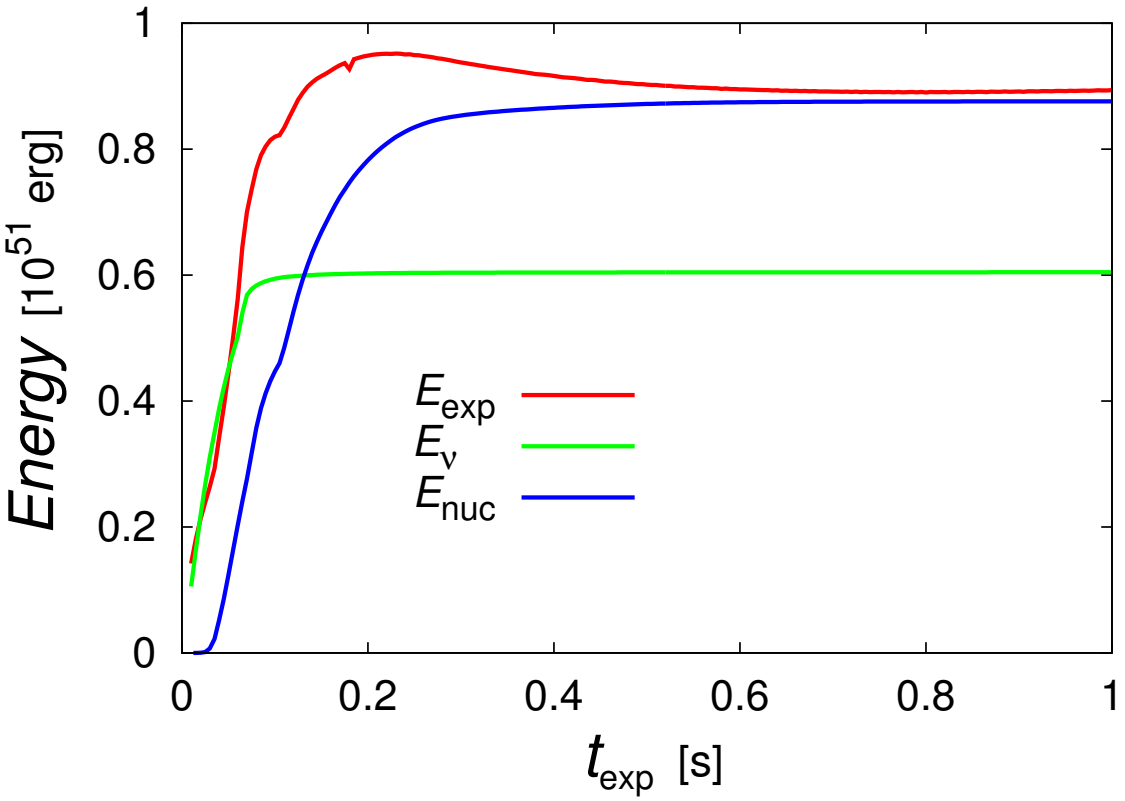

Figure 4.8: The time evolution of diagnostic explosion energy for the 1D fiducial model. The individual contributions from the neutrino heating (green line) as well as nuclear reactions (blue line) are also shown.

In order to confirm that the final explosion energy has been already reached in the above computation, we continue to evolve this model until the shock wave reaches the stellar surface. We shift both the outer and inner boundaries as mentioned in section 4.1.4 to avoid too severe CFL conditions at the innermost mesh point,. The result is presented in Fig. 4.9. It is clear that the diagnostic explosion energy is essentially constant for $t_{exp} \gtrsim 1$s. Also shown in the figure is the result for another model, in which the shock relaunch is delayed until $t_{pb} = 800$ms. The accretion late is $\sim 0.23 M_\odot$/s and the critical luminosity is $\sim 3.3 \times 10^{52}$erg/s for this 1D model. As is obvious from the figure, the asymptotic explosion energy is considerably smaller, $\sim 1.1 \times 10^{50}$erg, and we have to wait for ~ 2s before the diagnostic explosion energy is settled to the asymptotic value. This is a generic trend: as the shock relaunch is delayed, it takes more time to reach the final explosion energy.

4.2.3 Systematics

In this section, we look into the results of other models and see how generic what we have found so far for the fiducial model is. In Fig. 4.10 we show the asymptotic values of diagnostic explosion energy for different models as a function of the shock-relaunch time.

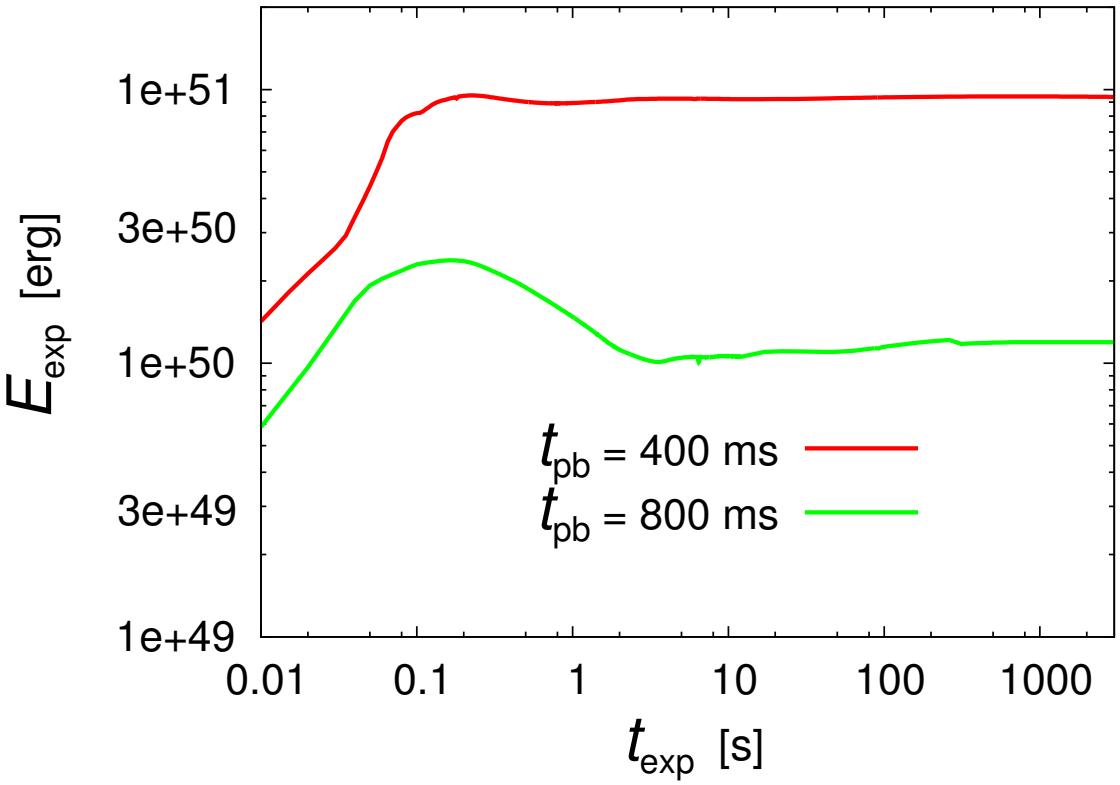

Figure 4.9: The long-term evolutions of diagnostic explosion energies for the 1D fiducial model as well as for the model of the latest shock relaunch.

We can clearly see that the explosion energy is a monotonically decreasing function of the shock-revival time. This is main due to the fact that the mass of accreting matter gets smaller as the time passes and is nothing unexpected (see e.g. [378]). It is stressed, however, this is the first clear demonstration of the fact with the nuclear reactions and EOS being taken into account consistently in sufficiently long computations, in which the diagnostic explosion energy is confirmed to reach the asymptotic value.

Also shown in the figure are the individual contributions to the diagnostic explosion energy from the nuclear reactions and neutrino heating. Both of them also decrease as the shock revival is delayed. It is found, however, that the contribution of the nuclear reactions diminishes more rapidly. This is simply due to the fact that the temperature rise by the shock passage is smaller in weaker explosions. Note that the explosion energy are smaller than the sum of the two contributions, since the accretion of gravitationally bound matter gives negative contributions to the explosion energy as mentioned already. It should be also emphasized that the recombination energy is eventually originated from the neutrino heating because the recombinations are necessarily preceded by the endothermic dissociations of heavy nuclei that exist prior to collapse and those consumed energies are replenished by neutrinos. The neutrino heating also plays a vital role to push the post-bounce configuration to the critical point and further heat up matter until they become

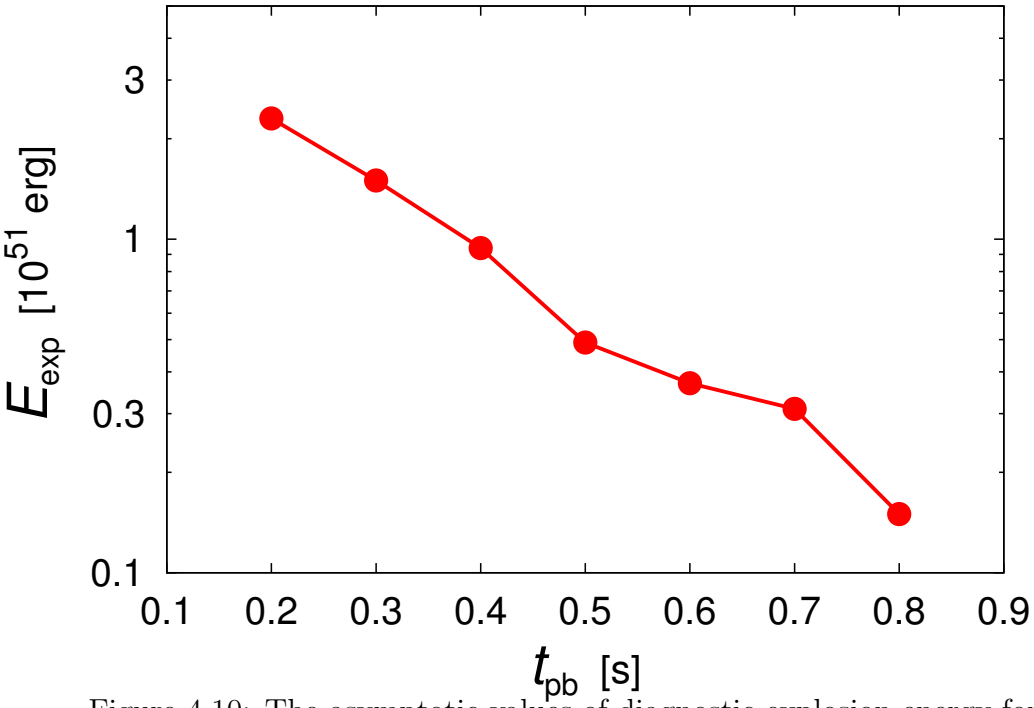

Figure 4.10: The asymptotic values of diagnostic explosion energy for all 1D models.

gravitationally unbound in the earliest phase of shock revival.

In Fig. 4.11 we further divide the contribution of nuclear reactions into those from the recombinations in and out of NSE as well as from the nuclear burnings. Roughly speaking, the re-assemble of nucleons to α particles occurs in the recombination in NSE and the further recombinations to heavier nuclei proceed in the environment out of NSE. As can be seen, all the contributions again decline as the shock relaunch is delayed. Regardless the recombination that occurs in NSE is the greatest contributor. The recombinations, both in and out of NSE, decline more rapidly than the nuclear burning and the latter contributes more than the recombination out of NSE for the model, in which the shock revival occurs at the latest time ($t_{pb} = 800$ms) and the weakest explosion is obtained. The reason why the nuclear burning declines more slowly is that the temperatures obtained by shock heating is roughly proportional to the quarter power of the explosion energy.

Next we turn our attention to the synthesis of ^{56}Ni, one of the most important observables in the supernova explosion. The synthesized mass of ^{56}Ni is correlated with the explosion energy [151]: the greater the explosion energy is, the more ^{56}Ni is produced. This is demonstrated in Fig. 4.12. In the upper panel we again present the asymptotic values of the diagnostic explosion energy, which we simply refer to as the explosion energy here, as a function of the mass accretion rate at shock relaunch. The corresponding shock-relaunch times are given in the figure. In the lower panel, the mass of ^{56}Ni in the ejecta is displayed also as a function of the mass accretion rate at shock relaunch. The ejecta was defined earlier to be the collection of the mass elements that have positive total energy density and radial velocity (see section 4.2.2). The positive correlation between the explosion energy

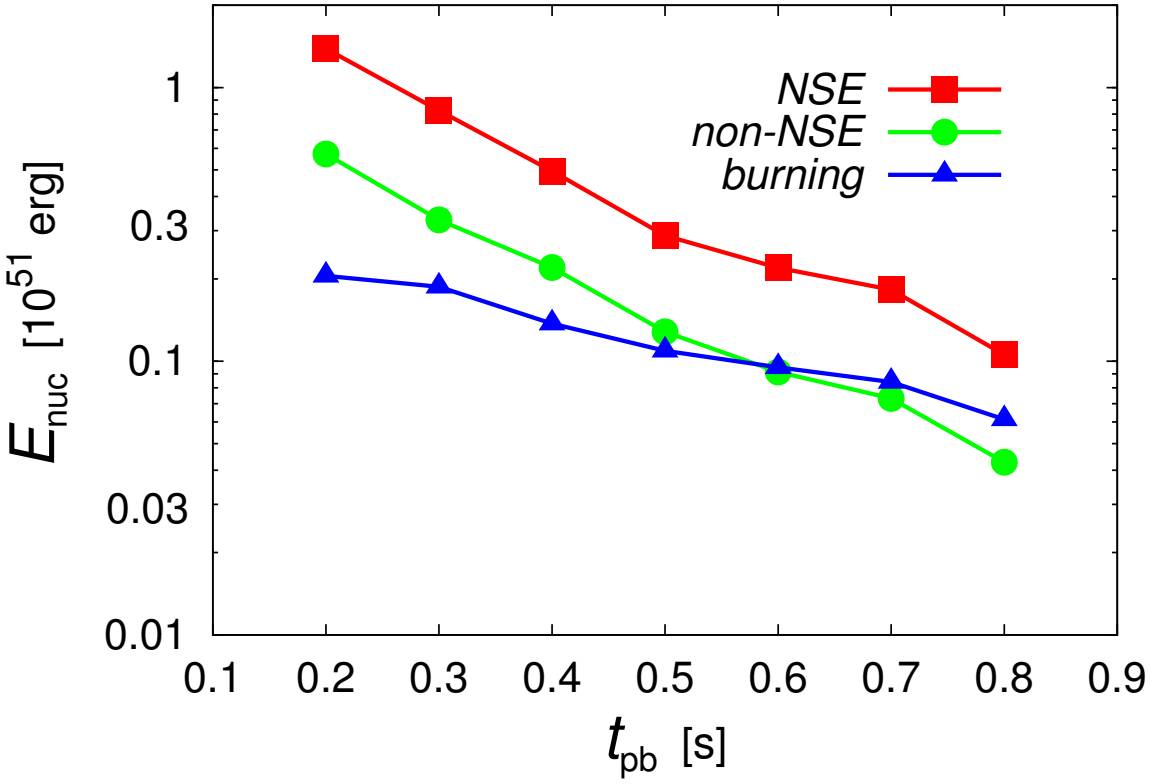

Figure 4.11: The individual contributions from the nuclear recombinations in NSE and those in non-NSE as well as nuclear burnings to the explosion energy.

and the mass of ^{56}Ni in the ejecta are evident.

In fact, ^{56}Ni may be produced too much in these 1D models. The canonical explosion energy ($\sim 10^{51}$erg) is attained only by the models that relaunch the stalled shock wave relatively early ($t_{pb} \lesssim 400$ms). On the other hand, the masses in the ejecta of ^{56}Ni synthesized for all these models are $\gtrsim 0.15 M_\odot$, which is substantially larger than the values estimated from observations, $\lesssim 0.1 M_\odot$ [391]. Note that the mass of ^{56}Ni ejected by SN1987A is estimated to be $\sim 0.07 M_\odot$ and corresponds to the shock-relaunch time of $t_{pb} \sim 600$ms in our 1D model; this rather late shock revival gives only a weak explosion of $\sim 0.4 \times 10^{51}$erg, smaller than the most likely explosion energy (0.9×10^{51}erg) derived observationally [205] . It is true that both of the observational estimates and the theoretical predictions presented here have uncertainties. In fact, the neutrino transport as well as evolutions of proto-neutron star, which are neglected and roughly mimicked in this paper, are the main source of uncertainties in the results shown above. We believe, however, that the general trends would be unchanged even if more sophisticated treatments were adopted. The above argument hence may be regarded as yet another reason that we do not believe that the 1D neutrino heating works.

To better understand the origin of the overproduction of ^{56}Ni we have done an ordinary calculation of explosive nucleosynthesis as a post-process for the densities, temperatures

Table 4.1: Comparison with an ordinary explosive-nucleosynthesis calculation.

Shock relaunch time [ms]	Explosion energy [10^{51}erg]		Proto-neutron star mass [$M_\odot$]		^{56}Ni mass [$M_\odot$]	
	1D model	thermal bomb	1D	thermal bomb	1D	thermal bomb
300	1.50	1.50	1.60	1.59	0.21	0.15
400	0.95	0 .94	1.67	1.64	0.15	0.086
500	0.50	0.60	1.70	1.73	0.10	0.043

and electron fractions obtained for the models presented above. In so doing, the so-called thermal bomb method, in which thermal energy is deposited initially in the innermost region, is employed [158]. The explosion energy and mass cut are chosen so that they agree with those of the original models. Interestingly the calculation of explosive nucleosynthesis consistently produces smaller amounts of ^{56}Ni, which is given in Table 4.2.3. In fact, the fiducial model reproduces the observational estimate for SN1987A much better, which is just a coincidence though. Figure 4.13 compares the distributions of peak temperature between the 1D fiducial model and corresponding thermal-bomb model. It is clear that the fiducial model has a larger amount of mass elements that achieve high enough temperatures to produce ^{56}Ni. It seems to take the neutrino heating mechanism a greater thermal energy to unbound the accreting envelope. This result may also be a caution in employing the thermal bomb method in the explosive nucleosynthesis calculations.

In fact, Young et al.(2007) [489] discussed uncertainty in nucleosynthetic yields with 1D spherically symmetric explosion models and showed that ^{56}Ni evaluated with the piston-driven model ($E_{\rm exp} = 1.2 \times 10^{51}$erg) is larger by a factor of 2-3 than that with the thermal-bomb model ($E_{\rm exp} = 1.5 \times 10^{51}$erg) with the same remnant mass. Our 1D neutrino-driven explosion models may be closer to the piston-driven explosion model than to the thermal-bomb explosion model.

4.2.4 Axisymmetric 2D models

In the following we focus on the effect of dimension. In section 4.1.3 we already showed that the critical neutrino luminosity is lowered in the axisymmetric 2D models than in the spherically symmetric 1D model for the same accretion rate at the shock relaunch. Performing 2D simulations further in Step 3, we are concerned with how and how much the results we obtained for 1D models so far are modified in 2D cases.

The input physics for 2D simulations is essentially the same as for the 1D model except for the perturbations added to the radial velocities with random magnitudes up to 1% at the beginning of Step 2. We have investigated the models, in which the stalled shock wave is relaunched at the post-bounce times of $t_{pb} = 200, 300, 400, 500$ and 600ms. For the models with $t_{pb} = 400, 500$ and 600ms, we further extend the domain twice later up to $r = 2 \times 10^7$km as already mentioned. This is necessary to determine the mass of the matter that eventually falls back. It turns out that the model with t_{pb} =600ms fails to explode, with all the shocked matter starting to falling back before the shock wave reaches the He-layer. We also tested the numerical convergence in the model with t_{pb} =400ms by increasing the numbers of radial or angular grid points. We found that the higher ridial resolution (700 mesh points instead of 500) does not make much difference. Incidentally, this is also the case in 1D. On the other hand, the finer angular mesh (90 grid points instead

of 60) yields the explosion energy and ^{56}Ni that are , respectively, 16% and 10% larger than those for the standard resolution.

4.2.5 Dynamics of aspherical shock revival

We first look at the post-relaunch dynamics of the $t_{pb} = 400$ms model, which is a 2D counterpart to the 1D fiducial model. As shown in Fig. 4.14, which displays the contours of entropy per baryon and mass fraction of ^{56}Ni, the shock expansion is highly aspherical, which was also demonstrated in e.g. [214, 325, 378]. The shock front is elongated in the direction of the symmetry axis. The shock propagates more rapidly in the northern hemisphere whereas matter attains higher entropy per baryon in the opposite hemisphere. These features conform with the dominance of $\ell = 1, 2$ modes owing to SASI. Here ℓ stands for the index of Legendre polynomials, which are included in the eigenfunctions of linearly unstable modes.

As mentioned in section 4.1.3, the shock revival occurs at a lower luminosity in the 2D model ($L_c = 4.2 \times 10^{52}$erg/s) than in the 1D counterpart ($L_c = 5.0 \times 10^{52}$erg/s). Unlike the 1D case, some matter continues to accrete, forming down drafts particularly in the equatorial region, until much late times after the shock revival. As a consequence the (baryonic) mass of neutron star is larger in the 2D case ($\sim 2.1 M_\odot$) than in the 1D case ($\sim 1.65 M_\odot$). This is actually a generic trend as shown later (see Fig. 4.17). Another interesting feature found in the 2D model is the distribution of maximum temperatures that each mass element attains, which is obtained from the Lagrangian evolutions of tracer particles distributed in the ejecta. Figure 4.15 shows the result in a histogram. It is evident that the mass that reaches $T = 5 \times 10^9$K is larger in 1D than in 2D. In the same figure we also show the distribution of electron fraction, Y_e(NSE), which is estimated when T becomes the boundary value of NSE, or 7×10^9K. Note that Y_e(NSE) is useful for the diagnosis of nuclear yields in ejecta. In the 1D case, there exist too massive ejecta with $Y_e(\mathrm{NSE}) \leq 0.49$, which will produce unacceptable amount of neutron-rich Ni isotopes and ^{64}Zn compared with the solar abundances as shown in Fujimoto et al.(2011) [129]. Their overproduction of the slightly neutron-rich ejecta with $Y_e(\mathrm{NSE}) \leq 0.49$ in the 1D case disappears in the 2D case owing to more efficient neutrino interactions. Multi-dimensional models are therefore preferable in the point of view of the Galactic chemical evolution of isotopes although they may depend on the treatment of neutrino transfer.

The post-relaunch evolutions are a bet different between the models with the earlier ($t_{pb} = 200$ and 300ms) and later ($t_{pb} = 500$ and 600ms) relaunch. As shown in Fig. 4.16, SASI is always dominated by the $\ell = 1, 2$ modes, making the shock front rather prolate generically with a marked equatorial asymmetry. In the models with the earlier shock revival is nearly isotropic, whereas in the models with the later shock relaunch the matter expansion is highly anisotropic , with large portions of post-shock matter continuing accretions. The difference seems to have an origin in the difference of the steady states obtained in Step 2. In the former the shock radii are large and the post-shock flows are slow. As a consequences the matters in the gain region is heated rather homogenously in the subsequent evolutions. For the latter, on the other hand, the gain region is narrow and the post-shock flows are faster, which tends to enhance inhomogenity in the subsequent heating , leading to the localized expansion.

The accretion continues until long after the shock is relaunched. The resultant mass of neutron star is larger in 2D than in 1D as pointed out already for the fiducial model and now shown in Fig. 4.17. As the shock revival is delayed and the critical luminosity gets

lower with the mass accretion rate beings smaller, the post-relaunch evolution becomes slower as in 1D. This is even more so for the 2D models, for which the critical luminosity is smaller than for 1D owing to the hydrodynamical instabilities (see Fig. 4.4). How these hydrodynamical features affect the explosion energy and nickel mass is our primary concern and will be addressed in the next section.

4.2.6 Diagnostic explosion energies and masses of ^{56}Ni in the ejecta

The diagnostic explosion energy is shown in Figure 4.18 as a function of t_{exp} for the 2D fiducial model, in which the stalled shock wave is relaunched at $t_{pb} = 300$ together with the model with $t_{pb} = 400$ms, the counter part to the 1D fiducial model. Also presented are the individual contributions from the neutrino heating and nuclear reactions. As in the 1D fiducial model (see Fig. 4.8), the neutrino heating is effectively closed at $t_{exp} \sim 100$ms. By this time the shock front has reached the location of $r \gtrsim 2,000$km, which is far enough from the proto-neutron star for the neutrino flux to become negligibly small. After the freeze-out of neutrino heating, the diagnostic explosion energy increases via the nuclear reactions such as the recombination of ^{4}He to heavier nuclei in the early phase and the Si and O burnings later on as shown in Fig. 4.19, in which the masses of n, p, ^{4}He, and α particles, ^{28}Si and ^{56}Ni are shown as a function of time.

The diagnostic explosion energies become almost constant at $t_{exp} \sim 600$ms in these models and the mass of ^{56}Ni reach their maximum values around $t_{exp} \sim 300$ms. These features are essentially the same as what we observed for the 1D counterpart (Figs. 4.6 and 4.8). However, big difference appear after $t_{exp} = 300$ms in the masses of heavy elements between 1D and 2D: significant fall-backs occur in 2D as can be seen in Fig.19. Incidentally, the ratio of the kinetic to internal energies in the ejecta is $\frac{E_{kin}}{E_{int}} \sim 4$ at $t_{exp} = 1000$sec for all the exploding models.

Figure 4.20 shows the explosion energies for all the 2D models in comparison with those for the 1D models. It is a general trends that the explosion energy is a monotonically decreasing function of the shock-relaunch time although the gradient is much steeper in 2D. It is also interesting that the explosion for a given shock-relaunch time is similar between 1D and 2D provided the shock revival is early enough to give an explosion energy of 10^{51}erg. This may imply that it is the mass accretion rate that primarily determines the canonical explosion energy. It should be noted, however, that the critical luminosity for a give mass accretion rate is smaller in 2D than in 1D (see Fig. 4.4). For a given neutrino luminosity, the explosion energy is hence larger in 2D except for very weak explosion by the late shock-relaunch. This is the advantage of non-spherical hydrodynamics that is commonly mentioned in the literature. For the model with $t_{pb} = 500$ms, the explosion energy is much smaller than for the 1D counter part. No explosion obtains in the model with $t_{pb} = 600$ms owing to the severe fall-back.

In Fig. 4.21 we present the individual contributions to the explosion energy from the neutrino heating and nuclear reactions for both 1D and 2D models, which should be compared with Fig. 4.10. It is evident that both contributions from the neutrino heating and the nuclear reactions drop much more quickly in 2D than in 1D as the shock revival is delayed; the contribution of the nuclear reactions decreases faster than that of the neutrino heating and , as a consequence, the former is dominant only for the models with earlier shock-relaunches ($t_{pb} \lesssim 300$ms). It is also interesting that the decay of the explosion energy is accelarated once the contribution of the nuclear reactions ceases to be dominant. It

hence seems that the energy release by the nuclear reactions is an important ingrediant for robust explosions. The reduction of the contribution from the nuclear reactions is directly related with the decrease of the mass elements in the ejecta that attain high peak temperatures, which we have pointed out already for the fiducial model (see Fig. 4.15) , as well as with the fall back in the 2D models. These reductions are slightly compensated for by the reduction in the (negative) contribution from the gravitational energy of accreting matter that is swallowed in the ejecta. This is another consequence of the fact that the accretion continues in 2D even after the shock is relaunched and not all the accreting matter is added to the ejecta.

The reduction of the contribution to the explosion energy from the nuclear reactions is also reflected in the production of ^{56}Ni, which is demonstrated in Fig. 4.22. It is apparent that the mass of ^{56}Ni is always smaller in 2D than in 1D as a function of the shock-relaunch time. It should be reminded that the 1D models tend to over-produce the nickels; as discussed in §4.2.3, if the typical mass of ^{56}Ni in the ejecta of CCSNe is $M_{\rm Ni} \lesssim 0.1{\rm M}_\odot$ as observations seem to indicate [391], the 1D models require that the shock should be relaunched later than $t_{pb} \sim 500$ms ; this implies a rather weak explosion ($E_{exp} \lesssim 0.5 \times 10^{51}$erg), however; no 1D model hence can give both the explosion energy and nickel mass in the appropriate range. In the 2D models, on the other hand, this problem is much relaxed. Indeed the explosion energy is large enough if the shock relaunch occurs earlier than $t_{pb} \sim 400$ms and the nickel is not over-produced if the shock is revived later than $t_{pb} \sim 300$ms. Although it is entirely a different issue whether and how the critical luminosity is obtained, this range of shock-relaunch time, $t_{pb} \sim 300 - 400$ms, may be regarded as the appropriate time for shock revival in fact. It is nice that the 2D models have an "allowed" range, since the hydrodynamics is inevitably non-spherical owing to the hydrodynamical instabilities. Whether three-dimensional hydrodynamics, which is the reality, alters the result for 2D will be an important issue and will be studied in the future.

Comparison between the abundances in SN ejecta and those in the solar system will possibly lead to the similar allowed range. Fujimoto et al.(2011) [129] performed detailed nucleosynthetic calculations for the ejecta of SN explosion from a $15M_\odot$ progenitor [476]. They were based on simulations of neutrino-driven aspherical explosion, which employed with a hydrodynamic code, that is similar to the one used in the present study but neglecting the energy generation through nuclear reactions. They showed that the explosions with $t_{\rm pb} \sim 200 - 300$ms give $E_{\rm exp}$ and $M(^{56}{\rm Ni})$ in the allowed range and that the abundances in the ejecta are similar to those in the solar system. Detailed nucleosynthesis studies taking into account of the energy generation via nuclear reactions will be interesting, since the feedback, which elevates entropy in the ejecta, will possibly enhance the amounts of ^{56}Ni and ^{44}Ti, which are slightly and highly underproduced in Fujimoto et al.(2011) [129], respectively.

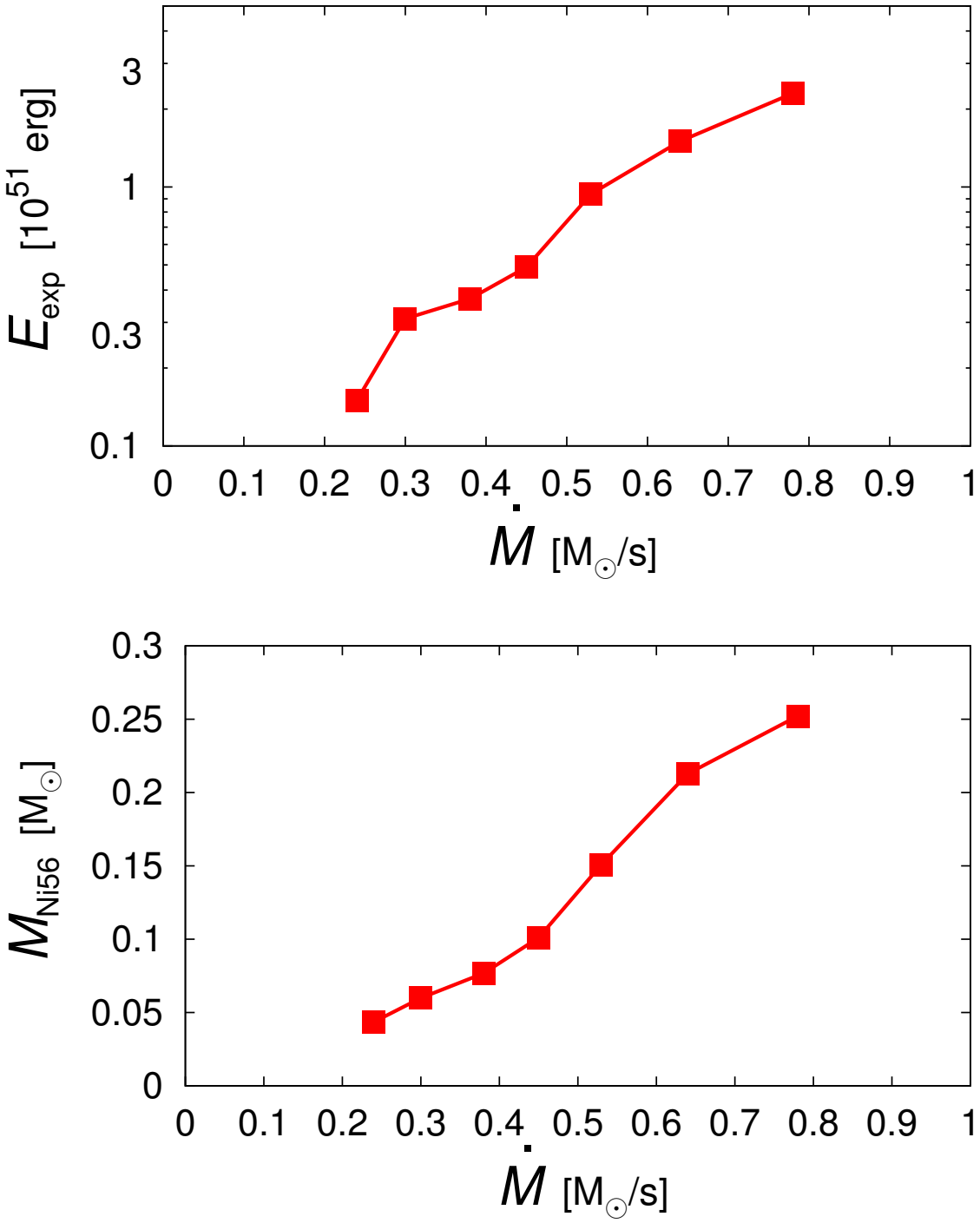

Figure 4.12: The explosion energies and ^{56}Ni masses for all 1D models.

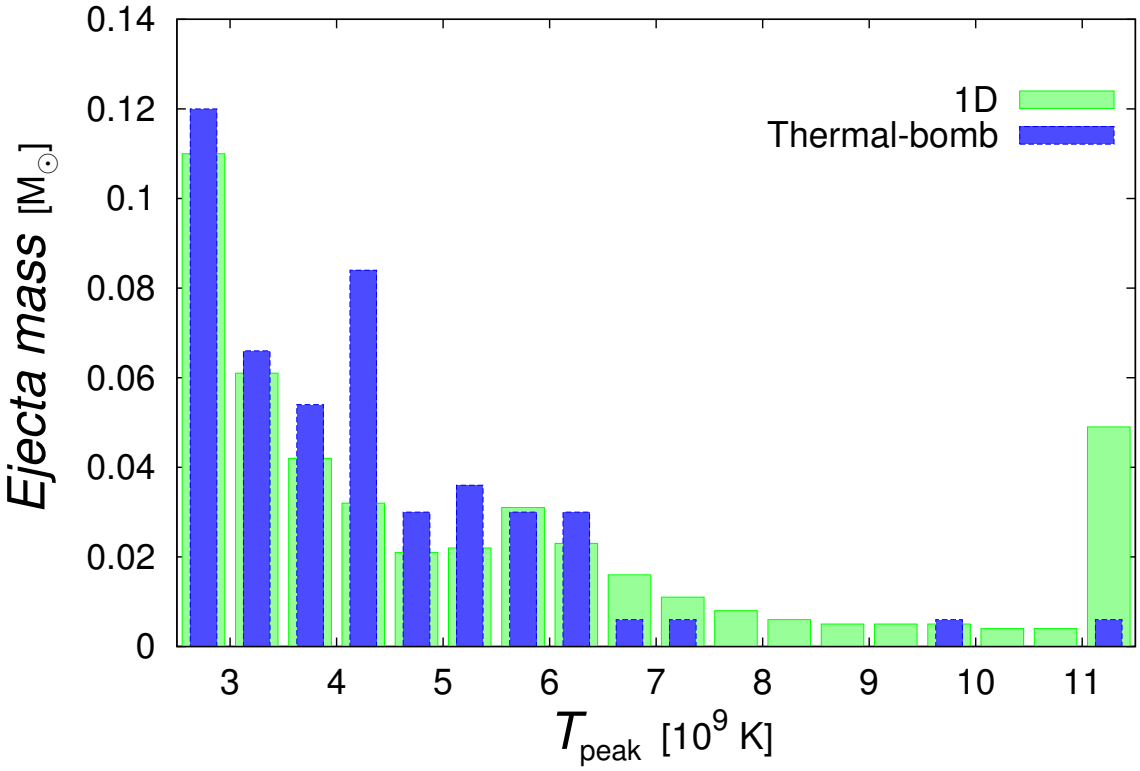

Figure 4.13: Comparison of the distributions of peak temperature between the 1D fiducial model and corresponding thermal-bomb model. The total mass of the matter that has the peak temperature higher than $T_9 = 5$ is $1.89 \times 10^{-1}\mathrm{M}_\odot$ for the 1D model whereas it is $1.20 \times 10^{-1}\mathrm{M}_\odot$ for the themal-bomb model.

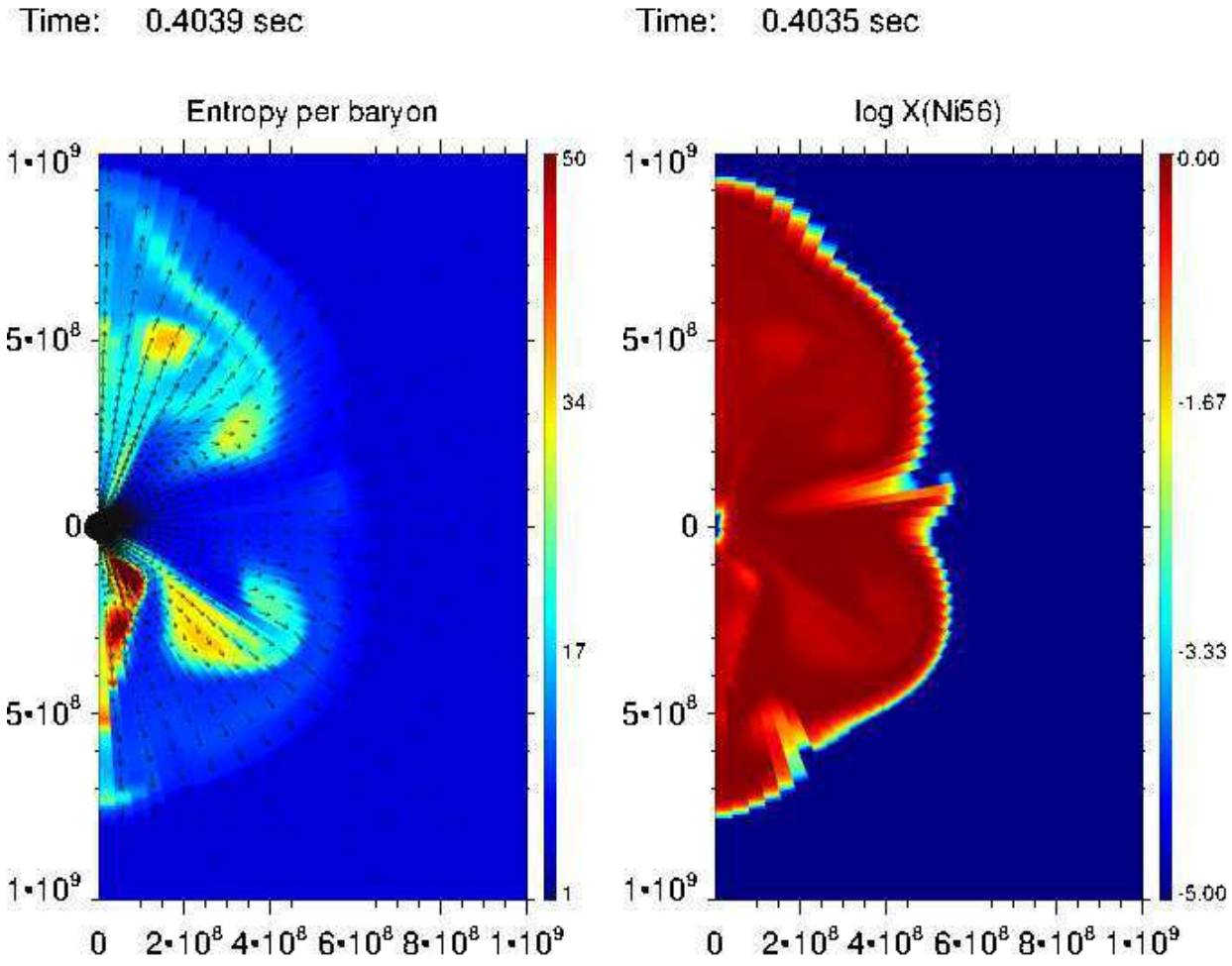

Figure 4.14: Contours of entropy (left panel) and mass fraction of ^{56}Ni (right panel) at $t_{exp} = 400$ms for the 2D model, in which the stalled shock revives at $t_{pb} = 400$ms.

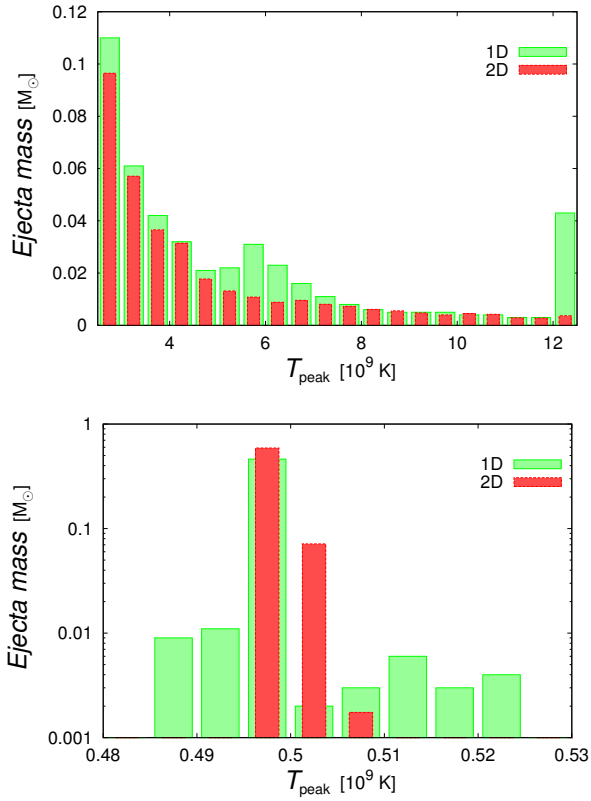

Figure 4.15: Comparison of the distributions of peak temperatures $T_{\rm peak}$ (left panel) and Y_e(NSE) (right panel) between the 1D fiducial model and the 2D counterpart. The total mass of the matter that has the peak temperature higher than $T_9 = 5$ is $1.89 \times 10^{-1}{\rm M}_\odot$ in 1D and $9.62 \times 10^{-2}{\rm M}_\odot$ in 2D.

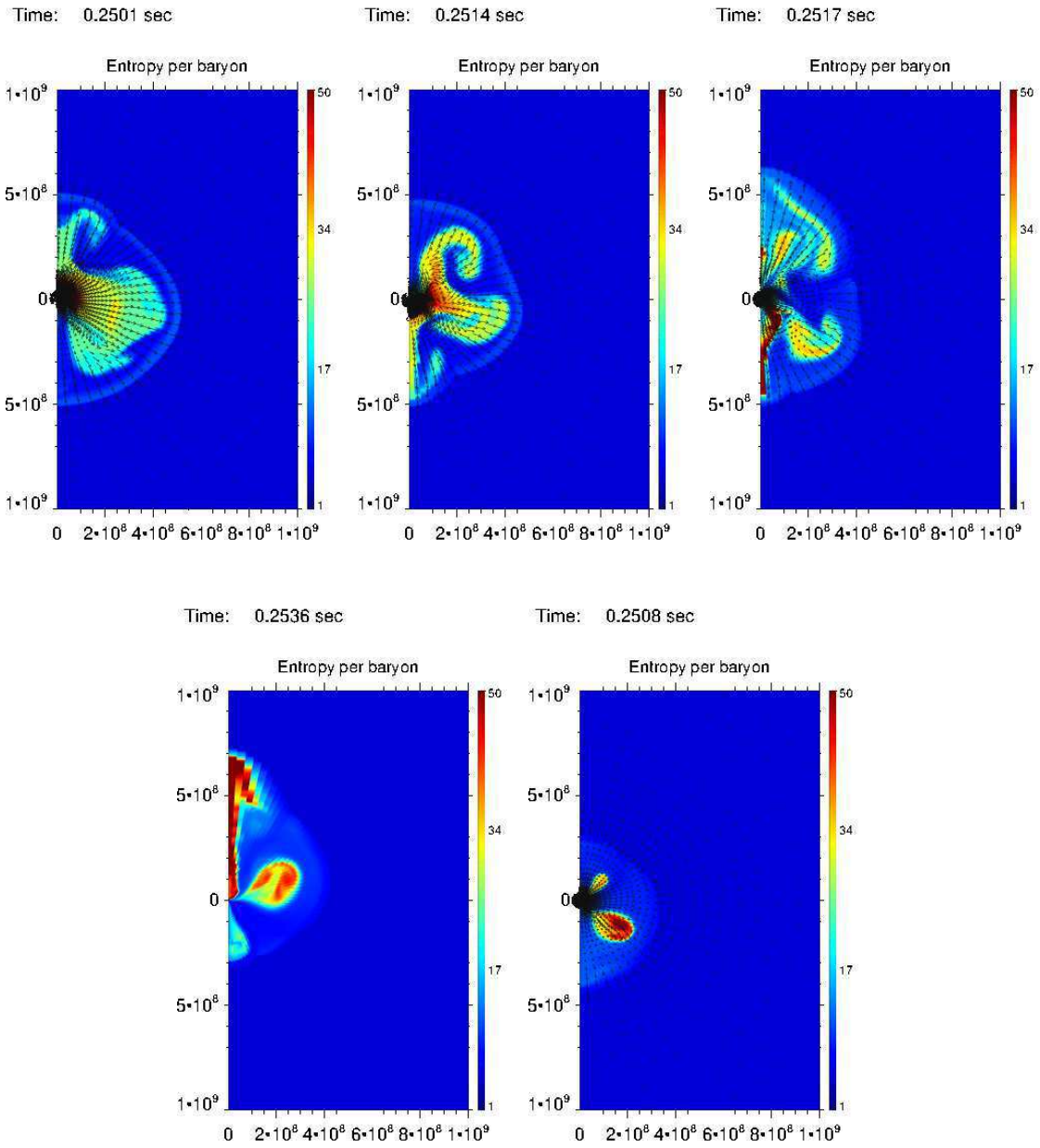

Figure 4.16: Post-shock-relaunch distributions of entropy per baryon in the meridian section for all the 2D models at $t_{\rm exp} \sim 0.25$s.

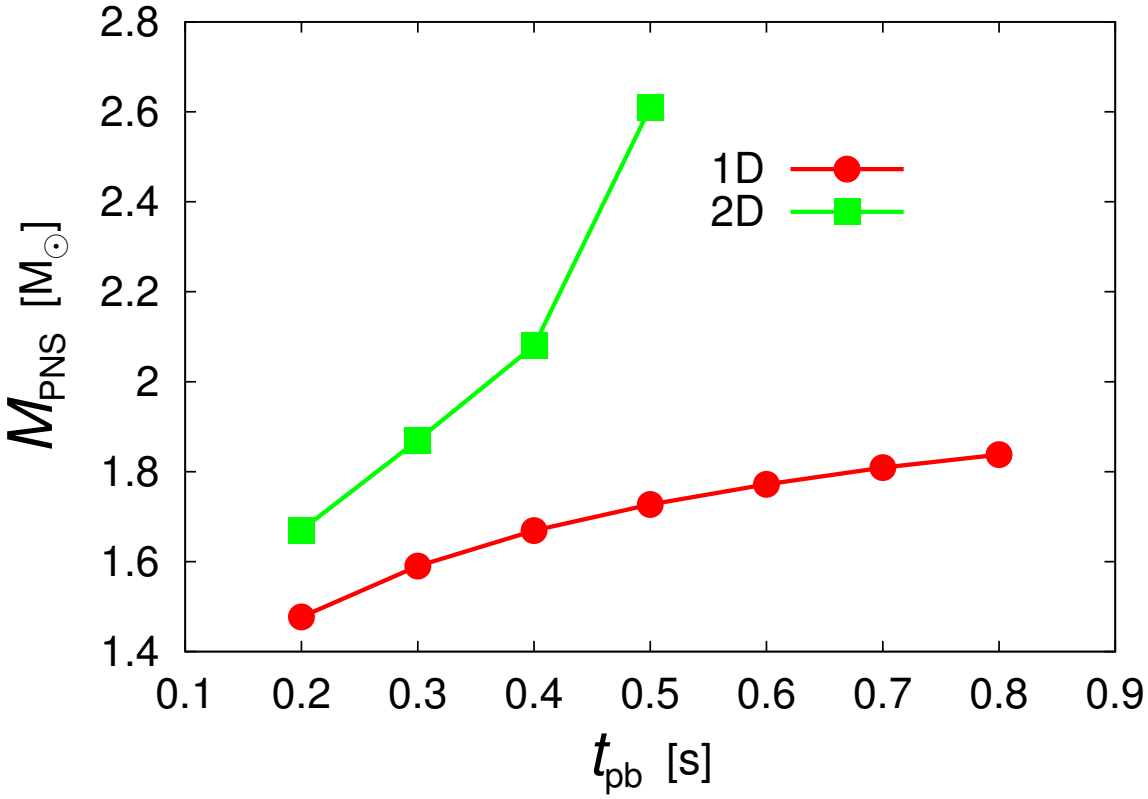

Figure 4.17: Comparison of the masses of proto-neutron stars at the end of computations between the 1D and 2D models.

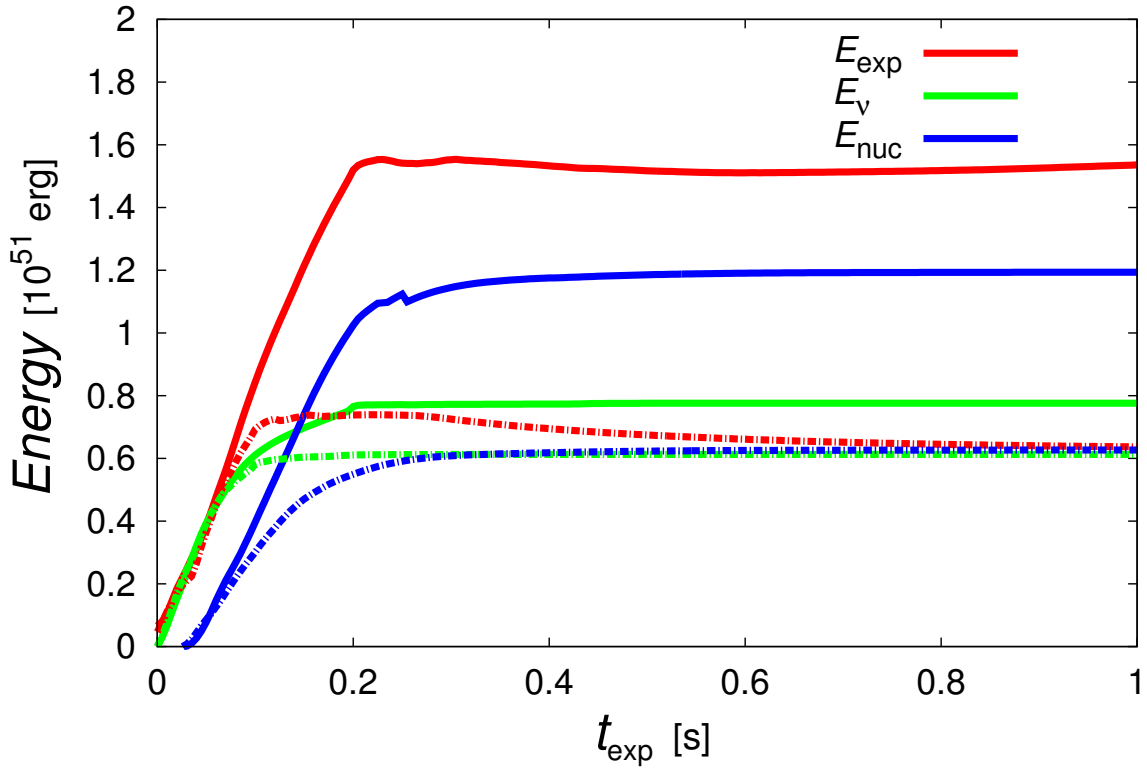

Figure 4.18: The time evolutions of diagnostic explosion energy for the 2D models, in which the shock is relaunched at $t_{pb} = 300$ms (solid line) and $t_{pb} = 400$ms (solid dotted line).

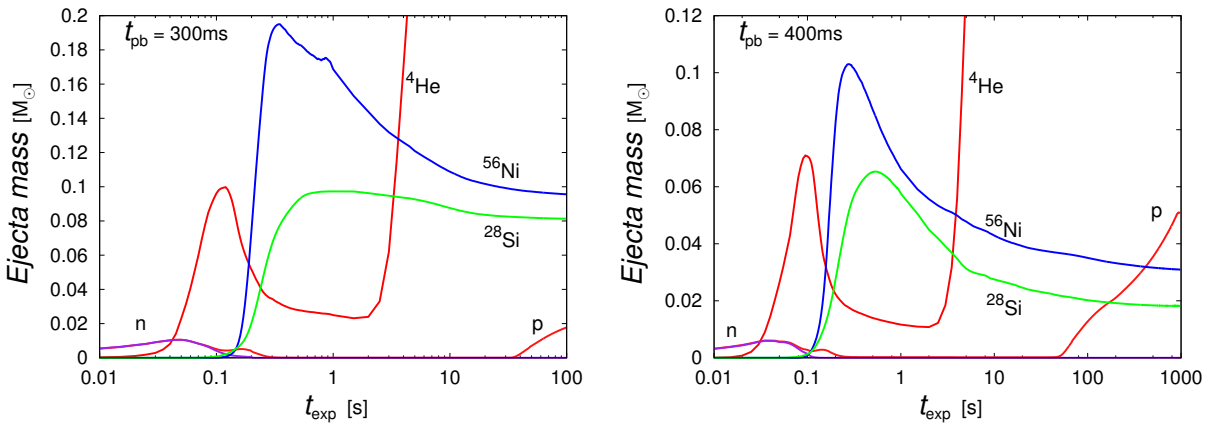

Figure 4.19: The time evolutions of masses of n, p, ^{4}He, ^{28}Si , and ^{56}Ni as a function of t_{exp} for the models with $t_{pb} = 300$(left panel) and 400ms(right panel).

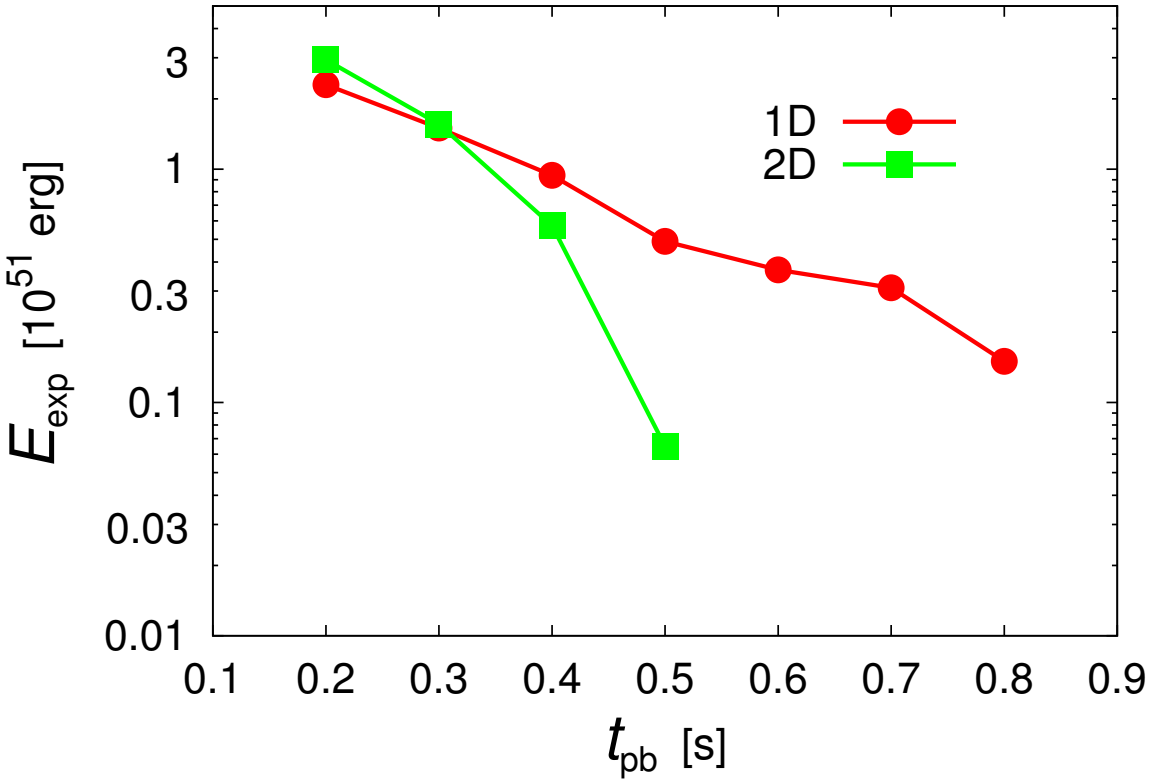

Figure 4.20: Comparison of the explosion energies between the 1D and 2D models.

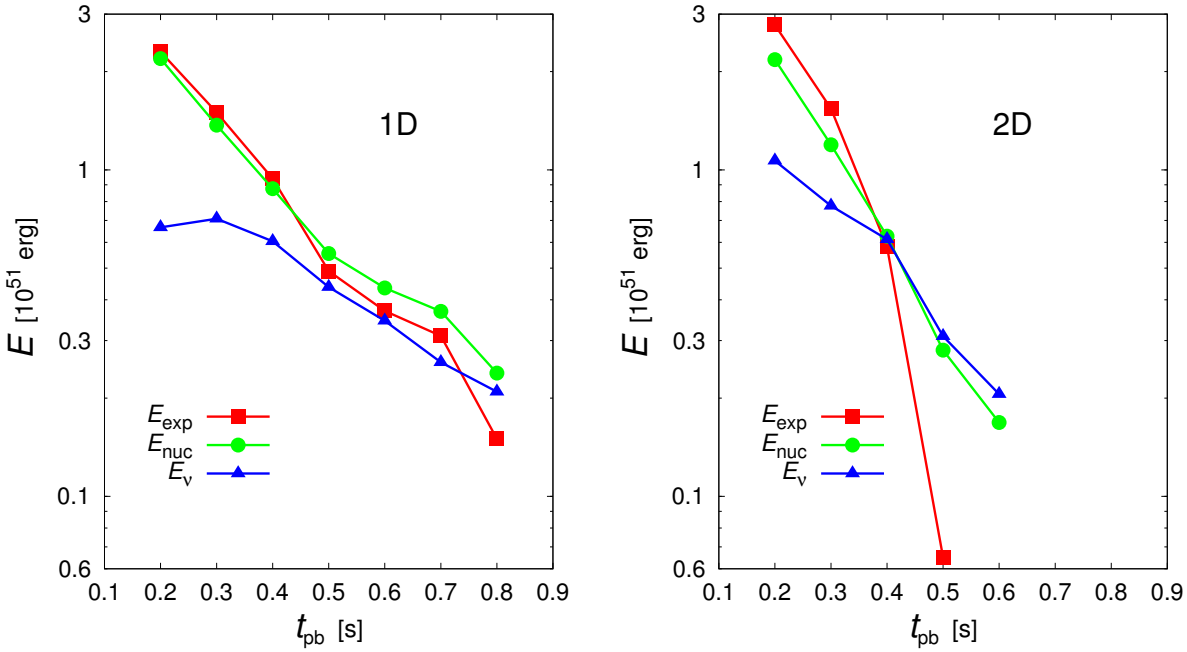

Figure 4.21: The individual contributions of neutrino heating and nuclear reactions to the explosion energy for all the 1D and 2D models.

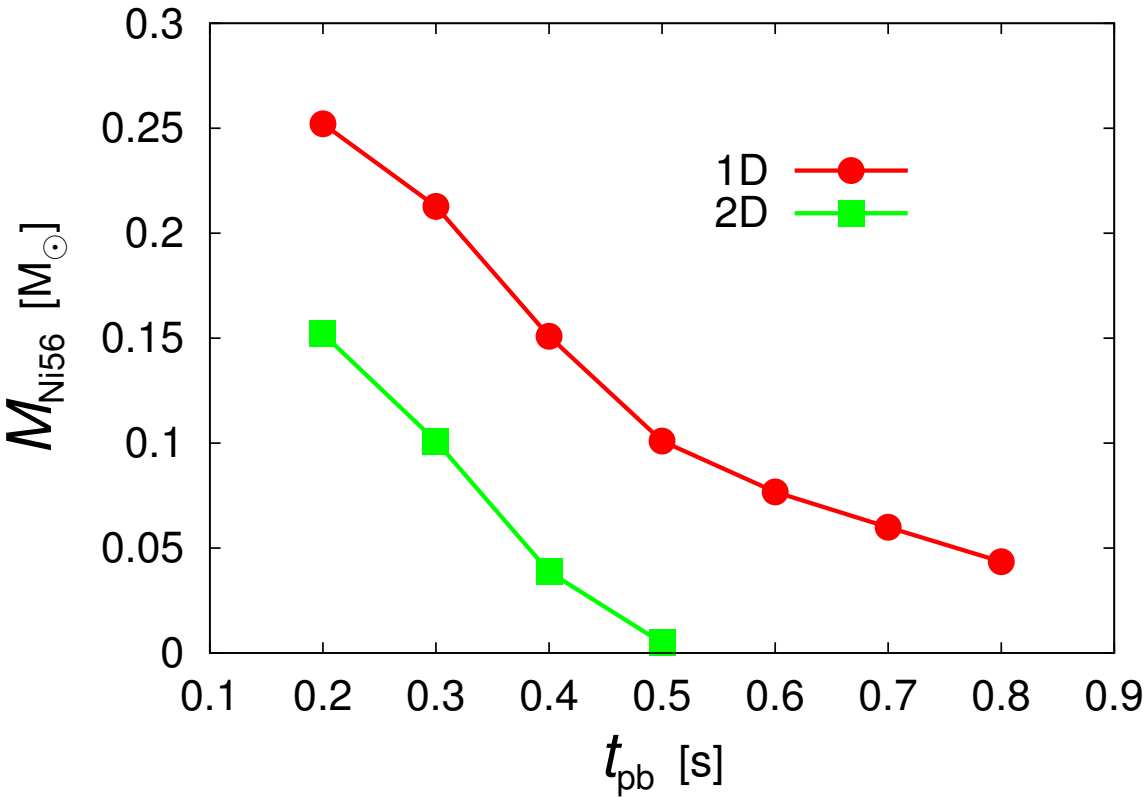

Figure 4.22: Comparison of ^{56}Ni masses in the ejecta between the 1D and 2D models.

4.3 Discussion

We have investigated by numerical experiments done in 1D and 2D the post-shock-relaunch evolutions in the neutrino heating mechanism. Taking into account the fact that the shock revival should occur somewhere on the critical line in the $L_{\nu,c}-\dot{M}$ diagram but exactly where is rather uncertain theoretically at present, we have treated the luminosity (or equivalently the mass accretion rate) at the shock relaunch as a free parameter that we vary rather arbitrarily. Only the post-bounce phase has been computed and we have discarded the central region ($r \lesssim 50$km) and replace it with the prescribed boundary conditions. We have also neglected the neutrino transport entirely and employed the light bulb approximation. The shock revival is hence induced by giving a critical luminosity at the inner boundary by hand.

The critical luminosity itself has been determined also by hydrodynamical simulations, since not the non-existence of steady state but the onset of hydrodynamical instabilities dictates the shock revival. The mass accretion rate as a function of time is obtained by the simulation of gravitational implosion of a massive star envelope. We have adopted a realistic $15M_\odot$ progenitor provided by Woosley & Heger (2007) [473]. In these computations, we have taken into account the nuclear reactions among 28 nuclei that include 14 α nuclei as well as their feedback to hydrodynamics consistently. As a result, we have confirmed that the critical luminosity is a monotonically decreasing function of the shock-relaunch time (or equivalently a monotonically increasing function of the mass accretion rate) and that 2D dynamics reduces the critical luminosity compared with 1D dynamics. This is due to the non-radial hydrodynamical instabilities and the resultant enhancement of neutrino heating in the former case.

After re-mapping, we have continued the simulations until long after shock revival. In fact, for some 1D models we have followed the post-shock-relaunch evolutions up to the shock breakout of the stellar surface, confirming that the diagnostic explosion energy has approached the asymptotic value much earlier and the shorter computation times for other models are sufficient indeed. We have employed the same set of input physics as in the simulations for the setup of initial conditions. Integrating the source terms in the equation of energy conservation, we have evaluated the individual contributions from the neutrino heating and nuclear reactions to the explosion energy. In so doing, we further divide the latter to the contributions from the recombinations in and out of NSE as well as from the nuclear burnings. The axisymmetric 2D simulations have been performed to elucidate the effect of multi-dimensionality on the outcome.

What we have found in these model computations are summarized as follows:

1. Immediately after shock relaunch the neutrino heating is the dominant source of the explosion energy but is terminated before long as the shock propagates outwards. Then the nuclear reactions take its place, with the recombinations of nucleons to α particles under the NSE condition occurring first. As the temperature decreases, the NSE becomes no longer satisfied. The recombinations of α particles to heavier elements proceed mainly in this non-NSE circumstance. When the temperature lowers further, the nuclear burnings of silicons and oxygens take place in the matter that flows into the shock wave. Matter that flows into the shock wave contributes negatively to the explosion energy, since it is gravitational bound.

2. The final explosion energy is a monotonically decreasing function of the shock-relaunch time (or equivalently an increasing function of the mass accretion rate at shock re-

launch) irrespective of the dimensionality of hydrodynamics. There is no big difference between 1D and 2D for the same mass accretion rate at the shock relaunch as long as it occur earlier $t_{pb} \lesssim 300$ms and the explosion is robust. The late relaunch in 2D leads to highly anisotropic expansion of matter with a large portion of the post-shock matter still accreting, which then yield very weak or no explosions. This implies that the mass accretion rate is the primary factor to determine the canonical explosion energy. Since the critical neutrino luminosity for a given mass accretion rate is lower in 2D than in 1D, the explosion energy for a given neutrino luminosity is larger except for very weak explosion.

3. As the shock relaunch is delayed, it takes longer the diagnostic explosion energy reaches the asymptotic value. In our 1D fiducial model, in which the stalled shock is revived at $t_{pb} = 400$ms and we obtain the explosion energy of $E_{exp} \sim 10^{51}$erg, the diagnostic explosion energy attains the asymptotic value in $t_{exp} \sim 600$ms whereas it takes $\sim$ 2s for the model, in which the shock relaunch is assumed to occur at $t_{pb} = 800$ms and the explosion energy is as low as $\sim 10^{50}$erg. The similar trend is also observed in the 2D models except for the case with $t_{pb} = 600$ms, in which no explosion obtains.

4. In 1D the nuclear reactions always overwhelm the neutrino heating. The difference becomes smaller as shock relaunch is delayed. To the nuclear reactions the recombinations of nucleons to α particles that occur mainly under the NSE condition are the dominant contributor, followed by the recombinations of α particles to heavier elements in the non-NSE condition. The nuclear burnings provide the smallest contribution except for the weakest explosion, which obtains for the latest shock-relaunch. In that case, the nuclear burnings beat the recombinations in non-NSE. In 2D, on the other hand, the neutrino heating and nuclear reactions give comparable contributions to the explosion energy with the latter being larger in stronger explosions and vice versa. Note, however, that the rather small contribution of neutrino heating is deceptive in the sense that it is the ultimate source of the energy obtained from the nuclear recombinations and that it is crucial to set the stage for shock revival, which is not accounted for in the diagnostic explosion energy.

5. In the 1D models nickels are overproduced owing mainly to a larges mass that achieves high peak temperatures compared with the ordinary calculation of explosive nucleosynthesis in post-process. In fact there is no 1D model that gives the typical values to the explosion energy and nickel mass simultaneously. Given observational and theoretical uncertainties, we are not certain how serious a problem this is for the moment. One may consider, however, that this is yet another reason to abandon the 1D neutrino heating model. In 2D, on the other hand, this problem is solved, opening up the allowed region in the shock-relaunch time around $t_{pb} \sim 300 - 400$ms , which produces the explosion energy and nickel mass in the appropriate range. This happens mainly in 2D because the mass of matter in the ejecta that attain high enough peak temperatures is smaller and the fall back is significant. This is in turn related with the fact that the expansion and accretion occur simultaneously in 2D, which is indeed reflected in the mass of proto-neutron star, which is larger in 2D at any post-bounce time.

In the present paper we have employed the single $15M_\odot$ progenitor model, which we think is one of the most representative to produce the typical Type IIP CCSN. Very recently

Ugliano et al.(2012) [448] reported a possible stochastic nature in the outcome of the shock revival in the neutrino heating mechanism based on systematic 1D hydrodynamical simulations. Although the stochasticity is less remarkable in the low mass end, it is hence mandatory to extend the current work to other progenitors and see how generic our findings obtained are in the next chapter. 3D models are also the top priority in the future work, since we know that 3D SASI is qualitatively different from 2D SASI we have studied in this paper [193]. It should be also recalled that Nordhaus et al.(2010) [317] claimed that shock revival is even easier in 3D than in 2D although controversies are still continuing [153].

If the critical luminosity is much lower in 3D than in 2D, the yield of ^{56}Ni may be reduced further in 3D. The complex flow pattern also have some influences on the nickel yield. We are particularly concerned about how the allowed region in the shock-relaunch time that is opened in 2D is modified in 3D. The relative importance of the nuclear reactions for the explosion energy compared with the neutrino heating is the highest in 1D. We are certainly interested in what about 3D.

One of the greatest uncertainties in the present study is the effect of the inner boundary condition that is imposed by hand. The artificial treatment employed in this paper results in the total mass injection from the inner boundary of about $7 \times 10^{-3} M_\odot$ in the 1D fiducial model, which contributes to the explosion energies and the ^{56}Ni masses by 2-3%. Although this may be a slight underestimate [11], we believe that better treatments will not change the conclusion of the paper qualitatively. The eventual answer should come from fully consistent simulations of the entire core, though. It is also true that the simple light bulb approximation adopted in this paper does not accurately account for accretion luminosities, in particular their correlations with temporally varing accretion rates as well as the differences between 1D and 2D. Hence the appropriate treatment of the neutrino transport, which is neglected completely in this paper, will be critically important. These caveats notwithstanding we believe that the results obtained in this paper are useful to understand the post-shock-relaunch evolution in the neutrino heating mechanism, particularly how the diagnostic explosion energy approaches the final value. One of the goals of our project is to seek, probably after more systematic investigations suggested above, the way to estimate the explosion energy from the early stage of post-shock-revival evolution, since realistic simulations may not be affordable for a few seconds after shock relaunch.

Chapter 5

Systematic Studies of the Post-Shock-Revival Evolutions in Core Collapse Supernovae with Parametric Progenitor Models

5.1 Introduction

In the last 10 years we have seen a remarkable progress in the theoretical modeling of core collapse supernovae (CCSNe) ([196, 223, 49] and the references therein) Massive stars of $\gtrsim 10M_{\odot}$ end their life as CCSNe and leave behind compact objects such as neutron stars and black holes. The mechanism of CCSNe has been elusive for more than a half century in spite of intensive investigations in the intervening years by many researchers. It is now pinned down to the problem of how to revive a stalled shock wave, though, which is generated by the core bounce following its gravitational collapse but is stagnated inside the core owing mainly to nuclear dissociations. The most promising at present is the so-called neutrino heating mechanism, in which a fraction of neutrinos emitted copiously by a nascent proto neutron star are re-absorbed by matter between the stalled shock wave and the gain radius, heating up them to expel the shock wave eventually. After many years of failed attempts, we have now a large number of numerical models that were successful in shock revival [266, 289, 427, 303, 414, 41]. This is mainly thanks to the ever increasing computational power as well as the implementation of elaborate numerical schemes, particularly for neutrino transport, which enabled us to perform long-term simulations in multi-spatial dimensions. Accompanied sophistications in the treatment of microphysics such as the nuclear equation of state and weak interactions between neutrinos and matter have also contributed to the improvement of the theoretical modeling.

It is certainly true that these models are promising candidates of the answer to the long-standing problem of CCSNe mechanism but one should not forget that the revival of the stalled shock wave that these simulations have demonstrated is just a necessary condition for supernova explosion but is not a sufficient condition. As a matter of fact, we know that the explosion energy of CCSNe is $\sim 10^{51}$erg canonically but most of these computations were not yet successful to obtain the number ([266, 289, 427, 303, 414] but see also [41]). Ni yields are another important quantities, since they decay radiatively and brighten the supernova ejecta later. We can infer the mass of synthesized Ni from the exponential decay observed in the light curve over hundreds of days after the initial brightening. It is typically

$\lesssim 0.1 M_\odot$ [151, 314, 451, 219, 390] It is not clear whether the most advanced theoretical models can indeed reproduce this quantity, since it takes many seconds for the mass of Ni in the ejecta to be settled. In fact, most of the successful simulations cited above were not able to extend their computations much beyond a second because the CPU time would be simply unaffordable or some physical processes that are important in the late phase were not incorporated in their models.

Taking a more phenomenological approach, we studied in the previous chapter how the explosion energy and Ni yields are determined after shock revival. We constructed steady, spherically symmetric accretion flows through a standing shock wave onto a proto neutron star (PNS) for different combinations of neutrino luminosity and mass accretion rate. Assuming that shock revival occurs somewhere on the critical curve, we ran both 1D and 2D hydrodynamical simulations to compute the evolutions that follow the shock revival induced by artificially increasing the neutrino luminosity slightly above the critical value. The central region that includes the PNS was excised and replaced by a time-dependent inner boundary condition prescribed appropriately. The neutrino transfer was approximated by the so-called light-bulb approximation. On the other hand, an NSE or non-NSE equation of state was employed in the region where it is appropriately. The use of latter in particular was combined with network calculations of nuclear reactions such as recombinations and fusions so that smooth transitions from one regime to the other should be guaranteed. The simulations were conducted long enough, for a few seconds normally but for more than a thousand seconds in some cases after shock revival so that the explosion energy and the Ni mass could be well settled.

We found in these experimental simulations that the neutrino heating becomes minor rather soon after shock revival as matter expands to larger radii. The energy of neutrinos were mainly consumed to lift up matter from the gravitational well and set the stage for shock revival. Then the recombinations of nucleons to alpha particles to heavier nuclei become the main contributors to the explosion energy (see also [337]). They proceed under NSE initially but some nuclear reactions cannot catch up the expansion and are frozen later. Then we need to employ the non-NSE equation of state together with the network calculations of nuclear abundances consistently. In the final stage the explosive nuclear fusions contribute relatively small energies. In the meantime, a fraction of matter falls back onto the PNS, decreasing the energy included in the ejecta as well as the Ni mass. The final explosion energy is obtained after the negative gravitational energy of the envelopes that are engulfed by the forward-propagating shock wave is accounted for. The time for the explosion energy and the Ni mass in the ejecta to be finally settled depends on the strength of explosion: it takes longer as the explosion energy gets smaller. It was also demonstrated, on the other hand, that the earlier the shock revival sets in, the larger the final explosion energy is. The Ni mass has the same trend. Interestingly, we found that the 1D models tend either to synthesize too much Ni ($\gtrsim 0.1 M_\odot$) or to produce too weak explosions ($\lesssim 0.5 \times 10^{50}$erg) and a fine tuning in the shock revival time seems necessary to reproduce the canonical explosion, which we interpreted as another setback for spherically symmetric explosions. Such a tuning was somewhat relaxed in 2D models.

These findings should certainly be confirmed by more realistic simulations. It is also important, however, to study their systematics, i.e., how they depend on, e.g., the progenitor structure, inner boundary condition, and so on, since we adopted a single progenitor of $15 M_\odot$ [473] and did not try different boundary conditions at the inner boundary. It is well known in fact that the structures of massive progenitors are very sensitive to small differences in mass as well as the numerical treatment of some physical processes such as

convections in the stellar evolution calculations [474, 473, 235, 407]. It is hence mandatory to see how robust our findings are when we change progenitors and this is exactly what we aim to clarify in this paper. In so doing, we did not use the progenitor models provided by stellar evolution calculations. Instead we constructed toy models of progenitors, in which non-rotating, hydrostatic configurations with an iron core in NSE, a Si+S mantle in QSE as well as other outer envelopes are calculated by employing parametrized distributions of entropy and electron fraction as a function of density. By so doing, we can vary the masses of these different layers rather arbitrarily. We are also able to obtain the abundance of various elements so that we could use them later for the network calculations.

These models are better suited for the systematic studies conducted in this paper than more realistic models. As mentioned above, the structures of the realistic models change in a complicated way as a function of mass [407] , which makes it difficult to interpret which features in the progenitor have what consequences. It is not helpful either that the progenitor models provided by different groups are sometimes very different [252, 97, 339, 487, 201] and the structures of massive stars are likely to be very sensitive intrinsically to some input physics as well as to numerical resolutions [407]. As shown later, adopting an appropriate entropy distribution and paying a proper attention to the transition condition at the layer boundary, we can capture the essential features in the massive progenitors.

The organization of this paper is as follows: the input physics and numerical method are described in Section2. Special emphasis is put on the construction of the toy models of progenitors. Section 3 is devoted to the results of 1D and 2D dynamical simulations: we first compute 1D collapses to obtain the accretion rates as a function of time for all models; we then construct spherically symmetric, steady shocked accretion flows for the accretion rates just obtained and a prescribed neutrino luminosity and use them as initial conditions for 1D and 2D hydrodynamical simulations; the dependence of the explosion energy and Ni mass on the progenitor structures are described in detail. Finally we summarize our findings and discuss some implications in Section 4.

5.2 Models and Numerical Methods

5.2.1 Outline of Methods

The methodology employed in this paper is essentially the same as that in the previous chapter. One single big difference is, as mentioned in Introduction, that multiple progenitor models are constructed systematically as described in the next subsection in detail and study the dependence of the energy and Ni mass in ejecta on the progenitor structure. In order to evaluate the asymptotic values of these quantities, we take the following four steps:

1. construct the toy models of pre-supernova stars with different masses of iron cores and Si+S layers.

2. run 1D hydrodynamical simulations of gravitational collapse of the pre-supernova models obtained in the first step, excising the central part and thus reducing the pressure support there by hand; this step is needed to obtain the mass accretion histories for these models, which are used in the following steps.

3. construct spherically symmetric, steady accretion flows through stalled shock waves for mass accretion rates obtained in the first step and neutrino luminosities, which are chosen to be close to the critical values for the assumed mass accretion rates.

4. run 1D and 2D hydrodynamical simulations for the accretion flows just constructed; small perturbations are added in the 2D computations; the matter distributions obtained in the first step are employed outside the shock wave; the neutrino luminosities change in time in a prescribed way; since the initial configurations are close enough to the critical states, shock revival takes place soon after the simulations are started; the ensuing evolutions are followed until the explosion energy is well settled.

It is noted that the third step in this paper is slightly different from the counter part in our previous paper. In the latter, the critical neutrino luminosities (see [52, 481, 344, 414] for details) were searched for given mass accretion rates, which was time consuming and not very important indeed, since the mass accretion rate is allowed to change in time in the last step. We are hence satisfied in this paper with the neutrino luminosities that are somewhat sub-critical but more or less close to the critical values. This strategy is similar to the one that was conceived by Murphy et al.(2008) [291] and is commonly used by others these days.

It should be also mentioned that the simulations in the final step are terminated when the energy in the ejecta becomes almost unchanged. In 1D models this also means the settlement of the Ni mass in the ejecta by that time. This is not the case, however, in 2D computations unfortunately, since larger fractions of ejecta tend to fall back at later times and it takes much longer to get the Ni mass settled: in some cases the explosion energy reaches the final value in ~ 1 sec whereas the Ni mass has not reached the asymptotic value yet even after $\sim 10 - 100$sec. The simulations are terminated before the Ni mass is finally settled in those cases, since a further computation would require us to take into account the outer envelopes such as helium and hydrogen layers, which would not be a trivial thing. It is also stressed that we are concerned with the influences of the structures of the stellar central region involving the iron core and Si+S layers on the shck revival and the dynamics that follows. We hence decide to avoid unnecessary complications in this paper. The earlier termination of simulations would underestimate the fall back and hence

overestimate the Ni mass. Then we should regard the numbers given in that case as upper limits, which would not spoil our arguments anyway.

5.2.2 Pre-supernova Models: Step 1

As we have mentioned already, we do not use realistic progenitor models that are put in the public domain by researchers of stellar evolutions [474, 252, 339, 487, 97] but instead construct toy models on our own. This is mainly because those realistic models have structures that are sensitive to the stellar mass as well as some physical processes, e.g., convections of various kinds, and their numerical implementations [235, 407], which would make it difficult to decipher what is the consequence of which effect. Since our studies are of experimental nature, "realism" is not very important and toy models that capture the essential features in massive stars' structures but still have some degrees of freedom to change key parameters, e.g., the masses of Fe core and Si+S layer rather arbitrarily are more useful. In this subsection, we present in detail the construction of such toy models. The details of pre-supernova construction have been already remarked in section 3.6.

In this paper we focus on the masses of the Fe core and Si+S layer. Six different combinations of three Fe core masses: $M_c = 1.3\mathrm{M}_\odot$, $1.4\mathrm{M}_\odot$ and $1.5\mathrm{M}_\odot$, and two Si+S layer masses: $M_{\mathrm{SiS}} = 0.09\mathrm{M}_\odot$ and $0.18\mathrm{M}_\odot$ are investigated. Given the Fe core mass, the central density is given by the following equation,

$$\rho_c\left(M_c\right) = 6.5 \times 10^9 \exp\left[-5 \ln 2 \left(M_c - 1.40\right)\right], \tag{5.1}$$

which is a fit to the correlation suggested in Fig. 3.16 (see the black dotted line in the figure). Then the hydrostatic equations are integrated from the center to the specified masses of the Fe core and Si+S layer to give the corresponding radii. The integration is actually continued to larger radii, with other outer layers being properly taken into account.

The six solutions are shown in Fig.5.1, which depicts the enclosed masses and entropies per baryon as functions of radius for the three Fe core masses with the Si+S layer mass of $M_{\mathrm{SiS}} = 0.09\mathrm{M}_\odot$ in the left panel and with $M_{\mathrm{SiS}} = 0.18\mathrm{M}_\odot$in the right panel, respectively. Note that we adopt different masses of C+O+He and He layers for the models with $M_c = 1.30\mathrm{M}_\odot$ and with $M_c = 1.40\mathrm{M}_\odot$ in the case of $M_{\mathrm{SiS}} = 0.09\mathrm{M}_\odot$ in order to avoid unrealistic He burnings although this has essentially no influence on the explosion energy and Ni mass.

It is evident that rather small differences in the core mass, $\Delta M_c = 0.10 M_\odot$, and the Si+S layer mass, $\Delta M_{\mathrm{SiS}} = 0.09 M_\odot$, cause noticeable changes in the $R - M_r$ relations and hence the density profiles in outer layers ($M_r \gtrsim 2\mathrm{M}_\odot$): the higher M_{SiS} tends to make the greater differences at large radii for t he same ΔM_c. The compactness introduced by O'Connor & Ott (2011) [321] also differs considerably among these models. The purpose of this paper is to study the consequences these differences may have on the shock revival, explosion energy and Ni mass later in the dynamics of CCSNe.

It is noteworthy that the hierarchy in compactness depends on where it is measured: heavier Fe-core models have higher compactnesses if they are measured in the silicon layer whereas the hierarchy is inverted outside the ONeMg layer. This is because the entropy is higher at $M_r \sim 1.5 - 2\mathrm{M}_\odot$ for lighter Fe-cores, making this layer more bloated. In the O+Ne+Mg envelope, $M_r \sim 2 - 2.7\mathrm{M}_\odot$, on the other hand, all models are assumed to have the same entropy again. Since the O+Ne+Mg envelope appears at lower densities in the models with heavier Fe-cores as can be seen in the lower panels of the figure, temperatures are higher in this layer for these models, which results in the more extended envelopes.

This feature was also reported in Baron (1990) [22] (see their models "105" and "107" in Figure.9), who attempted to construct different toy models, having similar parametric research in mind. They gave S and Y_e as functions of mass coordinate unlike in this paper, in which they are considered as functions of ρ. It seems that they paid little attention to

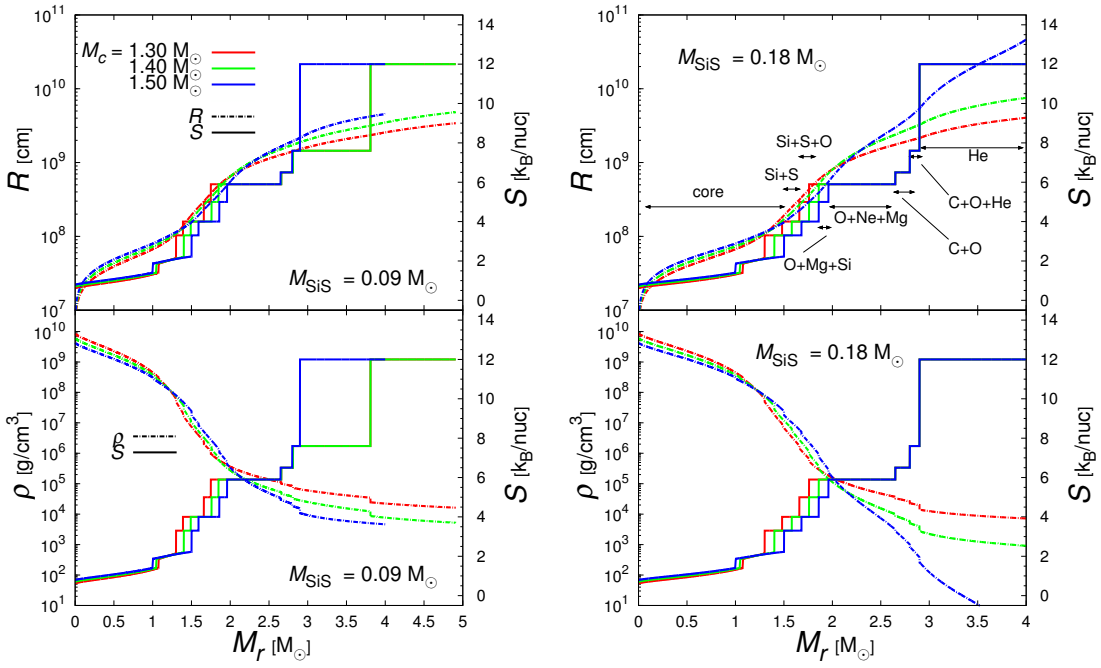

Figure 5.1: Entropies and radii as functions of mass coordinate (upper panels) and the corresponding density profiles (lower panels). The Si+S layer mass is chosen to be $M_{\rm SiS} = 0.09{\rm M}_\odot$ in the left panels and $M_{\rm SiS} = 0.18{\rm M}_\odot$ in the right panels. Colors specify the core mass: $M_c = 1.30{\rm M}_\odot$ (red), $1.40{\rm M}_\odot$ (green) and $1.50{\rm M}_\odot$ (blue), whereas solid and dotted lines represent the entropy and radius, respectively. The arrows illustrated in the top right panel depict the inital location of different chemical composition layers for $M_c = 1.50 M_\odot$

the correlation between S and Y_e, both of which are influenced by the electron capture on heavy nuclei in a similar way. Note also that the two masses, M_c and $M_{\rm SiS}$, can not be chosen completely arbitrarily with other parameters being fixed, since the resultant chemical compositions should be stable, i.e., the time scale of nuclear reactions should be longer than the dynamical time scale. It is found indeed that very high M_c and/or M_{sis} produce too large low-entropy regions and make it difficult to extend outer envelopes. Since we perform network calculations to follow the temporal evolution of chemical abundances, their models are not appropriate for our purpose.

5.2.3 Hydrodynamics

The numerical method employed in this paper for hydrodynamical computations is essentially the same as that in the previous section. The hydrodynamical evolutions are solved on the spherical coordinates with the axisymmetric Eulerian code ZEUS-2D [402, 159], which is extended by the authors so that chemical abundance evolutions could be treated consistently with a non-NSE EOS. For the 1D collapse computation (step 2 in section 5.2.1), 500 radial grid points are deployed to resolve 100km $\leq r \leq 20,000$km. For the simulations of shock revival and the subsequent evolution (steps 3 and 4), we employ 650 radial grid points in 1D and $(n_r, n_\theta) = (600, 76)$ mesh points in 2D, which covers the domain with 45km $\leq r \leq 20,000$km and $0 \leq \theta \leq 2\pi$. The central portion of the core is excised and replaced by a point mass located at the center, which exerts gravitational forces to the matter in the computational region. The temporal change in its mass is calculated from the matter flow going into the inner boundary. The inner boundary condition is essentially the same as in the previous chapter: all variables but radial velocity are copied from the innermost active mesh point to the ghost mesh points; the radial velocity is fixed until outflow occurs, in which case it is treated just in the same way as other variables except for the upper limit of 10^8cm/s; the densities on the ghost mesh points are also modified so that the entropy per baryon should not exceed $100k_B$. We use the same code both for 1D and 2D simulations, in the former of which we suppress motions in the θ direction.

We adopt the light bulb approximation instead of solving neutrino transfer and take into consideration only interactions of electron-type neutrinos and anti-neutrinos with nucleons when we conduct simulations in steps 3 and 4 for the shock revival and subsequent evolution. To approximately describe the neutrino-spheric radius, R_ν, and temperature, T_ν, that evolve in time due to PNS contractions, we employ the following analytical prescriptions for R_ν:

$$R_{\nu_e}(t_{300}) = 31.00 + 16.69 \cdot \exp\left(-\frac{t_{300}}{193}\right) \text{km}, \tag{5.2}$$

$$R_{\bar{\nu}_e}(t_{300}) = 27.00 + 16.45 \cdot \exp\left(-\frac{t_{300}}{211}\right) \text{km}, \tag{5.3}$$

and for T_ν:

$$T_{\nu_e}(t_{300}) = 6.00 - 0.67 \cdot \exp\left(-\frac{t_{300}}{200}\right) \text{MeV}, \tag{5.4}$$

$$T_{\bar{\nu}_e}(t_{300}) = 7.00 - 0.67 \cdot \exp\left(-\frac{t_{300}}{200}\right) \text{MeV}, \tag{5.5}$$

where t_{300} denotes the time in millisecond elapsed from 300ms post bounce. The prescriptions are determined so that they should fit more realistic simulations [303]. The luminosities of electron-type neutrinos and anti-neutrinos are assumed to be same, $L_\nu = L_{\nu_e} = L_{\bar{\nu}_e}$, gradually decay after the onset of explosion:

$$L_\nu(t) = \begin{cases} L_\nu & \text{before explosion,} \\ L_\nu \cdot \exp\left(-\dfrac{t_{300}}{800\text{ms}}\right) & \text{after explosion.} \end{cases} \tag{5.6}$$

Another major improvement from the previous work is the nuclear physics employed. In order to calculate chemical compositions more precisely, we deploy 297 nuclei ($Z \leqq 32$)

Table 5.1: A List of Nuclei considered in NSE.

Element	A_{min}	A_{max}	Element	A_{min}	A_{max}
n.....	1	1	Cl....	31	40
H.....	1	3	Ar....	33	44
He....	3	6	K.....	35	46
Li....	6	8	Ca....	37	49
Be....	7	11	Sc....	40	50
B.....	8	12	Ti....	42	52
C.....	10	15	V.....	44	54
N.....	12	17	Cr....	46	56
O.....	14	20	Mn....	48	58
F.....	17	21	Fe....	50	62
Ne....	18	25	Co....	52	63
Na....	20	26	Ni....	54	67
Mg....	21	28	Cu....	57	69
Al....	23	30	Zn....	59	72
Si....	25	33	Ga....	61	74
P.....	27	35	Ge....	63	78
S.....	29	38			

Note: Total number of nuclei is 297 with $Z \leqq 32$.

instead of 28 to describe NSE at $T_9 > 7.0$ (see the list in Table 5.1). At $T < 7 \times 10^9$K, where NSE no longer holds, on the other hand, the number is reduced to 28: n, p, D, T, ^{3}He, ^{4}He and 12 α-nuclei, i.e., ^{12}C, ^{16}O, ^{20}Ne, ^{24}Mg, ^{28}Si, ^{32}S, ^{36}Ar, ^{40}Ca, ^{44}Ti, ^{48}Cr, ^{52}Fe, ^{56}Ni, and 10 of their neutron-rich neighbors, that is, ^{27}Al, ^{31}P, ^{35}Cl, ^{39}K, ^{43}Sc, ^{47}V, ^{51}Mn, ^{53}Fe, ^{54}Fe and ^{55}Co. The other 269 nuclei are represented by a single (imaginary) inert nucleus in the network calculations.

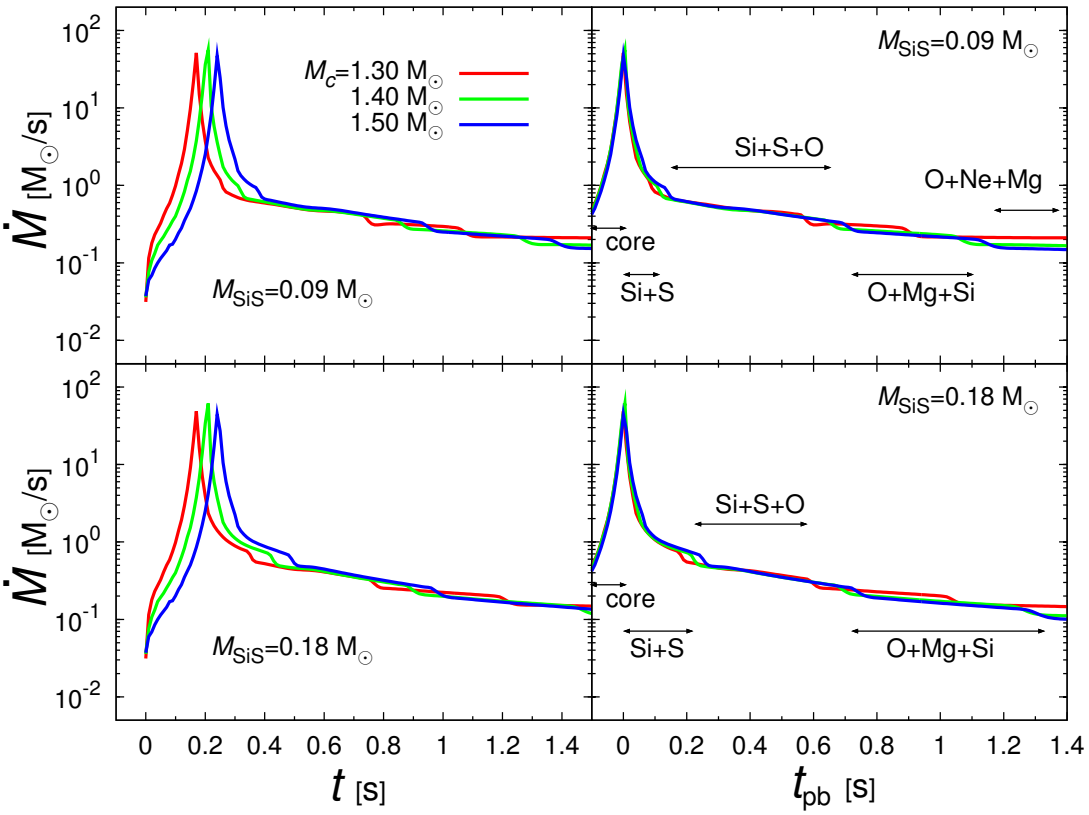

Figure 5.2: The time evolutions of the mass accretion rate at 100km for all models. The upper panels show the results for the models with $M_{\rm SiS} = 0.09{\rm M}_\odot$ whereas the lower panels are the counter parts for the models with $M_{\rm SiS} = 0.18{\rm M}_\odot$. In the left panels the time is measured from the onset of collapse while in the right panels the origin of time is shifted to the bounce time, which is defined to be the time, at which the mass accretion rate reaches maximum. The red, green and blues lines correspond to the core mass of $M_c = 1.30$, 1.40 and $1.50{\rm M}_\odot$, respectively. The arrows in the right panels indicate which layer is passing through $r = 100$km at which post bounce time for $M_c = 1.50 M_\odot$.

5.3 Results

5.3.1 Accretion Histories: Step 2

We present first the results of 1D computations of the collapse phase, i.e., Step 2 mentioned in section 5.2.1. The time evolutions of the mass accretion rates, $\dot{M}$, measured at $r = 100$km are depicted in Fig. 5.2. After the onset of collapse, $\dot{M}$ first rises rapidly, reaching $\sim 100{\rm M}_\odot$/s at maximum, and then drops rather quickly to $\sim 1{\rm M}_\odot$/s. The entire core shrinks to $r \leq 100$km at around the peak time, which roughly corresponds to the core-bounce time in realistic simulations and hence which we refer to as the bounce time in the following. The mass accretion rates decay more gradually thereafter with a few discernible steps, which correspond to the passages of layer boundaries. These behaviors are qualitatively consistent with Buras et al.(2006) [46] and Suwa et al.(2016) [414] as well as the previous

section.

It is interesting to point out that if we horizontally shift the curves of $\dot{M}$ for the models with different core masses but with the same Si+S mass so that the bounce times should coincide with each other, then the entire curves also agree rather well with each other as demonstrated in the right panels of Fig. 5.2, except that the steps occur at different post-bounce times. Comparing models with different $M_{\rm SiS}$ but with the same M_c, we find that the outer boundary of Si+S+O layer reaches $r = 100$km almost at the same post-bounce time irrespective of $M_{\rm SiS}$ although the outer edges of Si+S layer arrive at different times. This is mainly due to the fact that the enclosed mass at the outer boundary of the Si+S+O layer is common. It is interesting that the difference in $M_{\rm SiS}$ is reflected in the accretion of the Si+S layer alone, not affecting the infall of outer layers.

Note, in particular, that the mass accretion rates are nearly the same when the Si+S+O layer falls onto the radius of $r = 100$km, which occurs during the periods post bounce of $t_{pb} \sim 200 - 500$ms and $t_{pb} \sim 300 - 500$ms for the models with $M_{\rm SiS} = 0.09{\rm M}_\odot$ and with $M_{\rm SiS} = 0.18{\rm M}_\odot$, respectively (see the right panels of Fig. 5.2).

This fact can be understood as follows. Since matter is falling nearly freely, i.e., $v_r \propto (GM_r/r)^{1/2}$, the Lagrangian change in density is given by the mass conservation equation as

$$\begin{aligned} \frac{1}{\rho}\frac{D\rho}{Dt} &= -\frac{1}{r^2}\frac{\partial}{\partial r}\left(r^2 v_r\right), \\ &= \alpha\frac{v_r}{r}, \end{aligned} \tag{5.7}$$

in which α is expressed as

$$\alpha = \left(\frac{\partial \ln M_r}{\partial \ln r} - 1.5\right) \sim -1.35. \tag{5.8}$$

Here we have made use of the following evaluation,

$$\frac{\partial \ln M_r}{\partial \ln r} \sim \frac{R_c}{M_c}\frac{M_{Si}}{R_{Si}} \sim \frac{M_{Si}}{M_c} \lesssim 0.15. \tag{5.9}$$

$$\tag{5.10}$$

Using $v_r = Dr/Dt$, we integrate Eq. (5.7) to obtain

$$\rho(r) = \rho_0\left(\frac{r}{r_0}\right)^\alpha, \tag{5.11}$$

where the initial radius and density are denoted by r_0 and ρ_0, respectively. This equation describes the Lagrangian variation of the density for a particular fluid element, which is originally located at r_0 with the density ρ_0. In principle, the density profile at a give time is different from this Lagrangian variation with r. The latter approximates the former very well, though. In fact, the left panel of Fig. 7 shows with colored thick lines the density profiles of the three models with $M_{\rm SiS}$ at t_{pb}=100ms and 500ms. The progenitor structures are also displayed with thin lines. The colors specify the progenitors. The dotted line, on the other hand, indicates the power of -1.35, the approximate value of α in Eq. (16). It is evident that the density distributions obey the power-law for $r \lesssim 1000$km at t_{pb}=100ms and the region is extended to ~ 2000km at t_{pb}=500ms.

The right panel of Fig. 7 shows the Lagrangian changes in the densities and radii of the mass shells that reach $r = 100$km at $t_{pb} = 100$ms and 500ms. It is found from the

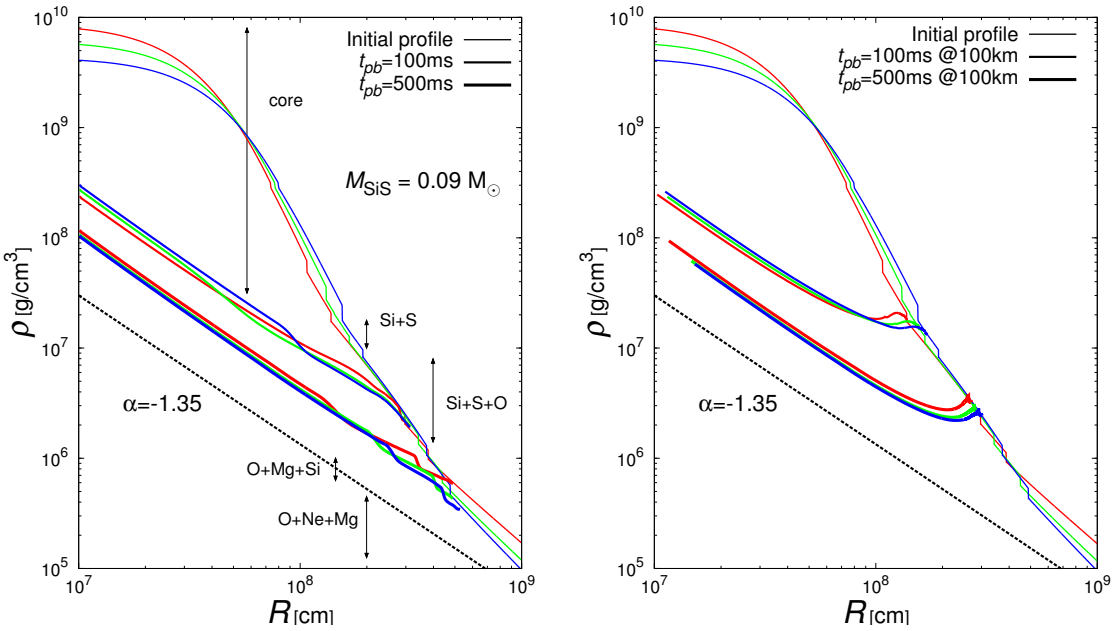

Figure 5.3: The density profiles for $M_{\rm SiS} = 0.09{\rm M}_\odot$ models. The left panel depicts snapshots at $t_{pb} = 100$ms (middle) and $t_{pb} = 500$ms (thick) while the right panel illustrates the mass shell trajectories which falls inside 100km at $t_{pb} = 100$ms (middle) and $t_{pb} = 500$ms (thick). The thin line represent the initial profile in the both panels. The colors show $M_c = 1.30{\rm M}_\odot$ (red), $1.40{\rm M}_\odot$ (green) and $1.50{\rm M}_\odot$ (blue), respectively and the dotted line indicates the power law of $r^{-1.35}$. The arrows in the left panel illustrate initial layer positions for $M_c = 1.50{\rm M}_\odot$.

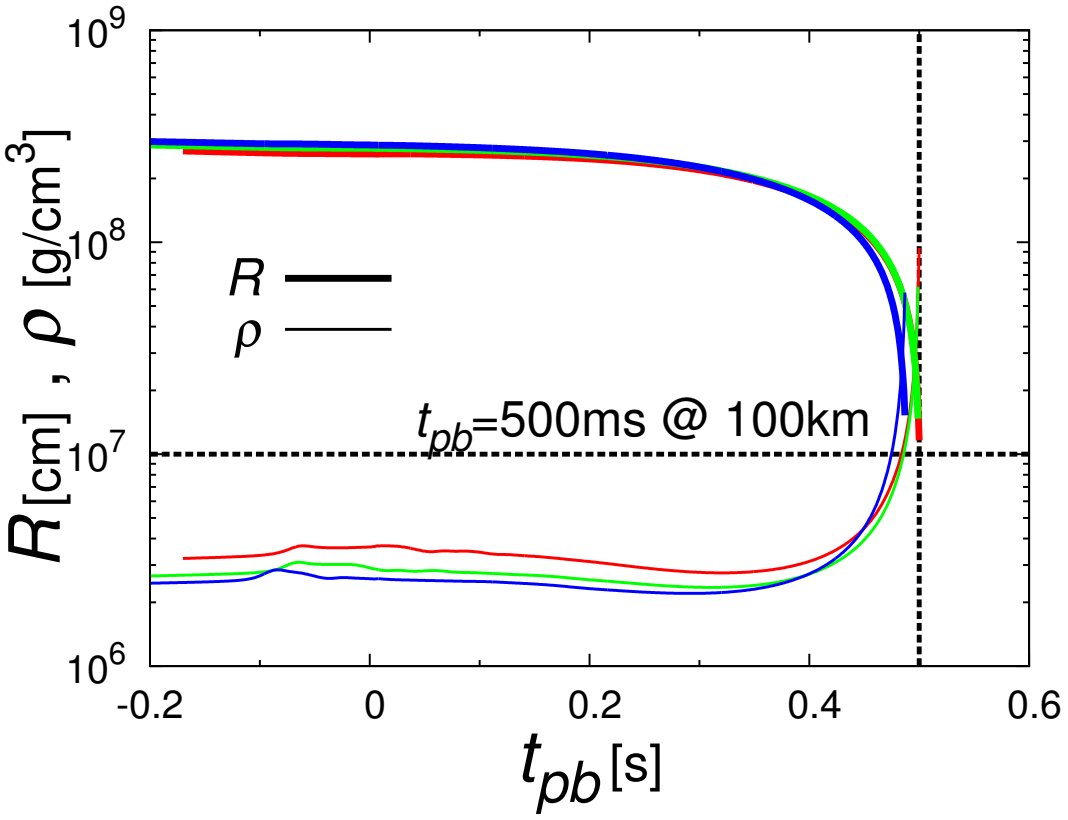

Figure 5.4: The time evolution of mass shells which reach 100km at $t_{pb} = 500$ms for different core models with the same Si+S mass, $M_{\rm SiS} = 0.09{\rm M}_\odot$. The thin and thick solid line represent density and radius, respectively and the colors correspond to core models, $M_c = 1.30{\rm M}_\odot$ (red), $1.40{\rm M}_\odot$ (green) and $1.50{\rm M}_\odot$ (blue).

two panels that the inner edge of the Si+S layer reaches $r = 100$km at t_{pb}=100ms whereas the outer boundary of the Si+S+O layer, which starts to infall at around the same time, arrives at $r = 100$km at t_{pb}=500ms, by which time the rarefaction wave has reached the O+Ne+Mg layer. It is clear from the right panel that as the infall of the mass shells proceeds, all the trajectories approach the power-law as expected. As a matter of fact, they seem to converge in spite of the fact that the density and radii at the start points are substantially different among different models. This is the reason why we obtain the very similar mass accretion rates at the same post-bounce time. Note that this is also the reason why the Eulerian density distribution at a given time is well approximated by the Lagrangian change for a certain mass shell. Although the former is actually given by the collection of the endpoints for different Lagrangian evolutions, these Lagrangian evolutions are close to each other owing to the above convergence property.

Figure 8 shows the temporal evolutions of the densities and radii of the mass shells that reach $r = 100$km at t_{pb}=500ms. As can be seen, these quantities do not change very much initially, and it is for the last 100ms during 700ms of excursions that the free fall is fully established and the density and radius change rather rapidly according to Eq.(20). Such a behavior may be the main reason for the convergence we have seen above. No doubt we need a larger number of models including those from groups L and H to judge how generic these findings are, since diverse accretion histories have been reported in the literature [414].

In reality, however, the accretion does not occur steadily and the free fall is a rough approximation to the actual matter velocities. In addition, α in Eq. (5.7) is not constant either in space or in time. As a result, the accretion histories are not the same completely among these models but the agreement is still remarkable and will be useful in analyzing the influences of the mass accretion history on the shock revival and subsequent evolutions. Note in particular the difference in the positions of the steps in the mass accretion rate as a function of time (see Fig. 5.2), which are produced by the passage of boundaries between different layers. This is a direct consequence of the different masses of Fe core and Si+S layer. As discussed later, it is reflected in the shape of the critical curve.

Table 5.2: The list of the steady solution properties at $t_{pb} = 300$ms in different neutrino luminosity.

model [a]	$\dot{M}$ $[M_\odot/\mathrm{sec}]$	M_g [b] $[M_\odot]$	R_g [c] [cm]	R_{sh} [d] [cm]	M_{PNS} [e] $[M_\odot]$
1.3S09Lnu2.0	5.20E-01	6.67E-03	8.61E+06	1.38E+07	1.49E+00
1.4S09Lnu2.0	4.94E-01	5.86E-03	8.56E+06	1.36E+07	1.56E+00
1.5S09Lnu2.0	5.13E-01	4.71E-03	8.43E+06	1.28E+07	1.65E+00
1.3S18Lnu2.0	4.47E-01	7.58E-03	8.79E+06	1.50E+07	1.50E+00
1.4S18Lnu2.0	4.50E-01	6.21E-03	8.64E+06	1.42E+07	1.58E+00
1.5S18Lnu2.0	4.71E-01	4.92E-03	8.48E+06	1.33E+07	1.66E+00
1.3S09Lnu2.3	5.20E-01	8.71E-03	8.84E+06	1.51E+07	1.48E+00
1.4S09Lnu2.3	4.94E-01	7.58E-03	8.75E+06	1.48E+07	1.56E+00
1.5S09Lnu2.3	5.13E-01	5.99E-03	8.55E+06	1.38E+07	1.64E+00
1.3S18Lnu2.3	4.47E-01	1.02E-02	9.09E+06	1.68E+07	1.49E+00
1.4S18Lnu2.3	4.50E-01	8.15E-03	8.86E+06	1.56E+07	1.58E+00
1.5S18Lnu2.3	4.71E-01	6.30E-03	8.61E+06	1.44E+07	1.66E+00
1.3S09Lnu2.5	5.20E-01	1.05E-02	9.04E+06	1.62E+07	1.48E+00
1.4S09Lnu2.5	4.94E-01	9.11E-03	8.91E+06	1.59E+07	1.56E+00
1.5S09Lnu2.5	5.13E-01	7.04E-03	8.66E+06	1.46E+07	1.64E+00
1.3S18Lnu2.5	4.47E-01	1.28E-02	9.34E+06	1.84E+07	1.49E+00
1.4S18Lnu2.5	4.50E-01	9.88E-03	9.05E+06	1.68E+07	1.57E+00
1.5S18Lnu2.5	4.71E-01	7.45E-03	8.75E+06	1.52E+07	1.66E+00

[a]The model names is consisted of core mass, type of Si+S mass and luminosity in order.
[b]Mass inside the gain region.
[c]Radius at gain region.
[d]Radius at shock front.
[e]The enclosed mass inside the inner boundary.

5.3.2 Critical Luminosity and Diagnostic Explosion Energy: Steps 3 & 4

To explore the shock revival by neutrino heating and the subsequent evolution with hydrodynamical simulations in 1D and 2D, we first construct spherically symmetric, steady, shocked accretion flows for initial conditions (Step 3 in section 5.2). They are characterized by three parameters, i.e., the mass accretion rate, neutrino luminosity and mass of PNS. As for the first and third parameters, we adopt the values obtained in the computations of the accretion histories in Step 2 at $t_{pb} = 300$ms. We have three options for the second parameter, i.e., the neutrino luminosity, on the other hand: $L_\nu = 2.0, 2, 3, 2.5 \times 10^{52}$erg/s, or $L_{\nu,52} = 2.0, 2.3, 2.5$, which are applied to each of the 6 progenitor models constructed in Step 1. The properties of these 18 shocked accretion flows are summarized in Table 5.2. Fig. 5.5 shows the entropy distributions for some models and illustrates their dependences on some model parameters such as the masses of Fe core and Si+S layer and neutrino luminosity. As known well, the stalled shock expands as the neutrino luminosity increases (see the left panel). It also occurs when the mass accretion rate is reduced as is the case for the doubled mass of the Si+S layer (see the right panel and the second column in Table 5.2). For larger core masses, the gravitational attraction gets greater, reducing the shock radius

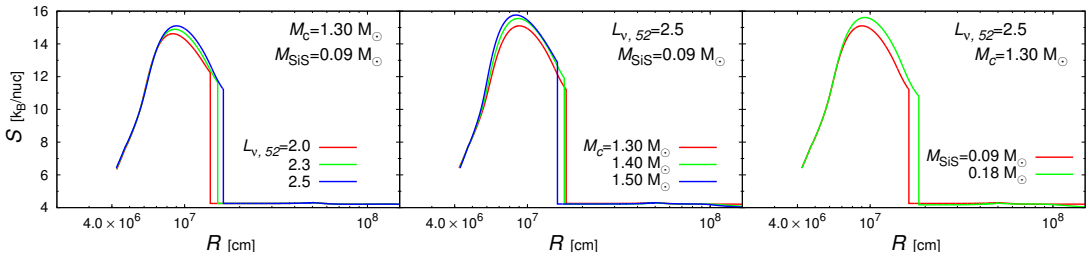

Figure 5.5: The entropy distributions of steady shock solution at t_{pb} = 300ms. The left panel : The three different luminosities with M_c = 1.30 and $M_{\rm SiS}$ = 0.09. Each colors show $L_{\nu,52}$ = 2.0 (red), $L_{\nu,52}$ = 2.3 (green) and $L_{\nu,52}$ = 2.5 (blue). The middle panel : The three different core masses with $M_{\rm SiS}$ = 0.09 and $L_{\nu,52}$ = 2.5. Each colors illustrate M_c = 1.30 (red), M_c = 1.40 (green) and M_c = 1.50 (blue). The right panel : The two different Si+S masses with M_c = 1.30 and $L_{\nu,52}$ = 2.5. Each colors depict $M_{\rm SiS}$ = 0.09 (red) and $M_{\rm SiS}$ = 0.18 (green).

(see the central panel). Note that the neutrino spheric radius is not linked to the core mass in our model, the neutrino luminosity is independent of the Fe core mass.

Using all of these 18 models as initial conditions, we run simulations, assuming spherical symmetry. We also conduct 2D computations for 8 models, which generate robust explosions in 1D. In these simulations we employ in the region outside the stalled shock wave the profiles of the accreting envelopes at t_{pb} = 300ms, which were obtained in the calculations of the accretion histories in Step 2. As a result of this, the mass accretion rate varies in time. We keep the neutrino luminosity constant in time until shock revival occurs. Once it occurs, we allow the neutrino luminosity to evolve in time according to Eq. 5.6. The results are summarized in Table 5.3, which will be used frequently later for discussion. In this table the mass accretion rates at the shock revival, $\dot{M}_{\rm rev}$, are sampled at r = 400km and are essentially the same as those on the shock front. The diagnostic explosion energy, which is denoted by E_{exp}, is defined as

$$E_{exp} = \sum_{v_r>0,\ e_{tot}>0} e_{tot}\ \Delta V, \tag{5.12}$$

in which the total energy density, e_{tot}, is given by the sum of kinetic (e_{kin}), internal (e_{int}) and gravitational (e_{grav}) energy densities as

$$e_{tot} = e_{kin} + e_{int} + e_{grav}; \tag{5.13}$$

the summation in Eq. (5.12) extends over the grid points with positive radial velocities, v_r, and total energy densities; ΔV stands for the cell volumes for these grid points. Note that the rest mass energy is not included in the internal energy in the above definition. The diagnostic energy is also used in judging shock revival: we consider that the stalled shock wave revives if the diagnostic energy reaches 10^{48}erg.

Table 5.3: Summary of the Explosion results in 1D and 2D.

Model	E_{exp} [foe]	M_{Ni} [$M_\odot$]	$t_{\rm rev}$ [a] [sec]	M_{PNS} [$M_\odot$]	$\dot{M}_{\rm rev}$ [b] [$M_\odot$/s]
1D					
1.3S09Lnu2.0	8.40E-01	8.80E-02	7.40E-01	1.68E+00	3.09E-01
1.4S09Lnu2.0	6.70E-01	7.00E-02	8.30E-01	1.78E+00	2.54E-01
1.5S09Lnu2.0	4.40E-01	4.95E-02	1.00E+00	1.91E+00	2.16E-01
1.3S18Lnu2.0	7.50E-01	7.50E-02	6.00E-01	1.62E+00	2.77E-01
1.4S18Lnu2.0	5.30E-01	5.70E-02	7.00E-01	1.73E+00	2.22E-01
1.5S18Lnu2.0	4.20E-01	4.67E-02	7.90E-01	1.85E+00	1.92E-01
1.3S09Lnu2.3	1.22E+00	1.08E-01	5.70E-01	1.60E+00	3.63E-01
1.4S09Lnu2.3	8.20E-01	9.05E-02	6.40E-01	1.72E+00	3.18E-01
1.5S09Lnu2.3	6.10E-01	7.20E-02	7.80E-01	1.85E+00	2.48E-01
1.3S18Lnu2.3	1.37E+00	1.09E-01	4.30E-01	1.54E+00	4.06E-01
1.4S18Lnu2.3	1.13E+00	9.10E-02	4.70E-01	1.64E+00	3.60E-01
1.5S18Lnu2.3	8.14E-01	7.20E-02	7.00E-01	1.78E+00	3.01E-01
1.3S09Lnu2.5	1.64E+00	1.49E-01	4.40E-01	1.51E+00	4.64E-01
1.4S09Lnu2.5	1.43E+00	1.22E-01	4.80E-01	1.63E+00	4.27E-01
1.5S09Lnu2.5	7.30E-01	8.40E-02	6.70E-01	1.82E+00	3.10E-01
1.3S18Lnu2.5	1.40E+00	1.24E-01	3.70E-01	1.52E+00	4.32E-01
1.4S18Lnu2.5	1.45E+00	9.60E-02	4.30E-01	1.61E+00	3.83E-01
1.5S18Lnu2.5	1.07E+00	9.40E-02	4.70E-01	1.73E+00	3.66E-01
2D					
1.3S09Lnu2.0	8.96E-01	3.95E-02	6.16E-01	1.63E+00	3.30E-01
1.4S09Lnu2.0	7.60E-01	6.08E-02	6.40E-01	1.72E+00	3.10E-01
1.3S18Lnu2.0	9.70E-01	3.45E-02	5.34E-01	1.60E+00	3.51E-01
1.4S18Lnu2.0	7.46E-01	4.03E-02	5.25E-01	1.72E+00	3.10E-01
1.3S09Lnu2.3	1.55E+00	1.01E-01	4.07E-01	1.53E+00	4.72E-01
1.4S09Lnu2.3	1.46E+00	1.08E-01	3.95E-01	1.61E+00	4.69E-01
1.3S18Lnu2.3	1.24E+00	7.71E-02	4.40E-01	1.50E+00	4.00E-01
1.4S18Lnu2.3	1.14E+00	6.27E-02	4.71E-01	1.64E+00	3.60E-01

[a] The shock revival time measured from post bounce.

[b] The mass accretion rate at $t_{\rm rev}$

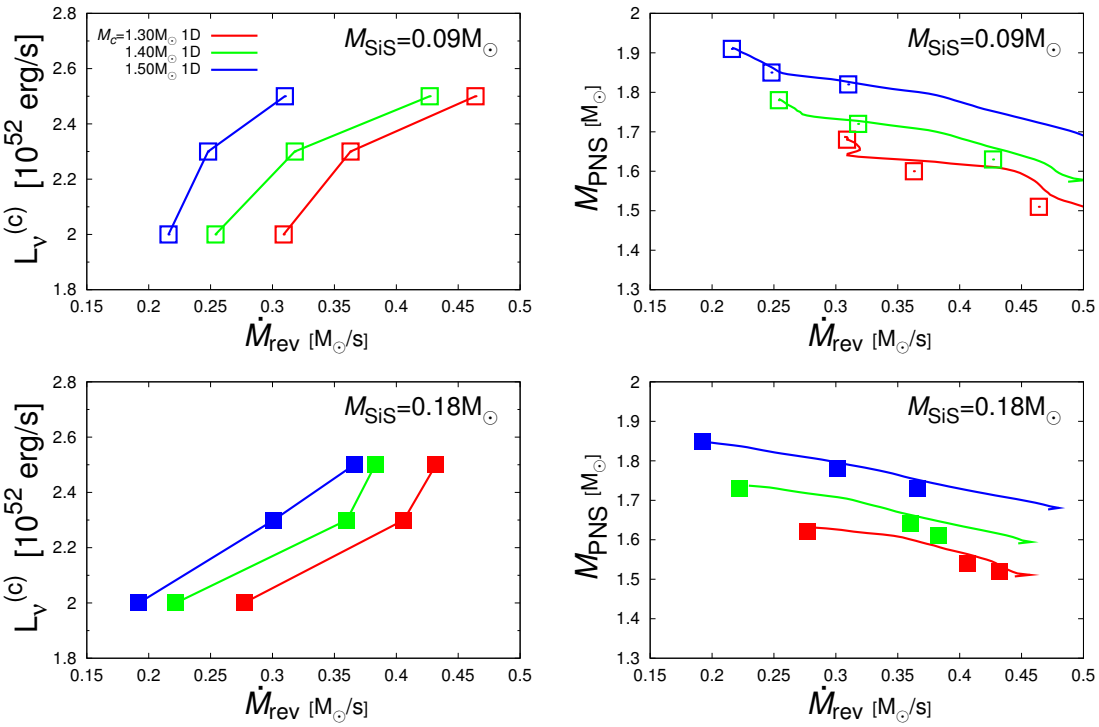

Figure 5.6: Critical luminosity curves and PNS mass evolutions. The left panel shows $\dot{M}$-L_ν relation which is called (the critical luminosity curves). $\dot{M}$ is measured at 400km. The right panels depict $\dot{M}$-M_{PNS} map which imply time evolution of M_{PNS}. The solid line trajectories are from $L_\nu = 2.0$ models and points indicate final masses of M_{PNS}. The colors used in every model prescribe different core mass models, $M_c = 1.30$ (red), $M_c = 1.40$ (green) and $M_c = 1.50$ (blue). The symbols also describe different Si+S layer mass, $M_{\rm SiS} = 0.09$ (open square) and $M_{\rm SiS} = 0.18$ (filled square). The lighter $M_{\rm SiS}$ models are shown in the top panels whereas the higher in the bottom panels.

Critical luminosity

The luminosities, mass accretion rates as well as PNS mass at shock revival are presented in Fig .5.6 for the 18 spherical models. The upper panels display the results for the models with $M_{\rm SiS} = 0.09{\rm M}_\odot$ whereas the lower panels are the counter parts for the models with $M_{\rm SiS} = 0.18{\rm M}_\odot$. The left panels exhibit the so-called critical curves, in which the neutrino luminosity at shock revival is regarded as a function of the mass accretion rate at the same time, $\dot{M}_{\rm rev}$. It is evident that critical luminosity is a monotonically increasing function of the mass accretion rate, which is consistent with other studies [291, 317, 153, 77, 194]. It is interesting to point out that the curve is upward convex for the models with $M_{\rm SiS} = 0.09{\rm M}_\odot$ while it is downward convex for the models with $M_{\rm SiS} = 0.18{\rm M}_\odot$. This is related with the locations of layer boundaries, at which the mass accretion rate decreases rapidly, and will be discussed more in detail shortly below. It is also clear that the larger the core mass is, the higher the critical luminosity is, since the gravitational binding becomes stronger.

In the right panels of Fig. 5.6, we give the trajectories of the mass accretion rate and PNS mass for different masses of Fe core and Si+S layer. As the time passes, the mass accretion rate gets lowered while the PNS mass becomes larger. Note that the mass accretion rates measured at $r = 400$km are independent of the neutrino luminosities. The points, at

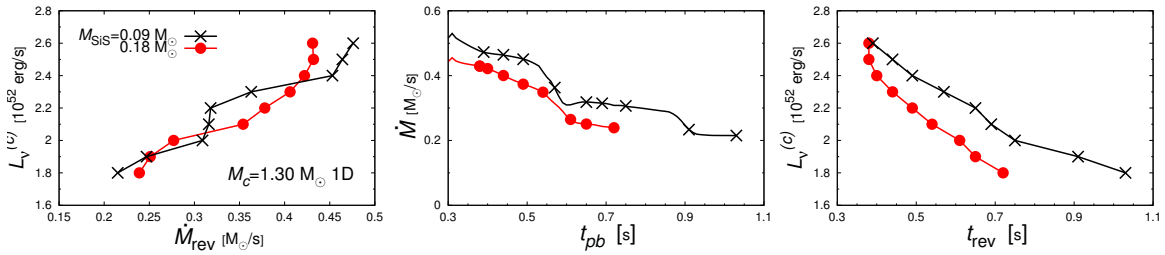

Figure 5.7: The high resolution L_ν outcomes for the two $M_c = 1.30\mathrm{M}_\odot$ models. Each panel demonstrates critical luminosities (left panel), the history of $\dot{M}$ (middle) and $L_\nu^{(c)}$ as a function of $t_{\rm rev}$ (right). Open and filled symbols represent $M_{\rm SiS} = 0.09$ (upper panels) and $0.18\mathrm{M}_\odot$ (lower panels) models, respectively.

which shock revival occurs for the 18 models, are marked with squares in the figure. As the luminosity decreases, shock revival is delayed and, as a result, the mass accretion rate becomes lower. Note that the positions of the squares are slightly off the trajectories. In fact, we employ the PNS masses at the end of simulations instead of those at shock revival in plotting these squares. Hence their vertical deviations from the trajectories indicate the masses gained or lost by PNS owing to the inflow or outflow of matter through the inner boundary after shock revival. In the 1D case, the mass is always lost, since the outflow is dominant via neutrino winds. This is not always the case in 2D as shown later, in which the neutrino-driven wind occurs more strongly.

In order to better understand the differences in the shape of the critical curves, we conducted additionally nine 1D simulations with $L_{\nu,52} = 1.8 - 2.6$ for the progenitor model with $M_c = 1.3\mathrm{M}_\odot$. Figure 11 shows the critical curves (left panel), the temporal evolutions of mass accretion rates (middle panel) and the critical luminosities as functions of the shock revival time (right panel). First of all, it is evident from the left panel that the convexity of critical curve changes as the shock revival time varies, i.e., each critical curve has portions that are upward- or downward convex. The comparison between the left and middle panels makes it clear that a plateau in the critical curve corresponds to a cliff in the curve of mass accretion rate (see, e.g., the model with $L_{\nu,52} = 2.3$ for $M_{\rm SiS} = 0.09$) and vice versa. The reason why the data points are sparse on the plateau and dense at cliff on the critical curve is simply because the duration of the plateau phase is shorter. As mentioned earlier, the mass accretion rate is lower for the model with $M_{\rm SiS} = 0.18\mathrm{M}_\odot$ than for the model with $M_{\rm SiS} = 0.09\mathrm{M}_\odot$ (see also the middle panel of Fig. 11). As a result, for a given neutrino luminosity shock revival tends to occur earlier for the former. Note that the shock radius is also larger from the beginning for the same model.

We find from the left and middle panels of Fig.11 that some models have almost the same mass accretion rate but have substantially different critical luminosities: e.g. the models with $L_{\nu,52} = 2.0, 2.1, 2.2$ for $M_{\rm SiS} = 0.09\mathrm{M}_\odot$. In order to understand this situation, we plot in Fig. 12 the time evolutions of the width $R_{sh} - R_g$ (top panel) and the mass M_g (middle panel) of the gain region as well as the mass accretion rates (bottom panel) as functions of time for these three models. From the top and middle panels it is apparent that shock revival occurs as a consequence of the growth of overstabilizing oscillations, which is consistent with previous papers (Ohnishi et al. and Fernand-Rodriguez). The instability is triggered by the passage of the boundary between the Si+S+O layer and the

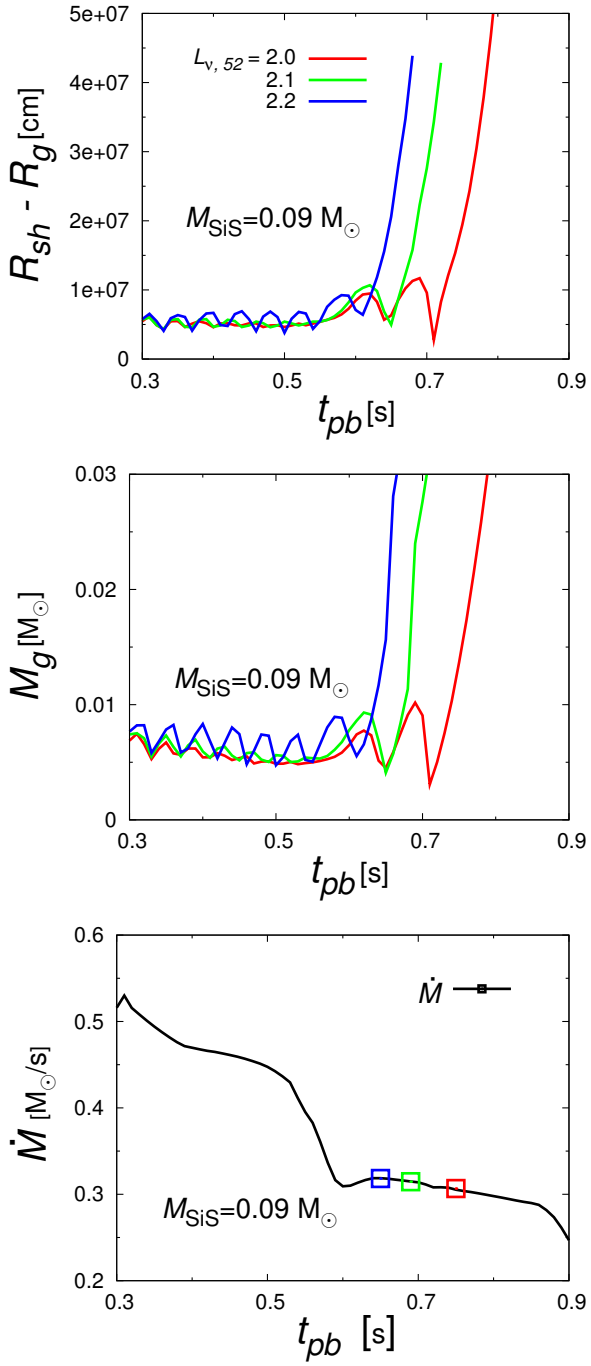

Figure 5.8: The time evolutions of $R_{sh} - R_g$ (top), M_g (middle) and $\dot{M}$ (bottom) in the part of plateau structure of the critical curve. Each color of lines and symbols corresponds to $L_{\nu,52} = 2.0$ (red), 2.1 (green) and 2.2 (blue), respectively.

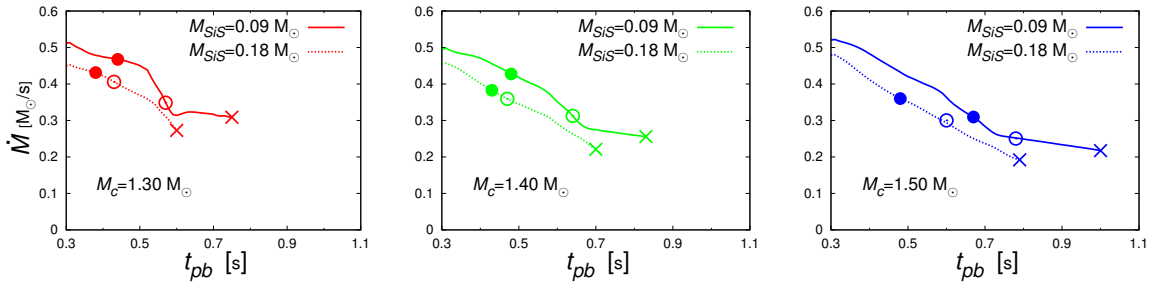

Figure 5.9: The mass accretion histories for 6 toy presupernova stages. The colors show the different core types, $M_c = 1.30$ (red), 1.40 (green) and 1.50M$_\odot$ (blue), whereas the line types correspond to $M_{\rm SiS} = 0.09$ (solid) and 0.18M$_\odot$ (dotted), respectively. The symbols illustrate the different neutrino luminosities at the shock revival time, $L_{\nu,52} = 2.5$ (filled circle), 2.3 (open circle) and 2.0 (cross).

O+Mg+Si layer at $t_{pb} \sim 550ms$. The important point is that the mass accretion rate changes by the passage of the layer boundary much more quickly than the shock radius does by the oscillations. This means that these three models become supercritical and hence unstable instantaneously by the passage of the layer boundary. It is also apparent that the difference in the shock revival time simply reflects the difference in the oscillation periods and growth times, which are longer for smaller neutrino luminosiities as shown by Yamasaki and Yamada (2007). Since the mass accretion rates change very slowly after the passage of the layer boundary, these models have almost identical accretion rates at shock revival.

In Fig. 13 we plot the time evolutions of the mass accretion rates and the shock revival points for the three core masses: $M_c = 1.30$M$_\odot$ (left panel), 1.40M$_\odot$ (middle panel) and 1.50M$_\odot$ (right panel). It is evident from these plots that shock revival is delayed for more massive iron cores. This is simply because of the stronger gravitational attraction. As mentioned above, the higher mass accretion rates for the model with $M_{\rm SiS} = 0.09$M$_\odot$ leads to the fact that it obtains shock revival later than the model with $M_{\rm SiS} = 0.18$M$_\odot$ irrespective of the core mass. It may be interesting to see for the highest luminosity ($L_{\nu,25} = 2.5$) case in the model with $M_{\rm SiS} = 0.09$M$_\odot$ that shock revival occurs before the passage of the boundary between the Si+S+O layer and the O+Mg+Si layer for the lighter cores with $M_c = 1.30$M$_\odot$ and 1.40M$_\odot$ whereas it happens during the passage for the heaviest core with $M_c = 1.50$M$_\odot$. As a result, the mass accretion rate at shock revival becomes smaller in this case than the counter part in the model with $M_{\rm SiS} = 0.18$M$_\odot$. In fact, the layer boundary is located at a larger radius in the latter progenitor model and shock revival occurs before its passage even for the heaviest core mass, which is also the reason why the critical curve is almost straight in this case.

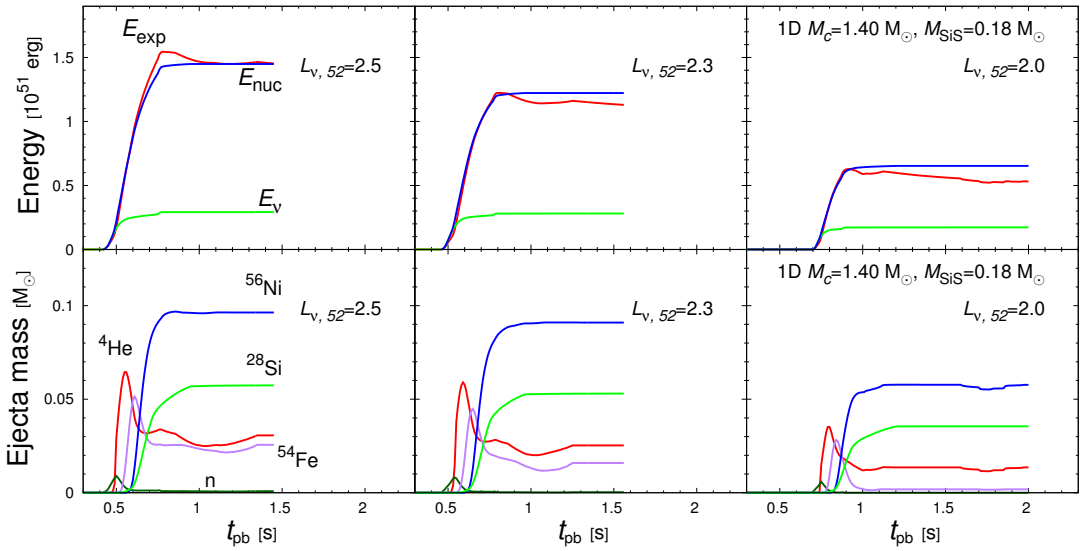

Figure 5.10: The time evolution of energies and ejecta masses forM_c = 1.40M$_\odot$ with $M_{\rm SiS}$ = 0.18M$_\odot$. The top panels : The time evolutions of a diagnostic explosion energy (red line), nuclear source (blue line) and neutrino source (green line). The bottom panels : The time evolutions of ejecta masses for α (red line), ^{56}56 (blue line), ^{28}Si (green line), ^{54}Fe (purple) and neutron (dark-green). The neutrino luminosities are chosen as L_ν =2.5 (left panel), 2.3 (middle panel) and 2.0 (right panel) $\times 10^{52}$erg/s, respectively.

Explosion energy and nickel mass

We turn attention to the explosion energies and Ni yields in the 1D models, which are summarized in the second and third columns in Table 5.3. For fixed masses of Fe core and Si+S layer, both the explosion energy and the mass of synthesized Ni monotonically decrease as the neutrino luminosity is reduced. This is consistent with the findings in the previous chapter This is a consequence of the delay of shock revival for lower neutrino luminosities (see the fourth column in the table), which results in turn in smaller mass accretion rates (the last column of the table).

In Figs. 5.10 - 5.12 presented are the time evolutions of these quantities. We show in addition the energies gained by neutrino heating, E_ν, and produced by recombinations and nuclear burnings, E_{nuc}, as well as the yields of some major elements as functions of time. The former two are evaluated, respectively, as

$$E_{nuc} = \sum_{v_r>0,\, e_{tot}>0} Q_{nuc}^{(n)}\, \Delta V\, \Delta t^{(n)}, \tag{5.14}$$

$$E_{\nu} = \sum_{v_r>0,\, e_{tot}>0} Q_{\nu}^{(n)}\, \Delta V\, \Delta t^{(n)}, \tag{5.15}$$

where $\Delta t^{(n)}$ is the time interval of the n-th time step in the simulations and $Q_{nuc}^{(n)}$ and $Q_{\nu}^{(n)}$ are the local energy production rates via the nuclear reactions and neutrino heating rate, respectively; the summation runs over the same grid points in Eq. (5.12).

We first compare the results for different neutrino luminosities, which are shown in Fig. 5.10. In the top panel the temporal changes of the energies given above are displayed for

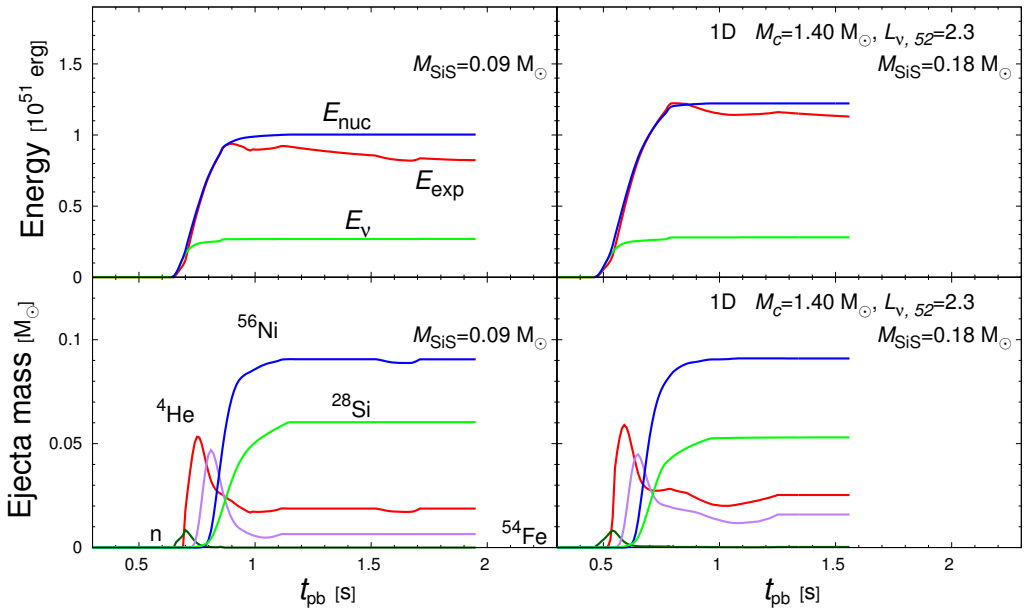

Figure 5.11: Same as figure.5.10 but illustrating different Si+S layer masses with $M_c = 1.40\mathrm{M}_\odot$ and $L_{\nu,52} = 2.3$.

the models with the Fe core mass of $M_c = 1.40\mathrm{M}_\odot$ and Si+S layer mass of $M_{\mathrm{SiS}} = 0.18\mathrm{M}_\odot$. In the bottom panels, on the other hand, the mass yields of ^{56}Ni, ^{54}Fe, ^{28}Si, ^{4}He and free neutron are presented. It is found from the top panels that lower luminosities delay shock revival indeed and result in smaller explosion energies. The same is true of the nickel mass yield, as is also evident from the bottom panels. The diagnostic explosion energy, E_{exp}, increases mainly by the nuclear energy releases from the recombinations to ^{4}He and heavier elements at first and via the nuclear burnings later. The later slow decline in the diagnostic explosion energy is caused by the engulfing of gravitationally bound envelopes and by some fall backs. Rather small contributions from neutrino heating are deceptive. It should be noted in fact that these energies are calculated only after shock revival. Most of the energy given by neutrino heating is consumed to lift matter up from the gravitational well and make it ready for expansion, which is not included in the evaluation of E_{exp}, however.

The productions of ^{4}He followed by ^{54}Fe and then ^{56}Ni are due to the recombinations while ^{28}Si is mainly synthesized by oxygen burnings. The difference in the final yield of ^{54}Fe contributes considerably to the difference in E_{nuc}. It is also seen that not all ^{4}He is consumed to assemble heavier elements and the so-called α-rich freeze-out takes place. This sequence of events are essentially the same as those we found in the previous chapter. It is mentioned that the wind contribution to E_{exp} is sometimes non-negligible and is the main reason why E_{nuc} is asymptotically larger than E_{exp} in some cases and smaller in others. We will comeback to this issue in section 5.3.2 and 5.3.3.

It is interesting to point out that the times of shock revival, t_{rev}, are not much apart between the models with $L_\nu = 2.5 \times 10^{52}$erg and 2.3×10^{52}erg but the explosion energies are substantially different. This corresponds to what we saw in the critical curve for the models with $M_{\mathrm{SiS}} = 0.18\mathrm{M}_\odot$ (the lower left panel of Fig. 5.6): the critical luminosities are different for not-so-different mass accretion rates.

Models with different Si+S layer masses are compared in Fig. 5.11, in which the core

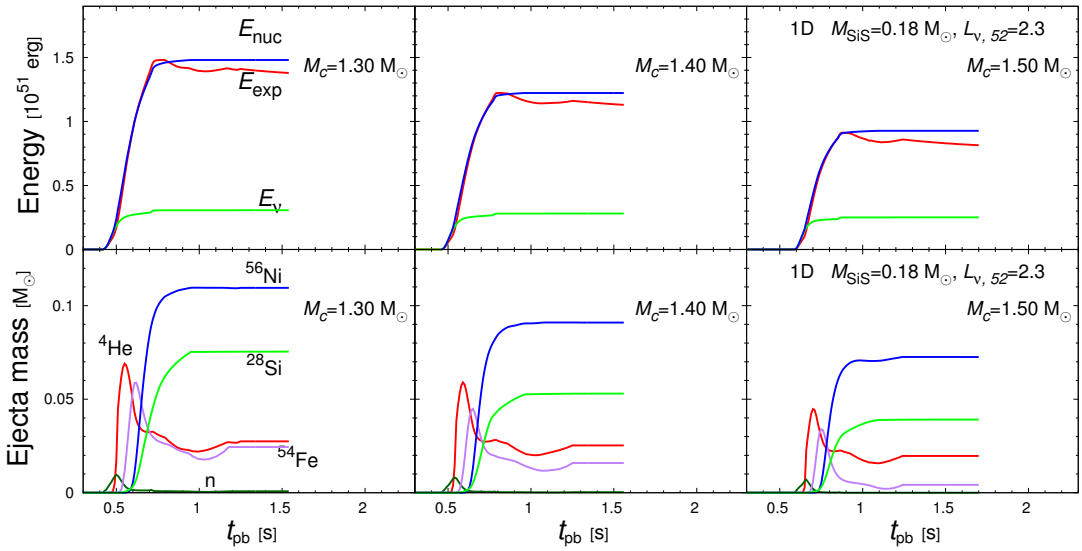

Figure 5.12: Same as figure.5.10 but illustrating different initial core masses with $M_{\rm SiS} = 0.18{\rm M}_\odot$ and $L_{\nu,52} = 2.3$.

mass and neutrino luminosity are fixed to $M_c = 1.40{\rm M}_\odot$ and $L_\nu = 2.3{\times}10^{52}$erg, respectively. The higher $M_{\rm SiS}$ induces an earlier and more energetic explosion since the growth rate of radial perturbation is larger than the mass accretion rate time scale. The difference in E_{nuc} reflects the yield of ^{54}Fe as in the previous cases. The synthesized ^{56}Ni are nearly the same between the two models. The PNS is more massive for $M_{\rm SiS} = 0.09{\rm M}_\odot$, reflecting the delay of shock revival in that case. These trends are common to other core mass models (see Table 5.3). For the lower luminosity case ($L_\nu = 2.0 \times 10^{52}$erg/s), on the other hand, shock revival is still delayed for the lighter Si+S layer but the accretion rate at the shock revival is larger for $M_{\rm SiS} = 0.09{\rm M}_\odot$ and, as a consequence, the explosion energy and the nickel yield are both greater for these models than those with $M_{\rm SiS} = 0.18{\rm M}_\odot$. Note that the PNS is still more massive for the delayed shock revival. This happens again because high $\dot{M}_{\rm rev}$ leads to the canonical explosion energy (see detail discussions in the next section and section. 5.3.3). In the higher luminosity models ($L_\nu = 2.5 \times 10^{52}$erg/s), the shock revival time behaves similarly to the first case ($L_\nu = 2.3 \times 10^{52}$erg/s): it is delayed for $M_{\rm SiS} = 0.09{\rm M}_\odot$. The accretion rates and hence the explosion energies and nickel masses are non-monotonic with the Si+S layer mass. In fact, they are larger for $M_{\rm SiS} = 0.09{\rm M}_\odot$ than for $M_{\rm SiS} = 0.18{\rm M}_\odot$ in the models with $M_c = 1.30$ and $1.40{\rm M}_\odot$ whereas the opposite is true for $M_c = 1.50{\rm M}_\odot$ which has already explained in section. 5.3.2.

Models with different core masses are exhibited in Fig. 5.12, in which the neutrino luminosity and the mass of Si+S layer are set to $L_\nu = 2.3$ and $M_{\rm SiS} = 0.18{\rm M}_\odot$, respectively. Robust explosions with $E_{exp} \gtrsim 1.0 \times 10^{51}$erg are obtained for smaller cores ($M_c = 1.30$ and $1.40{\rm M}_\odot$). The yield of ^{56}Ni is also a decreasing function of the core mass. These are common trends shared by other models (except for the model with $M_c = 1.30{\rm M}_\odot$, $M_{\rm SiS} = 0.18{\rm M}_\odot$ and $L_\nu = 2.5 \times 10^{52}$erg/s, in which shock revival occurs very early on ($t_{exp} = 0.37$s) but the explosion energy is a little bit smaller than the model with the heavier core of $M_c = 1.40{\rm M}_\odot$). This may seem to be simply due to the gravitational attractions by the central PNS but there is something more here, which we will discuss in section 5.3.2.

Figure 5.13 summarizes the explosion energies and nickel masses thus obtained in the

E_{exp} - M_{Ni} plane with some observational data taken from Pejcha et al.(2015) [343]. The upper left panel shows all 18 models, illuminating the clear correlation between them, which is well fitted by

$$M_{Ni} \propto E_{exp}^{0.70}. \tag{5.16}$$

This is consistent with our previous findings. It is interesting, however, that the correlation still holds among different M_c and/or $M_{\rm SiS}$ models. The other three panels display the correlation for different neutrino luminosities separately. It is apparent from these results that as the neutrino luminosity becomes lower, the location of data points in the plane shifts roughly from the upper right to the lower left part on the line that expresses the suggested correlation, which implies that the explosions get weaker and the nickel yield becomes smaller. Looking into the individual cases more closely, we find that the models with $L_\nu = 2.0\times10^{52}$erg/s is more strongly correlated whereas the models with higher luminosities have larger dispersions. This is mainly due to larger contributions from the neutrino wind in these models. It is also mentioned that the shock revival for $L_\nu = 2.5 \times 10^{52}$erg/s occurs around the Si/O interface, where $\dot{M}$ changes rapidly.

It has been commonly supposed that the typical explosion of core-collapse supernovae produces $E_{exp} \gtrsim 10^{51}$erg and $M_{Ni} \lesssim 0.1{\rm M}_\odot$ [151, 314, 451, 219, 390]. This corresponds to the lower right quadrant in each panel. It is evident that not many models, actually only three of them, fall in this region. Recent observations (for example, papers listed in Table. 1 in [342]) and their analysis [343] suggest that the explosion energy and the nickel mass are correlated and occupy the region indicated in the figure. It is clear that

This is also reflected in the fact that the fitted line traverses the region only the upper part of this. This means that it is difficult in 1D models to obtain the right combination of explosion energy and ^{56}Ni mass and that 56Ni tends to be overproduced. As demonstrated later the disagreement is resolved in the 2D models, which may be yet another support for the claim that multidimensionality is crucial for explosion.

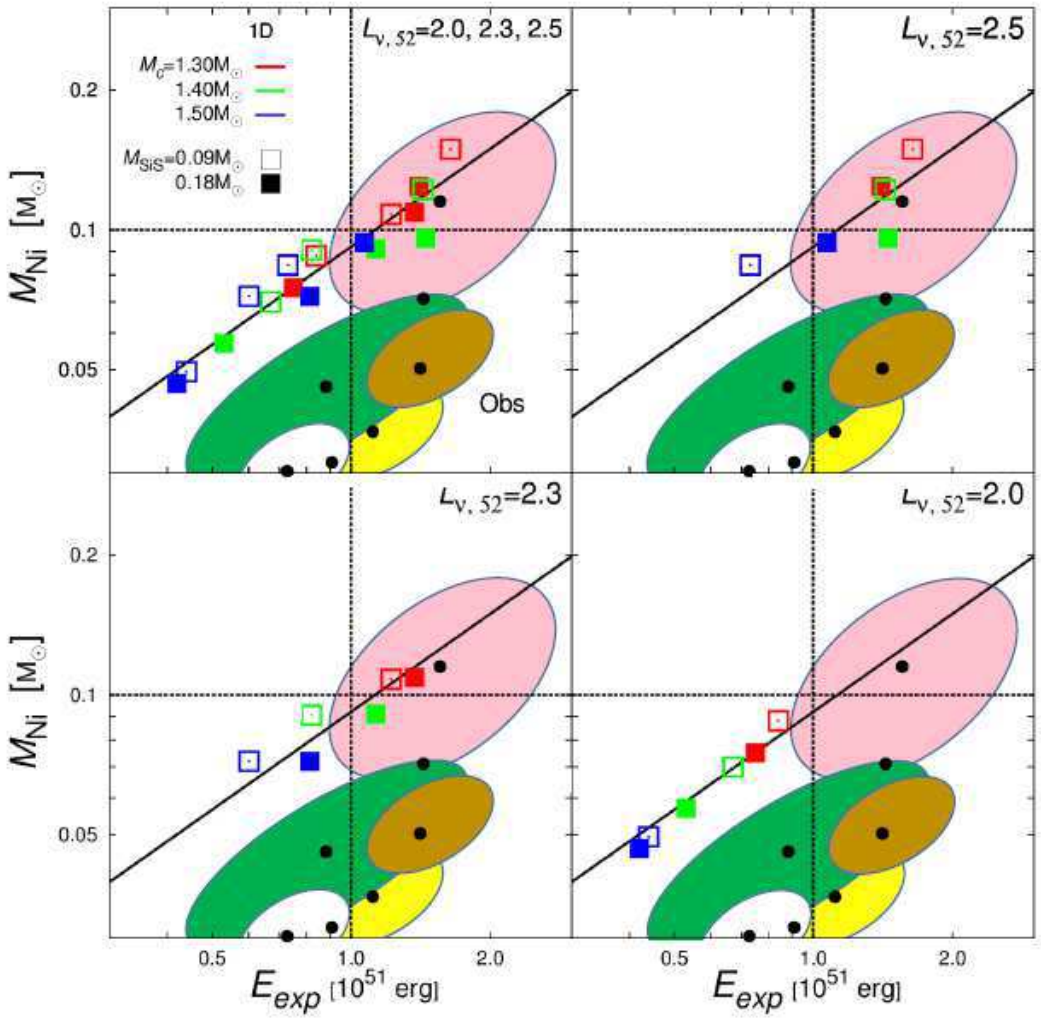

Figure 5.13: The relation between explosion energy and nickel mass. Each panels correspond to the results of $L_{\nu,52} = 2.0, 2.3, 2.5$ (top left panel), $L_{\nu,52} = 2.5$ (top right panel), $L_{\nu,52} = 2.3$ (bottom left panel) and $L_{\nu,52} = 2.0$ (bottom right panel), respectively. The colors used in every model prescribe different core mass models, $M_c = 1.30$ (red), $M_c = 1.40$ (green) and $M_c = 1.50 M_\odot$ (blue). The least-square line for 18 explosion models is indicated in all panels and observation data are reproduced from Pejcha et al.(2015) [343]. The symbols also describe different Si+S layer mass, $M_{\rm SiS} = 0.09$ (open square) and $M_{\rm SiS} = 0.18 M_\odot$ (filled square). The dashed lines are indicators of typical observation values.

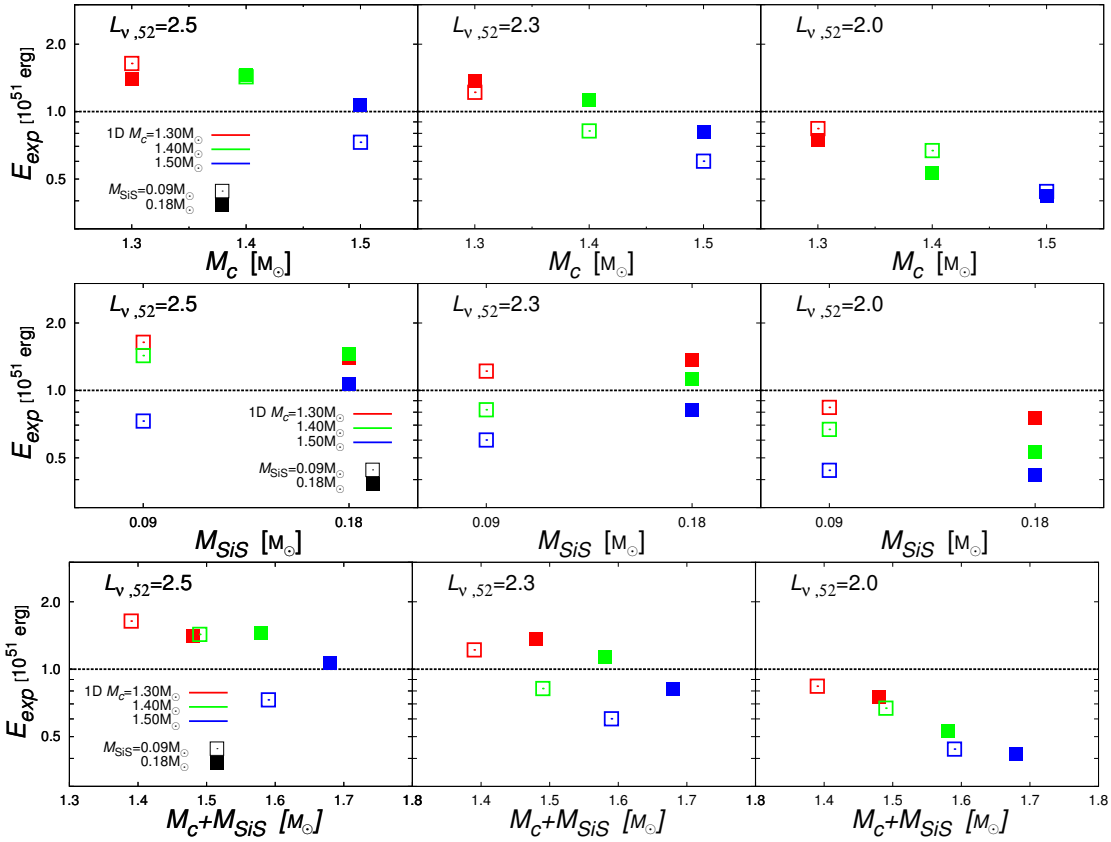

Figure 5.14: The explosion energy as function of initial parameters in 1D. The top, middle and bottom panels show the dependence of M_c, $M_{\rm SiS}$ and $M_c + M_{\rm SiS}$, respectively. The three different luminosity results are in order from the left ($L_{\nu,52} = 2.5$) to the right panels ($L_{\nu,52} = 2.0$). It should be noted that in top left panel the green open square symbols is hidden by the same green filled symbol.

Dependences of explosion energy on model parameters

Now we look into the dependences of the explosion energy on the parameters that characterize the progenitor structures. In Fig. 5.14 we focus on the masses of Fe core and Si+S layer. The top panels show for different neutrino luminosities how the explosion energy is affected by the Fe core mass. We can see clearly the general trend that E_{exp} declines as M_c increases. The dependence on the Si+S layer mass is not so simple, though, as can be inferred from these panels and is directly demonstrated in the middle panels, in which the results are exhibited in the $M_{\rm SiS}$-E_{exp} plane. It seems that there is no clear correlation between the explosion energy and the mass of Si+S layer. All we can find from the figure is the fact that the scatter of E_{exp} is larger in $M_{\rm SiS} = 0.09{\rm M}_\odot$. In the bottom panels we choose as the horizontal axis the sum of the masses of Fe core and Si+S layer. We can then find a similar trend to the Fe core mass but the correlation is much weaker except for the lowest L_ν case.

Much tighter correlation is found, however, if we choose the mass accretion rate at shock revival is adopted, which is demonstrated in the left panels of Fig. 5.15. Each panel

plots for one of the three neutrino luminosities the results for 6 progenitor models. The solid line is the least-square fit to all 18 data points. Given the scatters in Fig. 5.14, it is rather surprising that all the models fall so closely to the line. The correlation is found to be fitted as

$$E_{exp} \propto \dot{M}_{\rm rev}^{1.61}. \tag{5.17}$$

Larger $\dot{M}$ are favorable for strong explosions as long as shock revival occurs. In our 1D models, $\dot{M}_{\rm rev} \gtrsim 0.35 {\rm M}_\odot/{\rm s}$ is required to produce an explosion with $E_{exp} \gtrsim 10^{51}$erg

On the right panels of Fig. 5.15, we examine possible correlations between the explosion energy and the final PNS mass. The solid line is again the least square fit to all data. Although there may be a rough trend that the explosion energy gets smaller as the PNS mass becomes larger, the scatter around the fitting line is not so small. In fact, the following three combinations, $(M_c\,[{\rm M}_\odot], L_{\nu,52}) = (1.50, 2.5), (1.40, 2.3), (1.30, 2.0)$ for $M_{\rm SiS} = 0.09{\rm M}_\odot$, give almost the same E_{exp} although the PNS masses are substantially different among them. They have almost same mass accretion rates at shock revival, on the other hand. It should be noted that although larger PNS masses generate stronger gravitational attraction and are not favorable for shock revival in this respect, they are often a consequence of greater mass accretion rates, which are favorable for robust explosions. These competing effects result in the non-monotonic behavior of the explosion energy vs PNS mass. It is hence better to consider the influence of the PNS mass on E_{exp} only through $\dot{M}$.

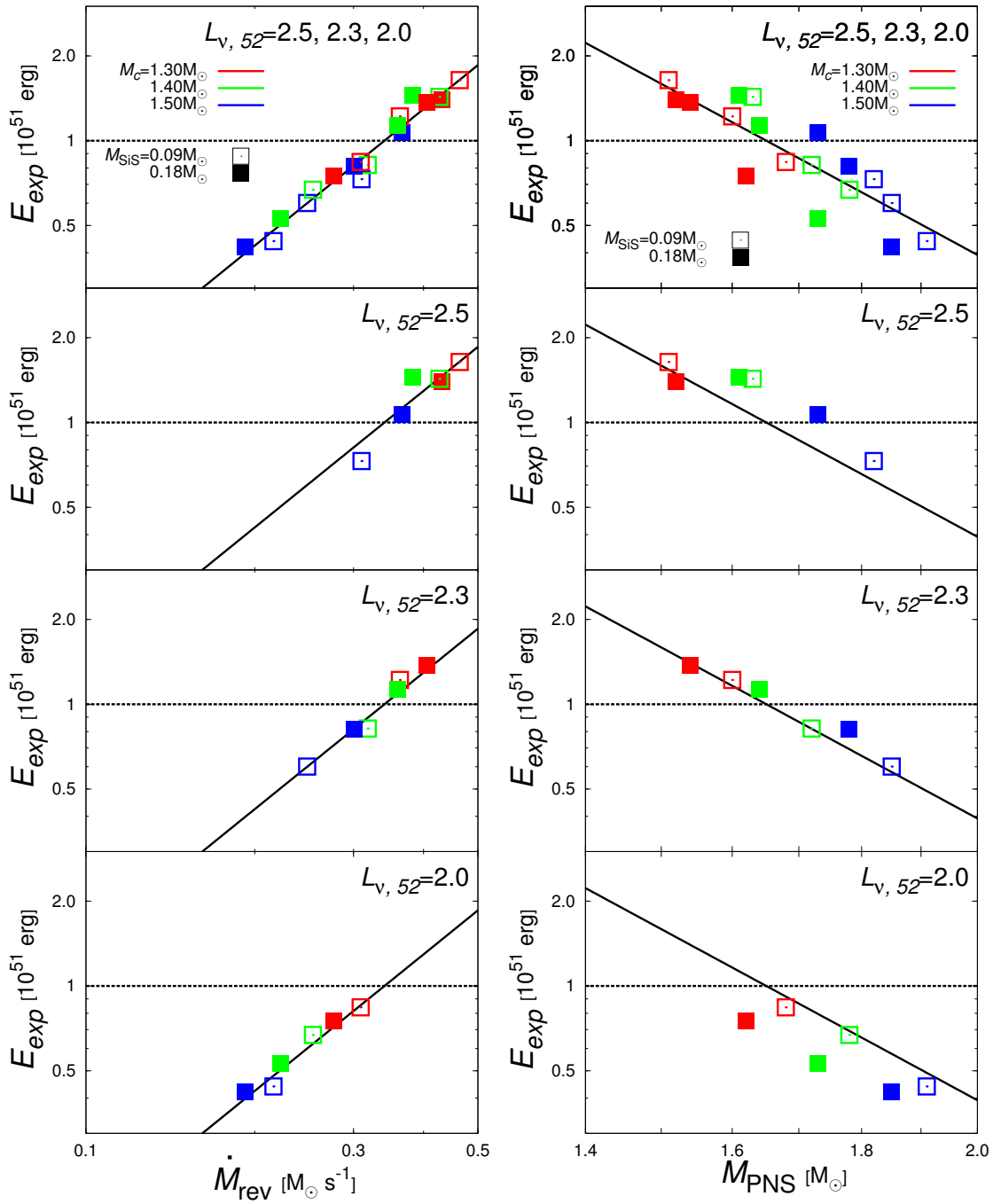

Figure 5.15: The physical properties of explosion energy in 1D. The left panel show mass accretion rate dependence on E_{exp} while the right panel proto-neutron star mass dependence on E_{exp}. The top, top middle, bottom middle and bottom panels correspond to all 3 luminosities, $L_{\nu,52} = 2.5$, $L_{\nu,52} = 2.3$ and $L_{\nu,52} = 2.0$ explosion models. The least-squared line of all 1D explosions for corresponding map is drawn in each panels.

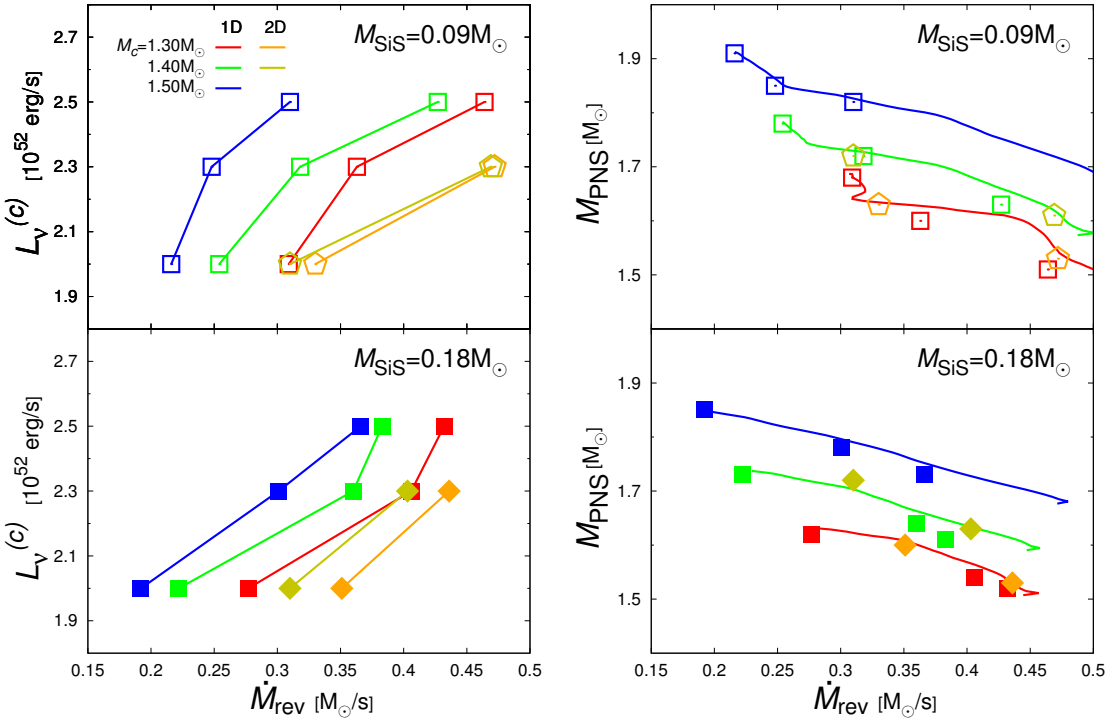

Figure 5.16: Same as figure.5.6 but including 4 pre-supernova models in 2D. The 2D results of $M_c = 1.30$ and 1.40M$_\odot$ are described as orange and dark-yellow, respectively. It should be noted that several symbols of 2D explosion are overlapped on those of 1D and even on different 2D model. For instance, in the top left panel symbol overlaps appear at $\dot{M}_{rev} \gtrsim 0.45M_\odot$/s (orange and dark-yellow) and $\dot{M}_{rev} \gtrsim 0.30M_\odot$/s (dark-yellow and red). Also in the both bottom left panels at $\dot{M}_{rev} \gtrsim 0.35M_\odot$/s (dark-yellow and green).

Axisymmetric 2D explosions

We turn our attention to 2D models, in which we assume axisymmetry. It has been demonstrated by different authors [154, 90, 293, 76, 427, 111, 109, 288] that the nature of turbulence is qualitatively different between 2D and 3D and that the shock dynamics is affected accordingly. It has been also shown that the difference between 2D and 3D is much smaller than that between 1D and 2D [317, 153, 77]. We hence expect that our 2D models will still be able to illuminate how the multi-dimensionality of dynamics modifies our findings so far obtained in the 1D models.

For 2D simulations, we employ only the models with $M_c = 1.30$ and 1.40M$_\odot$, since the heaviest core ($M_c = 1.50$M$_\odot$) models are likely to produce mostly under-energetic explosions except for the highest neutrino luminosity ($L_\nu = 2.5 \times 10^{52}$erg/s) case, which is also not considered in the following.

The critical neutrino luminosities are plotted in the left panels of Fig. 5.16 together with the 1D results presented already in Fig. 5.6. In most of the 2D models, shock revival sets in earlier at higher mass accretion rates than in the corresponding 1D cases. This is due to the hydrodynamical instabilities such as convection and SASI, which expedite shock revival by expanding the gain region and making the dwell time in the region longer, and is consistent with the previous findings by others [291, 377]. In the case of $L_\nu = 2.0 \times 10^{52}$erg/s, for

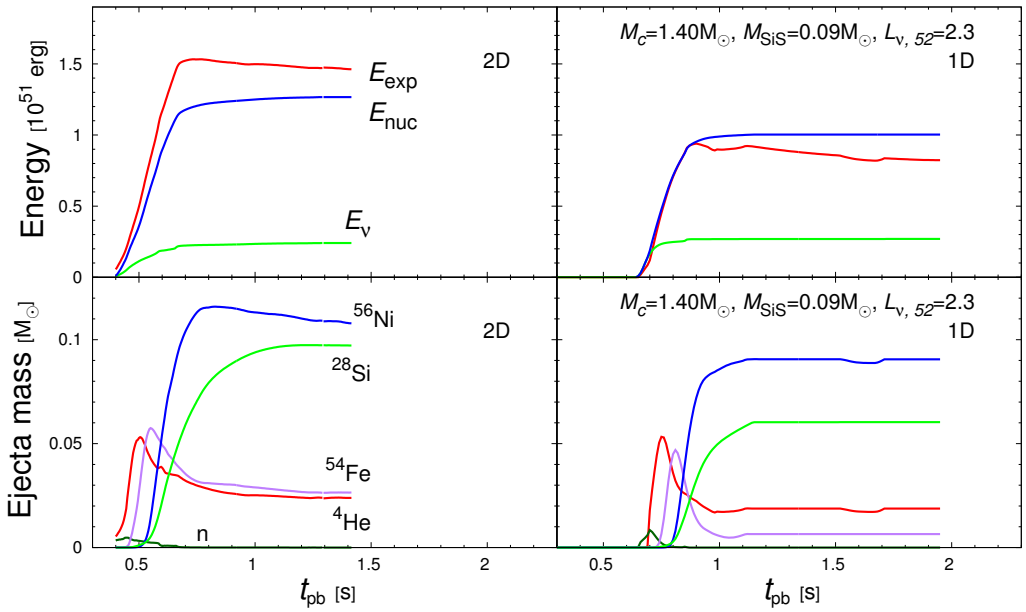

Figure 5.17: Same as figure.5.10 but comparing $(M_c, M_{\rm SiS}) = (1.40{\rm M}_\odot, 0.09{\rm M}_\odot)$ model in 1D with in 2D. The top panels show the time evolution of spherical model whereas the bottom panels those of axisymmetry, respectively. The neutrino luminosities are chosen as L_ν =2.3×10^{52}erg/s.

example, the shock revivals occur immediately after the Si/O interface hits the shock front in 2D, since the multi-dimensional effects just mentioned push the post-shock flows almost to the critical points prior to the encounter with the layer boundary and these models do not need to wait further when the interface actually hits the stalled shock wave.

It is found, however, that the models with $L_\nu = 2.3 \times 10^{52}$erg/s and $M_{\rm SiS} = 0.18{\rm M}_\odot$ have little difference between 2D and 1D.

The right panels present the mass accretion rates at shock revival together with the final values of PNS mass just as the right panels of Fig. 5.6. The solid lines are the trajectories for the designated models. The reason why the squares are not sitting on these lines is because the final values instead of the values at shock revival are employed for plotting these data (see also Fig. 5.6). The vertical distance between the trajectory and data point represents the mass gained or lost by PNS after shock revival. Since the fall back of matter is stronger in 2D in general, M_{PNS} tend to be heavier in 2D than in 1D.

The time evolutions of the explosion energy as well as the masses of some major elements in the ejecta are shown in Fig. 5.17 for the 2D model with $L_\nu = 2.3 \times 10^{52}$erg/s, $M_c = 1.40{\rm M}_\odot$ and $M_{\rm SiS} = 0.09{\rm M}_\odot$. For comparison, the corresponding 1D model is exhibited in the top panels. Thanks to the non-radial fluid instabilities, shock revival occurs much earlier in 2D. The higher mass accretion rate then results in the larger E_{exp}. It is noteworthy in this context that the curve of E_{exp} is always running below that of E_{nuc} in the top left panel for 1D whereas the opposite is true in the 2D model; the contribution from the neutrino heating rises more slowly and continues longer in 2D; the mass of ^{56}Ni in the ejecta is gradually decreasing at late times in 2D. These facts are all consequences of stronger neutrino winds,

i.e., outward matter flows from the inner boundary in our simulations. The neutrino wind mainly consists of hot nucleons earlier and α particles later, which will contribute to the explosion energy through recombinations. The addition of these fresh nucleons is the main reason for the more long-lasting neutrino heating in 2D. The later α particle ejection, however, also underestimate the neutrino heating and nuclear the recombination energy which should be provided outside the active calculation region (see also section. 5.3.3). The neutrino wind adds slightly neutron-rich matter to the ejecta, which later recombines to produce ^{54}Fe instead of ^{56}Ni. This is one of the reasons why the mass of synthesized ^{56}Ni is smaller in 2D than in 1D in general. It should be noted, however, that the neutrino wind is one of the most uncertain components in our simulations. In fact, it is actually dictated by the inner boundary condition imposed in our models (see also the previous chapter)although it should have been obtained from the self-consistent evolution of PNS. In fact, previous realistic simulations by other groups, e.g., Scheck et al.(2006), Marek & Janka 2009 and Bruenn et al.(2014) [378, 266, 41], demonstrated that the neutrino driven wind and its heating by neutrinos may last for more than $\sim$ 500ms, hence being one of the main contributors to the explosion energy. We demonstrate in the left panels of Fig. 5.18 that the explosion energy is tightly correlated with the mass accretion rate at shock revival. It is intriguing that the 2D models fall on the same line (see Eq. (5.17)) with the 1D models. On the other hand, the correlation between E_{exp} and M_{PNS} seems to become stronger in the 2D cases as shown in the right panels of Fig. 5.18 less scattered distribution and almost on the least-squared line in M_{PNS} dependence. It should be mentioned here that the PNS mass is more difficult to estimate in 2D, since the fall back is more violent and highly anisotropic and it takes place simultaneously with the neutrino wind. It will be hence necessary that a larger number of models are investigated to justify the above statement.

Finally, the explosion energies and masses of synthesized ^{56}Ni are plotted in Fig. 5.19 for all models including the 2D computations. One can easily recognize that the 2D results are qualitatively different from those for 1D unlike the correlation between E_{exp} and $\dot{M}_{\rm rev}$ demonstrated in Fig. 5.18. In fact, the stronger fall back and neutrino wind in 2D both tend to reduce the mass of ^{56}Ni in the ejecta compared with the 1D counter parts and the data points for 2D seem to be fitted by a steeper line (red solid line) although there is a scatter for the low-energy explosions. We showed earlier that the 1D models tend to produce too much nickel if they explode in the first place (see also Fig. 5.13) and that the correlation between the explosion energy and the nickel mass is qualitatively different from that suggested by the observations , which is yet another reason that 1D explosions are disfavored in the neutrino heating mechanism. In the 2D case, the reduced nickel production puts both the explosion energy and the Ni mass in the right region (see references in [41, 343]). This is consistent with the findings in my first study.

From the figure it may be said that the mass of Si+S layer affects the Ni synthesis more than the Fe core mass. It should be mentioned, however, that the precise estimation of the nickel mass in the ejecta is made difficult not only by the uncertainty in the neutrino wind but also by later interactions of the shock wave with the helium and/or hydrogen layers, which may cause further fall back. This issue will be discussed more in the last section. We mention the accuracy of our numerical simulations. To assess it, we conducted four more 2D computations with a finer radial or angular mesh for the parameter sets of (M_c/M$_\odot$, $M_{\rm SiS}$/M$_\odot$, $L_{\nu,52}$)=(1.30, 0.18, 2.3) and (1.40, 0.18, 2.0). We find in the computations with the larger number of radial grid points (150 up from 600) that both the explosion energy and the Ni mass are changed by less than 0.5% at most. In the case of the finer angular mesh with 124 grid points in the θ direction, the explosion energy is changed by $\sim$3%

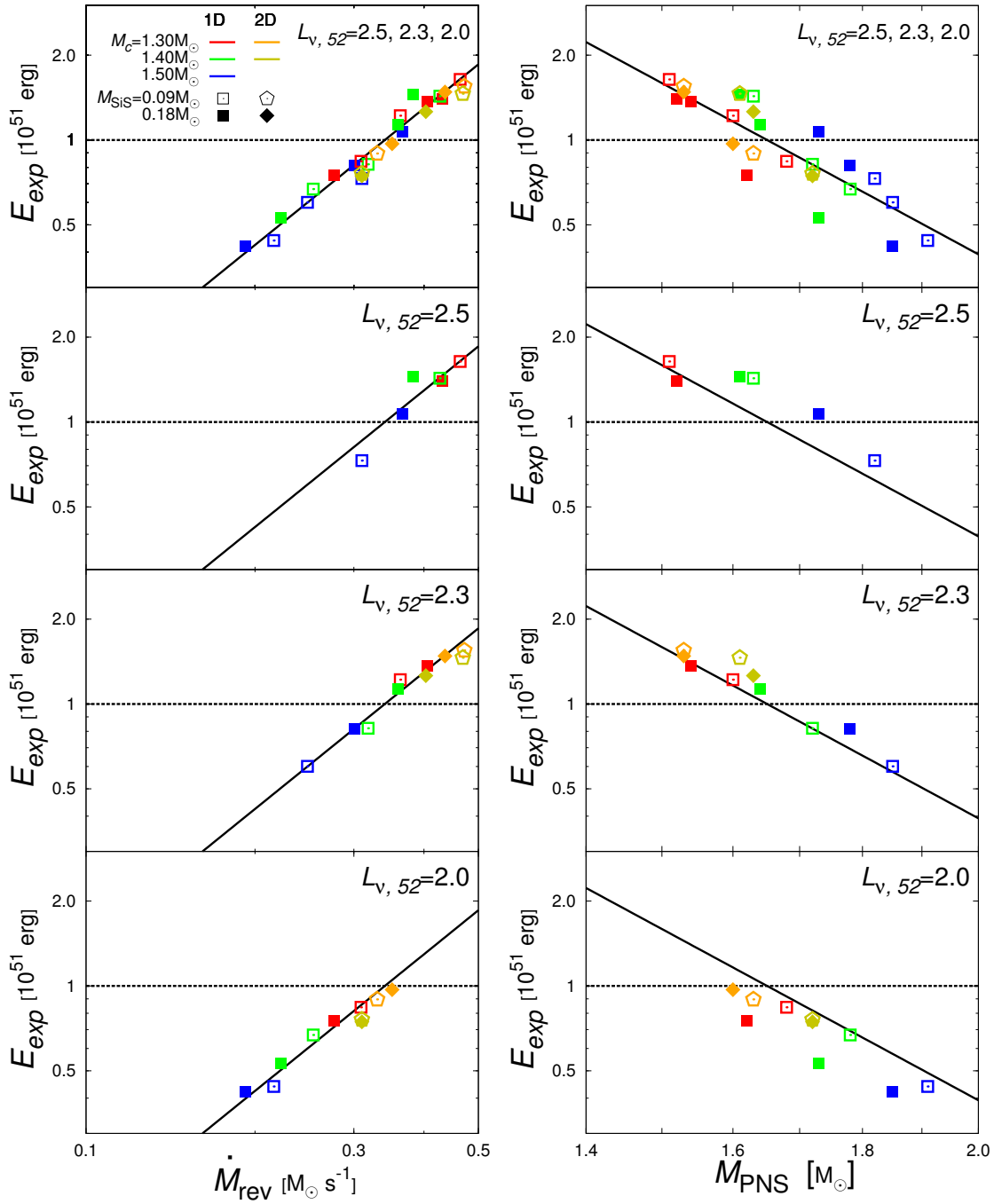

Figure 5.18: Same as figure.5.15 but with 8 axisymmetry explosions. The least-squared lines are also same with figure.5.15. Note that several symbols are overlapped, e.g., different dimensions of $(M_c, M_{\rm SiS}) = (1.40{\rm M}_\odot, 0.18{\rm M}_\odot)$ in $L_{\nu,52} = 2.3$ (filled dark-yellow and green) and two-dimension explosion of $M_c = 1.40{\rm M}_\odot$ with the different $M_{\rm SiS}$ in $L_{\nu,52} = 2.0$ (open and filled dark-yellow).

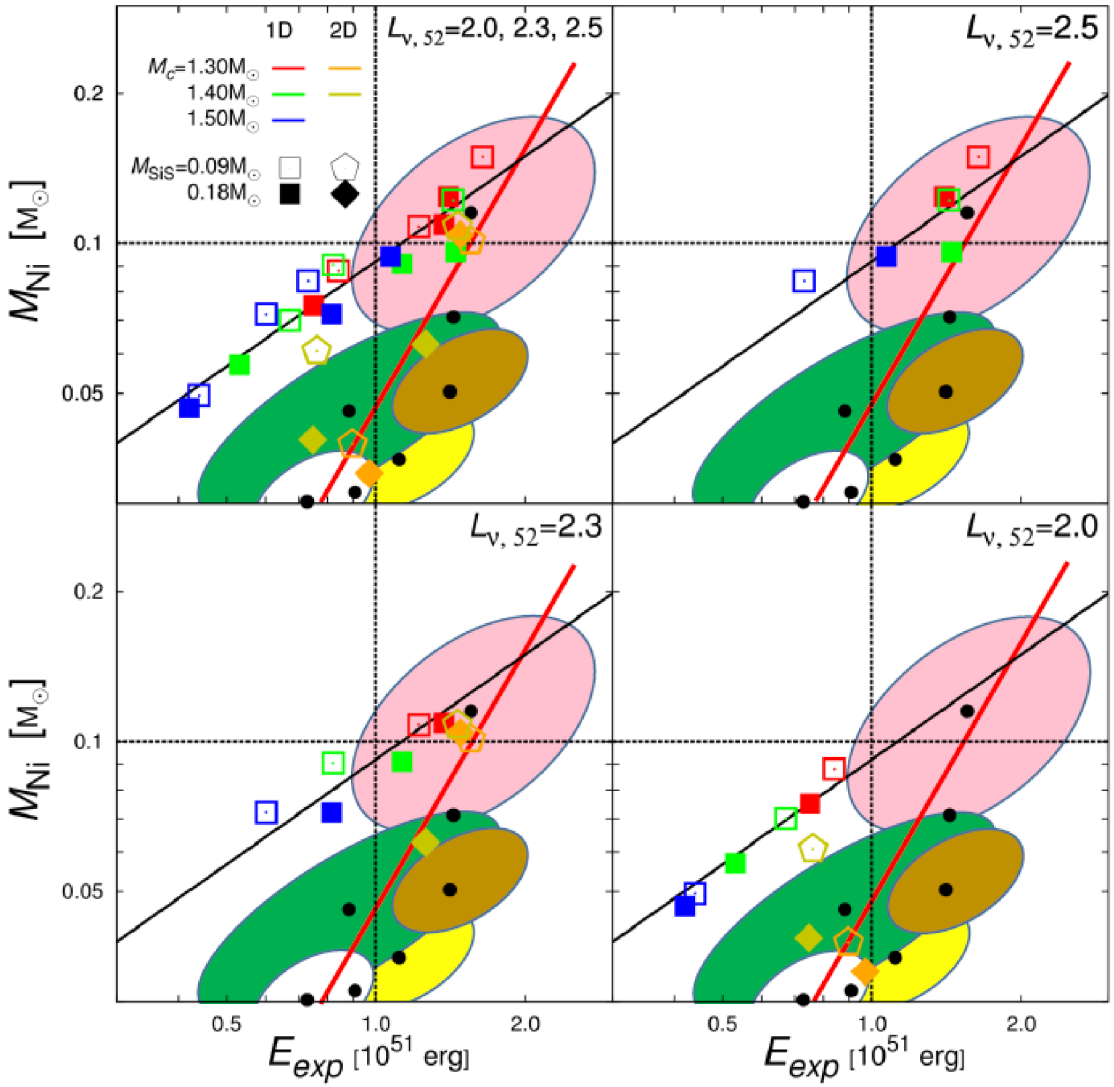

Figure 5.19: Same as figure.5.13 but $L_{\nu,52} = 2.3, 2.5$ are depicted with the additional 8 explosion calculations in 2D. The least-squared lines for 2D (red solid) drawn in each panels are also added from figure.5.13.

whereas the Ni mass is affected more with the difference of $\sim$10%, which is mainly caused by a greater fall back. These numerical errors, though not completely negligible, are not large enough to change the conclusions qualitatively, either.

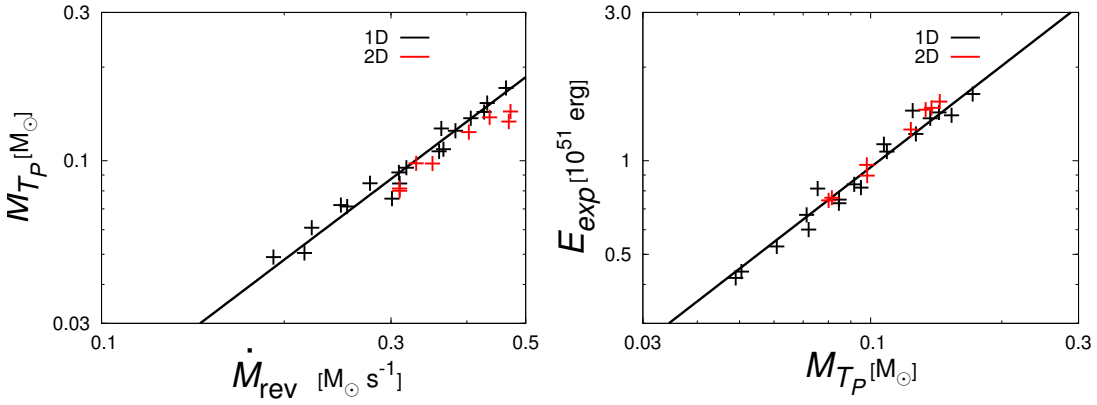

Figure 5.20: Properties of typical mass ejecta M_{T_P} (see its definition from eq.5.18). $\dot{M}_{rev}$-M_{T_P} relation is plotted in the left panel while E_{exp} is shown as a function of M_{T_P} in the right panel. Each colors indicates 1D(black) and 2D(red), respectively and the solid lines are least square line for 1D explosion models.

5.3.3 The correlation of E_{exp} and M_{T_P}

We have so far observed that the explosion energy, E_{exp}, is strongly correlated with the mass accretion rate at shock revival, $\dot{M}_{rev}$ irrespective of the dimension of dynamics. In this section, we look into the origin of this correlation more in detail. For that purpose we introduce a new quantity, the total mass, M_{T_P}, with the peak temperature higher than $T_P > 5 \times 10^9$K. Here the peak temperature is defined for each mass element as the highest temperature it attains during the expansion following shock revival. The threshold temperature, i.e., $T_P = 5 \times 10^9$K is a temperature, around which α particles are recombined to iron-group elements. M_{T_P} is hence the mass of the matter that experiences neutrino heating and recombinations, the two main contributors to the explosion energy. It is numerically evaluated as follows:

$$M_{T_P} = \sum_{T_{P,9}^{(\rm n)}>5.0,\, v_r^{(\rm n)}>0} \Delta m^{(\rm n)} \,, \tag{5.18}$$

in which the superscript n labels mass elements on the numerical mesh and $T_{P,9} = T_P/10^9$K is a normalized temperature; the condition $v_r^{(n)} > 0$ implies that only expanding matter should be summed.

In Fig. 24 we plot all the 1D (18 black crosses) and 2D (8 red crosses) in the $\dot{M}_{rev} - M_{T_P}$ (left panel) and $M_{T_P} - E_{exp}$ (right) panels. It is evident that they are closely related with one another regardless of the dimension again. The least square fits to them give the following power-law relations:

$$M_{T_P} \propto \dot{M}_{rev}^{1.47}, \; E_{exp} \propto M_{T_P}^{1.07}. \tag{5.19}$$

It is important that the explosion energy is almost linearly correlated with M_{T_P}, the fact suggesting that M_{T_P} is more directly related with the explosion energy. This will be endorsed by more detailed analyses in the following.

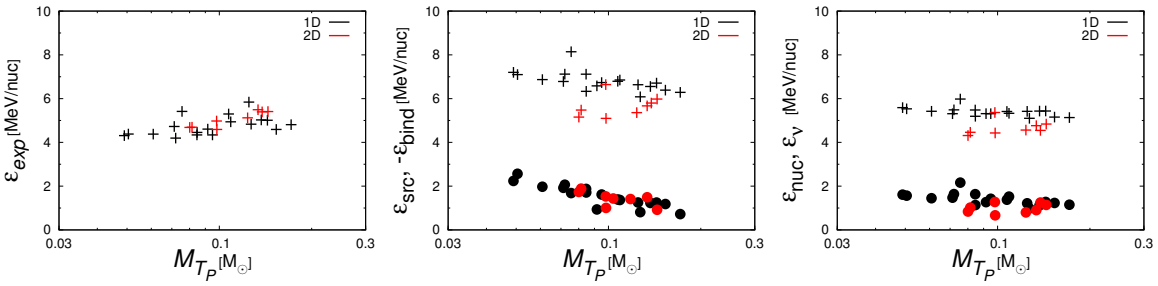

Figure 5.21: Explosion energy per nucleon and its contributions as a function of M_{T_P}. The left panel show the explosion energy per nucleon, ε_{exp}. The net heating source per nucleon, $\varepsilon_{\rm src}$ (cross), and the enevelpe binding energy per nucleon, $\varepsilon_{\rm bind}$ (circle) are plotted in the middle panel. The right panel depict two heating contributions per nucleon, $\varepsilon_{\rm nuc}$(cross) and ε_ν(circle). In all panels black and red symbols correspond to 1D and 2D explosion, respectively (see also exact definition in eq.5.20 and 5.22.)

We define the explosion energy per nucleon, $\varepsilon_{\rm exp}$, as well as the contribution to it from the nuclear reactions, $\varepsilon_{\rm nuc}$, and from the neutrino heating, ε_ν, as follows:

$$\varepsilon_{\rm exp} = E_{exp}/N_{T_P},\ \varepsilon_{\rm nuc} = E_{\rm nuc}/N_{T_P},\ \varepsilon_\nu = E_\nu/N_{T_P}, \tag{5.20}$$

in which N_{T_P} is the number of the nucleons that consist of M_{T_P}.

We also refer to the sum of the latter two as $\varepsilon_{\rm src} = \varepsilon_{\rm nuc} + \varepsilon_\nu$. We also pay attention below to the total energy per nucleon of the outer envelope, which is defined as

$$\varepsilon_{\rm bind} = E_{\rm bind}/N_{T_P}, \tag{5.21}$$

with $E_{\rm bind}$ being given by

$$E_{\rm bind} = \sum_{500km<R^{(\rm n)}} \Delta V^{(\rm n)} \cdot (e^{(\rm n)}_{kin} + e^{(\rm n)}_{int} + e^{(\rm n)}_{g}).. \tag{5.22}$$

Note that $E_{\rm bind}$ is negative owing to the gravitational binding although it contains the kinetic and internal energies , which are positive, as well.

We plot these quantities for all 1D and 2D models in Fig. 25, in which the horizontal axis is chosen to be M_{T_P}. First of all, it is clear that they are almost constant, indicating that not only the total explosion energy but each contribution except for $\varepsilon_{\rm bind}$ is also nearly proportional to M_{T_P}. If we look more closely, however, we can see some trends. In the left panel, in which the specific explosion energies are plotted, we can recognize that they increase slightly with M_{T_P}, having values of 4.5MeV $\lesssim \varepsilon_{\rm exp} \lesssim$ 6.0MeV, although there are some scatterings. The reason for this increase is understood from the middle panel, in which $\varepsilon_{\rm src}$ and $\varepsilon_{\rm bind}$ are plotted for M_{T_P}. It is found that they both decrease with M_{T_P}. Since the binding energy of the envelope is almost unrelated with M_{T_P}, the decrease of $\varepsilon_{\rm bind}$ is just a consequence of the increase of N_{T_P}, the denominator in Eq. (30), with M_{T_P}. The decline in $\varepsilon_{\rm src}$ is much more moderate and, as a result, the total explosion energy per nucleon increases as shown in the left panel. The right panel shows the contents of ε_{src}, i.e., $\varepsilon_{\rm nuc}$ and ε_ν. It is discernible that both of them decrease slightly as does $\varepsilon_{\rm src}$ in

the middle panel although 2D results appear to have opposite trend. This is due to the following reason: as M_{T_P} increases, the mass of the post-shock matter that has larger α fractions becomes greater, since the photo-dissociations to α occur at larger radii; as a result, the energy gain by later recombinations gets smaller; since the nucleons are mainly responsible for the neutrino heating, ε_ν is also reduced. Note that the values of $\varepsilon_{\rm nuc}$ are $\sim 5-6$MeV, which are similar to those evaluated at $r = 3000$km by [378], and are much larger than those of ε_ν, which is at most $\sim 1-2$MeV. This is partly because that those values are evaluated after shock revival whereas the neutrino heating has started much earlier on and is consumed mainly to lift up matter from the gravitational well. It should be also mentioned that the neutrino heating is also used to compensate for the loss by photo-dissociations. In this sense the recombination energy is actually originated from the neutrino heating. It is interesting to point out that $\varepsilon_{\rm bind}$ is roughly comparable to ε_ν.

The values of $\varepsilon_{\rm src}$ as well as $\varepsilon_{\rm nuc}$ and ε_ν are a bit smaller for 2D than for 1D, the fact which also seems to be the reason for the opposite trends we found in the middle and right panels between 1D and 2D models. This happens because these quantities are evaluated only in the computational domain, that is, outside the inner boundary we put artificially. In fact, in 2D models some of the matter flowing into the computational domain through the inner boundary, to which we refer as the wind below, has already recombined to α particles, which then results in the reduction of $\varepsilon_{\rm nuc}$ and ε_ν. This is all the more true for the 2D models with smaller M_{T_P}, producing the opposite trends mentioned above.

The nice thing with the correlation between E_{exp} and M_{T_P} is that the latter is fixed earlier than the former. In fact, M_{T_P} is determined by the time when the shock wave reaches $\sim 2000-3000$km in our models. It is true that the fall-back occurs later after the shock reaches ~ 5000km but these fall-back matter does not have much energy as has been argued in section 5.3.2. The correlation may be hence useful to estimate the explosion energy. There is one concern here, however. As mentioned above, the wind also contributes to the explosion energy, which is then expressed as

$$\begin{aligned} \varepsilon_{exp} &\sim \varepsilon_{\rm src} + \varepsilon_{\rm bind} + \varepsilon_{\rm wind} \\ &= \varepsilon_{\rm nuc} + \varepsilon_\nu + \varepsilon_{\rm bind} + \varepsilon_{\rm wind}. \end{aligned} \tag{5.23}$$

In this expression the wind energy is denoted by $\varepsilon_{\rm wind}$ (see [266, 41]). Although this is not a dominant contributor in our models, the correlation may be degraded if it is, since we cannot expect that it is strongly correlated with M_{T_P}. Our models have admittedly no predictive power on the issue, since the wind is rather sensitive to the inner boundary condition we impose by hand. As a matter of fact, the wind contribution seems to be substantial in more realistic simulations [55, 266, 115, 289] and we are afraid that this may be the reason why the explosion energy is fixed rather early on in our models compared with other realistic simulations [427, 303, 41, 288]. Systematic studies will be conducted on the wind in our forthcoming paper.

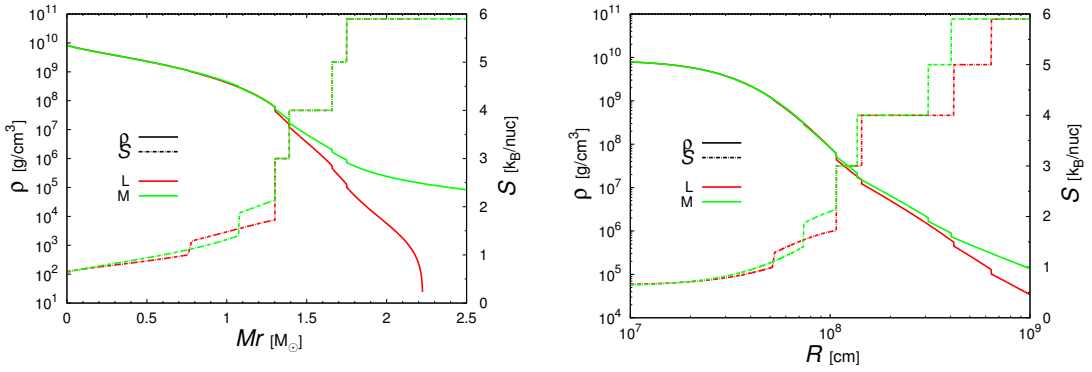

Figure 5.22: The density and entropy distribution of enclosed mass (the left panel) and radius (the right panel). The both panels depict the result of same parameter choice except for light (L: red) and medium (M: green) core function. The solid line denotes density whereas the dotted line entropy.

5.3.4 Some comments on our lightest core-mass models

In the models considered in this paper, there is a clear tendency regardless of spatial dimensions that the explosion energy gets larger as the core mass becomes smaller. This may seem at odds with some recent realistic simulations [427, 303, 41, 288] for light progenitors. In fact, they generically produced weak explosions of $E_{exp} \lesssim 0.1 \times 10^{51}$erg, e.g., for model s11.2 of $11.2M_\odot$ by WHW2002. It is true that the time of shock revival is self-consistently determined in these realistic simulations and that the post-shock flow is not steady in reality but we believe that they are not the main cause for the discrepancy mentioned above but the progenitor models are.

As discussed in section 5.2.2, the progenitor models can be classified into three groups labeled with "L", "M" and "H". In this paper we focus on group M, since the majority of progenitor models belongs to this group. We then employ the entropy and Y_e distributions, Eqs. (3.36) and (3.37), suitable for this group. Note that the lowest Fe-core mass models are also based on these relations. On the other hand, some of the light progenitor models obtained by realistic evolution calculations are known to be affiliated with group L. Model s11.2 of $11.2M_\odot$ by WHW2002 is indeed one of such models.

To see the difference between groups L and M, we show in Fig. 5.22 the density and entropy distributions for their members. In the left panel, the horizontal axis is the enclosed mass whereas the radius is adopted in the right panel. Note that only the entropy distributions, which are depicted with dashed lines, in the core as a function of density are different between the two models and the other parameters such as the masses of Fe core and Si+S layer are identical. It is interesting that the density distributions in the Fe core are more or less the same between the two models. Instead the difference manifests itself in the outer layers as is particularly evident in the left panel.

This may be understood as follows. In both models, the cores are in NSE and are mostly supported by degenerate electrons. As a result, the difference in entropy has a limited influence on the core structure. This is not the case near the core surface as well as in the Si+S layer. Since the entropy is smaller at the core surface for group L than for group M but it is identical in the adjacent Si+S layer for both groups, the entropy jump at the interface is greater in group L. As the densities are nearly the same at the core surface

between the two groups, this implies that the pressure is smaller for group L. Since the gravitational attraction is almost identical at the core surface as the mass and radius of the core are nearly the same, the pressure scale height is shorter for group L accordingly. This is reflected in the density scale height in the Si+S layer directly because the entropy is assumed to be identical for both group there. This is the reason why the density gradient steeper for group L than for group M as observed in the right panel of Fig. 5.22.

If such an entropy difference in the core is indeed responsible for the discrepancy of the explosion energies mentioned above between the recent realistic simulations and our experimental computations, it may suggest that we would obtain canonical explosions if we could obtain via evolution calculations progenitor models with relatively high entropies in small cores. Detailed analyses of groups L and H will be reported in the forthcoming paper.

5.4 Summary and discussion

We have conducted experimental 1D and 2D simulations to study shock revival and the subsequent evolutions in the post-bounce CCSNe. We have paid particular attention to the influences of progenitor structures, which are known to be diverse. Instead of employing the pre-supernova models provided by realistic stellar evolution calculations, we have constructed toy models, in which not only the Fe core mass but the proportion of outer layers can be also changed rather arbitrarily. In this paper, we have focused on the masses of the Fe core and adjacent Si+S layer. We have run both 1D spherically symmetric and 2D axisymmetric simulations of the shock revival and evolutions that follow, excising the central portion of the core and replacing it with the inner boundary conditions. We have investigated the dependences of the explosion energy and synthesized nickel mass, both of which are key observables in CCSNe, on some model parameters.

We have adopted the four-step strategy: (1) we first constructed the progenitor models with different Fe and SI+S layer masses; (2) we then calculated the mass accretion histories for these models, removing the central part and thus its pressure support in 1D simulations; (3) using the mass accretion rates at t=300ms post bounce, we obtained spherically symmetric, steady, shocked accretion flows for three neutrino luminosities; (4) we performed 1D and 2D simulations of shock revival and the ensuing evolutions for the configurations obtained in the previous step, employing the mass accretion histories sampled in the first step; the light bulb approximation was adopted with the appropriate time evolution of the neutrino luminosity being taken into account. In these 1D and 2D simulations, we have incorporated nuclear recombinations and burnings consistently with the multi-spices (non-NSE) EOS.

The main results are as follows:

1. Based on the realistic progenitor models by [474], we have first demonstrated that the progenitor's core structures can be categorized into three groups dubbed as L, M and H if one parametrizes the entropy and electron fraction as functions of density rather than radius or enclosed mass. Since the majority of massive star's cores seem to be affiliated with group M, we focus on this group in this paper. Groups L and H are meant for some of lighter and heavier cores and will be investigated separately in the forthcoming paper. We have taken into account seven outer layers of different chemical compositions and assumed uniform distributions for the entropy and abundance in each layer, setting appropriate values to them. We have constructed six progenitor models this way with different combinations of three Fe core masses, $M_c = 1.30$, 1.40 and $1.50 M_\odot$ and two Si+S layer masses, $M_{\rm SiS} = 0.09$ and $0.18 M_\odot$. We have found that for heavier Fe cores, the compactness, that is, the ratio of enclosed mass to radius, is larger in the Si layer but becomes smaller in the O+Ne+Mg layer. It has been also shown that more massive Si+S layers induce larger differences in the outer envelopes.

2. The accretion histories are found to be commonly characterized by the initial rise of $\dot{M}$ to a peak, which corresponds to the contraction of the entire Fe core into the radius of $\approx 100km$, and the ensuing rapid decline that is followed by the much slower decrease. There are a couple of steps, where the mass accretion rate drops suddenly. They are caused by the interfaces of different layers. It is interesting that the mass accretion histories for models with different Fe core masses are similar to each other if they are shifted in time so that the peaks of $\dot{M}$ should coincide with each other.

This is particularly so when the Si+S+O layer is accreting onto the shock wave, probably the most critical period for shock revival. The locations of the steps just mentioned are different, on the other hand, occurring earlier for smaller cores. It is also found that the increase in the Si+S layer mass from $0.09M_\odot$ to $0.18M_\odot$ results in the reduction of $\dot{M}$ by $\sim 10\%$.

3. Connecting the pairs of ($\dot{M}$, L_ν) at shock revival for the models with different neutrino luminosities, we have obtained the critical curves for different progenitor models both in 1D and 2D. In accord with the previous results by various researchers, the critical luminosity is a monotonically increasing function of the mass accretion rate. We have also found different convexities between the models with $M_{\rm SiS} = 0.09{\rm M}_\odot$ and $M_{\rm SiS} = 0.18{\rm M}_\odot$: the critical curve is upward convex for $M_{\rm SiS} = 0.09{\rm M}_\odot$ and downward convex for $M_{\rm SiS} = 0.18{\rm M}_\odot$. We have demonstrated that they just trail different portions of the mass accretion histories. At the vertical dent of the critical curve, different critical luminosities are obtained for almost the same mass accretion rates, since the rapid drop of $\dot{M}$ at the interface of different layers followed by the slow decline put these different luminosity models simultaneously in the states, where over-stable radial modes trigger shock revival. In the 2D models, shock revival occurs earlier or at larger $\dot{M}$ in general. Again the shape of the critical curve can be understood from the mass accretion rates around the shock revivals.

4. In line with the our previous findings (chapter **??**) the diagnostic explosion energy rises via neutrino heating initially and then the nuclear recombinations followed by nuclear burnings takes its place; it approaches the asymptotic value, gradually decreasing its value owing to gravitationally bound envelopes; the neutrino wind also contributes to the explosion energy both through its internal + kinetic energy and recombinations. As the neutrino luminosity decreases, shock revival is delayed, leading in general to smaller E_{exp} (see also the next item). Shock revival occurs earlier for heavier Si+S layers, since the mass accretion rate around shock revival is smaller for them. The dependence of E_{exp} on $M_{\rm SiS}$ is rather complicated, however: for the low neutrino luminosity, the accretion rates are larger for $M_{\rm SiS} = 0.09{\rm M}_\odot$ and, as a result, E_{exp} is also greater; for the high neutrino luminosity, on the other hand, the result depends on the core mass. It is true in general that larger core masses weaken explosions. The reason for this, however, is not the stronger gravitational attraction they exert on the ejecta but the smaller mass accretion rates they produce. The explosion energy is strongly correlated with the synthesized nickel mass irrespective of the progenitor structures. We have confirmed our previous findings that 1D explosions tend to produce either too much ^{56}Ni or too weak explosions and a fine tuning is necessary to obtain both of them in the right regime simultaneously. This problem is partially solved in 2D, in which shock revival tends to occur earlier and, as a result, E_{exp} is greater; stronger fall backs tend to reduce the nickel mass. The neutrino wind is also stronger and slightly neutron-rich. The latter fact further contributes to the reduction of nickel via the production of ^{54}Fe rather than ^{56}Ni.

5. We have observed that E_{exp} is tightly correlated with $\dot{M}$ at shock revival (see Fig. 5.18) irrespective of the dimension. We believe that this is a consequence of the fact that the mass of the matter that has the peak temperature higher than 5×10^9K is strongly correlated both with the explosion energy and the mass accretion rate at shock revival. The linear relation between E_{exp} and M_{T_P} may be useful to estimate the former, since

the latter is settled earlier. If the lasting neutrino wind gives non-negligible contributions to the explosion energy, which was not observed in this paper, this correlation will be weakened. Our findings suggest that multi-dimensional explosions at earlier times will be the recipe to produce an appropriate explosion energy and a nickel mass simultaneously. They are sensitive to modest differences, $\sim 0.1 M_{\odot}$, in the masses of the Fe core and/or Si+S layer mass. This may be responsible for the scatter in their observed values for type II supernovae.

This chapter is a sequel to the previous one, in which only a single progenitor was investigated. The systematic comparison of multiple progenitors in this paper has confirmed the previous findings. On the other hand, the tight correlation between the explosion energy and the accretion rate at shock revival that we have found in this paper is interesting and has a potential to extract the information on the progenitor, i.e., one may be able to constrain the mass accretion history if neutrino luminosities and/or gravitational waves provide us with the shock revival time [296]. We have seen that our light Fe core models tend to produce robust explosions rather than the other way around. If this is indeed because we employed the distributions of entropy and electron fraction for group M instead of group L, which is suitable exclusively for light progenitors, it may suggest a new path for robust explosions, i.e., the neutrino-heating driven explosions from smaller cores with rather high entropies, which might have evaded the current stellar evolution calculations. Binary interactions [348, 235, 392], treatments of various convections [268, 201], uncertainties in nuclear reactions rates [43] and entrainments by complex multi-dimensional turbulent motions in convectively stable zones [58, 16, 15] may merit further investigations in this respect.

This study is just the first step of a series of papers. It will be extended to 1) the investigations of the remaining groups L and H, 2) the comparison of our toy models with other realistic progenitor models available to us, 3) the systematic study of the dependences on other model parameter including the boundary conditions, and 4) the application to rotational stars.

Chapter 6

Summary & conclusion

For about past five years, the considerable efforts enable to compute the realistic multi-dimension simulations, thus the first principle calculations. It is certainly true that these models are promising candidates of the answer to the long-standing problem of CCSNe mechanism but one should not forget that the revival of the stalled shock wave that these simulations have demonstrated is just a necessary condition for supernova explosion but is not a sufficient condition. In fact, almost all numerical simulations that have reported successful shock revival have yielded energies of ejecta that are substantially smaller than the canonical value of 10^{51}erg. Although the authors claim that the energies are still increasing at the end of their simulations and might reach appropriate values should the computations be continued long enough, a convincing demonstration remains to be done. In addition to the explosion energy, the mass of neutron star as well as nucleosynthetic yields should be also reproduced properly in the successful supernova simulations. Therfore, the main topic of the theory is now starting to pay attention to what is exact condtion of powerful explosion and particularly what kind of precollapse structure expedite to obtain those canonical explosion, i.e. "initial problem". So far the practical stellar evolution calculations of massive stars are still in progress due to the complicated convection theory, the effect of rotation, the presence of mass loss events and the resolution dependence. Hence, it is mandatory to progress our understanding in what kind of physics determine the observational evidence.

In so doing, we first perform some experimental simulations in spherical symmetry and axisymmetry to understand the post-shock-revival evolution of core-collapse supernovae. Assuming that the stalled shock wave is relaunched by neutrino heating and employing the so-called light bulb approximation, we induce shock revival by raising the neutrino luminosity by hand up to the critical value, which is also determined by dynamical simulations. We incorporate nuclear network calculations with a consistent equation of state in the simulations to account for the energy release by nuclear reactions and their feedback to hydrodynamics. Varying the shock-relaunch time rather arbitrarily, we investigate the ensuing long-term evolutions systematically, paying particular attention to the explosion energy and nucleosynthetic yields as a function of this relaunch time, or equivalently the accretion rate at shock revival. We study in detail how the diagnostic explosion energy approaches the asymptotic value and which physical processes contribute to the explosion energy in what proportions as well as their dependence on the relaunch time and the dimension of dynamics. We find that the contribution of nuclear reactions to the explosion energy is comparable to or greater than that of neutrino heating. In particular, recombinations are dominant over burnings in the contributions of nuclear reactions. Interestingly 1D

models studied in this paper cannot produce the appropriate explosion energy and nickel mass simultaneously, overproducing nickels, whereas this problem is resolved in 2D models.

Next we suggest a new experimental approach to conduct a systematic study in core collapse supernovae (CCSNe) theory. Instead of employing realistic models provided by stellar evolution calculations, which are sometimes of stochastic nature as a function of stellar mass on the main sequence, we provide toy pre-supernova stages which controlled core and silicon sulfer (Si+S) layer masses with solving NSE and QSE compostions respectively.

We also demonstrated 1D and 2D hydrodynamic simulations with light bulb approximation using 6 models from core collapse to explosion in order to study the dependence of the interior structures of pre-supernova stages on both explosion energies and nickel masses.

During the core collapse our simulation showed that Si+S layer masses reflects the time evolution of mass accretion rates after bounce. Furthermore, the critical luminosity shape is directly influenced by mass accretion history, Si+S layer mass, due to the timing when contact discontinuity pass through shock surface. We also found that the explosion energy is tightly correlated with mass accretion rate at shock revival irrespective of dimension and the lighter iron cores but with rather high entropies, which are yet to be produced by realistic stellar evolution calculations, may produce the more energetic explosions and the larger amounts of nickel masses. Our simulation confirmed neccesity of early time explosion to reproduce 10^{51} erg which is qualitatively coincide with the first study. When the Si+S layer masses are lighter, mass accretion rates are enhanced so that the heavy core mass models are prevented from producing powerful explosion.

Since the first study only conduct a single progenitor model which is statistically not enough, our next propose is to extend a research to more than one stellar object. I revisit presupernova structure dependence on supernova modeling in experimental way once more. A previous study done by Baron [22] investigated the relation between core structure and kinetic energy of shock. We arranged the stellar interior in more plausible way by reflecting present stellar evolution model results.

I improved or employed different approaches from the first study; the determination of critical curve is more realistic and employed the different inner boundary conditions. Moreover, the size of nuclear set in NSE rather more increase and connected smoothly to nuclear reaction network via introducing averaged remaining nuclei. In this paper, we studied the influence of the progenitor structure on the dynamics systematically. In order to expedite our understanding of the systematics, we constructed progenitor models parametrically instead of employing realistic models provided by stellar evolution calculations, which are sometimes of stochastic nature as a function of stellar mass on the main sequence. They are obtained by solving hydrostatic equations, with the NSE core, QSE layer, envelopes of different elements as well as their transitions being considered appropriately. This is mandatory, since we also performed nuclear network calculations in the simulations. Changing the mass of the iron core in NSE and that of silicon plus surfer (Si+S) layer, which is in QSE, we prepared 6 progenitor models, for which we first computed spherically symmetric contraction to obtain the mass accretion histories and then performed 1D and 2D hydrodynamical simulations of the shock revival and subsequent evolutions to find the critical luminosities, asymptotic explosion energies and Ni yields as well as their dependence on the progenitor structure. In so doing, the light bulb approximation was employed for neutrino transfer. We found that the models with lighter iron cores produce more energetic explosions and larger amounts of nickel in general, since shock revival occurs earlier. The mass of the Si+S layer is also important in the mass accretion

history after bounce and that the mass accretion rates are enhanced for smaller masses of the Si+S layer so that heavy cores could not produce powerful explosions. Based on our findings we will suggest the progenitor structure that would be favorable for the supernova explosion as we observe it.

The several difference appear between the first and second studies. First, the absolute critical luminosity values are completely altered. Second, the criterion of $\dot{M}$ for canonical explosion is different. Third, the multi-dimension effect is more sensitive to both E_{exp} and M_{Ni} in previous than in present which is due to the amount of solid angle of neutrino heated ejecta. The proto-neutron star evolution is one of main difference in the two researches and strongly associated with the critical luminosity, mass accretion rate and solid angle. Limiting in the solid angle, the smaller luminosity models may be correspond to the smaller solid angle.

However, although several quantitative differences are exist, the qualitative properties does not change by employing the different PNS evolution. Hence, the approach in this paper extract the contribution from infalling matter to explosion energy and the power law relation between $\dot{M}$ and E_{exp} (eq.5.17) will be good indicator of isolating the neutrino wind contribution by measuring the deviation from the power law. We compensate further analysis to future works. Furthermore, the other variation of core structure, e.g. entropy distribution, will be also investigated with rather more realistic neutrino treatment such as GR1D code (O'Connor2015).

I will close this paper with the last remarks. Recently there have been many open source codes which cover from stellar evolution to providing light curves. In addition, some hydrodynamical codes and EoS tabulars are also exposed so that one can rearrange their own CCSNe codes. Hence, the exciting era has come for studying CCSNe and I hope this paper may have helped readers who have trouble in studying CCSNe theory for supporting comprehension of theoretical parts and encouraged them to join in this challenging fields.

Acknowledgment

At the very first, I wish to acknowledge my supervisor, Prof. Shoichi Yamada, for giving me a chance to engage in exciting physics researches. None to mention his keen scientific insight, I have been supported by his proper kindness and considerable patients. Besides I have learned many things from his attitude toward studies, especially the importance of passion and challenge which often change situations in better way. It has been, however, one of the most difficult task for him to supervise and advice. My only feeling right now is gratitude.

I also want to thank and apologize two referee, Prof. Keichi Maeda and Prof. Hideyuki Suzuki, for suspending my thesis assessment for a year and many thanks for accepting my referee again.

Next, I wish to thank my collaborators, S. Fujimoto and H. Nagakura. Without their help my first paper would not be accomplished. I also sincerely thank H. Nagakura for keeping on encouraging me with many words and letting me participate in his works.

T. Yoshida has provided many basic idea of nuclear reaction in practical aspects which is very central part of the thesis. He also give me the substantial knowledge of stellar evolution. Let me take this occasion to offer my thanks. I also wish to thank N. Ohnishi for letting me use his hydrodynamic code which owes basic part of the thesis.

All my knowledge about equation of states are yielded by S. Yamada, K. Nakazato, M. Takano, K. Sumiyoshi N. Yasutake and S. Furusawa. They demonstrated the attractive features of nuclear physics and guided me to the entrance of nuclear astrophysics. I am sincerely grateful to their kindness in answering my basic questions.

I am very grateful to current and ex-members of Yamada and Maeda laboratory for letting me join in their stimulating discussions and helping me understand intuitive and vivid picture of the true nature. I am truly fortunate to meet them during my youth age.

Especially the presence of K. Takahashi and R. Hirai, it was also my pleasure to spend much time for not only fruitful word exchanges but also coffee break communication. Owing to their bright personalities, it was much comfortable for me to study in the lab. I also should thank Hirai for helping me solve somehow “ difficult ” computational problems.

I should thank again to the current members in the laboratory since their kindness have pulled me back to the research life. I hope some part of this thesis will assist some of junior colleagues to understand several physics associated with core collapse supernova theory.

I am also grateful to my contemporary colleagues, in other word my precious friends, T. Sanada, B. Shikita, R. Wakebe, M. Oasa and T. Tanaka, for providing many memories of discussions and drinking.

Finally, I will close the remark with my parents ’ great support during my study. Nothing has been done without their patients and encouragements. I also dedicate this thesis to my late grandfathers and my grandmothers who are now bravely fighting against their illness.

Appendix A

Theory and numerics in steller evolution

A.1 Time scales

First, it is prior to investigating the physical properties of stellar interior, especially timescales. There are three typical timescales, i.e. dynamical timescale $\tau_{\rm dyn}$, Kelvin Helmholtz timescale $\tau_{\rm KH}$ nuclear timescale $\tau_{\rm nuc}$. It should be noted that $\tau_{\rm KH}$ is often equivalent to thermal timescale $\tau_{\rm heat}$ which is the typical time scale of thermal conductivity. Each typical time scale is estimated as

$$\tau_{\rm dyn} \sim \sqrt{\frac{R^3}{GM}} \sim 2.0 \times 10^{-2} \left(\frac{R}{R_\odot}\right)^{3/2} \left(\frac{M}{M_\odot}\right)^{-1/2} \text{days} \tag{A.1}$$

$$\tau_{\rm KH} \sim E_{\rm int}/L \sim \frac{GM^2}{2rL} \sim 1.5 \times 10^7 \left(\frac{R}{R_\odot}\right)^{-1} \left(\frac{M}{M_\odot}\right)^{2} \left(\frac{L}{L_\odot}\right)^{-1} \text{years} \tag{A.2}$$

$$\begin{aligned} \tau_{\rm nuc} &\sim \frac{E_{\rm nuc}}{L} \sim 10^{-1} - 10^{-2} \times \frac{XMc^2}{L} \\ &\sim 10^{10} \left(\frac{M}{M_\odot}\right)^{1} \left(\frac{L}{L_\odot}\right)^{-1} \text{years (H burning stage)} \end{aligned} \tag{A.3}$$

along with stellar radius R, total mass M and radiative luminosity L, respectively. If one takes typical solar values, for example, the magnitude relation of three timescales is given as

$$\tau_{\rm nuc} \gg \tau_{\rm KH} \gg \tau_{\rm dyn}. \tag{A.4}$$

Equation (A.4) implies that the most of stellar evolution phase, especially main sequence age, may be safely assumed to be in both hydrostatic and thermal equilibrium. Any disturbance in hydrostatic star should be quenched unless the object is oscillating or start runaway phenomena, e.g. either collapse or explosion. When the system is hydrostatic, the total energy of system is able to achieve the virial theorem which is useful prescription for understanding stellar property. For ideal gases, the energy conservation for the total stellar object can be rewritten as

$$\frac{d}{dt}\left(\frac{\Omega}{2}\right) = L_{\rm nuc} - L - L_\nu \tag{A.5}$$

where Ω is the gravitational energy of entire stellar system. When $L_{\rm nuc}$ is balanced with L the gravitational energy remain unchanged and system can treated as thermal equilibrium,

Table A.1: Nuclear burning stages and time scales. The table is referred to Hix et al.(1999) [178].

Burning Stage	ρ_c ($\mathrm{g\,cm^{-3}}$)	T_c (GK)	τ (yr)	L_{phot} (ergs/s)	L_ν (ergs/s)	Primary Reactions
			For a 1 $M_\odot$star			
Hydrogen	150	0.015	1×10^{10}	3.9×10^{33}	-	PP chain
Helium	2.0×10^{5}	0.15	4×10^{8}	1.6×10^{35}	-	Triple α
			For a 20 $M_\odot$star			
Hydrogen	5.6	0.040	1.0×10^{7}	2.7×10^{38}	-	CNO Cycle
Helium	9.4×10^{2}	0.19	9.5×10^{5}	5.3×10^{38}	$<\times10^{36}$	Triple α
Carbon	2.7×10^{5}	0.81	3.0×10^{2}	4.3×10^{38}	7.4×10^{39}	$^{12}\mathrm{C}+{}^{12}\mathrm{C}\rightarrow{}^{20}\mathrm{Ne}+\alpha$
Neon	4.0×10^{6}	1.7	0.4	4.4×10^{38}	1.2×10^{43}	$^{20}\mathrm{Ne}+\gamma\rightarrow{}^{16}\mathrm{O}+\alpha$
Oxygen	6.0×10^{6}	2.1	0.5	4.4×10^{38}	7.4×10^{43}	$^{16}\mathrm{O}+{}^{16}\mathrm{O}\rightarrow{}^{28}\mathrm{Si}+\alpha$
Silicon	4.9×10^{7}	3.7	0.01	4.4×10^{38}	3.1×10^{45}	$^{28}\mathrm{Si}+7\alpha\rightarrow{}^{56}\mathrm{Ni}$

thus it maintains a constant interior temperature. On the other hand during nuclear depletion, $L_{\mathrm{nuc}} \sim 0$, the binding energy becomes more negative and start to contract. As a consequence, the temperature increases so that luminosity is enhanced and the next energy generation is provided by the further nuclear reaction processes. For instance, the imbalance of source terms induces an expansion of the envelope adjacent to the He core and leads to red giant before helium ignition, hence, the Kelvin-Helmholtz timescale can be regarded as the measure of thermal structure recovery. In general, the dominant time scale of stars is given by the rates of nuclear reaction. But how these timescales change if stellar masses are massive ? Table A.1 shows the some answer to this question. Firstly, when mass of stars are around $1M_\odot$, their life time is almost 10^{10} years and nuclear fusion proceeds only the next helium burning because of low temperature of core T_c. In the case of massive stars the situation becomes quite different. The life time reduced 10^{6-7} years due to those slightly higher T_c and much lower core density ρ_c which leads much smaller opacity therefore higher luminosity.

After the onset of helium burning nuclear fusion takes place one by another if the stellar mass is relatively large. In fact, nuclear burnings in the advanced stages are greatly accelerated by relatively high T_c, due to large neutrino emission (see the discussion in section 2.4.2 below), and timescales achieve less and less, e.g. $\tau_{\mathrm{KH}} \sim \tau_{\mathrm{nuc}}$ as shown in table A.1. As the nuclear burning stage proceeds, onion ring structures finally appear which is consisted of H envelope at the outermost layer and iron core at the innermost layer just before induced-collapse.

Most of all massive stellar evolution codes is based on hydrostatic state under spherical symmetry. The main task of these codes are to calculate the mass conservation, momentum conservation, energy equation, chemical abundances evolution and thermal structure which corresponds to the energy transport from one mass layer to another. The resaon why they cannot, however, perform dynamical simulations in multi-dimension easily is that there is a large gap of time scale between convection overturn and nuclear burning. Furthermore, The acceleration term can be omitted when the typical time scale is dominated by nuclear burning. This inertia term becomes important mainly after the onset of the core collapse and massive star can be discribed as hydrostatic state almost in its entire life. The main difficulty is how to include the effect of the mixing between different layers precisely.

A.2 Convection criterion in MLT

Stars usually generate nuclear burning energy around its center and deposite this extra energy via either thermal conduction or convection. The dominant energy trasport process is determined by the degree of $|dT/dr|$, e.g. the large value for thermal conduction and the small value for convection, which is usually obtained after solving basic equaitons. In fact, it is not apparent how to treat convections since they should result from dynamical fluid motion. Mixing length theory (MLT) is, however, one of the most widely applied in stellar evolution field due to its simple assesment of whether stellar interior is radiatively or convectively dominant. According to this theory, let's consider the displacement of element with keeping entropy and chemical composition unchanged. If one assumes the motion of element is sufficiently slower than sound speed, pressure of element, P_e, is balanced with those of surrounding, P, because the pressure deviation immediately propagates by thermal timescale , thus $P_e = P$. Since surrounding is hydrostatic, the equation of motion at $r = r_0 + \Delta\xi$ is given by

$$\rho \frac{d^2\Delta\xi}{dt^2} = -\Delta\rho g \tag{A.6}$$

where $\Delta\rho = \left(\left(\frac{d\rho}{dr}\right)_e - \frac{d\rho}{dr}\right)\Delta\xi$. Choosing independent thermodynamical variables as (P, S, μ), the equation can be proceeded as

$$\rho \frac{d^2\Delta\xi}{dt^2} = -g\Delta\xi \left(\left(\frac{\partial\rho}{\partial S}\right)\frac{dS}{dr} + \left(\frac{\partial\rho}{\partial\mu}\right)\frac{d\mu}{dr} \right) \tag{A.7}$$

since the deviations with respect to S and μ caused by the displacement is 0. This formulation is often seen in CCSNe theory and indicates that the system is always unstable if dS/dr is negative under no chemical gradient. The situation turns out to be difficult when $d\mu/dr$ is non-zero, e.g. proto-neutron star surface with $\mu = Y_e$.

In contrast, if one considers independent thermodynamical variables as (P, T, μ) instead, the equation can be transformed as

$$\frac{d^2\Delta\xi}{dt^2} = -\frac{g\delta}{H_P}\left(\nabla_e - \nabla + \frac{\phi}{\delta}\nabla_\mu\right) \tag{A.8}$$

$$\nabla = \left(\frac{\partial \ln T}{\partial \ln P}\right) \tag{A.9}$$

$$\nabla_e = \left(\frac{\partial \ln T}{\partial \ln P}\right)_e \tag{A.10}$$

$$\nabla_\mu = \left(\frac{\partial \ln \mu}{\partial \ln P}\right) \tag{A.11}$$

$$\phi = \left(\frac{\partial \ln \rho}{\partial \ln T}\right)_{P,\mu} \tag{A.12}$$

$$\delta = \left(\frac{\partial \ln \rho}{\partial \ln \mu}\right)_{P,T} \tag{A.13}$$

where H_P is scale height; ∇ and ∇_μ are determined by stellar structure while ∇_e is proper to matter, thus EoS, respectively [215]. Therefore, the necessary conditions of unstable (convection driven) and stable (radiation dominant) become following relations:

$$\nabla \gtrless \nabla_e + \frac{\phi}{\delta}\nabla_\mu \tag{A.14}$$

or using $\nabla_{\rm rad}$ and $\nabla_{\rm ad}$,

$$\nabla_{\rm rad} \gtrless \nabla_{\rm ad} + \frac{\phi}{\delta}\nabla_{\mu} \tag{A.15}$$

where upper and lower inequility represent convective unstable and stable, respectively. Equation (A.15) with and without ∇_{μ} term are traditionally called "Leudox criterion" and "Schwarzchild criterion", respectively, and is commonly used for the determination of the right hand side in the energy transport equation.

A.3 Basic equations

In the first of this appendix, one has seen the large difference of timescales in dynamical, Kelvin-Helmoholtz(KH) and nuclear reaction process by large orders of magnitude. Since the one of important interests in astrophysics is the fate of stellar objects which are governed by mainly nuclear reaction process, this situation restricts one to compute in straightforward approach, e.g. running hydrodynamical simulations. Therefore, some simplified treatment is necessary for practical calculations. As a matter of fact, almost all massive stellar evolution codes are based on hydrodynamic equations in one dimension, namely, mass conservation, momentum conservation, energy equation, chemical abundances evolution and energy transport equation which directly relies on temperature structure. The acceleration term can be omitted when the typical time scale is dominated by nuclear burning, while this inertia term becomes important mainly after the onset of the core collapse and massive stars can be described as hydrostatic state almost in its entire life. Hence, the basic equations are represented as following relations:

$$\frac{\partial r}{\partial M_r} = \frac{1}{4\pi r^2 \rho} \tag{A.16}$$

$$\frac{\partial P}{\partial M_r} = \frac{GM_r}{4\pi r^4} - \frac{1}{4\pi r^2}\frac{\partial^2 r}{\partial t^2} \tag{A.17}$$

$$\frac{\partial L}{\partial M_r} = \epsilon_{\rm nuc} - \epsilon_{\nu} + \epsilon_g \tag{A.18}$$

$$\frac{\partial T}{\partial M_r} = -\frac{GM_r T}{4\pi r^4 P}\nabla \tag{A.19}$$

$$\begin{aligned} \nabla &= \nabla_{\rm rad} \qquad \text{if} \quad \nabla_{\rm ad} < \nabla_{\rm rad} \\ &= \nabla_{\rm MLT} \sim \nabla_{\rm ad} \qquad \text{otherwise} \end{aligned} \tag{A.20}$$

$$\frac{\partial Y_k}{\partial t} = \frac{\partial Y_k}{\partial t}_{reac} + \frac{\partial}{\partial M_r}\left((4\pi r^2\rho)^2 D_{\rm mix}\frac{\partial Y_k}{\partial M_r}\right) \tag{A.21}$$

where $\epsilon_{\rm nuc}$ and ϵ_{ν} in the energy conservation are nuclear energy generation and neutrino energy loss, respectively. The term ϵ_g represents energy production or loss from structure contraction or expansion, which is expressed as

$$\epsilon_g = -T\frac{\partial s}{\partial t} \tag{A.22}$$

$$= -c_P\frac{\partial T}{\partial t} + \frac{\delta}{\rho}\frac{\partial P}{\partial t} \tag{A.23}$$

where δ is identified as $\delta = -\left(\frac{\partial \ln \rho}{\partial \ln T}\right)_P$. When the star reaches thermal equilibrium, this term turns out to be 0. The dimensionless variables ∇s used in the energy transport

equation (eq. (A.19)) are given by following relations;

$$\nabla = \frac{d\ln T}{dr}\Big/\frac{d\ln P}{dr} \tag{A.24}$$

$$\nabla_{\rm rad} = \frac{3}{16\pi acG}\frac{\kappa L_r P}{M_r T^4} \tag{A.25}$$

$$\nabla_{\rm ad} = \left(\frac{\partial\ln T}{\partial\ln P}\right)_S = 1 - \frac{1}{\Gamma} \tag{A.26}$$

where Γ is adiabatic index and relies on EoS. This expressions are widely adopted in stellar evolution fields and their magnitude relations are important indicator for mixing process of star interiors. It should be emphasized that $\nabla_{\rm MLT}$ is given by mixing-length theory (MLT) and one will see it is almost same as $\nabla_{\rm ad}$ (see the end of this appendix).

The time derivatives appear in momentum, energy and chemical abundance equations , however,each of them are characterized by typical time scales which are mentioned in previous section. It should be stressed once more that the most typical timescale in stellar evolution is $\tau_{\rm nuc}$ and as long as this secular time is sufficiently large, one can isolate the chemical abundance evolution from the rest of conservation equations.

When one attempts to solve momentum conservation, the inertia term $\partial^2 r/\partial t^2$ is normally omitted except for collapse epoch since bulk motion is rapidly stabilized in dynamical time scale τ_{dyn}. As a consequence, in most of stellar evolution phases hydrostatic equilibrium is good approximation. For another time derivative term ϵ_g appears in the energy conservation which changes with $\tau_{\rm KH}$. If thermal equilibrium is established, e.g. main-sequence stage, then ϵ_g can be neglected and the energy equation reduces to ordinary differential equaitons (ODEs). Moreover, in all advance burnings, such as carbon, oxygen and silicon core burnings, neutrino loss L_ν rules the cooling effect rather than radiation luminosity L and balances with $L_{\rm nuc}$. As a result, energy release from structure change is almost negligible. Then ϵ_g can be separated from hydrostatic (eq.A.17) in numerical calculation (see the next section for details).

As a matter of fact, one may already noticed that the timescales are crucial to stellar evolution and approximating the governing equations. However, many situations are not as evident as the main-sequence stages, for instance,

(1) RG phase (density gradient change over quite wide range),

(2) rather rapid evolution, thus $\tau^{\rm (c)}_{\rm heat} \ll \tau_{\rm ev} \ll \tau^{\rm (env)}_{\rm heat}$), where $\tau_{\rm ev}$ is evolution time scale and $\tau^{\rm (c)}_{\rm heat}$ and $\tau^{\rm (env)}_{\rm heat}$ are heating transfer timescale of core and envelope, respectively. The thermal conductivity time scale $\tau_{\rm heat}$ is evaluted as following relations:

$$\tau_{\rm heat} \sim 4\pi r^2 H_P \rho C_P T/L_{\rm rad}$$

$$= \frac{H_P\rho C_P T}{(4acT^4/3\kappa\rho H_P)} \tag{A.27}$$

$$= 3C_P\kappa\rho^2 H_P^2/4acT^3, \tag{A.28}$$

where κ and C_P denote opacity and heat conductivity, respectively. Such situation frequently appears in large neutrino loss, unstable nuclear flash, rapid mass accretion and the adjacent mass shell to core,

(3) dynamical collapse or explosion,

(4) transition from quasi static ($\tau \sim 10^3$yrs) to dynamical phase ($\tau \sim$ 1sec),

(5) the total mass evolution which is attributed to regriding mesh point in Lagrange frame and

(6) the mass change of stellar core , e.g. shell burning and/or convective penetration.

Therefore, the dominant time scales may be different from each individual grids and the equations are stiff for which the implicit method seems to be suitable. The accuracy and stability, however, highly depend on the numerical treatment so that calculation of stellar evolution is rather challenging issue as well as its pure physics [405].

A.4 Numerical strategy

For the centeral portion of star the inner boundary values of P and T should be given while R and L should be determined at the surface of star. In post-main sequence phase, however, one encounters the insensitive of the structure change to surface boundary values and it is quite difficult to obtain the complete stellar structure by shooting method. The strategy of computing the basic equations is follows; the independent variable is chosen as $x_k = \ln M_r$ while $4+N_{\rm nuc}$ dependent variables are rewritten as $y^{(n)}_{1,k} = \ln P$, $y^{(n)}_{2,k} = \ln r$, $y^{(n)}_{3,k} = \ln T$, $y^{(n)}_{4,k} = \ln L$ and $\ln Y_{{\rm numb},\,j}$ $(j = 1, N_{\rm nuc})$. These reformulated relations are solved along with equation of state (EoS). The superscript n and subscript k denote the number of time steps and spacial grid points, respectively. Hereafter, subscript is represents the 4 components of variables $y_{i,k}$. The RHS terms of the basic equations (eq.A.16 - A.19) are treated as function of ρ and T whereas ϵ_g and acceleration term $\partial^2 r/\partial t^2$ are derived by difference method [405]. For the first step, spatial ODEs from eq.(A.16) to eq.(A.19) are solved simultaneously with fixed time n and the fixed compositions $Y^{(n)}_{{\rm numb},\,j}$. It is convenient to rewrite these equations as following forms;

$$\frac{\partial y_i}{\partial x} = f_i(y, x), \tag{A.29}$$

thus the difference equation can be written as

$$\frac{y^{(n)}_{i,k+1} - y^{(n)}_{i,k}}{x_{k+1} - x_k} = \beta_i f_i(y^{(n)}_k, x_k) + (1 - \beta_i) f_i(y^{(n)}_{k+1}, x_{k+1}), \tag{A.30}$$

where each β corresponds to a degree of implicit scheme with respect to spatial difference. The explicit method is suitable for rapid evolution, e.g. thermal instability, dynamical collapse and even extensive neutrino loss, while the implicit method is favorable for relatively slow evolution, e.g. nuclear burning. Instead of preparing large matrix, these equations can be solved much more efficient by employing Heney method. More detailed discussions are represented in the next section and also, for instance, [404, 405, 339].

It should be stressed that the variation of solutions result from the parameter varieties in Henyey method. Unless numerical instabilities take place, the choice of β_i may be favorable for taking 1/2 in terms of accuracy. When the nuclear time scale is comparable to the other timescales, e.g. the thermal conductivity after a termination of He burning, β_i should be altered to either 0 or 1 otherwise one should keep $\beta_i = 0$ or 1 from the beginning of calculation so as to ensure the numerical stabilities. As a matter of fact, there is no convincible choice of the parameter sets so that each groups engaged in stellar

calculaiton choose their own parameter sets individually. A treatment of the time derivative terms is also an important issue. These terms, especially the acceleration, cause numerical oscillation which violates structure evolution seriously. Paying attention to the time scales, some groups exclude d^2r/dt until the temperature reaches the certain value which competes with dynamical time scales whereas other groups include it only inside C/O core region.

A.5 Henyey method

As already introduced in the previous section, the basic equations are represented as

$$\frac{\partial y_i}{\partial x} = f_i(y, x) \tag{A.31}$$

where the independent variable $x_k = \ln M_r$ where as dependent variables y_i $(i = 1, 4)$ are defined as

$$y_{1,k}^{(n)} = \ln P, \tag{A.32}$$
$$y_{2,k}^{(n)} = \ln r, \tag{A.33}$$
$$y_{3,k}^{(n)} = \ln T, \tag{A.34}$$
$$y_{4,k}^{(n)} = \ln L, \tag{A.35}$$

and equation (A.31) can be rewritten with parameter β_i in a following formulation:

$$\frac{y_{i,k+1}^{(n)} - y_{i,k}^{(n)}}{x_{k+1} - x_k} = \beta_i f_i(y_k^{(n)}, x_k) + (1 - \beta_i) f_i(y_{k+1}^{(n)}, x_{k+1}). \tag{A.36}$$

Since we are concerned with extremely long timescale, implicit or semi-implicit method should be selected so that eq. (A.36) for next time step is represented as

$$\frac{y_{i,k+1}^{(n+1)} - y_{i,k}^{(n+1)}}{x_{k+1} - x_k} = \beta_i f_i(y_k^{(n+1)}, x_k) + (1 - \beta_i) f_i(y_{k+1}^{(n+1)}, x_{k+1}) \tag{A.37}$$
$$= \beta_i f_i(y_k^{(n)} + \delta y_k, x_k) + (1 - \beta_i) f_i(y_{k+1}^{(n)} + \delta y_{k+1}, x_{k+1}) \tag{A.38}$$
$$= \beta_i \left(f_i(y_k^{(n)}, x_k) + \left(\frac{\partial f_i}{\partial y_j} \right)_k \delta y_{j,k} \right)$$
$$+ (1 - \beta_i) \left(f_i(y_{k+1}^{(n)}, x_{k+1}) + \left(\frac{\partial f_i}{\partial y_j} \right)_{k+1} \delta y_{j,k+1} \right) \tag{A.39}$$

where $y_i^{(n+1)} = y_i^{(n)} + \delta y_i$. Hence, the objective is now pinned down to solving δy so that $4k_{max}$ linear equations are fulfilled with the following relation along with $\Delta x_k = x_{k+1} - x_k$;

$$0 = \left(\beta_i \Delta x_k \left(\frac{\partial f_i}{\partial y_j} \right)_k + \delta_{ij} \right) \delta y_{j,k}$$
$$+ \left((1 - \beta_i) \Delta x_k \left(\frac{\partial f_i}{\partial y_j} \right)_{k+1} - \delta_{ij} \right) \delta y_{j,k+1}$$
$$+ \left(\beta_i \Delta x_k f_i(y_k^{(n)}, x_k) + (1 - \beta_i) \Delta x_k f_i(y_{k+1}^{(n)}, x_{k+1}) \right) - y_{i,k+1}^{(n)} + y_{i,k}^{(n)}, \tag{A.40}$$

or, for alternative forms,

$$
\begin{aligned}
0 &= A_{ij,k}\delta y_{j,k} + B_{ij,k}\delta y_{j,k+1} + d_{i,k}, && \text{(A.41)}\\
A_{ij,k} &= \left(\beta_i \Delta x_k \left(\frac{\partial f_i}{\partial y_j}\right)_k + \delta_{ij}\right),\\
B_{ij,k} &= \left((1-\beta_i)\Delta x_k \left(\frac{\partial f_i}{\partial y_j}\right)_{k+1} - \delta_{ij}\right)\delta y_{j,k+1},\\
d_{i,k} &= \left(\beta_i \Delta x_k f_i(y_k^{(n)}, x_k) + (1-\beta_i)\Delta x_k f_i(y_{k+1}^{(n)}, x_{k+1})\right) - y_{i,k+1}^{(n)} + y_{i,k}^{(n)}.
\end{aligned}
$$

Usually the maximum number of spatial grid is given as large value so that the solution of $4k_{max} \times 4k_{max}$ inverse matrix needs huge computational cost. Equation (A.42), however, shows that the non-zero matrix elements is only concentrated around diagonal regularly so that the large matrix is characterized as band matrix. Furthermore, if $\delta y_{3,k-1}$, $\delta y_{4,k-1}$, $\delta y_{1,k}$ and $\delta y_{2,k}$ are put together in one group, one will find the interesting relations below;

$$
\left\{
\begin{array}{llllll}
0 &= A_{3j,k-1}\delta y_{j,k-1} &+B_{3j,k-1}\delta y_{j,k} &+0\cdot\delta y_{j,k+1} &+d_{3,k-1},\\
0 &= A_{4j,k-1}\delta y_{j,k-1} &+B_{4j,k-1}\delta y_{j,k} &+0\cdot\delta y_{j,k+1} &+d_{4,k-1},\\
0 &= 0\cdot\delta y_{j,k-1} &+A_{1j,k}\delta y_{j,k} &+B_{1j,k+1}\delta y_{j,k+1} &+d_{1,k},\\
0 &= 0\cdot\delta y_{j,k-1} &+A_{2j,k}\delta y_{j,k} &+B_{2j,k+1}\delta y_{j,k+1} &+d_{2,k},
\end{array}
\right. \qquad \text{(A.42)}
$$

so that the equations turn out to be recursive form, i.e.

$$
\begin{aligned}
\mathbf{S}_{k-1}\cdot\delta y_{k-1} + \mathbf{P}_k\cdot\delta y_k &= \mathbf{Q}_k\cdot\delta y_{k+1} + q_k, && \text{(A.43)}\\
\mathbf{S}_{k-1} &= \begin{pmatrix} A_{31,k-1} & A_{32,k-1} & A_{33,k-1} & A_{34,k-1}\\ A_{41,k-1} & A_{42,k-1} & A_{43,k-1} & A_{44,k-1}\\ 0 & 0 & 0 & 0\\ 0 & 0 & 0 & 0 \end{pmatrix}, && \text{(A.44)}\\
\mathbf{P}_k &= \begin{pmatrix} B_{31,k-1} & B_{32,k-1} & B_{33,k-1} & B_{34,k-1}\\ B_{41,k-1} & B_{42,k-1} & B_{43,k-1} & B_{44,k-1}\\ A_{11,k} & A_{12,k} & A_{13,k} & A_{14,k}\\ A_{21,k} & A_{22,k} & A_{23,k} & A_{24,k} \end{pmatrix}, && \text{(A.45)}\\
\mathbf{Q}_k &= -\begin{pmatrix} 0 & 0 & 0 & 0\\ 0 & 0 & 0 & 0\\ B_{11,k} & B_{12,k} & B_{13,k} & B_{14,k}\\ B_{21,k} & B_{22,k} & B_{23,k} & B_{24,k} \end{pmatrix}, && \text{(A.46)}\\
q_k &= -\begin{pmatrix} d_{3,k-1}\\ d_{4,k-1}\\ d_{1,k}\\ d_{2,k} \end{pmatrix}. && \text{(A.47)}
\end{aligned}
$$

If new matrix $\mathbf{R}_k$ and vector r_k which fulfill

$$
\begin{aligned}
\mathbf{R}_k &= \left(\mathbf{S}_{k-1}\cdot\mathbf{R}_{k-1} + \mathbf{P}_k\right)^{-1}\cdot\mathbf{Q}_k, && \text{(A.48)}\\
r_k &= \left(\mathbf{S}_{k-1}\cdot\mathbf{R}_{k-1} + \mathbf{P}_k\right)^{-1}\cdot\left(q_k - \mathbf{S}_{k-1}\cdot r_{k-1}\right), && \text{(A.49)}
\end{aligned}
$$

are introduced, more convenient formula are available, i.e.

$$
\delta y_k = \mathbf{R}_k\cdot\delta y_{k+1} + r_k, \qquad \text{(A.50)}
$$

so that the sequence equations connect the stellar center of δy with surface grid of δy. As a consequence, the problem becomes much easier and the procedure keeps on ascending by substituting $y_k^{(n)}$ for $\widetilde{y_k}^{(it)}$ and updating $\widetilde{y_k}^{(it+1)} = \widetilde{y_k}^{(it)} + \delta y_k$ until δy_k is converged to 0 for all k which means that the values $\widetilde{y_k}$ are safely identified as $y_k^{(n+1)}$. This approach is well known as Henyey elimination method and has been employed for standard calculation in the stellar evolution field.

It should be noted that if matrix elements $A_{jj'} = 0$ in all j component, $y_{j'}$ can be separated from the other components. Sugimoto (1970) [404] and Sugimoto et al.(1981) [405] proposed the numerical technique for constructing solution in order to avoid numerical instability. In fact, if one choose $\beta_3 = 0, \beta_4 = 1$ or $\beta_3 = 1, \beta_4 = 0$ for heat conduction and $\beta_1 = 0, \beta_2 = 1$ or $\beta_1 = 1, \beta_2 = 0$ for dynamical collapse, the calculation is guaranteed to run stably. These fact can be understood by considering the eigen values of δy_i, $\lambda_\pm$, which is given by

$$\lambda_\pm \sim \left(\frac{\tau_s(r)}{U\Delta t}\right)^{1/2} + O(1) \tag{A.51}$$

$$U = \frac{d\ln M_r}{d\ln r} \tag{A.52}$$

$$\tau_s(r) = \frac{r}{c_s} \tag{A.53}$$

where c_s is sound speed and $\Delta t = t^(n+1) - t^(n)$. Furthermore, it should be noted that the stability conditions of implicit method and explicit scheme impose $\Delta \gtrsim \tau_s(r)$ and $\Delta \lesssim \tau_s(\Delta r)$, respectively. As a matter of fact, the scheme is safely applicable to implicit one so that one only needs to examine the latter condition, i.e. $\Omega = \left(\frac{\tau_s(r)}{U\Delta t}\right)$ is the extremely large case. In accordance with the two studies, when β_is are given the appropriate values, the leading term of matrix components of $\mathbf{R}$ contributes to the solution of the explicit one which generates neither heat nor rarefaction wave propagation while the rest of terms are propotional to Ω^{-2} and rapidly vanish. Hence, the scheme become suitable for both slow and rapid evolution, respectively. Once the structure is determined by above procedures, one should evolve the chemical abundances from $t^{(n)}$ to $t^{(n+1)}$ in implicit method with both reaction and diffusion, update the information of EoS and convection criterion, if necessary, and repeat the procedure until the termination of calculation.

It is interesting that there is an alternative method for evoluting after carbon-oxgen burning instead of Henyey elimation (Sugimoto 2011 in private communication). In the late burning stages energy loss is dominated by pair and plasmon neutrino process ($T > 5 \times 10^8$K) rather than the radiative process around the core. As a result, the energy conservation is balanced solely between the nuclear energy generations and neutrino energy loss. Since the positive energy source is now less ineffcient, the net energy gain is negative and dS/dt is less important than past evolution phases . Instead of indetifying $\ln L_r$ as an independent variable, entropy S is developed so that the two equations, eq. (A.18) and (A.19) can be discarded from the basic equaitons. The latter equation, the spatial distribution of T, are replaced with EoS since $S(M_r)$, $P(M_r)$ and chemical elements are given. Therefore, the implicit calculations are reduced to only two variables, i.e. $\ln P$ and $\ln r$, which will be much easier to handle the evolution of the massive star. Since the numerical treatment alters to explicit scheme, the time interval should be chosen properly to suppress the time derivative terms, i.e. dS/dt and d^2r/dt. Note that if the calculation region extends outside the active L_ν, the varition of L_r is still responsible for energy transfer

so that this method is no longer valid, e.g. outer region from He/C interface.

A.6 Mixing length theory

One of the problems in calculation is the presence of the term ∇ in the right hand side of energy transport equation which is still unknown function. To close the basic equations, it is quite obvious for the radiation dominant case ($\nabla = \nabla_{\rm rad}$). In contrast, when the convection become important in the energy transport, one has to add an advection energy flux of moving element. Hence, the heat transport suppose to be modified in following equations

$$F_{tot} = F_{\rm rad} + F_{\rm conv} \tag{A.54}$$

$$F_{\rm rad} = \frac{4acG}{3}\frac{M_r T^4}{\kappa P r^2}\nabla_{\rm rad} \tag{A.55}$$

$$F_{\rm conv} = \rho c_P v_{\rm conv} \delta T \tag{A.56}$$

where c_P is heat capacity at constant P and $v_{\rm conv}$ is the convective speed. Then the problem is pinned down to how to express ∇ as function of $\nabla_{\rm ad}$, $\nabla_{\rm rad}$ and EoS properties to obtain the solution. It is well known that mixing length theory (MLT) is available for closing the equations. The idea of MLT is given as follows; a blob in a convective unstable layer floats up from the bottom, dissipates its energy by the thermal condution and totally mixes up with surronding after it travels along a certain distance. In eq. (A.19), the convection stability condition adopts Schwartzchild criterion while there is another condition called Ledoux criterion which includes the stabilization of mean molecular weight on convection which has been already remarked in section A.2. Ledoux criterion is usually stricter than Schwaltzchild criterion. These two conditions are often used in many stellar evolution code and affect the stellar structure dramatically. Mixing length parameter $\alpha_{\rm mix} = l_{\rm mix}/H_P$ are often determined by solar stars and usually in order of unity.

If one follows the procedure written in Kippenhahn (1990) [215], the convection heating transport can be represented as

$$F_{\rm conv} = \rho c_P T \left(\frac{l_{\rm mix}}{2H_P}\right)^2 \sqrt{\frac{1}{2} g \left(\frac{\partial \ln P}{\partial \ln T}\right)_{\rho,\mu}} H_P (\nabla - \nabla_e)^{3/2}, \tag{A.57}$$

$$v_{\rm conv} = \sqrt{\frac{1}{8} g \left(\frac{\partial \ln P}{\partial \ln T}_{\rho,\mu}\right)_{\rho,T} \frac{l_{\rm mix}^2}{H_P}} (\nabla - \nabla_e), \tag{A.58}$$

$$\frac{\nabla_e - \nabla_{\rm ad}}{\nabla - \nabla_e} = \frac{6acT^3}{\kappa \rho^2 c_P l_{\rm mix} v_{\rm conv}}, \tag{A.59}$$

where ∇_e is gradient property of the blob element and assuming that the temperature of the blob element is smoothed by the radiative conduction.

Finally, by eliminating ∇_e, the equation becomes a cubic equation

$$(\xi - U)^3 + \frac{8U}{9}(\xi^2 - U^2 - W) = 0 \tag{A.60}$$

$$\xi^2 - U^2 = \nabla - \nabla_{\rm ad} \tag{A.61}$$

$$U = \frac{3acT^3}{\kappa \rho^2 c_P l_{\rm mix}^2} \sqrt{\frac{8H_P}{g(\partial P/\partial T}_{\rho,\mu}} \tag{A.62}$$

$$W = \nabla_{\rm rad} - \nabla_{\rm ad} \tag{A.63}$$

which enables to obtain ∇. This cubic equation is associated with simplified turbulence eddy motions. However, it is well known that superadiabaticity $\nabla - \nabla_{\rm ad}$ is extremely small when convection is dominant. If one takes typical values of the hydrostatic stellar interior as

$$\rho \sim \frac{3M}{4\pi R^3},\ c_P T \sim \frac{\Gamma}{\Gamma - 1} P, \sqrt{g H_P} = \sqrt{\frac{P}{\rho}},\ P \sim \frac{GM}{R} \tag{A.64}$$

an simple order estimation of $\nabla - \nabla_{\rm ad}$ is given as

$$\nabla - \nabla_{\rm ad} \sim 10^{-8} \left(\frac{L}{L_\odot}\right)^{2/3} \left(\frac{M}{M_\odot}\right)^{-5/3} \left(\frac{R}{R_\odot}\right)^{5/3} \tag{A.65}$$

by considering the balance between $F_{\rm conv}$ and $L/4\pi R^2$. This fact implies that the convection carries away energy so efficient that only small velocity is required ($v_{\rm conv} \sim 10^{-4} c_s$). In many practical simulations, superadiabaticity yields similar negligible order ($10^{-5} - 10^{-7}$) and even multi-dimensional calculation showed 10^{-4} in amplified turbulent convection zone [272, **?**]. Hence, when the part of stellar interior fulfill the Schwartzchild instabilty condition, ∇ can be safely substituted for $\nabla_{\rm ad}$. Nevertheless, one still has to solve this equation due to the estimation of diffusion coefficient which is associated with Brunt-Väisälä frequency in the chemical abundance evolution.

Appendix B

Neutrino transport solvers

If one desires to handle beyond the simplified neutrino treatment, e.g. the light bulb approximation [325] or analytical heating source [291], it is inevitable to employ neutrino transport solver. From eq.(2.23) in section. 2.2, the heating rate is consisted of three important components, i.e. neutrino luminosity, neutrino averaged energy and averaged flux factor and these physical variables are completely relevant to the neutrino distribution emitted from PNS surface and also each grid of matters. Moreover, the canonical explosion energy is different by two orders of magnitude less than gravitational energy which implies that the severe numerical accuracy, e.g. much less than 1%, is required for the neutrino heating mechanism.

It is well known that neutrino is safely treated as free streaming particle through transparent regime while its propagation obeys diffusion process inside the neutrino sphere. The main concern of CCSNe modelers is, thus, concentrated on how to handle semi-opaque regime where the neutrino distribution function deviates from Fermi-Dirac which should be carefully treated by Boltzmann equation as well as radiation transfer equation. Furthermore, since neutrino cross sections, σ_ν, rely on its own energy, i.e.

$$\sigma_\nu \propto \varepsilon^2, \tag{B.1}$$

the neutrino sphere should be defined in each energy in principle so that larger amount of high energy components may be emitted and it may enhance the average energy. Although the methodology in this paper is irrespective of realisitic neutrino transport since the aim is to conduct the experimental study, it is still significantly important to understand what kind of numerical schemes are commonly adopted and how to interpret their outcomes.

It seems that the background physics and numerical techniques often leads to serious trouble and confusion for non-experts. Therefore, this section is dedicated to those readers by starting short review of radiation transport and presenting the comparison of state-of-the-art neutrino tranport solvers in the end.

There are a enormous number of text books and previous works for radiation hydrodynamics. Here, I just hold on enumerating excellent references of neutrino transports and mainly focus on the comparison of different methods utilized in CCSNe theory. See several text books [349, 285, 65] for the fundamental concept for the radiation transport and introduction part of papers [248, 328, 409, 345, 202, 368] for its significant improvement history in CCSNe. It is fortunate for japanese readers that there are also helpful documents provided by Kotake and Suzuki (lecture note;[**?**]) and Ohnishi (article; [**?**]).

B.1 Radiation transfer equations

Instead of giving neutrino distribution function f_ν by hand, e.g. $f_\nu = f_\nu^{(\mathrm{eq})}$ (Fermi-Dirac), let's first start from introducing the governing equation of f_ν;

$$\frac{1}{c}\frac{\partial f}{\partial t} + \frac{\partial f}{\partial s} = \left[\frac{1}{c}\frac{\delta f}{\delta t}\right]_{\mathrm{collision}}, \tag{B.2}$$

where the variable s represents the path length of neutrino and it is well known as Boltzmann equation (or Boltzmann transfer equation; BTE). The left hand side of eq.(B.2) infers the advection whereas the right hand side is source term which is usually called collision term. The collision term is consisted of creation and destruction reaction process, e.g. absorption, emission and scattering.

If coordinate and momentum are chosen as cartesian x^i and as p^i, respectively, and general relativity effect is ignored, $\partial/\partial s$ can be regarded as

$$\begin{aligned}\frac{\partial}{\partial s} &= \frac{\partial x^i}{\partial s}\frac{\partial}{\partial x^i} + \frac{\partial p^i}{\partial s}\frac{\partial}{\partial p^i} &\text{(B.3)}\\ &= \frac{\partial x^i}{\partial s}\frac{\partial}{\partial x^i} &\text{(B.4)}\end{aligned}$$

since neutrino feels no external force. If one considers only isoenergetic scattering takes place for simplicity, the neutrino distribution function is subjected to following equation:

$$\begin{aligned}\frac{1}{c}\frac{\partial f_\nu}{\partial t} + \boldsymbol{n}\cdot\nabla f_\nu &= j_\nu\left(1-f_\nu\right) - \frac{1}{\lambda_\nu}f_\nu \\ &+ \iint d\mu' d\phi \frac{\nu^2}{c(2\pi\hbar c)^3}\mathcal{R}_{\mathrm{IS}}^0(\cos\theta)\left(f_\nu(\mu') - f_\nu(\mu)\right)\end{aligned} \tag{B.5}$$

where superscript ' denotes an initial state symbol and $\boldsymbol{n} = \boldsymbol{x}/s$ is the normalized propagtion direction, j_ν and λ_ν are emissivity and mean free path of absorption, respectively.

The integration term in the right hand side is contribution of iso-scattering process: $\mathcal{R}_{\mathrm{IS}}^0$ is iso-scattering kernel and $\cos\theta$ is given as

$$\cos\theta = \boldsymbol{n}\cdot\boldsymbol{n}' = \mu\mu' + \left(\left(1-\mu^2\right)\left(1-\mu'^2\right)\right)^{1/2}\cos\left(\phi-\phi'\right). \tag{B.6}$$

Note that if the right hand side in eq.(B.5) becomes zero, neutrino settele on chemical equilibrium so that f_ν is equivalent to $f_\nu^{(\mathrm{eq})}(\mu, T)$, where T and μ are matter temperature and chemical potential of neutrino, respectively. The chemical potential is balanced with elements which are relevant to charged current process. It is convenient for further discussion to introduce new scattering kernel $\phi\left(\boldsymbol{n}, \boldsymbol{n}'\right)$;

$$\begin{aligned}\phi\left(\boldsymbol{n},\boldsymbol{n}'\right) &= \frac{1}{\sigma_\nu^{(\mathrm{sc})}}\frac{d\sigma_\nu^{(\mathrm{sc})}}{d\Omega} &\text{(B.7)}\\ \int d\Omega'\ \mathcal{R}_{\mathrm{IS}}^0\ (\cdots) &= \kappa_\nu^{(\mathrm{sc})}\int d\Omega'\ \frac{1}{\sigma_\nu^{(\mathrm{sc})}}\frac{d\sigma_\nu^{(\mathrm{sc})}}{d\Omega'}\ (\cdots) \\ &= \kappa_\nu^{(\mathrm{sc})}\int d\Omega'\ \phi\left(\boldsymbol{n},\boldsymbol{n}'\right)\ (\cdots) &\text{(B.8)}\\ \kappa_\nu^{(\mathrm{sc})} &\sim \rho\sigma_\nu^{(\mathrm{sc})} &\text{(B.9)}\end{aligned}$$

where $\sigma_\nu^{(\mathrm{sc})}$ and $\kappa_\nu^{(\mathrm{sc})}$ are scattering cross section and coeffecient, respectively. It is apparent from eq. (B.7) and (B.8) that $\phi\left(\boldsymbol{n},\boldsymbol{n}'\right)$ indicates that the probability density of scattering direction holds symmetry and normalized by solid angle, thus

$$\phi\left(\boldsymbol{n},\boldsymbol{n}'\right) = \phi\left(\boldsymbol{n}',\boldsymbol{n}\right) \tag{B.10}$$

$$\int d\Omega'\,\phi\left(\boldsymbol{n},\boldsymbol{n}'\right) = 1 = \int d\Omega\,\phi\left(\boldsymbol{n},\boldsymbol{n}'\right). \tag{B.11}$$

By defining Specific intensity, I_ν, as

$$dE_\nu = I_\nu \boldsymbol{n}\cdot d\boldsymbol{S} d\nu d\Omega dt, \tag{B.12}$$

$$I_\nu = c\,h\nu\,g\,\frac{\nu^2}{(hc)^3}\,f_\nu, \tag{B.13}$$

where g is the degeneracy. The physical meaning of I_ν corresponds to neutrino energy traveling in direction $\boldsymbol{n}$ per area per time per solid angle per frequency so that dE_ν in eq. B.12 is the amount of neutrino energy crossing through dS confined to an element of solid angle $d\Omega$, during a time dt and in frequency interval $d\nu$.

As a consequence, eq. (B.5) can be rewritten into the radiation transfer equation;

$$\begin{aligned}\frac{1}{c}\frac{\partial I_\nu}{\partial t} + \boldsymbol{n}\cdot\nabla I_\nu &= \eta_\nu - \kappa_\nu^{(\mathrm{ab})} I_\nu \qquad\qquad (\mathrm{B.14})\\ &- \kappa_\nu^{(\mathrm{sc})} I_\nu \int d\Omega'\,\phi\left(\boldsymbol{n},\boldsymbol{n}'\right) + \kappa_\nu^{(\mathrm{sc})}\int d\Omega'\,\phi\left(\boldsymbol{n},\boldsymbol{n}'\right) I_\nu\left(\mu'\right)\\ &= \eta_\nu - (\kappa_\nu^{(\mathrm{ab})} + \kappa_\nu^{(\mathrm{sc})}) I_\nu + \kappa_\nu^{(\mathrm{sc})}\int d\Omega'\,\phi\left(\boldsymbol{n},\boldsymbol{n}'\right) I_\nu\left(\mu'\right) \qquad (\mathrm{B.15})\end{aligned}$$

or, since the coordinate is cartesian,

$$\frac{1}{c}\frac{\partial I_\nu}{\partial t} + \nabla\cdot(\boldsymbol{n} I_\nu) = \eta_\nu - (\kappa_\nu^{(\mathrm{ab})} + \kappa_\nu^{(\mathrm{sc})}) I_\nu + \kappa_\nu^{(\mathrm{sc})}\int d\Omega'\,\phi\left(\boldsymbol{n},\boldsymbol{n}'\right) I_\nu\left(\mu'\right) \tag{B.16}$$

where η_ν, $\kappa_\nu^{(\mathrm{sc})}$ are emissvity and absorption coeffecient, respectively. It should be noted that the equation (B.15) takes into acount only isoenergetic process for scattering and one should add either incoherent scattering or pair-creation/anhilation reactions for more general cases (see table 2.4 in section 2.2).

Using this specific intensity given by eq. (B.13, one can discuss matter interaction based on Euler equations via energy-momentum tensor $T^{\alpha\beta}_{\mathrm{rad}}$;

$$T^{\alpha\beta}_{\mathrm{rad}\,\nu} = \frac{1}{c}\int d\Omega d\nu\, n^\alpha n^\beta I_\nu \tag{B.17}$$

where suffix α and β denote space-time components, respectively, and n^α is null vector. From this representation, monochromatic energy density $T^{0\,0}_{\mathrm{rad}\,\nu} = E_\nu$, energy flux $T^{0\,i}_{\mathrm{rad}\,\nu} = F^i_\nu$ and radiative pressure $T^{i\,j}_{\mathrm{rad}\,\nu} = P^{ij}_\nu$ are naturally determined and taking the zeroth and first momentum equations in terms of $\boldsymbol{n}$, i.e. operating $\int d\Omega\,1$ and $\int d\Omega\,\boldsymbol{n}$ to eq. (B.16), one obtains

$$\frac{\partial E_\nu}{\partial t} + \nabla\cdot\boldsymbol{F}_\nu = 4\pi\eta_\nu - \kappa_\nu^{(\mathrm{ab})} c E_\nu \tag{B.18}$$

$$\frac{1}{c}\frac{\partial \boldsymbol{F}_\nu}{\partial t} + c\nabla\cdot\boldsymbol{P}_\nu = -\chi_\nu \boldsymbol{F}_\nu \tag{B.19}$$

where $\chi_\nu = \kappa_\nu^{(\mathrm{ab})} + \kappa_\nu^{(\mathrm{sc})}$. It is interesting that the integral scattering term vanishes due to the generic trends of $\phi(\boldsymbol{n}, \boldsymbol{n}')$, i.e. eq. (B.10) and eq. (B.11), and assumption of forward-backward scattering balance.

Equation (B.18) and (B.19) are description for a single frequency ν so that, by summing up (integrating) all frequencies, one obtain following relations:

$$\frac{\partial E_{\mathrm{rad}}}{\partial t} + \nabla \cdot \boldsymbol{F}_{\mathrm{rad}} = \int d\nu \left(4\pi\eta_\nu - \kappa_\nu^{(\mathrm{ab})} c E_\nu\right) \equiv G^0 \tag{B.20}$$

$$\frac{1}{c}\frac{\partial \boldsymbol{F}_{\mathrm{rad}}}{\partial t} + c\nabla \cdot \boldsymbol{P}_{\mathrm{rad}} = -\int d\nu\, \chi_\nu \boldsymbol{F}_\nu \equiv c\,\boldsymbol{G} \tag{B.21}$$

where E_{rad}, $\boldsymbol{F}_{\mathrm{rad}}$ and $\boldsymbol{P}_{\mathrm{rad}}$ are neutrino energy density, energy flux density and pressure, respectively, as well as radiation.

Recalling that the divergence of total energy-momentum tensor $T^{\alpha\beta}_{\mathrm{tot}} = T^{\alpha\beta}_{\mathrm{mat}} + T^{\alpha\beta}_{\mathrm{rad}}$ is zero;

$$T^{\alpha\beta}_{\mathrm{tot}\,;\,\beta} = T^{\alpha\beta}_{\mathrm{mat}\,;\,\beta} + T^{\alpha\beta}_{\mathrm{rad}\,;\,\beta} = 0 \tag{B.22}$$

then in Newton limit, which impose gravitational weak field and relatively slow bulk velocity, the expression can be rewritten as

$$\frac{\partial}{\partial t}\left(\rho e + \frac{1}{2}\rho v^2 + E_{\mathrm{rad}}\right) + \nabla \cdot \left(\left(\frac{1}{2}\rho v^2 + \rho h\right)\boldsymbol{v} + \boldsymbol{F}_{\mathbf{rad}}\right) = -\rho \boldsymbol{v} \cdot \nabla\phi \tag{B.23}$$

$$\frac{\partial}{\partial t}\left(\rho \boldsymbol{v} + \frac{1}{c^2}\boldsymbol{F}_{\mathbf{rad}}\right) + \nabla \cdot (\rho \boldsymbol{v}\boldsymbol{v} + \boldsymbol{P}_{\mathrm{rad}}) + \nabla p = -\rho \nabla\phi \tag{B.24}$$

where ρ, e, p, h and $\boldsymbol{v}$ correspond to density, specific internal energy density, pressure, specific enthalpy density and bulk velocity of matter, respectively. As a consequence, the interaction between matter and radiation can be represented as

$$\frac{\partial}{\partial t}\left(\rho e + \frac{1}{2}\rho v^2\right) + \nabla \cdot \left(\left(\frac{1}{2}\rho v^2 + \rho h\right)\boldsymbol{v}\right) = -G^0 - \rho \boldsymbol{v} \cdot \nabla\phi \tag{B.25}$$

$$\frac{\partial}{\partial t}(\rho \boldsymbol{v}) + \nabla \cdot (\rho \boldsymbol{v}\boldsymbol{v}) + \nabla p = -\boldsymbol{G} - \rho \nabla\phi \tag{B.26}$$

which are quite similar to the deviation of photon radiation transfer case. The expressions eq. (B.25) and (B.26) are radiation transport hydrodynamic equations. It should be noted that neutrino interaction is usually taken into acount only for the energy conservation due to the weak momentum exchange which is easily estimated as follows. As one encounter similar discussion of Eddington limit, neutrino and gravitational force per nucleon, i.e. $f^{(\nu)}$ and $f^{(\mathrm{grav})}$, respectively, can be roughly estimated as

$$f^{(\nu)} = \frac{c}{\lambda}\frac{\epsilon_\nu}{c} = \frac{L_\nu}{4\pi r^2 c}\sigma_0 \left(\frac{\epsilon_\nu}{m_e c^2}\right)^2, \tag{B.27}$$

$$f^{(\mathrm{grav})} = G\frac{M m_b}{r^2}, \tag{B.28}$$

where λ and L_ν are mean free path of absorption and neutrino luminosity, respectively and σ_0 is the typical cross section of weak interaction, hence, $\sigma_0 = 1.705 \times 10^{-44}\mathrm{cm}^2$. Therefore, the ratio of the two forces is evaluated as

$$\frac{f^{(\nu)}}{f^{(\mathrm{grav})}} = 8.07 \times 10^{-4} \left(\frac{L_\nu}{10^{52}\mathrm{erg}}\right)\left(\frac{\epsilon_\nu}{15\mathrm{MeV}}\right)\left(\frac{M}{1.4\mathrm{M}_\odot}\right)^{-1} \tag{B.29}$$

which depicts that the contribution of neutrino is smaller by three order of magnitude, i.e. the effect is safely neglected. It should be worth while to pointing out that the typical heating rate of neutrino can be also represented in the same way;

$$q_\nu^{(+)} = \frac{c}{\lambda}\epsilon_\nu \sim 80 \left(\frac{L_{\nu,\,52}}{r_7^2 \langle \mu \rangle} \epsilon_{\nu,\,15} \right) \ \mathrm{MeV/nuc/s} \tag{B.30}$$

which is almost comparable to eq. (2.23) in section 2.2.

Meanwhile, there is important difference between photon and neutrino since neutrino and its anti-particle affect the lepton number. The divergence of lepton number flux is also zero as well as energy-momentum tensor so that

$$\frac{\partial}{\partial t}\left(\rho Y_l\right) + \nabla \cdot \left(\rho Y_l \boldsymbol{v}\right) \ = \ 0 \tag{B.31}$$

where Y_l is lepton number fraction. The equation can be rewritten in follwing way;

$$\frac{\rho}{m_b}\frac{dY_e}{dt} = \sum_n \mathrm{s}_n \int d\Omega \int d\nu \, \kappa_{\nu,n}^{(\mathrm{ab})} \left(I_{\nu,n} - B_{\nu,n}^{(\mathrm{FD})} \right) \tag{B.32}$$

where subscript n is the symbol of neutrino species, $\mathrm{s}_n = 0, \pm 1$ for corresponding n and $B_{\nu,n}^{(\mathrm{FD})}$ is Fermi-Dirac function which depends on chemical potenital and temperature of matters [4]. The last equilibrium term results from the detailed balance relation in emission and absorption. It is highly recommended that one should read the references enumerated in the beginning of this section (for instance, see appendixes in Bruenn (1985) [37], especially for scattering treatment, e.g. (A6), (A8), (A33), (C5), (C49) and (C50)).

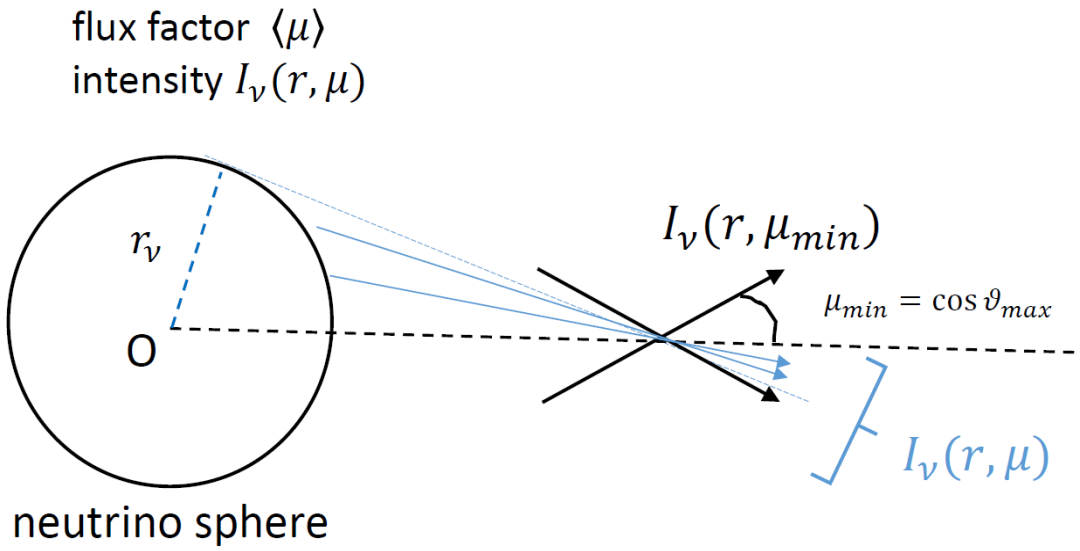

Figure B.1: The geometric meaning of angular distribution of intensity $I_\nu(r, \mu)$.

Furthermore, when numerical schemes are in discussion, a non-negligible difference appears in the flux factor $\langle \mu \rangle$. The physical meaning of $\langle \mu \rangle$ can be interepreted as the geometrical distribution of f_ν or I_ν. The schematic picture of the dependence of μ on intensity is depicted in Fig. B.1 (see figures in Thompson et al.(2003) or Ott et al.(2008) [433, 328] for more clear images). Since neutrinos escape from various points on neutrino

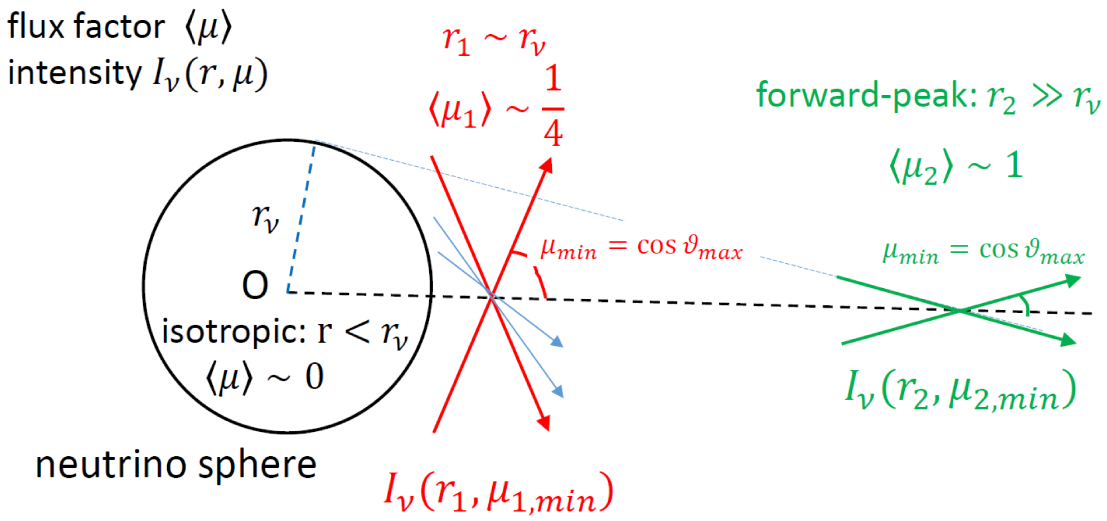

Figure B.2: The typical values of flux factor $\langle\mu\rangle$. Three cases are represented in the figure, isotropic (black), semi-transparent (red) and free-streaming (green).

sphere, several rays arrive at a given position. It should be noted that intensity is also affected by the contribution of either scattering or emission.

The typical values of flux factor is represented in Fig. B.1. Inside the proto-neutron star neutrino is distributed isotropically so that there is no special direction and $\langle\mu\rangle$ should be identified as zero while the neutrino show forward-peak and the flux factor is equivalent to unity (the green rays in the figure) where the point is sufficiently far from neutrino sphere. It is well known that around the neutrino sphere flux factor is usually given as 1/4 [195] (see the red rays in Fig. B.1). There is a good fitting function in 1D for this flux factor which is proposed by [378]. In fact, the true picture should be yielded by multi-dimensional simulation and one should be careful for validity of the fitting [408].

As a matter of fact, one should be careful that the solution for I_ν (or f_ν) is not explicitly debated. The next section is devoted to introduce how they can be obtained.

B.2 Neutrino transport solvers

The development of both radiation and neutrino transport has been accelerated so far. In case of CCSNe, there are mainly three major schemes for realistic neutrino transports;

1) discrete-ordinate (Sn) method

2) momentum equation series

3) Monte Carlo method

where the first method directly solves discretized difference form of the Boltzmann equation (eq. (B.5)), where as the next one carrying out expanding μ momentum sequences of the radiation transfer equation, i.e. eq. (B.15), along with a closure relation so as to truncate the equations. The two approaches are same with calculating f_ν or I_ν in deterministic way. On the contrast, the last is a probabilistic approach so that the basic idea is completely different from the other two. Instead of tracing the neutrino ray, it follows trajectries of packets, the ensemble of particles, and the physical states of packets, e.g. location

and frequency, alter via random numbers. The reaction processes such as absorption and scattering are also given by the random numbers.

It is noteworthy that all introduced methods above are usually based on either special relativity (SR) or Newtonian, however, the gravitational effect may be also important and there are also studies under full GR which is one of the most challenging issues.

Table B.1: Neutrino transport scheme and application

dimension [a] (hydro)		1D	2D	3D
ME	FLD [e]	Levermore1981 (-), Bruenn1985 (1D), Herant1994 (2D), Burrows1995 (1D), Messer1998 (1D), Fryer2002 (3D)	Livne2004 (-), Walder2005 (2D), Swesty2009 (-), Dolence2015 (2D) Dolence2015 (2D)	
	IDSA [f]	Libendorfer2009 (1D), Suwa2010 (2D), Suwa2014 (2D), Nakamura2014 (2D) Takiwaki2012 (3D), Takiwaki2014 (3D)	Chan2015 (2D)	
	M_1 [g]	SchinderBludman1989, DganiCernohorsky1991, KoernerJanka1992, Obergalinger2011, Roedig2012, Just2015, O'Connor2015		Shibata2011 (-), Cardall2013 (-), Kuroda2012 (3D), Kuroda2015 (3D)
	VEF [h]	Burrows2000 (-), Rampp2002 (-), Buras2006 (2D), Hubeny2007 (-), Marek2009 (2D), Müller2010 (2D, GR)		
S_n [b]		Mezzacappa1993 (1D), Yamada1999 (1D,GR), Liebendorfer2001(1D,GR), Liebendorfer2004(1D,GR) Sumiyoshi2005 (1D,GR), Lentz2012 (1D, GR)	Ott2008 (2D), Brandt2011 (2D)	Sumiyoshi2012 (-), Nagakura2014 (-)
CF [c]		Lentz2012 (1D,GR)		Cardall2003 (-), Cardall2013b (-), Shibata2014 (-)
MC [d]		Tubbs1978, 1979, 1980 (-), Janka1992 (-), Keil2003 (-), Abdikamalov2012 (1D)	- -	

[a] The dimension of transport scheme
[a] Momentum Equations
[b] Discrete Ordinated Method
[c] Conservative Form
[d] Monte Carlo
[e] Flux Limited Diffusion
[f] Isotropic Diffusive Source Approximation
[g] Algebraic Eddington Factor (AEF)
[h] Variable Eddington Factor

Table B.2: The computational characters of neutrino transport schemes

	S_N method	Momentum equation series	Monte carlo
Computational cost	low	high	medium
Memory	small	large	medium
anisotopy	poor	fine	fine
opaque	fine	medium	poor
scattering	poor	medium	fine

(1) Discrete ordinate method (S_n method; note that the symbol 'S' usually indicates the abbrevation of short characteristic)

In spherical coordinate, the deratives of momentum terms in the advection terms are retained in curvilinear space so that BTE is modified as following representations:

$$\frac{1}{c}\frac{\partial f_\nu}{\partial t} + \mu\frac{\partial f_\nu}{\partial r} + \frac{1-\mu^2}{r}\frac{\partial f_\nu}{\partial \mu} = \left[\frac{1}{c}\frac{\delta f_\nu}{\delta t}\right]_{\rm collision}, \tag{B.33}$$

where the term $\partial/\partial\mu$ result from momentum derivative for the curvilinear coordinate.

Extending to three dimension, the equation become much more complicated;

$$\begin{aligned}\frac{1}{c}\frac{\partial f_\nu}{\partial t} + \mu_\nu\frac{\partial f_\nu}{\partial r} + \frac{\sqrt{1-\mu_\nu^2}\cos\phi_\nu}{r}\frac{\partial f_\nu}{\partial \theta} + \frac{\sqrt{1-\mu_\nu^2}\sin\phi_\nu}{r\sin\theta}\frac{\partial f_\nu}{\partial \phi} \\ + \frac{1-\mu_\nu^2}{r}\frac{\partial f_\nu}{\partial \mu_\nu} - \frac{\sqrt{1-\mu_\nu^2}\sin\phi_\nu}{r}\frac{\cos\theta}{\sin\theta}\frac{\partial f_\nu}{\partial \phi_\nu} = \left[\frac{1}{c}\frac{\delta f_\nu}{\delta t}\right]_{collision}.\end{aligned} \tag{B.34}$$

where the angles defined in Fig. B.2 [409, 408].

For the numerical calculation, the equation can be rewritten in the conservative form as,

$$\begin{aligned}\frac{1}{c}\frac{\partial f_\nu}{\partial t} + \frac{\mu_\nu}{r^2}\frac{\partial}{\partial r}(r^2 f_\nu) + \frac{\sqrt{1-\mu_\nu^2}\cos\phi_\nu}{r\sin\theta}\frac{\partial}{\partial\theta}(\sin\theta f_\nu) + \frac{\sqrt{1-\mu_\nu^2}\sin\phi_\nu}{r\sin\theta}\frac{\partial f_\nu}{\partial\phi} \\ + \frac{1}{r}\frac{\partial}{\partial\mu_\nu}[(1-\mu_\nu^2)f_\nu] - \frac{\sqrt{1-\mu_\nu^2}}{r}\frac{\cos\theta}{\sin\theta}\frac{\partial}{\partial\phi_\nu}(\sin\phi_\nu f_\nu) = \left[\frac{1}{c}\frac{\delta f_\nu}{\delta t}\right]_{\rm collision}.\end{aligned} \tag{B.35}$$

It should be stressed that the equation is valid when the neither SR nor GR is important. In fact, in CCSNe simulations the one percent energy conversion is mainly concerned so that the contribution of high velocity and gravitational effects may be also carefully treated. Furthermore, the selection of frame is not straightforward since the advection terms (LHS of BTE) have easier form in inertial (laboratory frame) whereas the collision terms (RHS of BTE) show handful form(see chapter 4 in Mihalas & Mihalas (1984) [285]; for Japanese see also [**?**]). Usually many researches have employed the comoving frame since BTE is integro-partial differential equation whose integral terms are non-linear. Hence, the scattering terms become too complicated if the variables are written in laboratory frame. In this section, however, both doppler shift and gravitational redshift are discarded for simplicity in the equations.

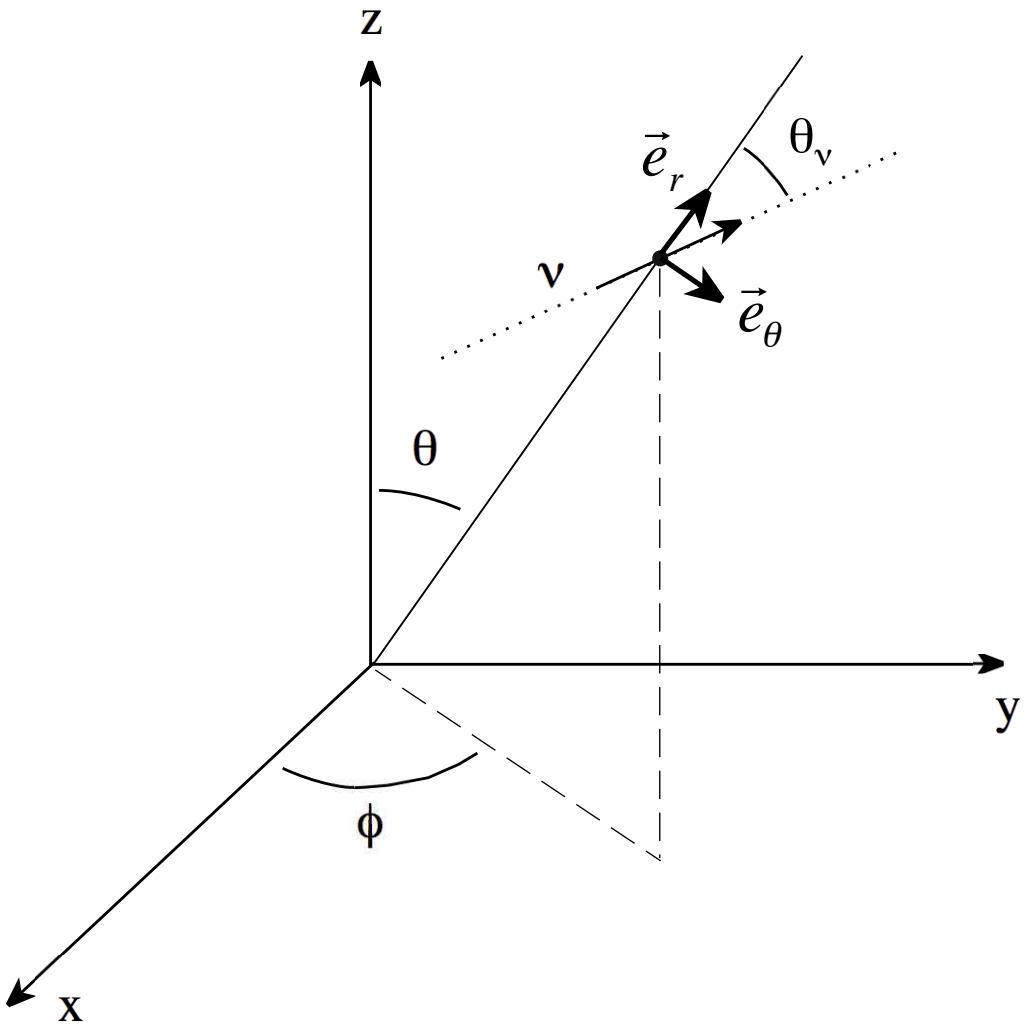

Figure B.3: The orientation of angular variables used in eq. (B.34) which is taken from [408].

If stellar interiors are either opaque or transparent, the traveling process of neutrino is diffusive or free-streaming, respectively. However, if the system is semi-transparent, the neutrino distribution function should be obtained by solving radiation transport theory, i.e. the Boltzmann equation. There are several approaches to calculate Boltzmann equation which generally has 6+1 (r, θ, ϕ, ϵ, Θ, Φ, t) dimensions.

The straightforward way is direct discretization of the Boltzmann equation and this is called S_n method. It is apparent that S_n method holds no approximation in physics in principle while the huge computational resources are required for the timescales problem: The dynamical time scale inside proto-neutron star can be estimated as

$$t_{\rm dyn} = \sqrt{\frac{1}{G\rho}} \sim 10^{-3}{\rm s} \left(\frac{\rho}{10^{14}\ {\rm g/cm^3}} \right)^{-1/2} \tag{B.36}$$

whereas the typical reaction time scale can be regarded as

$$t_{\rm weak} = \frac{\lambda_{\rm weak}}{c} \sim 10^{-8}{\rm s} \left(\frac{\varepsilon_\nu}{10{\rm MeV}} \right)^{-2} \left(\frac{\rho}{10^{14}\ {\rm g/cm^3}} \right) \tag{B.37}$$

where mean free path $\lambda = (n_{\rm b}\sigma_\nu^{(typ)})^{-1}$ and typical cross section $\sigma_\nu^{(typ)}$ can be roughly given as

$$\sigma_\nu^{(typ)} \sim \frac{G_{\rm F}^2}{(hc)^4}\varepsilon_\nu^2 \sim 10^{-44}{\rm cm}^2\left(\frac{\varepsilon_\nu}{m_e c^2}^2\right) \tag{B.38}$$

$$\frac{G_{\rm F}}{(hc)^3} = 1.16{\rm GeV}^{-2} \tag{B.39}$$

Since $t_{\rm dyn} \ll t_{\rm weak}$, the numerical treatment for BTE should be calculated in implicit way for time evolution. As a result, the considerably large sparse matrix, $N_{\rm matrix} \times N_{\rm matrix}$, where

$$\begin{aligned} N_{\rm matrix} &= N_{\rm space} \times N_{\rm momentum} \\ &= (\text{total spatial grid size}) \times (\text{total mometum space grid size}) \end{aligned} \tag{B.40}$$

should be prepared in case of S_N method (see [409, 222] for details).

It is noteworthy to pointing out that coarse angular grids yield crude estimation of free streaming limit and this issue is so called "ray effect". If one desires to obtain accurate results in 3D the computational ability with exaflops scale is required and still higher performance platforms is necessary for incorporating inelastic scattering, doppler effect and gravitational redshift [222].

Furthermore, in axisymmetry case the dimension reduces only 5+1, i.e. r, θ, ϵ, Θ, Φ, t, and even in a spherical symmetry case, the dimension of Boltzmann equation is still 3+1, i.e. r, ϵ, Θ, t, which is affordable with more than petascale supercomputer, e.g. K computer. The calculation still needs teraflops scale even if the neutrino energy dependence is neglected, gray transport scheme.

(2) Moment equations

To avoid this difficulties, integrating the (n)-th moments of the solid angle of the momentum space helps reducing the dimension of equations. This operation results in much faster calculation and smaller memories for carrying out numerical calculation. As a matter of fact, the problem is that the (n)-th moment equation includes the (n+1)-th moment term and the truncation condition should be prepared in order to close the last series of equation which means the methods are not exact but approximation.

One of the simplist way is adopting flux-limited diffusion scheme (FLD; the 0th moment) which characterizes energy density flux, $\boldsymbol{F}_\nu$, directly to energy density E_ν. Meanwhile, there is the other way by using Eddington factor $f_\nu^{(\rm Edd)}$ which is defined as

$$\boldsymbol{f}_\nu^{(\mathbf{Edd})} \equiv \frac{\int d\Omega\, \boldsymbol{nn} I_\nu}{\int d\Omega\, I_\nu} \tag{B.41}$$

$$f_\nu^{(\rm Edd)} = \frac{P_\nu}{E_\nu} = \frac{\int d\Omega\, \mu^2 I_\nu}{\int d\Omega\, I_\nu}, \tag{B.42}$$

where $f_\nu^{(\rm Edd)}$ is given function so that eq. (B.19) can be truncated and the equations are ready to be solved. There are several ways to give the closure relation, e.g. M_1 closure scheme (the 1st momentum) and variable Eddington factor scheme (VEF; the 2nd moment).

These closure relations are frequently employed in "realistic" CCSNe simulations and one of the important characters are listed below;

1. Flux-limited diffusion (FLD)
   FLD is radiation transport solver imposing the 0th moment closure. It connects the opaque region with free streaming region by using an analytical "flux-limiter" function. Λ, e.g.

$$\begin{aligned} \boldsymbol{F}_\nu &= -\frac{c}{\chi_\nu}\Lambda(E_\nu, \partial_i E_\nu, \chi_\nu)\nabla E_\nu, && \text{(B.43)} \\ &\rightarrow c\boldsymbol{n}E_\nu \qquad \text{(free-streaming)}, && \text{(B.44)} \\ &\rightarrow -\frac{c}{3\chi_\nu}\nabla E_\nu \qquad \text{(isotropic)}, && \text{(B.45)} \end{aligned}$$

   which is represented as a function of absorposivity χ_ν, energy density E_ν and gradient components of E_ν. The flux limiter Λ is chosen by hand so that it is handful for numerical resource both in memory and time which permits to employ multi-group energy, i.e. MGFLD, or deploy relatively high resolutions [419, 420]. In addition, this method is useful for solving the central dense part of star where the neutrino distribute isotropic. Nevertheless, the function Λ only ensures the numerical stability while physical validity in semi-transparent regime is poorly guaranteed. since physical constraints are only given by the behavior of the two limit, opaque and transparent so that there are many freedoms to choose the function of Λ, e.g. Mayle & Wilson and Levermore & Pomraning [285]. Moreover, FLD violates causality since the time evolution of radiation energy density is represented as diffusion equation.

2. M_1 closure (Analytical Eddington factor; AEF)
   When closure condition is given at the 1st moment level this scheme is called M_1 closure. If radiative tensor P_ν^{ij} is regarded as an analytical function of E_ν, e.g.

$$\frac{P_\nu^{ij}}{E_\nu} = \frac{1-f_\nu^{(\mathrm{Edd})}}{2}\delta^{ij} + \frac{3f_\nu^{(\mathrm{Edd})}-1}{2}n^i n^j, \qquad \text{(B.46)}$$

   it is apparent that the second moment fulfill following relations in the two physical limits

$$\begin{aligned} P_\nu^{ij} &= \frac{1}{3}E_\nu\delta^{ij}, \qquad P_\nu = \frac{1}{3}E_\nu \qquad \text{(isotropic)}, && \text{(B.47)} \\ P_\nu^{ij} &= n^i n^j E_\nu, \qquad P_\nu = E_\nu \qquad \text{(free-streaming)}. && \text{(B.48)} \end{aligned}$$

   In addition, if Eddington factor only relies on flux factor $\langle\mu\rangle$, hence,

$$f_\nu^{(\mathrm{Edd})} = f_\nu^{(\mathrm{Edd})}(\langle\mu\rangle) \qquad \text{(B.49)}$$

   the equation is finally closed. Thanks to the relationship in the higher order, anisotropic energy flux can be treated more accurately than FLD. It is well known that M_1 pass the shadow test problem which show how much radiation flow are forbidden behind an obstacle whereas FLD demonstrate no shadow [202]. Furthermore, a large advantage of this approach is that the equations are classified as hyperbolic partial differential equation which guarantees the causality and is highly suited for SR and GR. So far leakage scheme (see [345] and references therein) which can only handle the cooling process was the standard choice for simulating GR neutrino transport such as compact star merger [382, 320, 217, 110] , however, many studies have started to employ

M_1 for GR neutrino transport ([319, 202] and reference therin). In fact, it should be stressed that there is a serious deficient in this approach. For instance, if multiple neutrino rays intersect at a single point, e.g. two beaming interaction test, the rays demonstrate scattering properties so that the wrong solutions are obtained in such anisotropy case.

3. Variable Eddington factor (VEF)
   One of the most proper schemes for neutrino solvers is VEF which treats the 2nd moment equations. However, the methodology is not as straightforward as the other two solvers since it determines Eddington factor without employing any analytical function. The idea is given as following way; firstly, BTE can be rewritten by using

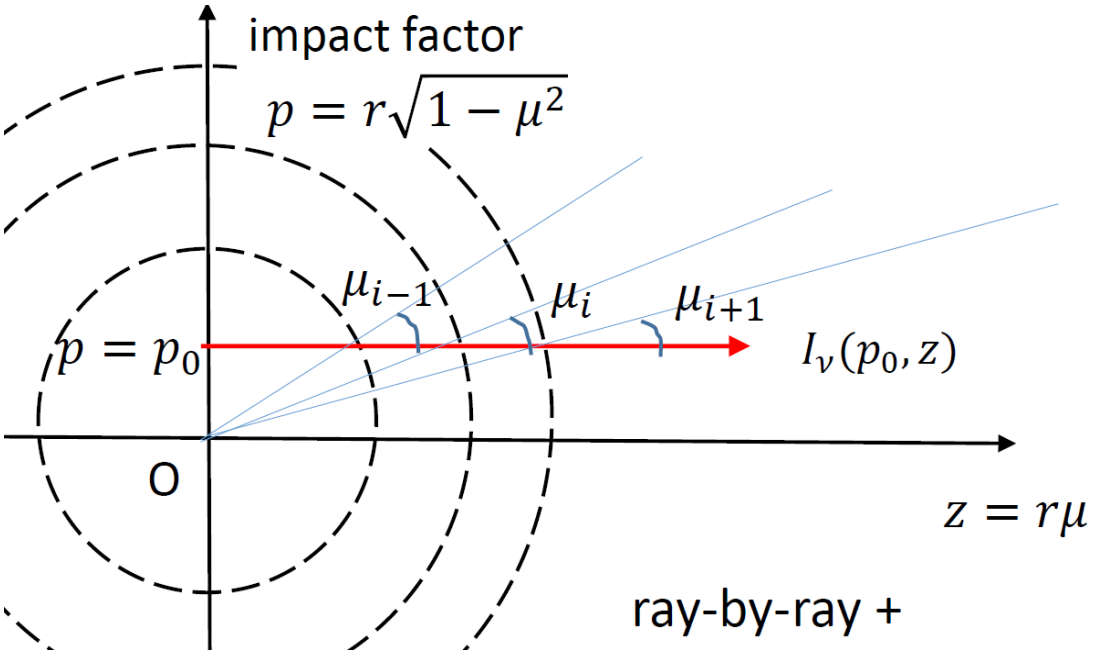

Figure B.4: The new two independent variables z and p for Feauterier method. Radiation transfer is solved along the horizontal directions (red) for each impact parameter p.

new variables, i.e. path length $z = r\mu$ and impact factor $p = r\sqrt{1-\mu^2}$ (see Fig. B.4), instead of employing r and μ;

$$\frac{\partial I_\nu}{\partial z} = \eta_\nu - \chi_\nu I_\nu. \tag{B.50}$$

The equations are integrated along each ray and , especially under spherical symmetry, the certain choice of ray called ray-by-ray plus (or tangent ray) method gives the exact solution with efficient number of rays which saves the computational costs.

The advantage of ray-by-ray plus are illustrated in Fig. B.5. The different rays intersect with the different points, thus the different angles, at the same radius which is drawn in the upper panel. If the system ensure spherical symmetry, the estimation of intensity at a fixed radius, $I(r_0, \mu)$, can be calculated by collecting the information from those crossing points (the lower panel). As a consequence, the number of intersection points between rays and radii is equivalent to the resolution of neutrino traveling direction for the intensities.

Turning attention to two variables $I_\nu(+\mu)$ and $I_\nu(-\mu)$ where $0 \leq \mu \leq 1$, one can define new combination of two intensities, $\mathcal{J}_\nu$ and $\mathcal{H}_\nu$, thus

$$\mathcal{J}_\nu = \frac{1}{2}\left(I_\nu(+\mu) + I_\nu(-\mu)\right) \tag{B.51}$$

$$\mathcal{H}_\nu = \frac{1}{2}\left(I_\nu(+\mu) - I_\nu(-\mu)\right). \tag{B.52}$$

Then, the radiation transfer equation can be rewritten as following convenient forms

$$\frac{\partial \mathcal{J}_\nu}{\partial z} = \chi_\nu \mathcal{H}_\nu \tag{B.53}$$

$$\frac{\partial \mathcal{H}_\nu}{\partial z} = \chi_\nu \mathcal{J}_\nu - j_\nu \tag{B.54}$$

or

$$\frac{1}{\chi_\nu}\frac{\partial}{\partial z}\left(\frac{1}{\chi_\nu}\frac{\partial \mathcal{J}_\nu}{\partial z}\right) = \mathcal{J}_\nu - \mathcal{S}_\nu \tag{B.55}$$

where $\mathcal{S}_\nu \equiv \eta_\nu/\chi_\nu$ is source function. This formula is so called Feautrier equation or formal solution and usually known as VEF in the CCSNe field. Since the formulation is represented as the second derivative equation, it ensures second-order accuracy and the solution $\mathcal{J}_\nu$ is guranteed to be positive for all mesh points as long as the source function is positive.

Hence, the new ray intensities with outgoing and ingoing directions are defined in this scheme and the calculation are based on Feautier method which imposes the isotropic scattering in a comoving frame and no time variation during the hydrodynamical timescale (see [**?**] for the detailed idea; Rampp2002 and Buras Ph.D for computational implements). However, it should be emphasized that this treatment is only valid in spherical geometry and the enormous number of ray tracer should be prepared in the higher dimension for each spatial grid points.

It is noteworthy that recently a modified FLD scheme has been developed by Liebendörfer [251] so called isotropic diffusion source approximation (IDSA). The main difference between the usual the 0-th moment scheme and IDSA is that the evaluation of the fluxes and flux factor relies not on the local intensity gradient but on non-local distribution of sources which avoid giving an incorrect direction.

The main idea of this scheme is decomposition of the neutrino distribution function f_ν into isotropic trapping particles, $f^{\rm t}_\nu$, which are represented correctly in optically thick region and free streaming particles, $f^{\rm s}_\nu$, which are valid in optically thin region, i.e. $f_\nu = f^{\rm t}_\nu + f^{\rm s}_\nu$. Then the BTE can be seperated into two equations;

$$\frac{1}{c}\frac{\partial f^{\rm t}_\nu}{\partial t} + \mu\frac{\partial f^{\rm t}_\nu}{\partial r} + \frac{1-\mu^2}{r}\frac{\partial f^{\rm t}_\nu}{\partial \mu} = \eta_\nu(1 - f^{\rm t}_\nu) - \chi_\nu f^{\rm t}_\nu - \Sigma \tag{B.56}$$

$$\frac{1}{c}\frac{\partial f^{\rm s}_\nu}{\partial t} + \mu\frac{\partial f^{\rm s}_\nu}{\partial r} + \frac{1-\mu^2}{r}\frac{\partial f^{\rm s}_\nu}{\partial \mu} = -(\eta_\nu + \chi_\nu) f^{\rm s}_\nu + \Sigma \tag{B.57}$$

where Σ, which is called diffusion source in the original paper, indicates the conversion from the trapped distribution to free streaming distribution. The diffusive source is regarded as isotropic and takes 0 and η_ν in free-streaming limit and chemical equilibrium limit,

respectively. In case of diffusion limit, $f_\nu^{\rm t}$ and $f_\nu^{\rm s}$ can be identified as the 0th and 1st order of magnitudes, respectively, so that Σ is consisted of a diffusion form of the trapping particle and an averaged constribution of the streaming particle to matter absorption (see detailed discussion in [251]). IDSA enable to conduct rapid calculation by incorporating ray-by-ray method. Although $f_\nu^{\rm s}$ is equilibrium with matter and should be evolved implicitly, $f_\nu^{\rm s}$ can be separetly treated, by definition, and calculated in explicit method. This fact is much favorable for speeding up numerical calculations which makes great advantage if one compares with other transport schemes. In fact, the extension of multi-dimesion is not so apparent for the presence of the source term and Berninger et al.(2013) [26] have pointed out that IDSA still has some mathmatical issues.

It should be noteworthy that the gravitational effect changes outcomes of the CCSNe simulations by around 10% and may also be important contribution to successful explosion. Although the realistic one dimensional simulations demonstrated the failure in the shock revival, many simulations reported GR effect is favorable for neutrino heating owing to the deeper graviational potential well. Hence, a scheme with conservation form in GR is also required in multi-dimension which are one of the most challenging topic in astrophysical fields [63, 62, 101, 386]. Not to mention its complex formalism and metrics calculation, there are technical difficulties in multi-dimensional GRRHD simulations since density is coupled with Lorentz factor, velocity in laboratory frame and also enthalpy. Moreover the transfer equations originally possess proper stiff collision terms and require non-linear iterations so that it more easily failes in numerical convergence.

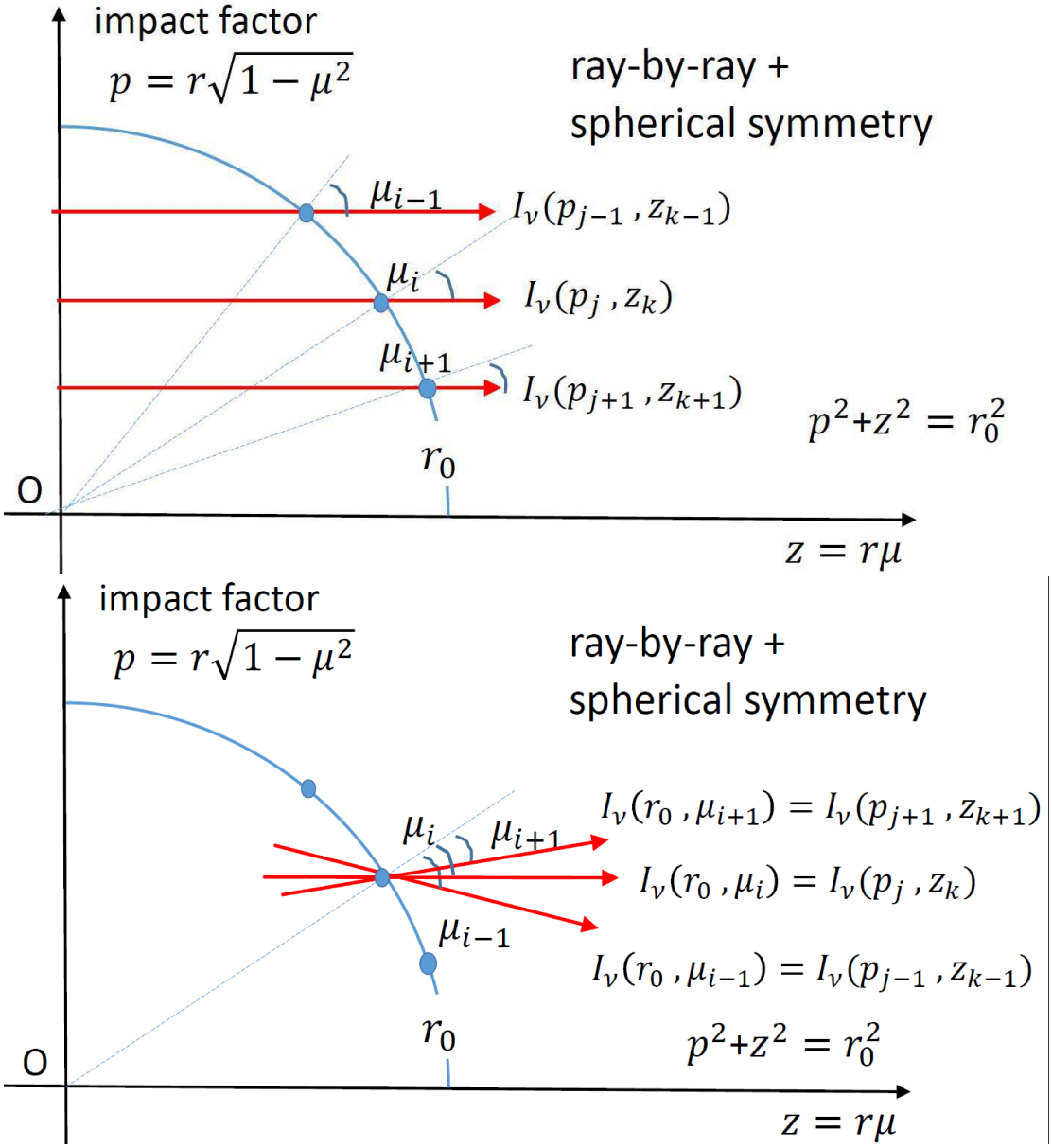

Figure B.5: The reconstruction of the intensity from the function of z and p to those of r and μ. If the grids are orientated in same radius, each ray hit on the different points with their own μ (the upper panel). Under the spherical symmetry condition, these points collect the dependence of μ on intensity individually so that $I_\nu(r, \mu)$ is obtained by estimating $I_\nu(z, p)$ (the lower panel).

(3) Monte carlo method

As long as the neutrino transport is solved by either Boltzmann equation or its moment equation, one cannot evade the difficulties of changing the geometry and/or extending ti higher dimension. Furthermore, implementing additional physics such as doppler shift and graviational redshift in advection terms yield even more complicated formalisms which require considerable modification in the original calculations. In addition, the informations of neutrino are obtained along the each ray so that the intensity changes time by time. As a consequence, the equation relies on other rays and seems to be hardly paralellized.

There is an alternative transport solver so called Monte Carlo radiation transfer (MCRT) which is based on stochastic approach and has been historically utilized in general radiation transfer (see in chapter 2.1), it is usually familiar with reproducing light curves, spectrum and polarization in various astrophysical fields, e.g. hot star wind, massive star formation, nebula, supernova and so on (see [104, 311, 156]). There are also application to GR [92] and even implemented in GRMHD [371].

Instead of following rays, MC traces individual particle so that each energy, thus intensity, is unchanged whereas frequency and direction alter during propagation. A large advantage of using this method is that it is much more convenient to incorporate a larger set of scattering process as well as other physics, change geometry and extend to higher dimension which are problematic in the deterministic approaches. Moreover, each wave packet is is regardless of the others so that these properties are suitable for parallelization in photon radiation. On the other hand, it should be stressed that this is not always the case for neutrinos since they are fermion and imposed on Fermi-blocking which needs other particle information.

On the contrast, there are several deficiency. For instance, MC is coincided with BTE when prepared sample number is infinity otherwise statistical error is present which is crucial to the equilibration of matter-radiation interaction. Moreover, huge computational time is consumed in highly opaque due to a enormous number of scattering process. MC also requires not small size of computational memories so as to manage large number set of particle informations. Recently, monte carlo radiation transfer has been utilized by CCSNe modelers for neutrino transport as well as photon radiation,. Although there are several previous studies [443, 444, 197, 207], the application to neutrino heating mechanism has yet been progressed for many years compared with the deterministic approaches. This is because, in addition to the proper characters of the method itself, the generic trends of fermion hinder the efficiency of calculation. For instance,

- the opacities of neutrino depends on energy scales,
- the difficulties of equilibrium treatment, e.g. the upper limit in magnitude of distribution function, leads to a large number of sample particles,
- the presence of Fermi-blocking may be not suitable for parallelization and
- both energy and number conservations should be guaranteed accurately.

However, it seems that the recent stochastic approach has been shed light once more. Thanks to development of numerical techniques and high performance platforms, some researcheres have recently attempted to incorporate monte carlo method for neutrino transport not only for CCSNe [4] but also for the other phenomena of compact object, e.g. compact stars merger [365].

Hence, it may be worth while to introducing this alternative technique. Procedures used in CCSNe are similar to the ordinary photon transport method in many aspects so that it will be useful to refer several studies of MCRT in radiation fields [256, 104, 204, 156, 311, 368].

The idea of MCRT is based on following components; preparing not a single particle but an ensemble of particles which is called packet or super-particle, creating packets from radiative source and matter emission, propagating all packets inside computational domain and incorporating scattering and/or absorption which destroys packets. It should be carefully taken into acount that these radiation packets exchange mainly energy with matter so that temperature structure should updated after the propagation.

The details of each procedure are enumerated below;

(i) discretiazation into packet
Monte carlo simulation trace packet which is identified as the ensemble of radiation with the same frequence so that energy of a single packet for frequency ν, $E_{\nu,\mathrm{p}}$, is represented as

$$E_{\nu,\mathrm{p}} \;=\; w_{\nu,\mathrm{p}}\, h\nu \tag{B.58}$$

where $w_{\nu,\mathrm{p}}$ is weight of the packet. Historically, Avery & House (1968) [19] first carried out a calculation under constant $w_{\nu,\mathrm{p}}$. Meanwhile, Abbott & Lucy (1985) [3] imposed constant $E_{\nu,\mathrm{p}}$ throughout calculation instead which has been widely utilized so far since not the number but the energy conservation is rather important for photon radiation. Although a number contained in each energy packet, thus $w_{\nu,\mathrm{p}}$, alters as well as frequency ν by fluid interactions, their energy remains fixed in the rest frame.

A condition that each single packet is indivisible yield another convenience [256] which means that packet itself can be either created or destroyed but is prohibited in spliting into multiple packet. It is interesting that the indivisible method can treat all cascade channels correctly if the sample number is suffeciently large [257, 311].

Since many astrophysical objects are radiation dominant and the reaction (cooling) time scale is much shorter than dynamical time scale, the system is well identified as radiative equilibrium (thermal balance) which infers that the energy balance of abosrption and emission is fulfilled [257, 156]. As a result, these packet trends are suitable for determining the temperature structure with small iterations. Harries, however, has purposed a scheme which is applicable to non-radiative equilibrium [156].

In addition to the series of Lucy's studies [256, 257], the idea of discretization is also written carfully in following papers [104, 204, 311, 368].

(ii) packets creation
Packets are generated by radiative source which can be either point or surface boundary and matter emission. For instance, if finite volume source with black body spectrum produces steady luminosity, L_{s}, $E_{\nu,\mathrm{p}}$ is given by controling the number of packets N_{rad};

$$E_{\nu,\mathrm{p}} = \frac{L_{\mathrm{s}}\Delta t}{N_{\mathrm{rad}}}. \tag{B.59}$$

Frequency, direction and location of packets are selected in random way [156] in non-relativistic case. This operation is also valid for relativistic case if one selects comoving frame [311]. It should be stressed that the statistical errors depend on $N_{\rm rad}$ by $\propto 1/\sqrt{N_{\rm rad}}$. This infers that the packet number should increase by second order of magnitude so as to suppress the error by an order.

The contribution of matter is quite similar to that of source except luminosity $L_{\rm m}$ is determined by emissivity of individual cells and the probability density of propagation angle is slightly different. It should be, however, noted that the way of creation from matter is affected by numerical schemes which is implemented so as to enhance numerical efficiency, e.g. implicit monte carlo (IMC) method [4, 368].

(iii) propagation

After providing new packets and determining flight directions in random way, the packets travel through the matters as well as census packets, i.e. remaining packets from previous step. Each packet is treated separetely and the flight distance, reaction process types and, if neccessary, scattering directions are determined by random numbers which are defined in the range from 0 to 1. As already mentioned in the detrministic case, propagation and collision are handful in inertial and comoving frame, respectively. The great virtue of MCRT is that these two processes can be separated so that many simulations usually employ mixed frame.

Moreover, the propagation length is relevant to the optical depth. If one focuses on absorption and scattering, the radiation transfer equation can be rewritten as

$$\begin{aligned} \frac{dI_\nu}{ds} &= -(\kappa_\nu + \sigma_\nu) I_\nu \quad \text{or} \\ \frac{dI_\nu}{d\left(\kappa_\nu + \sigma_\nu\right) s} &= -I_\nu \end{aligned} \tag{B.60}$$

so that, using $d\tau_\nu = ds\,(\kappa_\nu + \sigma_\nu)$, I_ν is propotional to $\exp(-\tau_\nu)$. Hence, normalized absorption probabitlity at τ_ν, $P^{(\rm prob)}_{\nu,\,\rm abs}$, can be evaluated as

$$P^{(\rm prob)}_{\nu,\,\rm abs} = 1 - \exp(-\tau_\nu) \tag{B.61}$$

One can introduce a random number $\xi_{\rm col}$ which is relevant to optical depth where the collision takes place;

$$\tau_\nu = -\ln(1 - \xi_{\rm col}). \tag{B.62}$$

Since it doesn't lose generality, one can substitute $\xi_{\rm col}$ for 1-$\xi_{\rm col}$ so that the propagation length d_c is finally represented as

$$\begin{aligned} d_c &= \frac{1}{\kappa_\nu + \sigma_\nu} \left(-\ln \xi_{\rm col}\right) \\ &= \lambda_\nu^{(\rm mfp,\,tot)} \left(-\ln \xi_{\rm col}\right). \end{aligned} \tag{B.63}$$

According to Ercolano et al.(2003) [104], Lucy proposed another propagation method [256]. In this new methodology, the distance between particle and cell boundary, d_b,

which is represented as $d_b = \min_{\text{cell}} \|\boldsymbol{x}_{\text{cell}} - \boldsymbol{x}_k\|$, is added and if d_b is shorter than d_c, the particle move to the cell boundary with generating new random number for next optical depth. It is interesting that the introduction of new random number produce no bias (see [256, 104]).

In addition, if thermodynamical variables of background matters depends on time, one supposes to introduce distance d_t which photon travels through during time interval Δt, i.e. $c\Delta t$. When d_t is the shortest among the three distance, the praticle just travel toward this end point without changing direction. Hence, time dependent MCRT usually employs the assessment of this three distance [204, 156, 311].

(iv) albedo

Once d_c is chosen as the propagation length, one should determine which reaction processes take place next. The reactions are selected by introducing new random number ξ_{reac}. For instance, if one employs certain threshold value scattering process happens under a following condition;

$$\frac{\sigma_\nu}{\kappa_\nu + \sigma_\nu} > \xi_{\text{reac}} \qquad \text{scattering} \tag{B.64}$$

otherwise absorption takes place and equation (B.64) is known as albedo condition. If the absorption takes place the packet is destroyed and omitted from computational domain otherwise two random numbers ξ_μ, ξ_ϕ are chosen for the scattering direction. When the scattering is isotropic, the new direction $\boldsymbol{n}^{(\text{new})}$ is given as

$$\mu = 2\xi_\mu - 1 \tag{B.65}$$

$$\phi = 2\pi\xi_\phi \tag{B.66}$$

$$\boldsymbol{n}^{(\text{new})} = \begin{pmatrix} \sqrt{1-\mu^2}\cos\phi \\ \sqrt{1-\mu^2}\sin\phi \\ \mu \end{pmatrix}. \tag{B.67}$$

One the other hand, if one desires to take anisotropic scattering, e.g. Rayleigh or Mie scattering, into account, probabitily should be constructed by scattering kernel presented in eq. (B.7).

It should be noted that if there are multiple-reactions in system absorption and scattering opacities are modified as following way;

$$\kappa \longrightarrow \sum_{r_j} \kappa_{r_j} \tag{B.68}$$

$$\sigma \longrightarrow \sum_{r_j} \sigma_{r_j} \tag{B.69}$$

where the subscript r_j indicates the label of reaction such as excitation and de-excitation of ions or inelastic scattering process between ion and electron. The collision process are chosen by searching which reaction bin contains ξ_{reac}. Hence, the opacity calculations are one of the most time consuming parts among MCRT procedure. Furthermore, it is not straight forward to interprete these opacities as feasible probability, however, the detailed treatment of line and macro-atom processes are beyond this paper.

(v) MC estimator (the construction of radiation field)

After all the propagation processes are accomplished the radiation properties should be reproduced by the information of photon packets since the net energy excahnge in each cell should be taken into account for dynamics, and one may desire to reproduce spectral and other infomations which are one of the most major concerns in astronomy. Furthermore, if considering system is semi-opaque, e.g. convective atmosphere, shock breakout, stellar explosion and CSM interaction, MCRT should be solved along with hydrodynamical equations (eq. (B.25) - eq. (B.26)) since the other radiation characters such as energy flux density and pressure are substantial.

In so doing, there are several methods, e.g. Och et al.(1998) [318] and Lucy (1999) [256] and Lucy method is introduced in this paper due to more feasible numerical techniques, hence, wider application [104, 204, 286, 156, 311, 368].

Recalling that the relation between mean intensity J_ν and energy densiy E_ν satisfies

$$E_\nu = \frac{4\pi}{c} J_\nu, \tag{B.70}$$

one can can easily obtain J_ν in each cell if the value of E_ν is given. Lucy (1999) has found that an estimation of E_ν turns to be feasible

if one interprets that packets outside the cell also contributes to energy density of the cell. The contributions of eack packets are weighted by accomodation times in the cell. As a consequence, the estimation is represented as following;

$$[E_\nu]_{\rm cell} = \frac{1}{V_{\rm cell} c \Delta t} \sum_{\text{all } \lambda\text{s in cell}} E_{\nu,{\rm p}} l_\lambda \tag{B.71}$$

where $V_{\rm cell}$ is the finite volume of cell, λ is a trajectory inside the cell and l_λ is the path length of λ at frequency ν. Equation (B.71) implies that l_λ/c is residue time during Δt. Hence the mean intensity in the cell, $[J_\nu]_{\rm cell}$, is represented as

$$[J_\nu]_{\rm cell} = \frac{1}{4\pi V_{\rm cell}} \sum_{\text{all } \lambda\text{s in cell}} E_{\rm p} \frac{l_\lambda}{\Delta t}. \tag{B.72}$$

It should be emphasized that eq. (B.72) is applicable to not only spherical but also more general geometry with rather precise statistics.

Furthermore, there is another virtue of using Lucy estimator [256, 104, 204, 311]. Since Lucy path method is irrespective of whether absorption takes place or not the formulation is also accurate in even small absorption rate region. According to Noebauer et al.(2012) [311], the RHS of eq. (B.20) and (B.21) for the photon radiation in a cell is given by

$$G_0^0 = \left[\frac{1}{V_{\rm cell} \Delta t} \sum_\nu \sum_{\lambda_{\rm tr}} \kappa_0(\nu_0) l_{\lambda_{\rm tr}} E_{\nu,{\rm p},0} \right] - \kappa_0(\nu_0) a T_{\rm cell}^4 \tag{B.73}$$

$$G_0^i = \frac{1}{c V_{\rm cell} \Delta t} \sum_\nu \sum_{\lambda_{\rm tr}} \chi_0(\nu_0) l_{\lambda_{\rm tr}} E_{\nu,{\rm p}\,0} n_0^i \tag{B.74}$$

where $T_{\rm cell}$ is the temperature of matter and a subscript "0" presents that the variables are evaluated in comoving frame. The summations $\sum_\nu$ and $\sum_{\lambda_{\rm tr}}$ are operated over all frequency and trajectory in the cell during time interval Δt, respectively. These formulations enhances signal to noise ratio as well as J_ν and enables to employ less sample numbers [104, 204, 311]. As a result, the reduction of error supports the fast convergence of temperature strucuture under radiative equilibrium approximation where the first and second terms are canceled out in eq. (B.73) [256, 204].

On the other hand, it should be noted that the radiative equiibrium is only adopted when an equilibration time scale is shorter than the dynamical time scale. Harries has purposed a scheme which is applicable to non-radiative equilibrium [156]. In their calculation, the indivisible method is discarded in order to solve optical thick region efficiently.

The order of the operations listed above is depicted in Fig. 3.8 in Noebauer et al.(2012) [311]. From the previous explaination, one may notice how different this stochastic approach is from the deterministic and how they correspond to each other by introducing MC estimator.

In order to obtain correct answers, however, statistical error should be reduced sufficiently. Although several techniques such as energy packet and MC estimator are implemented, the packet number issue is still one of the main concerns which is directly relelvant to computational running time. Furthermore, MC becomes far more ineffecient when particle encounters into optical thick region since huge collision numbers, thus many operations, take place for a single packet.

There are, however, several numerical methods so as to avoid the problem, e.g. modified random walk (MRW) [116], implicit monte carlo diffusion (IMD) [137, 72] and discrete diffusion monte carlo (DDMC) [82, 83, 81]. Some of astrophysical studies applied these approximations, for instance, Min et al.(2009) [286] and Robitaille et al.(2011) [367] incorporated MRW for the dust grain investigation whereas Abdikamalov et al. (2012) [4], Wollaeger & Rossum (2013) [471] and Roth & Kasen (2015) [368] employed DDMC with several improvements. The enumerated approaches are based on stochastic mehods which is, however, different from MC while there is also hybrid method with deterministic approach [469].

In addition, monte carlo calculation also suffers from numerical stiffness as well as the detrministic cases since the weak interaction time scale, eq. (B.37), is far shorter than the dynamical time scale, eq. (B.36). To obtain numerical stablilty and accuracy, there is a method called implicit monte carlo (IMC) which has been first invented by Fleck & Cummings [117] and interprete the time discretized raditaive transfer equation with linear approximation instead (see more details in Wollaber's thesis [468]).

The basic concept of this method is reformulation of collision terms in the radiation transfer equation. The emissivity term is treated in semi-implicit in time direction via IMC so that absorption rate is separated into effective scattering and effective absorption [468, 4]. The ratio of separation is characterized by Fleck factor, $f_{\rm n,Fleck}$, which is estimated as

$$f_{\rm n,Fleck} = \frac{1}{1+\alpha\Delta t_{\rm n}\beta c\kappa} \tag{B.75}$$

$$= \frac{1}{1+\alpha\Delta t_{\rm n}/\Delta t_{\rm int}} \tag{B.76}$$

where α indicate the extent of time implicit, thus energy density at interval time, $E^{*}_{\rm rad}$, is represented by those of the current and next time step as follwing;

$$E^{*}_{\rm rad} = \alpha E^{(n)}_{\rm rad} + (1-\alpha) E^{(n+1)}_{\rm rad} \tag{B.77}$$

while β is dimensionless variables;

$$\beta = \frac{\partial E_{\rm mat}}{\partial E_{\rm rad}}. \tag{B.78}$$

It should be noted that α is the free parameter which should be chosen from 0.5 to 1 for numerical stability and the opacites are all defined as time-centered value which is usually estimated from the previous time step, therefore the collision length is estimated by this averaged opacities. Equation (B.76) help to understand that the denominator of Fleck factor contains the ratio of Courant condition time scale, $\Delta t_{\rm n}$, to typical interaction time scale, $\Delta t_{\rm int}$, which is given as a follow;

$$t_{\rm int} = \frac{l_{\rm mfp}}{c}\beta \sim \frac{l_{\rm mfp}}{c}\frac{\rho {\rm N_{avo}} k_{\rm B} T}{aT^4} \tag{B.79}$$

where $l_{\rm mfp}$ is mean free path of absorption and $\rm N_{avo}$ is avogadro number so that β can be interpreted as the number of absorption event.

In IMC method, the physical absorption κ turns out to be effective absorption $f_{\rm n,Fleck}\,\kappa$ and the rest of contribution, $(1-f_{\rm n,Fleck})\,\kappa$, is regarded as effective scattering. As a result, the source terms of specific energy of matter is altered and this modification is substantial to determine the new temperature structure after the packet evolution. Furthermore, the emission number of packet is also affected [368]. It is interesting to point out that the formulation of Fleck factor is useful since if $f_{\rm n,Fleck}$ is unity, in other words, the interaction time is rather longer than the dynamical timescale, the effective absorption is coincide with the physical one which become similar to the ordinary (or explicit) MC method. On the contrast, if $f_{\rm n,Fleck}$ is nearly zero, the absorption events are all replaced with the effective scattering which stabilize numerical noises. The validity of IMC is confirmed by Larsen & Mercier [239] and Wollaber [468].

It should be stressed that the implementation of IMC provide a modification of either progation or albedo. Abdikamoalov [4] employed a variance reduction which assumes that collision distance is evaluated by only scattering opacity and add an absorption distance $d_{\rm a}$. The new distance is given by following formulation;

$$d_{\rm a} = -\frac{1}{\kappa^{\rm (ab)}_{\nu}} \ln \zeta \tag{B.80}$$

where ζ is not a random number but some certain threshold, thus the absorption distance is calculated in deterministic way [117]. On the other hand, Wollaeger [471, 470] and Roth [368] employed the modified albedo and physical propagation length by replacing physical absorption rate with effective absorption.

As a matter of fact, the main issue is how to apply MCRT to CCSNe mechanism. Although already mentioned many time in this section, it should be emphasized that the numerical steps should be treated carefully in following aspects;

- First, energy packet loses its advantage since neutrino also affects Y_e, i.e. the number weight $w_{\nu,{\rm p}}$ becomes important.
- Second, statistical noise should be handled much more carefully due to the upper limit value of distribution function.

- Third, parallelization may become ineffecient because of Fermi-blocking.
- Last, the difficulty of equilibrium calculation is attribute to the presence of chemical potential and also needs to carry out fermi-integral.

It should be noted that, in terms of the first and last points, the difficulty appears in applying IMC since the time evolution of Y_e should be taken into account (eq. (B.32)) and specific energy of neutrino relies on Y_e as well as those of matter so that the formalisms, e.g. Fleck factor, becomes still more sophisticated by introducing effective lepton number scattering opacities [4]. As a result, the estimation of Fleck factor should be changed appropriately and specific energy and Y_e for the next time step are calculated by incorporating the new opacities, thus temperature strucuture is determined by the two upgraded thermodynamical variables.

Hence, MCRT for neutrino are still quite challenging. If one attempts to perform this new neutrino solver in the current computational platform, it still need to provide some other elegant techniques otherwise one has to wait until the further future generation for affordable computational ability.

Finally, the characters of all schemes are summarized in table B.2 and table B.1. In table B.1 the several simulations solving neutrino transport are listed and distinguished by the type of schemes applied. The symbol $(\cdot)$ denotes the dimension of hydrodynamics and an expression (-) means no hydrodynamical background is utilized.

B.3 Impacts on CCSNe simulations by different numerical radiation schemes

The various transport solvers are introduced in the previous section. In this section, the main topic is turned to how these schemes affect the CCSNe outcomes. It has been well known that FLD usually overestimates $\langle\mu\rangle$, the degree of forward-peaked, i.e. underestimates the neutrino heating rate [199, 277, 480]. Nevertheless, this assessment is only carried out under spherical symmetry for long time and further investigation has been awaited until the computational power reaches the exsa scale which is affordable in the current platform.

As a consequence, the current concern turns out to be the examination of how appropriate the single-angular scheme are by demonstrating multi-angle discrete-ordinate method. Ott et al.(2008) [328] employed two dimensional RHD for both non-rotating and fast rotating stars and compared their S_N scheme with the traditional MGFLD scheme.

In multi-dimension case hydrodynamic instabilites are frequently observed (see section C) and the presence of SASI produce asymmetry which induce deviations of the two neutrino transport solvers. Since the dominant unstable mode is l=1 or 2, both schemes represent increase of neutrino mean energy and energy flux in the polar direction while multi-angle approach depicts higher values and larger deviation between the polar and equatoral region. Moreover, due to its basic idea of approximation, MGFLD shows rather isotropic trend in gain region thus smear out the deviation between the polar and equatoral plane. In case of fast rotation progenitor, the rotation provides oblate neutrino sphere which emits higher mean energy and a larger amount of flux in polar directions. As a consequence, it is interesting that S_N method triggers SASI earlier than MGFLD. From futher examination, Brandt et al.(2011) [35] explored that multi-angle transfer smears the variation in the neutrino distributions owing to an averaging effect.

It should be stressed that, although the asymmetry of neutrino emission appears due to deformation provided by SASI or rotation, multi-angle method does not always support shock revival in positive way since the net heating rate is also relevant to the equatorial plane and spatial distribution of density in late bounce time [328].

Meantime, there is very few discussion about the validity of ray-by-ray approximation. Fortunately, thanks to the current computer scaling, Sumiyoshi & Yamada (2015) [408] have demonstrated multi-angle S_N method in three dimension so as to assess how accurate ray-by-ray is. They carried out the comparison by turning off the polar and azimuthal terms in equation (B.34), i.e. regarding the radial traveling intensity as ray-by-ray approach. There are considerable difference between the two method in the variation of energy density and flux along the radial rays. The ray-by-ray method either overestimates or underestimates them by about 20% whereas multi-angle smears out the gaps between different rays. As a matter of fact, in terms of neutrino heating rate, these deviations cancel out each others so that the difference in energetics reduces by $\sim$2% while the multi-angle takes higher value in their numerical setup.

Dolence et al.(2015) [91] conducted 2D newtonian simulation incorporating multi-angle MGFLD solver and also examined how this multi-angle method is different from the previous simulations with 1D neutrino solver. They tried to pursue several works which succeeded in blasting shock with different schemes [266, 412, 289, 41, 303, 414] , yet, they found no explosion which is contradicted to those previous studies.

Therefore, each Boltzmann equation solver has its own advantages and shortcomings while there are also common features among all schemes and it is hardly to say that the dependence of numerical schemes on CCSNe simulation has been well investigated.

Lentz revisted how general relativity [245] and the types of neutrino reaction process [244] influence on the dynamics by using the same code in Liebendörfer et al.(2005) [249] which is fully realistic in one dimension. The studies confirmed non-negligible impacts on heating rate and emphasized the importance of general relativity effects, e.g. redshift, velocity dependence term, and realistic neutrino reactions including inelastic scattering and pair anhilation process. Further analyses should be continued for understanding what part of physics is indispensible for the shock revival and explosion energy.

Appendix C

Multi-dimensional instability

Until the beginning of early 00's, simulations with the realistic physics are limited to spherical symmetry which provide no successful explosion. The failures in 1D seems to enforce theoretical modelers to move to multi-dimensional calculation. So far, the importance of multi-dimensional motion has been confirmed by not only highly developed simulations but also aspherical observaion evidences. There are two major instabilities which are strong candidate to yield explosion, i.e. convection and SASI. Foglizzo et al.(2006) [121] and Guilet & Foglizzo (2012) [145] suggested that the comparison between Brunt-Väisälä frequency and advection timescale would be important indicator by a semi-analytical approach. In this section I mainly focus on brief review of this two multi-dimension effect.

It would be more helpful to persue the details of the two instabilites in Janka et al.(2012), Burrows (2013), Kotake et al.(2013) [196, 49, 220] and the recent review written by Foglizzo et al.(2015) [120]. For further disccusion about convection, the turbulence analyses in CCSN context are also introduced in the last part of this section. To obtain the idea of the closure problem and modeling issue in turbulence equations, see also Garaud et al.(2010), Canuto et al.(2011) and Meakin & Arnett (2010) [135, 58, 274] for details.

C.1 Multi-dimension fluid effect

Semi-analytical approaches in 1D revealed the presence of critical neutrino luminosity against the mass accretion rate on stagnant shock so that the onset of blast is triggered once the neutrino luminosity come to larger than this peculiar value [52, 481, 344].

As mentioned already in section 2.2, the critical luminosities is affected by the dimensionality of system. Several studies have demonstrated the multi-dimension flow pattern could enhance the residue time scale τ_{adv} and the estimation of the runaway condition is given by

$$\frac{\tau_{\rm heat}}{\tau_{\rm adv}} \lesssim 1, \tag{C.1}$$

$$\tau_{\rm heat} = \int_{r_{\rm gain}}^{r_{\rm sh}} \frac{de_{\rm int}}{Q_\nu}, \tag{C.2}$$

$$\tau_{\rm adv} = \int_{r_{\rm gain}}^{r_{\rm sh}} \frac{dr}{v_r}, \tag{C.3}$$

(see [195, 434, 48, 377]). As a matter of fact, even though it addresses the qualtative trend, the estimation is not accurate and some further discussions are represented in section 2.5.

These condition is relevant to competition between heating time and dwell time inside the gain region [291, 196]. When the heating timescale comes to shorter than the advection timescale, the pressure below the shock achieve adequate extent to blow the large ram pressure and the blast wave starts to expand. It is reported that multi-dimensional flow patterns are likely to extend the dwell time inside the gain region and reduce the critical luminosity.

The typical non-radial flow motion is convection. Negative entropy gradient is likely to generate convection overturn in gain layer where net neutrino heating rate is positive. This mixing provide more homogenous temperature profile which will lead to slight increase in heating rate [199, 168, 53, 283].

Many previous researches pointed out that convective motion driven by chemical inhomogenity may also occur near PNS surface and enhance the neutrino heating rate efficiency, although this expectation end up with failure since the convection only take place in deeper portion of PNS (see section. 2.2 and 2.4).

Meanwhlile, Blondin et al.(2003) [30] found an alternative non-spherical instability called standing accretion shock instability (SASI) which show sloshing shock motion induced by radial velocity perturbations with polar angle dependence. The discovery of SASI is owing to adopt axis symmetry instead of equatoral symmetry for sake of remarkable computational resources. This new instability has been paid attention since it trigger shock expansion without any heating source when it is discoverd and also increase the duration of stay in gain region. Whether convection or SASI is dominant come to the next interest.

C.2 Instability driven conditions

Usually convection is likely to lie beneath the shock wave where entropy gradient is negative. Janka et al.(1996) [199] found that unstable convective overturns in 2D enhance the heating efficient and make the system easier to explode than in spherical symmetry case. However, the exchanges of gravity energies between high and low entropy layers take certain time to grow instability otherwise the convection seed sink into PNS. Foglizzo et al.(2006) [121] found that it is helpful to introduce dimensionless variable χ which is the ratio of advection time scale to bouyancy time scale:

$$\chi \equiv \int_{\text{gain}}^{\text{shock}} \omega_{\text{buoy}}(z) \frac{\mathrm{d}z}{v}, \tag{C.4}$$

$$\omega_{\text{buoy}} \equiv G^{\frac{1}{2}} \left| \frac{\nabla P}{\gamma P} - \frac{\nabla \rho}{\rho} \right|^{\frac{1}{2}} = \left(\frac{\gamma - 1}{\gamma} G \nabla S \right)^{\frac{1}{2}} \sim \left(\frac{G}{H} \right)^{\frac{1}{2}}. \tag{C.5}$$

where ω_{buoy} is given by Brunt-Väisäla frequency and expressed by the gravitational acceleration G and pressure scale height H. It is the condition $\chi < 3$ which is likely to be satisfied when strong neutrino absorptions happen or matters advect longer through gain region owing to shock radius expansion. As a result, the developed buoyont bubble pushs the shock further out and helps to revive stagnent shock. This fact is strongly confirmed by Murphy et al.(2011) and Murphy et al.(2013) ([295, 293]; see the end of this section).

On the other hand, in SASI case, the instablilty enhancements are frequently seen in relatively lower mode such as l=1, 2 since these lower modes possess maximum growth rate. Furthermore, this sloshing instability becomes rather important when $\chi > 3$ which is completely opposite condition of convection driven instability because the mechanism

of SASI is relies on the advection-acoustic cycle [121, 325, 483, 377, 291]. The cycle is composed of vorticity advecting downward and acoustic wave propagting upward. The vorticity is generated by unspherical accretion flow when they pass through stagnent shock front at first and transfers its energy to acoustic wave as it hits on the PNS surface. The sound wave provides another fresh vorticity when it perturbates the shock. The perturbed shock also start to show oscillation which is completely different from convective instability. During this round trip, advection time scale is dominant, hence, SASI requires χ to take large value for sufficent grow.

Meanwhile, Blondin et al.(2007) [29] have reached to a different conclusion. They insisted tht SASI mechanism is based on reflection of acoustic wave between shock and proto-neutron star which is called acoustic-acoustic cycle (see the right panel of Fig. C.1). Many dynamical simulations, however, demonstrated that the instabilty cycle, the real part of growth rate, $\omega_{\rm r}$, is rather suitable for the vortix-acoustic cycle.

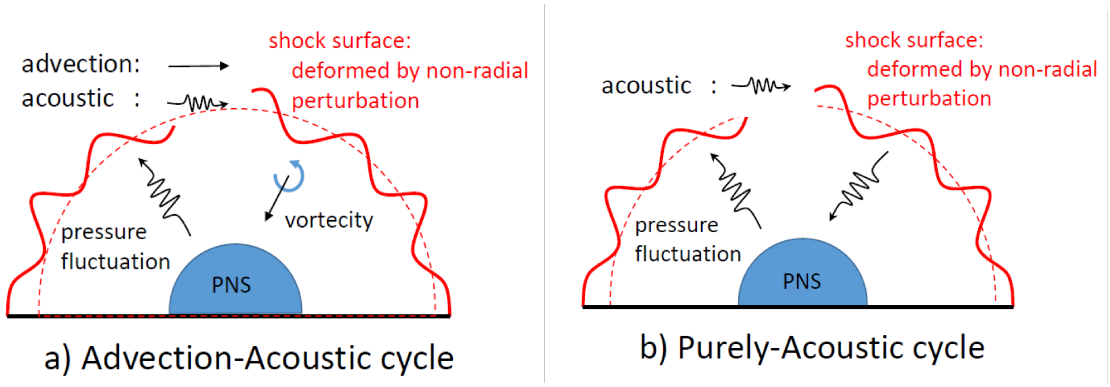

Figure C.1: The schematic pictures of two SASI mechanisms: a) advection-acoustic cycle and b) purely acoustic cycle.

Furthermore, it is noteworthy that the linear analysis study for SASI mechanism has been progressed by [145]. The past series of analytical works [118, 119, 121, 483, ?] are based on WKB approximation which permits to decompose acoustic wave into upward and downward componenets linearly and this operation is only valid under high frequency mode $\omega \gg r_{sh}/c_s$. In order to become free from this mode restriction and achieve the correct conclusion for the SASI mechanism, Guilet & Foglizzo(2012) [145] progressed their analysis and confirmed that time scale of SASI prefers the advection-acoustic cycle which still support the previous studies.

In fact, there remains a fundamental question; how do we distinguish these two instabilities? There are several linear analysis studies, e.g. Yamasaki & Yamada (2007) [483], who proposed that SASI and convection are in the family of oscillation mode and non-oscillation mode, respectively. This is because the real part of growth rate indicates the periodical motion of the stalled shock deformation.

The schematic picture of the two instabilities are shown in Fig.C.2. Although the average shock radius is unchanged in marginal state, SASI provides the periodic change in the shock surface shape for $l > 0$ modes whereas the convection yields no deformation since it maintains the system homogenous. Therefore, oscillation ($\omega_{\rm r} \neq 0$) and non-oscillation ($\omega_{\rm r} = 0$) modes are charaterized by SASI and convection, respectively.

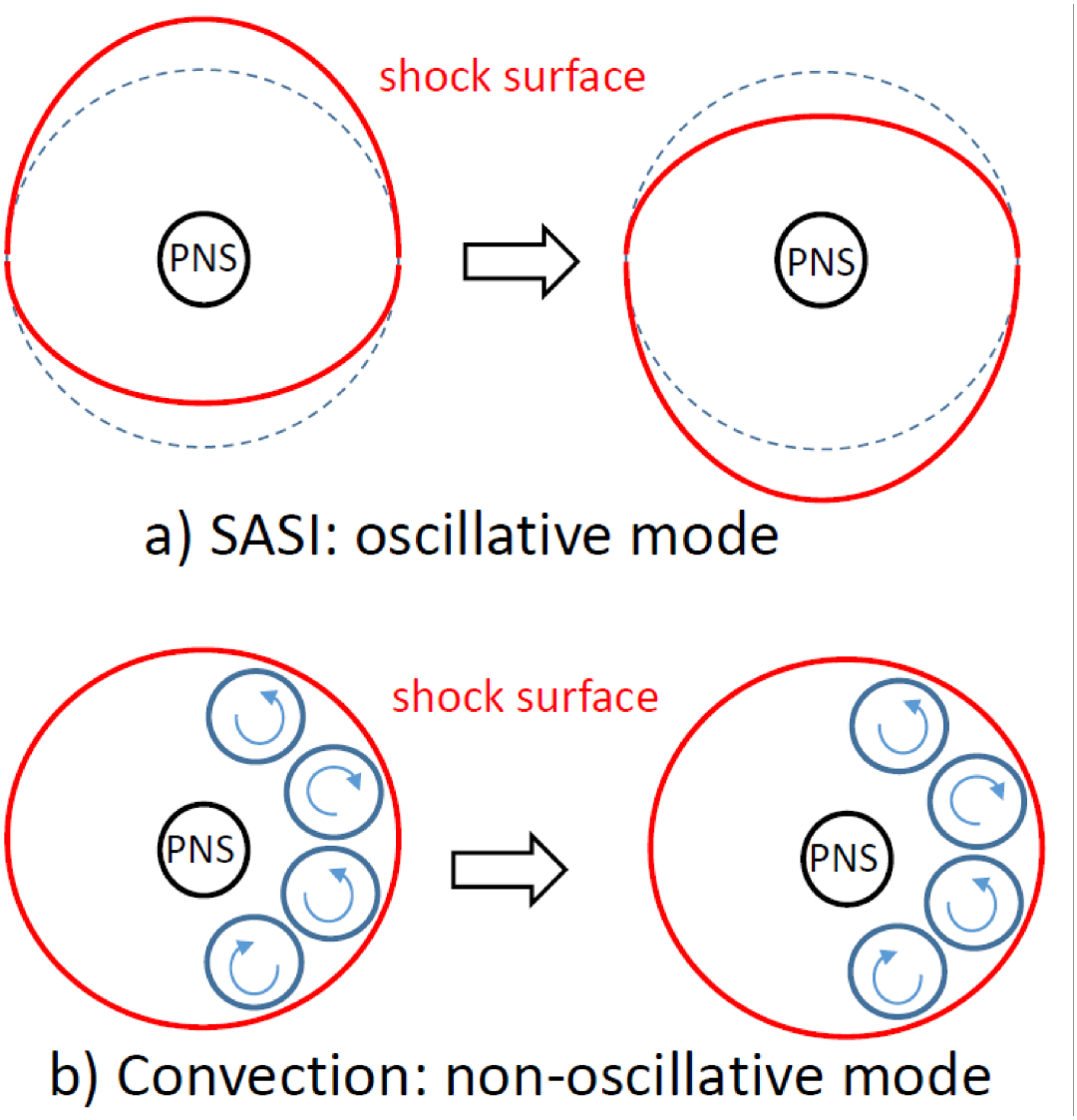

Figure C.2: The two different instability motions correspond to the real part of growth rate. The upper panel depict an oscillative shock deformation of SASI while the lower panel represent no shock deformation for convective motion.

C.3 Going to three dimension

These semi-analytical and dynamical researches have ensured a large advantage of non-spherical fluid dynamics in 2D. However, going from two-dimension to three-dimension, the situation is not straight forward. It is well known that Nordhaus et al.(2010) [317] show the lower critical luminosity curve in 3D than that in 2D while Hanke et al.(2012) [153] obtained completely opposite results. This conflict originates from the presence of large scale buoyancy bubbles which appeared in the former case but dissipated to much smaller scales in the latter one (see more interesting discussion in [5]).

A list of simulations illustrated in table C.1 demonstrates which instabilities are dominant and the resluts of some simulations in the table are selected for addressing the current discrepancy in CCSNe simulations. For instance, employing two distinguishable progenitor models, $8.1M_{\odot}$ and $27M_{\odot}$, Müller et al.(2012) [290] performed the state-of-the-art two

dimensional simulations. It is surprising that they succeed in exploding the heavier progenitor without artificial heating effciency. They concluded that this success is attributed to SASI whereas the lighter model results from the convection instability. It should be noted that for $27M_{\odot}$ model this outcome is definetly contradict with Ott et al.(2013) [329] who used the exactly same progenitor.

Hanke et al.(2013) [154] calculated numerical hydrodynamics in two and three dimension with both elaborate and parametric neutrino transport scheme [290, 378] to see the impact of instability on the shock revival evolution. As a matter of fact, no large shock expansion is seen yet so that they concluded that SASI is not predominant but play a key role in shock deformation in 3D rather than those in 2D. The larger non-radial energies and the faster growth-rate are taken place in early shock evolutionaly phase in the higher dimension calculation and convection instability is found to be the secondary effect. They infered that the discrepancies from other researches may be owing to the implement of neutrino transport which will influence the neutrino sphere position and also neutrino mean energy. Eventually, the accretion-flow dynamics and growth condition of instability become different so that the conclusions are obtained in the opposite way. It should be, however, noted that the onset times of shock expansion are earlier in 2D.

Couch et al.(2013) [77] performed a 3D core-collapse simulation using FLASH, an open source code based on Newtonian hydrodynamic, in which neutrino leakage scheme is incorporated. They investigated how the stagnent shock dynamics is affected by the large amplitude non-radial perturbations which is expected to be present in Si/O layer ([17]; see also chapter 2.4). They explored that this initially large perturbation supports the shock revival, thus confirms the importance of initial fluctuation configurations in steller interior. In semi-analytic approach, Takahashi et al.(2014) [425] found that the supersonic flow with non-linear perturbation grows linearly which is propotional to l mode until they reach the shock front. In this sense, the high aspherical deformation will be responsible for driving shock expansion.

Müller et al.(2015) [288], however, performed their newly developed GRHD simulations in 2D and pointed out that the initial perturbation assumed in [77] is not appropriate since the velocity fields break the divergence free condtion, i.e. anelastic condition ($\nabla \cdot (\rho v) = 0$), and may induce the strong artifact convections. Furthermore, preparing various sets of initial perturbation patterns, they found that low modes, such as $l = 1, 2$, are more favorable for shock revival than relatively high modes. It is noteworthy that their calculations have demonstrated that the high l mode are not efficient to creat the low modes so that the presence of the initial large perturbation in high modes is subordinate for the explosion mechanism.

It is interesting to point out that the more complicated transfer of angular momentum leads to the additional flow pattern in 3D. Iwakami et al.(2008) [193] calculated three-dimensional simulation with starting from steady shock solution and explored that the flow pattern extend not only sloshing motion but also spiral and buoyant bubble structure and the new patterns are more likely to appear near the critical luminosity curve (see also [194]).

The reason why many researcheres support the presence of SASI is that this phenomenom seems to be viable approach for the illustration of high speed pulsar kick and spin. The ejected matters may carry momentum in perticular direction by the presence of global $l = 1$ mode asymmetry which is induced by either convection or SASI. The nacent neutron star supposed to be the counterpart of this powered ejecta in one-sided which is expected to explain high velocity pulsar kick. Scheck et al.(2006) [378] founded that the

distribution of expected kick velocity in their calculation is compatible with the observation. Moreover, Blondin et al.(2007)[29] suggested the possibility of SASI for explaining neutron star spin by discarding axisymmetry. Non-spherical symmetry with slight initial perturbations generates spiral mode $m = \pm 1$ in $l = 1$ mode, even simulation starts from non-rotating massive stars. Guilet & Fernández(2014) [144] estimated the amount of the angular momentum transport by using anlalytical approach and their spin periods were similar to values obtained by the numerical simulation in [472]. Hence, these multi-dimensional instabilities are likely to be candidate of mechanism for explaining neutron star kick and spin observations.

It is, however, noteworthy that there is an issue called "SASI myth" named by Burrows (2013) [49]. While SASI may play key role in the CCSNe theory, several numerical counter parts depict spiral modes rather than sloshing modes of SASI in 3D (see table C.1) and Burrows (2013) doubted that this mode is produced by axisymmetry restriction. Hence, whether SASI phenomena is artificial or not is the current open question and might be settled by neutrino signals and gravitional waves [220].

In 3D (and also 2D) the presence of turbulence is also crucial to CCSNe dynamics. The problem is which instabilities are responsible for inducing turbulence with large hot bubbles. It is interesting to point out that Yamasaki & Yamada(2006) [482] investigated the effect of large hot bubbles under assumptions that convection flow smears the entropy, isentropic, and all internal energy converted immediately to bulk fluid energy. As a result, the magnitude of critcal curve reduces by about half in this maximum effecienct case. Although they have demonstrated that convection possess potentailly non-negligible feedback to shock reival, this fact is, however, too optimistic so that further realistic analyses should be necessary for more precise quantitative discussion. Meanwhile, there is a useful approach called Renolds Average Decomposition (RAD) which separates the hydrodynamical variables into the mean (reference) flow and fluctuation (turbulence) flow, for instance,

$$\rho = \rho^{(0)} + \rho^{'} \tag{C.6}$$
$$v_i = v_i^{(0)} + v_i^{'} \tag{C.7}$$
$$S = S^{(0)} + S^{'} \tag{C.8}$$

where $\langle \cdot \rangle = \cdot^{(0)}$ is usually taken from large samples average and the prime in super script denotes the fluctuation part. Since the unknown higher order variables are added, e.g. the Reynolds stress $\bar{R}_{ij} = \langle v_i' v_j' \rangle$, flux $\bar{F}_i = \langle v_i' S' \rangle$ and variance $\bar{Q} = \langle S'^2 \rangle$, the difficulty in solving RAD is the determination of the closure equations appropriately ao that the truncations should be optimized in case by case.

It should be stressed that the background flow in astrophysical phenomena, anelastic condition is more suitable. This is because, although it is quite similar to Boussinesq approximation, the anelastic apporximation discards uniform density assumption and entropy is deployed for the independent variable instead of temperature. It should be noted that this approximation is valid only if the turbulence in system is sub-sonic, namely low mach number, so that turbulence velocity can be treated as an higher order correction (see an appendix in [135]). There are also some problems in energy conservation undere this condition [36]. in CCSN case, the turbulence beneath the shock is unique compared with stellar evolution since the background entropy variation exists in post shock region. This entropy structure is attributed to the net neutrino heating and the basic equations should be modified in proper.

From investigating the axisymmetry simulations of CCSN, Murphy et al.(2011) [295] proposed the new closure relation for the basic equations for the averaged flow. They

pointed out that the traditional closure modeling used in either experiment or stellar evolution provides merely little proper trends of turbulence inside shock. For instance, since pre-collapse convection in the gain region showed that the large-scale plums are responsible for transporting kinetic energy flux, entropy flux and entropy variance, the gradient-diffusion approximation (Launder & Sandham (2002) [243]) are not appropriate since their second-order Renolds correlations are based on local approximation. They also attempt the algebraic modeling as well as MLT which substitute the differential term for algebraic formulation with assumption of local balance in buoyancy driving and dissipation. Although this approach demonstrates better coincidence with the simulation, the discrepancy is not small due to the local approximation. As a result, using the some of algebraic expression for the 2nd correlation closure, they modified the source terms of entropy evolution, i.e. the turbulent luminosity and dissipation. The formulation of turbulence luminosity relies on the magnitude and location of peak luminosity and also the end point of convective region which is determined consistently by the energy conservation in integral form. Moreover, turbulent dissipation is given by the balance of total buoyancy work and dissipation inside the convective region. This self-similar modeling with the global constraints reproduces the outcomes of dynamical simulation quite well and justifies the importance of Renolds pressure which is completely dropped in Yamasaki & Yamada (2006)[482].

Murphy et al.(2013) [293] extended their simulation to 3D and also investigate the similiar analysis for the basic equations of mean fluid. The results persue that total buoyanacy driving balances with dissipation especially near the onset of explosion. After the modification of the entropy equation, neutrino power $P_\nu = L_\nu \tau$ could be equivalent to the convection power which is the total amount of turbulent luminosity and dissipation. It is interesting that the turbulent luminosity linearly scale with the neutrino power and it is less efficient for driving convetion in 2D. They also insisted that the kinetic turbulence term in momentum equaiton plays inevitable role in expanding the shock radius especially in 3D. The research also concluded that turbulent convection is more important than SASI in their parametric 3D simulation and similar results are explored by other studies , e.g. [329, 90]. In addition, some researcher did not find any sloshing properties in three-dimension (e.g., [50, 90, 153]) and are skeptical about the presence of SASI. For example, Burrows et al.(2012) [50] insisted that the striking feature of $l = 1$ SASI mode may be artifact phenomena produced by axisymmetry and its inverse cacade.

Fernandéz et al.(2014) [111] analized the two instabilities near the criterion of explosion and demonstrated that a spherical Fourier-Bessel decomposition is available to extract signatures of the interplay of SASI and convection. SASI-dominated models form large scale and high entropy bubbles. In this case it is important to keep its scale longer than shock oscillation unless it losts the oppotunity to explode. On the other hand, convection-dominated models also produce similar structure bubbles by gathering smaller-scale from buoyant activities. The behavior of angular spectrum manifested inverse turbulent cascade at large l which is connected to construct large-scale convection while SASI holds $l = 2$ peak power. They confirmed that the parameter χ is a good measure of which instabilities is dominated. However, once explosions are activated, it is difficult to find out which instability process strongly affect to the subsequent dynamical evolution.

Table C.1: The list of multi-dimension calculations with different dominant instabilities. See also Melson et al.2015 [276]

	SASI aided			convection dominant		
2D	Blondin +03 Scheck +06 Ott +08 Müller +12, +13, +14	Janka +05 Burrows +07 Marek & Janka +09	Ohnishi +06 Murphy +08 Suwa +10, +13	Herant +94 Mezzacappa +98 Murphy +11	Burrows +95 Buras +03	Janka +96 Buras +06
3D	Hanke +12, +13 Müller +12, +15	Takiwaki +12, +13	Bruenn +13, +14	Iwakami +08 Ott +12 Couch +13, +14	Nordhaus +10 Ott +13 Dolence +13	Burrows +12 Iwakami +14 Murphy +13

Appendix D

Equation of states near nuclear density

In this section, I mainly review the basic idea of EoS properties, especially how these properties are characterized in practical EoS studies, e.g. Lattimer & Swesty (1991) [241] and Shen et al.(1998) [385]. The further improvment after those two EoS is addressed in section 2.3.

D.1 Physical properties of parameterized EoS at T=0

Firstly, it will be helpful to start from the empirical formulation of internal energy of "homogeneous" nuclear matter at zero temperature case. The formulation is suitable for especially understanding the properties of cold NS since NS can be assumed as the extremly large object which is consisted of pure neutron. In this case, if $T = 0$ the Helmholtz free energy is regarded as the bare internal energy, hence, it should take minimum at the nuclear saturation density. The bulk energy density $E_{\rm bulk}$ [MeV/nuc], is consisted of kinetic energy and nuclear potential, however, it is rather convenient to separate $E_{\rm bulk}$ from iso-spin independent term, $E_{\rm nuc}$ [MeV/nuc], and iso-spin dependent term, $E_{\rm sym}$ [MeV/nuc]; the traditional form of $E_{\rm nuc}$ [MeV/nuc] is represented as a following relation;

$$E_{\rm bulk}(n, Y_p) = E_{\rm nuc}(n) + E_{\rm sym}(n) \cdot (1 - 2Y_p)^2, \tag{D.1}$$

$$E_{\rm nuc}(n) = E_0 + \frac{K}{18}\left(\frac{n - n_0}{n_0}\right)^2 + \frac{K'}{162}\left(\frac{n - n_0}{n_0}\right)^3, \tag{D.2}$$

$$E_{\rm sym}(n) = J_0 + \frac{L}{3}\left(\frac{n - n_0}{n_0}\right), \tag{D.3}$$

where n and Y_p are number density and proton fraction, respectively and the coefficents K, J_0, L and K' are incompressibility, symmetry energy, slope and skewness, respectively. The meaning of each coeffecient is represented in Fig. D.1. Imcompressiblity K and symmetry energy J_0 are curvature and the energy difference between complete asymmetry matter, $Y_p = 0$, and symmetry matter, $Y_p = 0.50$, at the saturation point. In addition it is apparent that L is called slope since it is a tangent value of $E_{\rm bulk}$ curve at n_0 [331, 401].

Furthermore, K, K' and L are the measure of stiffness since pressure P [MeV/fm^3] are

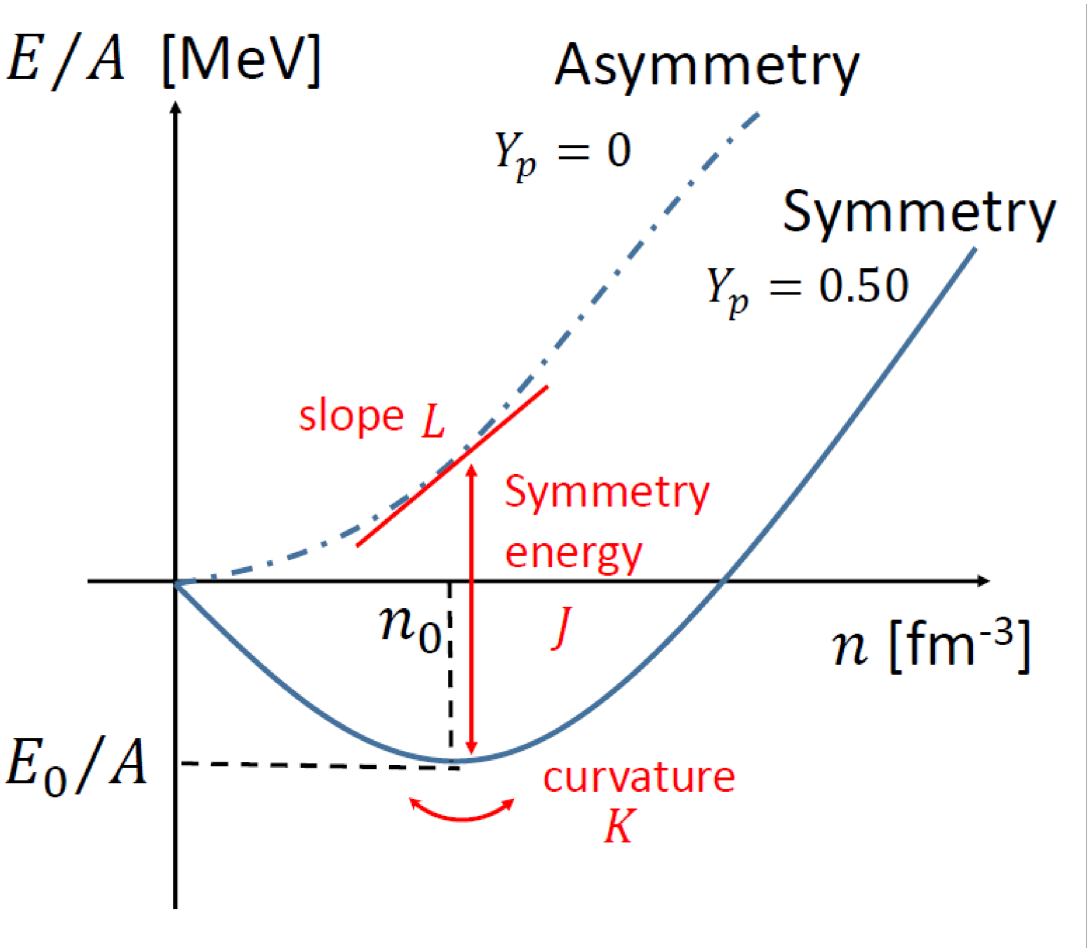

Figure D.1: The nuclear internal energy per baryon as function of number density. n_0 and E_0/A are saturation point density and bulk energy at that point, respectively. E/A for symmetry matter is represented as solid line while those for asymmetry matter is drawn in dot-dashed line.

given as

$$P = -\left(\frac{dE_{\rm bulk}}{d1/n}\right) \tag{D.4}$$

$$= n_0 \left(\frac{n}{n_0}\right)^2 \left[\frac{K}{9}\left(\frac{n-n_0}{n_0}\right) + \frac{K'}{54}\left(\frac{n-n_0}{n_0}\right)^2 + \frac{L}{3}\cdot(1-2Y_p)^2\right]. \tag{D.5}$$

It should be noteworthy that symmetry energy J_0 is tightly associated with the mixture of compositions since it has a following relation with chemical potentials μ_n and μ_p under beta-equilibrium;

$$\mu_n - \mu_p = -\left(\frac{\partial E_{\rm bulk}}{\partial Y_p}\right) \tag{D.6}$$

$$\sim 4\,(1-2Y_p)\,E_{\rm sym}(n). \tag{D.7}$$

Therefore, the symmetry energy influences reaction rates of neutrino charged current, i.e. lepton number, and the variaiton of neutrino mean energy which is relevant to neutron and proton mean-field potentials. As it has been already explained in section.2.2 that the mass

of the inner core can be roughly estimated as eq. (2.13), a large value of J_0 crucially affects the dynamics and strength of shock front (see the discussion in section 2.3 and 2.5).

As a matter of fact, large freedom of parameter choices are still left and thermal properties above the nuclear saturation density are hardly determined. The ab initio calculations are substantial to achieve the true nuclear interaction form and precise EoS behavior.

It should be stressed that the idea of this parameterized EoS is valid only when the considering system can be assumed as uniform matter where nucleons are undistinguishable from each other. On contrary, when density is below the saturation point heavy nuclei appear to be dominant elements so that there is a boundary which separates nucleon inside of nucleus from those outside of nucleus (see Fig. D.2 and D.3). Hence, additional terms should be needed to characterize this inhomogeneous system.

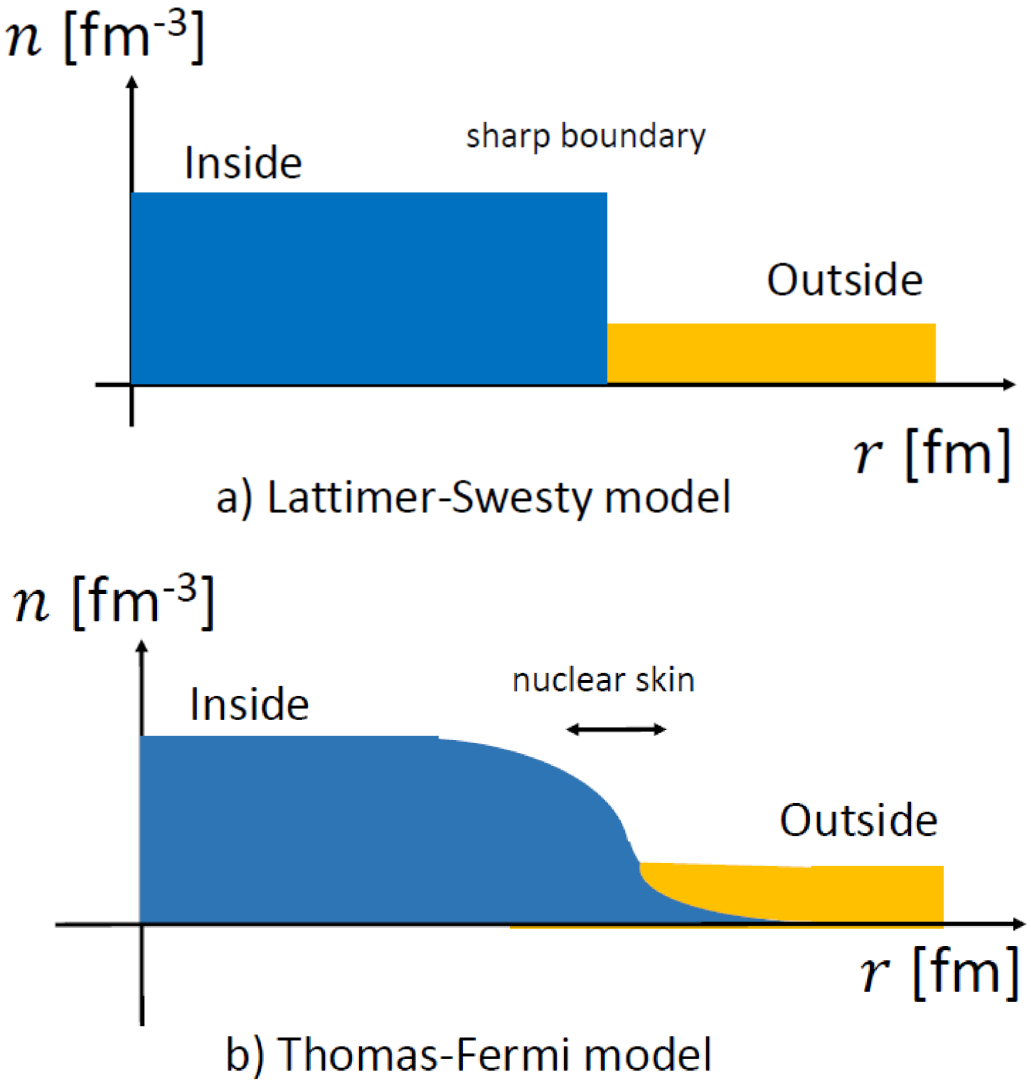

Figure D.2: The radial distributions of nuclear number density in inhomogenous nuclear matter. Nucleon are isolated from inside (blue) to outside (yellow). The Liquid-drop model (top) and Thomas-Fermi approximation (bottom) are represented.

Moreover, between the transition from 10^{13}g/cc (the bottom left panel in Fig. D.3) to 10^{14}g/cc (the bottom right panel in Fig. D.3), the nuclear structure continously alters its shape which is determined by the lowest free energy. This phase transition is so called

nuclear pasta and crucial not only to EoS itself but also to weak interaction rate. The details are discussed in the next sections by introducing the two well known EoS.

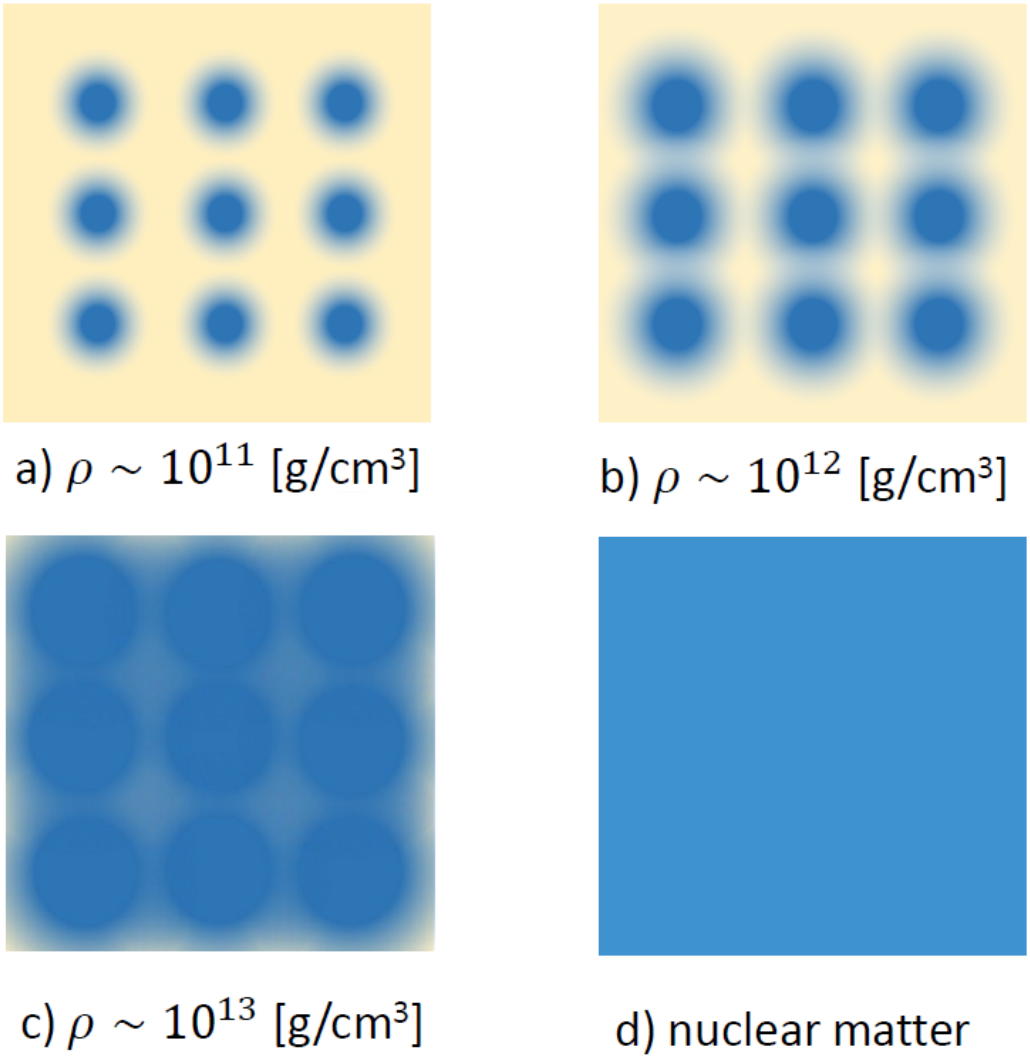

Figure D.3: A sketch of spatial distributions of nuclei with various density regime. The colors indicate samething as Fig. D.2

Furthermore, EoS needs to be extend to finite temperature because the peak temperature increase $T_c \gtrsim 30$MeV after bounce. Most of all EoS modelers carry out the minimization of Helmholtz free-energy by introducing entropy formulation which is similar to that in ideal gas case.

The difficulty of making finite temperature EoS is owing to incorporate excited states and modification in distribution function for all particles in system which also affect the defination of entropy due to many body correlation in wave functions. In the case of mean field approximation, however, the hamiltonian of nuclear matter is altered to no mutual interaction between each states , i.e. only the diagonal terms present in the density matrix and expressed as sumation of individual states energies interacting with the external field. The Helmholtz free energy per baryon, F, and entropy per baryon, S, are, therefore,

identified as

$$F = E - TS \tag{D.8}$$

$$S = -k_B \sum_0 \int \frac{d^3p}{(2\pi\hbar)} \left(f_i \ \ln \ f_i \ + (1-f_i) \ \ln \left(1-f_i\right)\right) \tag{D.9}$$

$$E = E_{\rm bulk} + (\text{inhomogoneous} \quad \text{contributions}) \tag{D.10}$$

where f_i is distribution function of species i which is safely assumed as Fermi-Dirac. The equation of state should be most stable state so that the free energy, F, defined as eq.D.8 takes the smallest value at the given ρ, T and Y_p under the constraints of number conservation for each species.

D.2 Classical EoSs

It was polytrope EoS which first applied to numerical calculation at the beginning of CCSNe studies since thermodynamical properties around the saturation point is highly uncertain. After 90's the theoretical progresses have been done successfully and eventually provided two practical EoSs which is still most widely used at present; one is Lattimer-Swesty EoS (LS; [241]) which is constructed under non-relativistic homogeneous nuclear matter with Skyrme-interaction potential and inhomogeneous compressive liquid drop whereas the other is Shen, Toki, Oyamatsu and Sumiyoshi EoS(STOS or Shen; [385]) which is based on relativistic mean field (RMF) for nuclear matter and applied Thomas-Fermi approximation to sub-nuclear matter.

It should be noted that the coefficents K and J_0 and the minimum energy E_0 in the parametric form EoS can be easily reproduced by following relations;

$$E_0 = E_{\rm nuc}(n_0) = E_{\rm bulk}(n = n_0, Y_p = 0), \tag{D.11}$$

$$E_{\rm sym}(n) = \frac{1}{2}\frac{\partial^2 E_{\rm bulk}}{\partial(1-2Y_p)^2}, \tag{D.12}$$

$$K = n^2 \left(\frac{\partial^2 E_{\rm bulk}}{\partial n^2}\right), \tag{D.13}$$

$$J_0 = E_sym(n_0). \tag{D.14}$$

In this section I firstly exhibit the difference between the two EoS in the treatment of homogenous matter. In LS EoS, the bulk internal energy, $E_{\rm bulk,\,LS}$ [MeV/cm^3], is based on the mean filed Skyrme type nuclear interaction which obeys zero range density potential [387] and reproduces many of the global properties of nuclei, e.g. nuclei radius, the minimum energy and saturation points. They fitted much simpler form as following;

$$E_{\rm bulk,\,LS}(n, Y_p, T) = \Sigma_i \frac{\hbar^2 \tau_i}{2m^*} + \left[a + 4bY_p(1-Y_p)\right] n_b^2 + c n_b^{1+\delta} - Y_p n_b \Delta \tag{D.15}$$

where $Y_p = n_p/n_b$, $\Delta = 1.293$MeV is the mass difference and m^* is density dependent effective mass. The first, second and third term represents kinetic energies baryon (T dependence), two-body interaction and the multi-body interactions, respectively. The parameters a, b, c, δ are associated with experimental values, thus incompressibilty K, symmetry energy J_0, saturation density n_0, effective mass m^* and nuclear binding energy B (see the details in [241]). It should be stressed that the degree of freedom is left so that "K" can be designed freely and the original paper prepared K =180, 220 and 375MeV. As

the kinetic term is given by non-relativistic form, there is physical shortcome in aspects of causality violation while the general relativity correction should be implemented for CCSN simulations and especially disccusion of NS structure.

In contrast, STOS is founded on relativistic mean fields which is consisted of baryon and meson in homogeneous matter The effective Lagrangian $\mathcal{L}_{\rm RMF}$ is given as

$$\begin{aligned}
\mathcal{L}_{\rm RMF} &= \mathcal{L}^{\rm (f)}_{\rm baryon} + \mathcal{L}^{(f)}_{\rm meson} + \mathcal{L}^{\rm (int)}_{\rm BM} + \mathcal{L}^{\rm (int)}_{\rm self} && \text{(D.16)}\\
\mathcal{L}^{\rm (f)}_{\rm baryon} &= \bar{\psi}_b \left(i\gamma_\mu \partial^\mu - M_b - g_\sigma \sigma - g_\omega \gamma_\mu \omega^\mu - g_\rho \gamma_\mu \tau_a \rho^{a\mu} \right) \psi_b && \text{(D.17)}\\
\mathcal{L}^{\rm (f)}_{\rm meson} &= \frac{1}{2}\partial_\mu \sigma \partial^\mu \sigma - \frac{1}{2} m_\sigma^2 \sigma^2 \\
&+ \left(-\frac{1}{4} W_{\mu\nu} W^{\mu\nu} + \frac{1}{2} m_\omega^2 \omega_\mu \omega^\mu \right) \\
&+ \left(-\frac{1}{4} R^a_{\mu\nu} R^{a\mu\nu} + \frac{1}{2} m_\rho^2 \rho^a_\mu \rho^{a\mu} \right) && \text{(D.18)}\\
\mathcal{L}^{\rm (int)}_{\rm BM} &= -\bar{\psi}_b \left(g_\sigma \sigma + g_\omega \gamma_\mu \omega^\mu + g_\rho \gamma_\mu \tau_a \rho^{a\mu} \right) \psi_b && \text{(D.19)}\\
\mathcal{L}^{\rm (int)}_{\rm self} &= -\frac{1}{3} g_2 \sigma^3 - \frac{1}{4} g_3 \sigma^4 \\
&+ \frac{1}{4} c_3 \left(\omega_\mu \omega^\mu \right)^2 && \text{(D.20)}
\end{aligned}$$

where ψ_b, σ, ω and ρ are nucleons (proton and neutron), scalar-isoscalar meson, vector-isoscalar meson and vector-isovector meson, respectively, and $W_{\mu\nu} = \partial^\mu \omega^\nu - \partial^\nu \omega^\mu$ and $R^a_{\mu\nu} = \partial^\mu \rho^{a\nu} - \partial^\nu \rho^{a\mu} + g_\rho \epsilon^{abc} \rho^{b\mu} \rho^{c\nu}$. The sign of scalar meson term in eq. (D.18) is taken "+" due to consistency between particle number and energy while those of vector meson terms are opposite because real particles hold its physical meaning in spatial components. Hence, if number of real particles increase, energy becomes larger. Note that nucleon are regarded as iso-symmetry so that $M_p = M_n = 983$MeV which implies mass difference is not take into account. Moreover, the non-linear terms which is the contribution of self interactions scalar meson (σ^3, σ^4) reduce incompressibility K, thus they soften EoS. On the contrast, the quadratic vector self interaction term (ω^4) refers to relativistic Bruckner Hartree-Fock term which produce proper repulsive force. All parameters, meson masses and coupling constants, are determined to take the minimum value at the saturation density and fitted to the experimental data ($n_0 = 0.16$ fm^{-3}, $E_0 = -16MeV$). Several parameter sets are permitted and STOS adopts TM1 parameter sets [403].

It is notewirthy that the bulk energy for STOS $E_{\rm bulk,\ STOS}$ is given by following relations;

$$\begin{aligned}
T^\mu_\nu &= -g^\mu_\nu \mathcal{L}_{\rm RMF} + \frac{\partial \mathcal{L}_{\rm RMF}}{\partial \left(\partial_m u \Psi_i \right)} \partial_\nu \Psi_i && \text{(D.21)}\\
E_{\rm bulk,\ STOS} &= \langle T^{00} \rangle && \text{(D.22)}
\end{aligned}$$

where T^μ_ν and Ψ_i are energy-momentum tensor and the simplified symbols for the quantum fields, respectively and $\langle T^{00} \rangle$ denotes the expected value of energy density with respect to Ψ_i. It has been presented that EoS can be roughly characterized by eq. (D.3) and the bulk incompressibility K and symmetry energy J are thought to be the important components for blast wave dynamics and neutrino emission properties. In case of the two EoSs cases, LS has $K = 180, 220$ [MeV] and $J = 29.3$ [MeV] which are both control parameters while STOS has $K = 281$ [MeV] and $J = 36.9$ [MeV]. The difference in K are due to the absence and presence of relativity. Inclusion of relativity effect hardens EoS because the negative energy states produce strong repulsive force in high density region and contributes to extra

pressure so that they can be regarded as effective three-body interaction in non-relativity limit. This trend is favorable for the evidence of observed maximum neuron star mass. If one evaluates adabatic index $\Gamma = \left(\frac{\partial P}{\partial \rho}\right)_S$ at nuclear density, LS180 gives $\Gamma_{LS} \sim 2.2$ while STOS gives much higher value, $\Gamma_{STOS} \sim 2.9$ [196]. This consequence makes us easier to realize the stiffness of individual EoSs.

However, even in extension of relativistic mean field EoS, boson exotic matters, such as pion and hyperon, soften the system too much due to its condensation. The maximum neutron star mass change from $2.1M_\odot$ to $1.56M_\odot$ when one add hyperon [192].

D.3 Inhomogenous matter

When we consider a system filled with an inhomogeneous nuclear matters, there suppose to be boundary between inside and outside of nuclei which is occupied by nucleon or other light nuclei. This nuclei "shapes" are determined by the balance between the surface and Coulomb term and some of EoS modelers have adopted quite different treatments between each others. There is also interesting phenomena called nuclear "pasta" (inhomogeneous crystalline) which tends to occur at $\rho \sim \rho_0$, thus the transition from inhomogeneous to homogeneous system [363, 330, 165]. In this section, the two methods are introduced for treating sub-nuclear density matter; LS EoS adopts the compressive liquid drop model with finite temperature [242] whereas STOS computes Thomas-Fermi approximaiton for sub-nulear density regime.

In liquid drop model, considered terms for mass formula are equivalent to Weinzacker-Bethe formulaton, i.e. bulk, surface, Coulomb, shell and pairing energy. The coefficients of each terms are regarded as parameters and chosen to be fulfilled with the experemental evidence, for instance, the saturation density $n_0 = 0.17\text{fm}^{-2}$, minimum energy per nucleon $E_0 = -16\text{MeV}$ and other individual nuclear mass data. It will be convenient for the interpretation of dynamical simulations to apply LS EoS since K and J_0 are given by hand, thus well controlled. It also has advantage of incorporating nuclear shapes for the nuclear "pasta" phase and either droplet or bubble is employed in LS EoS. The problem appears, however, when the system is significantly different from experimental situtaion such as supernova or nascent neutron star where hot, dense and asymmetry matters are dominated.

On the other hand, Thomas-Fermi approximation employed by STOS is a self-consistent theory as well as Hartree-Fock theory. The difference from Hartree-Fock method is that the overall shell effects which are responsible for the deformation of nuclei are averaged while it is enabled to treat the large ensemble system such as NS.

The idea of nuclear Thomas-Fermi approximation is just as same as the original case which is applied to atomic system, i.e. the nuclear interaction potential depends on density profile of nuclei structure and is taken into account its back reaction [297, 298].

Recalling the original Thomas-Fermi approximation density distribution of electron in atomic system are calculated by solving charge neutrality condition

$$\Delta\phi = 4\pi n_{\mathrm{e}}\left(\phi\right), \tag{D.23}$$

where electron charge density n_e also directly relies on electric potential ϕ so that it is no more uniform and vice versa [231]. Hence, the variation of density distribution is iterated under the several interaction potential parameters until the system achieve settlement, in other word, self-consistency is guaranteed.

Moreover, the nucleus "skin" is taken into account in STOS whereas LS assumes it as sharp boundary between inside and outside, thorefore it is completely dropped in their calculation. The diffusion of nucleon can be acted as a finite-range force in the nucleus system so that the number density gradient term, $E_{\rm grad}$, is adopted to the nuclear internal energy, instead of surface term in LS. The width of skin parameter are added and nuclear shape is regarded as droplet for all inhomogeous nuclear phase in STOS. As a consequence, the nuclear binding energy, $E_{\rm bind}$, is wrriten in two way

$$-E_{\rm bind} = E_{\rm bulk,\,LS} + E_{\rm surf} + E_{\rm Coul,\,LS} \qquad \text{(liquid drop)}, \tag{D.24}$$

$$= E_{\rm bulk,\,STOS} + E_{\rm grad} + E_{\rm Coul,\,STOS} \qquad \text{(Thomas} - \text{Fermi)}, \tag{D.25}$$

where the detail expression are written in the original papers. It should be noted that the surface term in Thomas-Fermi method is, however, not exactly as same as those in liquid drop model but different by factor 2 under beta-equilibrium condition (see the details in [331]).

The two EoS approaches should implement additional microphysics, e.g. shell effect, pairing terms and/or incorporating density and temperature dependence. They are, however, both using empirical relations and hold large uncertainty about nuclear fission barrieres so that binding energies are not applicable to calculate the precise r-process. It should be also stressed that both EoS handle only averaged heavy nuclei (single nucleus approximation; SNA) which neglects the light nuclei reactions and cause difficulty to access smoothly to non-NSE. The improvement of latter part is one of our scopes in this paper (see section 3.1.3). From the failed 1D studies in CCSNe a number of EoS comparisons are demonstrated and there are several coincidence.

For stiff EoS, it is reported that central density is not raised as high as those in soft eos and the position of shock formation at bounce moves outward. Hence, enclosed mass of inner core is slightly larger ($\Delta M_{\rm ic} = 0.1 M\odot$) which avoids serious energy drain due to photodissociation ($E_{\rm bind} \sim 8.8$MeV per baryon) so this fact seems to be advantage of explosion. The lower central density, however, also influences neutrino sphere radius, i.e. proto-neutron star becomes less compact. Although neutrino sphere will become closer to gain radius and ascend inverse flux factor which enhance heating rate inside the gain region, these tendencies often yield negative effect for shock revival due to lower temperature and luminosity at neutrino sphere. Hence even there are no successful explosion, the softer EoS tend to produce more efficient heating than stiffer one. Applying different eos results in very subtle and sophisticated difference as we've seen above. The influence of EoS on post bounce evolution cannot easily understand by single peculiar property.

If we turn attention to recent studies, for instance, Suwa et al.(2013)[413] compared LS180, LS220, LS375 and STOS and carried out Newtonian hydrodynamical simulations in 1D and 2D which implement IDSA for neutrino transport solver (see appendix B). It is interesting that neutrino mean energy and approxiamte neutrino sphere radius are remarkably similiar in both one- and two-dimension. It is well known that general relativity and heavy lepton type flavors (μ, τ) provide deeper gravitaional well and larger internal energy loss, respectively. Hence, the absence of these ingredient makes PNS less compact and the diffrence between STOS and LS180 much smaller than [411]. It seems that the first $200 - 300$ms behaviors of heating efficency and $L_{\nu_e, \bar{\nu_e}}$ are essential for neutrino heating mechanism and the difference in EoS produces slight change of these properties which play critical role in the successful explosion.

Bibliography

[1] M. G. Aartsen, M. Ackermann, J. Adams, J. A. Aguilar, M. Ahlers, M. Ahrens, D. Altmann, T. Anderson, C. Arguelles, T. C. Arlen, and et al. Multimessenger search for sources of gravitational waves and high-energy neutrinos: Initial results for LIGO-Virgo and IceCube. *Phys. Rev. D*, Vol. 90, No. 10, p. 102002, November 2014.

[2] D. C. Abbott and L. B. Lucy. Multiline transfer and the dynamics of stellar winds. *ApJ*, Vol. 288, pp. 679–693, January 1985.

[3] D. C. Abbott and L. B. Lucy. Multiline transfer and the dynamics of stellar winds. *ApJ*, Vol. 288, pp. 679–693, January 1985.

[4] E. Abdikamalov, A. Burrows, C. D. Ott, F. Löffler, E. O'Connor, J. C. Dolence, and E. Schnetter. A New Monte Carlo Method for Time-dependent Neutrino Radiation Transport. *ApJ*, Vol. 755, p. 111, August 2012.

[5] E. Abdikamalov, C. D. Ott, D. Radice, L. F. Roberts, R. Haas, C. Reisswig, P. Mösta, H. Klion, and E. Schnetter. Neutrino-driven Turbulent Convection and Standing Accretion Shock Instability in Three-dimensional Core-collapse Supernovae. *ApJ*, Vol. 808, p. 70, July 2015.

[6] A. Akmal, V. R. Pandharipande, and D. G. Ravenhall. Equation of state of nucleon matter and neutron star structure. *Phys. Rev. C*, Vol. 58, pp. 1804–1828, September 1998.

[7] M. Alford, K. Rajagopal, S. Reddy, and F. Wilczek. Minimal color-flavor-locked-nuclear interface. *Phys. Rev. D*, Vol. 64, No. 7, p. 074017, October 2001.

[8] A. S. Almgren, J. B. Bell, and M. Zingale. MAESTRO: A Low Mach Number Stellar Hydrodynamics Code. *Journal of Physics Conference Series*, Vol. 78, No. 1, p. 012085, July 2007.

[9] G. Altavilla, M. T. Botticella, E. Cappellaro, and M. Turatto. Supernovae and Gaia. *Ap&SS*, Vol. 341, pp. 163–178, September 2012.

[10] J. P. Anderson, S. M. Habergham, P. A. James, and M. Hamuy. Progenitor mass constraints for core-collapse supernovae from correlations with host galaxy star formation. *MNRAS*, Vol. 424, pp. 1372–1391, August 2012.

[11] A. Arcones, H.-T. Janka, and L. Scheck. Nucleosynthesis-relevant conditions in neutrino-driven supernova outflows. I. Spherically symmetric hydrodynamic simulations. *A&A*, Vol. 467, pp. 1227–1248, June 2007.

[12] D. Arnett. *Supernovae and Nucleosynthesis: An Investigation of the History of Matter from the Big Bang to the Present*. 1996.

[13] D. Arnett, C. Meakin, and P. A. Young. Turbulent Convection in Stellar Interiors. II. The Velocity Field. *ApJ*, Vol. 690, pp. 1715–1729, January 2009.

[14] W. D. Arnett. Analytic solutions for light curves of supernovae of Type II. *ApJ*, Vol. 237, pp. 541–549, April 1980.

[15] W. D. Arnett. 3D and Some Other Things Missing from the Theory of Massive Star Evolution. In G. Meynet, C. Georgy, J. Groh, and P. Stee, editors, *New Windows on Massive Stars*, Vol. 307 of *IAU Symposium*, pp. 459–469, January 2015.

[16] W. D. Arnett and C. Meakin. Toward Realistic Progenitors of Core-collapse Supernovae. *ApJ*, Vol. 733, p. 78, June 2011.

[17] W. D. Arnett and C. Meakin. Toward Realistic Progenitors of Core-collapse Supernovae. *ApJ*, Vol. 733, p. 78, June 2011.

[18] W. D. Arnett, C. Meakin, and M. Viallet. Chaos and turbulent nucleosynthesis prior to a supernova explosion. *AIP Advances*, Vol. 4, No. 4, p. 041010, April 2014.

[19] L. W. Avery and L. L. House. An Investigation of Resonance-Line Scattering by the Monte Carlo Technique. *ApJ*, Vol. 152, p. 493, May 1968.

[20] C. Badenes, J. Harris, D. Zaritsky, and J. L. Prieto. The Stellar Ancestry of Supernovae in the Magellanic Clouds. I. The Most Recent Supernovae in the Large Magellanic Cloud. *ApJ*, Vol. 700, pp. 727–740, July 2009.

[21] E. Baron, H. A. Bethe, G. E. Brown, J. Cooperstein, and S. Kahana. Type-II supernovae from prompt explosions. *Physical Review Letters*, Vol. 59, pp. 736–739, August 1987.

[22] E. Baron and J. Cooperstein. The effect of iron core structure on supernovae. *ApJ*, Vol. 353, pp. 597–611, April 1990.

[23] E. Baron, J. Cooperstein, and S. Kahana. Type-II supernovae in 12-solar-mass and 15-solar-mass stars The equation of state and general relativity. *Physical Review Letters*, Vol. 55, pp. 126–129, July 1985.

[24] J. F. Beacom and M. R. Vagins. Antineutrino Spectroscopy with Large Water Čerenkov Detectors. *Physical Review Letters*, Vol. 93, No. 17, p. 171101, October 2004.

[25] K. Belczynski, G. Wiktorowicz, C. L. Fryer, D. E. Holz, and V. Kalogera. Missing Black Holes Unveil the Supernova Explosion Mechanism. *ApJ*, Vol. 757, p. 91, September 2012.

[26] H. Berninger, E. Frenod, M. Gander, M. Liebendorfer, and J. Michaud. Derivation of the Isotropic Diffusion Source Approximation (IDSA) for Supernova Neutrino Transport by Asymptotic Expansions. *ArXiv e-prints*, December 2012.

[27] H. A. Bethe and J. R. Wilson. Revival of a stalled supernova shock by neutrino heating. *ApJ*, Vol. 295, pp. 14–23, August 1985.

[28] S. I. Blinnikov, N. V. Dunina-Barkovskaya, and D. K. Nadyozhin. Equation of State of a Fermi Gas: Approximations for Various Degrees of Relativism and Degeneracy. *ApJS*, Vol. 106, p. 171, September 1996.

[29] J. M. Blondin and A. Mezzacappa. Pulsar spins from an instability in the accretion shock of supernovae. *Nature*, Vol. 445, pp. 58–60, January 2007.

[30] J. M. Blondin, A. Mezzacappa, and C. DeMarino. Stability of Standing Accretion Shocks, with an Eye toward Core-Collapse Supernovae. *ApJ*, Vol. 584, pp. 971–980, February 2003.

[31] S. A. Bludman, I. Lichtenstadt, and G. Hayden. Homologous collapse and deleptonization of an evolved stellar core. *ApJ*, Vol. 261, pp. 661–676, October 1982.

[32] S. E. Boggs, F. A. Harrison, H. Miyasaka, B. W. Grefenstette, A. Zoglauer, C. L. Fryer, S. P. Reynolds, D. M. Alexander, H. An, D. Barret, F. E. Christensen, W. W. Craig, K. Forster, P. Giommi, C. J. Hailey, A. Hornstrup, T. Kitaguchi, J. E. Koglin, K. K. Madsen, P. H. Mao, K. Mori, M. Perri, M. J. Pivovaroff, S. Puccetti, V. Rana, D. Stern, N. J. Westergaard, and W. W. Zhang. ^{44}Ti gamma-ray emission lines from SN1987A reveal an asymmetric explosion. *Science*, Vol. 348, pp. 670–671, May 2015.

[33] E. Böhm-Vitense. Über die Wasserstoffkonvektionszone in Sternen verschiedener Effektivtemperaturen und Leuchtkräfte. Mit 5 Textabbildungen. *Zeitschrift für Astrophysik*, Vol. 46, p. 108, 1958.

[34] M. T. Botticella, S. J. Smartt, R. C. Kennicutt, E. Cappellaro, M. Sereno, and J. C. Lee. A comparison between star formation rate diagnostics and rate of core collapse supernovae within 11 Mpc. *A&A*, Vol. 537, p. A132, January 2012.

[35] T. D. Brandt, A. Burrows, C. D. Ott, and E. Livne. Results from Core-collapse Simulations with Multi-dimensional, Multi-angle Neutrino Transport. *ApJ*, Vol. 728, p. 8, February 2011.

[36] B. P. Brown, G. M. Vasil, and E. G. Zweibel. Energy Conservation and Gravity Waves in Sound-proof Treatments of Stellar Interiors. Part I. Anelastic Approximations. *ApJ*, Vol. 756, p. 109, September 2012.

[37] S. W. Bruenn. Stellar core collapse - Numerical model and infall epoch. *ApJS*, Vol. 58, pp. 771–841, August 1985.

[38] S. W. Bruenn. The prompt-shock supernova mechanism. I - The effect of the free-proton mass fraction and the neutrino transport algorithm. *ApJ*, Vol. 340, pp. 955–965, May 1989.

[39] S. W. Bruenn. The prompt-shock supernova mechanism. II - Supranuclear EOS behavior and the precollapse model. *ApJ*, Vol. 341, pp. 385–400, June 1989.

[40] S. W. Bruenn and T. Dineva. The Role of Doubly Diffusive Instabilities in the Core-Collapse Supernova Mechanism. *ApJL*, Vol. 458, p. L71, February 1996.

[41] S. W. Bruenn, E. J. Lentz, W. R. Hix, A. Mezzacappa, J. A. Harris, O. E. B. Messer, E. Endeve, J. M. Blondin, M. A. Chertkow, E. J. Lingerfelt, P. Marronetti, and K. N. Yakunin. The Development of Explosions in Axisymmetric Ab Initio Core-Collapse Supernova Simulations of 12-25 $M_\odot$ Stars. *ArXiv e-prints*, September 2014.

[42] S. W. Bruenn, E. A. Raley, and A. Mezzacappa. Fluid Stability Below the Neutrinospheres of Supernova Progenitors and the Dominant Role of Lepto-Entropy Fingers. *ArXiv Astrophysics e-prints*, April 2004.

[43] L. Buchmann. New Stellar Reaction Rate for 12C(alpha , gamma) 16O. *ApJL*, Vol. 468, p. L127, September 1996.

[44] L. Buchmann. Comments on the $^{12}C(\alpha, \gamma)^{16}O$ reaction rate. *Nuclear Physics A*, Vol. 758, pp. 355–362, July 2005.

[45] R. Buras, H.-T. Janka, M. T. Keil, G. G. Raffelt, and M. Rampp. Electron Neutrino Pair Annihilation: A New Source for Muon and Tau Neutrinos in Supernovae. *ApJ*, Vol. 587, pp. 320–326, April 2003.

[46] R. Buras, H.-T. Janka, M. Rampp, and K. Kifonidis. Two-dimensional hydrodynamic core-collapse supernova simulations with spectral neutrino transport. II. Models for different progenitor stars. *A&A*, Vol. 457, pp. 281–308, October 2006.

[47] R. Buras, M. Rampp, H.-T. Janka, and K. Kifonidis. Improved Models of Stellar Core Collapse and Still No Explosions: What Is Missing? *Physical Review Letters*, Vol. 90, No. 24, p. 241101, June 2003.

[48] R. Buras, M. Rampp, H.-T. Janka, and K. Kifonidis. Two-dimensional hydrodynamic core-collapse supernova simulations with spectral neutrino transport. I. Numerical method and results for a $15M_{\odot}$ star. *A&A*, Vol. 447, pp. 1049–1092, March 2006.

[49] A. Burrows. Colloquium: Perspectives on core-collapse supernova theory. *Reviews of Modern Physics*, Vol. 85, pp. 245–261, January 2013.

[50] A. Burrows, J. C. Dolence, and J. W. Murphy. An Investigation into the Character of Pre-explosion Core-collapse Supernova Shock Motion. *ApJ*, Vol. 759, p. 5, November 2012.

[51] A. Burrows and B. A. Fryxell. A Convective Trigger for Supernova Explosions. *ApJL*, Vol. 418, p. L33, November 1993.

[52] A. Burrows and J. Goshy. A Theory of Supernova Explosions. *ApJL*, Vol. 416, p. L75, October 1993.

[53] A. Burrows, J. Hayes, and B. A. Fryxell. On the Nature of Core-Collapse Supernova Explosions. *ApJ*, Vol. 450, p. 830, September 1995.

[54] A. Burrows and J. M. Lattimer. The prompt mechanism of Type II supernovae. *ApJL*, Vol. 299, pp. L19–L22, December 1985.

[55] A. Burrows, E. Livne, L. Dessart, C. D. Ott, and J. Murphy. Features of the Acoustic Mechanism of Core-Collapse Supernova Explosions. *ApJ*, Vol. 655, pp. 416–433, January 2007.

[56] A. Burrows, S. Reddy, and T. A. Thompson. Neutrino opacities in nuclear matter. *Nuclear Physics A*, Vol. 777, pp. 356–394, October 2006.

[57] A. Burrows and R. F. Sawyer. Effects of correlations on neutrino opacities in nuclear matter. *Phys. Rev. C*, Vol. 58, pp. 554–571, July 1998.

[58] V. M. Canuto. Stellar mixing. I. Formalism. *A&A*, Vol. 528, p. A76, April 2011.

[59] V. M. Canuto and I. Mazzitelli. Further improvements of a new model for turbulent convection in stars. *ApJ*, Vol. 389, pp. 724–730, April 1992.

[60] E. Cappellaro, M. T. Botticella, G. Pignata, A. Grado, L. Greggio, L. Limatola, M. Vaccari, A. Baruffolo, S. Benetti, F. Bufano, M. Capaccioli, E. Cascone, G. Covone, D. De Cicco, S. Falocco, M. Della Valle, M. Jarvis, L. Marchetti, N. R. Napolitano, M. Paolillo, A. Pastorello, M. Radovich, P. Schipani, S. Spiro, L. Tomasella, and M. Turatto. Supernova rates from the SUDARE VST-OmegaCAM search. I. Rates per unit volume. *A&A*, Vol. 584, p. A62, December 2015.

[61] E. Cappellaro, R. Evans, and M. Turatto. A new determination of supernova rates and a comparison with indicators for galactic star formation. *A&A*, Vol. 351, pp. 459–466, November 1999.

[62] C. Y. Cardall, E. Endeve, and A. Mezzacappa. Conservative 3+1 general relativistic variable Eddington tensor radiation transport equations. *Phys. Rev. D*, Vol. 87, No. 10, p. 103004, May 2013.

[63] C. Cardall and A. Mezzacappa. Conservative formulations of general relativistic kinetic theory. *Phys. Rev. D*, Vol. 68, No. 2, p. 023006, July 2003.

[64] L. J. Caroff, P. D. Noerdlinger, and J. D. Scargle. Transfer of Resonance-Line Radiation in Differentially Expanding Atmospheres. I. General Considerations and Monte Carlo Calculations. *ApJ*, Vol. 176, p. 439, September 1972.

[65] J. I. Castor. *Radiation Hydrodynamics*. November 2004.

[66] J. I. Castor, D. C. Abbott, and R. I. Klein. Radiation-driven winds in Of stars. *ApJ*, Vol. 195, pp. 157–174, January 1975.

[67] A. Chieffi and M. Limongi. Pre-supernova Evolution of Rotating Solar Metallicity Stars in the Mass Range 13-120 M and their Explosive Yields. *ApJ*, Vol. 764, p. 21, February 2013.

[68] A. Chieffi, M. Limongi, and O. Straniero. The Evolution of a 25 $M_?$ Star from the Main Sequence up to the Onset of the Iron Core Collapse. *ApJ*, Vol. 502, pp. 737–762, August 1998.

[69] A. Chieffi and O. Straniero. Isochrones for hydrogen-burning globular cluster stars. I - The metallicity range (Fe/H) from -2 to -1. *ApJS*, Vol. 71, pp. 47–87, September 1989.

[70] C. Chiosi, G. Bertelli, and A. Bressan. New developments in understanding the HR diagram. *ARA&A*, Vol. 30, pp. 235–285, 1992.

[71] M. Cignoni and M. Tosi. Star Formation Histories of Dwarf Galaxies from the Colour-Magnitude Diagrams of Their Resolved Stellar Populations. *Advances in Astronomy*, Vol. 2010, p. 158568, 2010.

[72] M. A. Cleveland, N. A. Gentile, and T. S. Palmer. An extension of implicit Monte Carlo diffusion: Multigroup and the difference formulation. *Journal of Computational Physics*, Vol. 229, pp. 5707–5723, August 2010.

[73] S. A. Colgate and R. H. White. The Hydrodynamic Behavior of Supernovae Explosions. *ApJ*, Vol. 143, p. 626, March 1966.

[74] B. Côté, C. Ritter, B. W. O'Shea, F. Herwig, M. Pignatari, S. Jones, and C. Fryer. Uncertainties in Galactic Chemical Evolution Models. *ArXiv e-prints*, September 2015.

[75] S. M. Couch. The Dependence of the Neutrino Mechanism of Core-collapse Supernovae on the Equation of State. *ApJ*, Vol. 765, p. 29, March 2013.

[76] S. M. Couch and E. P. O'Connor. High-resolution Three-dimensional Simulations of Core-collapse Supernovae in Multiple Progenitors. *ApJ*, Vol. 785, p. 123, April 2014.

[77] S. M. Couch and C. D. Ott. Revival of the Stalled Core-collapse Supernova Shock Triggered by Precollapse Asphericity in the Progenitor Star. *ApJL*, Vol. 778, p. L7, November 2013.

[78] J. J. Cowan, F.-K. Thielemann, and J. W. Truran. The R-process and nucleochronology. *Phys. Rep.*, Vol. 208, pp. 267–394, November 1991.

[79] P. B. Demorest, T. Pennucci, S. M. Ransom, M. S. E. Roberts, and J. W. T. Hessels. A two-solar-mass neutron star measured using Shapiro delay. *Nature*, Vol. 467, pp. 1081–1083, October 2010.

[80] P. A. Denissenkov, M. Pinsonneault, D. M. Terndrup, and G. Newsham. Angular Momentum Transport in Solar-type Stars: Testing the Timescale for Core-Envelope Coupling. *ApJ*, Vol. 716, pp. 1269–1287, June 2010.

[81] J. D. Densmore, K. G. Thompson, and T. J. Urbatsch. A hybrid transport-diffusion Monte Carlo method for frequency-dependent radiative-transfer simulations. *Journal of Computational Physics*, Vol. 231, pp. 6924–6934, August 2012.

[82] J. D. Densmore, T. J. Urbatsch, T. M. Evans, and M. W. Buksas. A hybrid transport-diffusion method for Monte Carlo radiative-transfer simulations. *Journal of Computational Physics*, Vol. 222, pp. 485–503, March 2007.

[83] J. D. Densmore, J. S. Warsa, and R. B. Lowrie. Stability analysis and time-step limits for a Monte Carlo Compton-scattering method. *Journal of Computational Physics*, Vol. 229, pp. 3691–3705, May 2010.

[84] L. Dessart, A. Burrows, E. Livne, and C. D. Ott. Multidimensional Radiation/Hydrodynamic Simulations of Proto-Neutron Star Convection. *ApJ*, Vol. 645, pp. 534–550, July 2006.

[85] L. Dessart and D. J. Hillier. Supernova radiative-transfer modelling: a new approach using non-local thermodynamic equilibrium and full time dependence. *MNRAS*, Vol. 405, pp. 2141–2160, July 2010.

[86] L. Dessart and D. J. Hillier. Non-LTE time-dependent spectroscopic modelling of Type II-plateau supernovae from the photospheric to the nebular phase: case study for 15 and 25 M progenitor stars. *MNRAS*, Vol. 410, pp. 1739–1760, January 2011.

[87] L. Dessart, D. J. Hillier, E. Livne, S.-C. Yoon, S. Woosley, R. Waldman, and N. Langer. Core-collapse explosions of Wolf-Rayet stars and the connection to Type IIb/Ib/Ic supernovae. *MNRAS*, Vol. 414, pp. 2985–3005, July 2011.

[88] L. Dessart, D. J. Hillier, R. Waldman, and E. Livne. Type II-Plateau supernova radiation: dependences on progenitor and explosion properties. *MNRAS*, Vol. 433, pp. 1745–1763, August 2013.

[89] H. Dimmelmeier, C. D. Ott, H.-T. Janka, A. Marek, and E. Müller. Generic Gravitational-Wave Signals from the Collapse of Rotating Stellar Cores. *Physical Review Letters*, Vol. 98, No. 25, p. 251101, June 2007.

[90] J. C. Dolence, A. Burrows, J. W. Murphy, and J. Nordhaus. Dimensional Dependence of the Hydrodynamics of Core-collapse Supernovae. *ApJ*, Vol. 765, p. 110, March 2013.

[91] J. C. Dolence, A. Burrows, and W. Zhang. Two-dimensional Core-collapse Supernova Models with Multi-dimensional Transport. *ApJ*, Vol. 800, p. 10, February 2015.

[92] J. C. Dolence, C. F. Gammie, M. Mościbrodzka, and P. K. Leung. grmonty: A Monte Carlo Code for Relativistic Radiative Transport. *ApJS*, Vol. 184, pp. 387–397, October 2009.

[93] H. Duan and J. P. Kneller. TOPICAL REVIEW: Neutrino flavour transformation in supernovae. *Journal of Physics G Nuclear Physics*, Vol. 36, No. 11, p. 113201, November 2009.

[94] R. G. Eastman, S. E. Woosley, T. A. Weaver, and P. A. Pinto. Theoretical light curve of a Type 2p supernova. *ApJ*, Vol. 430, pp. 300–310, July 1994.

[95] P. Eggenberger, G. Meynet, A. Maeder, R. Hirschi, C. Charbonnel, S. Talon, and S. Ekström. The Geneva stellar evolution code. *Ap&SS*, Vol. 316, pp. 43–54, August 2008.

[96] P. P. Eggleton. The evolution of low mass stars. *MNRAS*, Vol. 151, p. 351, 1971.

[97] S. Ekström, C. Georgy, P. Eggenberger, G. Meynet, N. Mowlavi, A. Wyttenbach, A. Granada, T. Decressin, R. Hirschi, U. Frischknecht, C. Charbonnel, and A. Maeder. Grids of stellar models with rotation. I. Models from 0.8 to 120 M at solar metallicity (Z = 0.014). *A&A*, Vol. 537, p. A146, January 2012.

[98] J. J. Eldridge, R. G. Izzard, and C. A. Tout. The effect of massive binaries on stellar populations and supernova progenitors. *MNRAS*, Vol. 384, pp. 1109–1118, March 2008.

[99] J. J. Eldridge and C. A. Tout. The progenitors of core-collapse supernovae. *MNRAS*, Vol. 353, pp. 87–97, September 2004.

[100] A. S. Endal and S. Sofia. The evolution of rotating stars. II - Calculations with time-dependent redistribution of angular momentum for 7- and 10-solar-mass stars. *ApJ*, Vol. 220, pp. 279–290, February 1978.

[101] E. Endeve, C. Y. Cardall, and A. Mezzacappa. Conservative Moment Equations for Neutrino Radiation Transport with Limited Relativity. *ArXiv e-prints*, December 2012.

[102] E. Epelbaum, H.-W. Hammer, and U.-G. Meißner. Modern theory of nuclear forces. *Reviews of Modern Physics*, Vol. 81, pp. 1773–1825, October 2009.

[103] R. I. Epstein and C. J. Pethick. Lepton loss and entropy generation in stellar collapse. *ApJ*, Vol. 243, pp. 1003–1012, February 1981.

[104] B. Ercolano, M. J. Barlow, P. J. Storey, and X.-W. Liu. MOCASSIN: a fully three-dimensional Monte Carlo photoionization code. *MNRAS*, Vol. 340, pp. 1136–1152, April 2003.

[105] T. Ertl, H.-T. Janka, S. E. Woosley, T. Sukhbold, and M. Ugliano. A Two-parameter Criterion for Classifying the Explodability of Massive Stars by the Neutrino-driven Mechanism. *ApJ*, Vol. 818, p. 124, February 2016.

[106] K. Farouqi, K.-L. Kratz, L. I. Mashonkina, B. Pfeiffer, J. J. Cowan, F.-K. Thielemann, and J. W. Truran. Nucleosynthesis Modes in The High-Entropy Wind of Type II Supernovae: Comparison of Calculations With Halo-Star Observations. *ApJL*, Vol. 694, pp. L49–L53, March 2009.

[107] K. Farouqi, K.-L. Kratz, B. Pfeiffer, T. Rauscher, F.-K. Thielemann, and J. W. Truran. Charged-particle and Neutron-capture Processes in the High-entropy Wind of Core-collapse Supernovae. *ApJ*, Vol. 712, pp. 1359–1377, April 2010.

[108] R. Fernández. Hydrodynamics of Core-collapse Supernovae at the Transition to Explosion. I. Spherical Symmetry. *ApJ*, Vol. 749, p. 142, April 2012.

[109] R. Fernández. Three-dimensional simulations of SASI- and convection-dominated core-collapse supernovae. *MNRAS*, Vol. 452, pp. 2071–2086, September 2015.

[110] R. Fernández and B. D. Metzger. Delayed outflows from black hole accretion tori following neutron star binary coalescence. *MNRAS*, Vol. 435, pp. 502–517, October 2013.

[111] R. Fernández, B. Müller, T. Foglizzo, and H.-T. Janka. Characterizing SASI- and convection-dominated core-collapse supernova explosions in two dimensions. *MNRAS*, Vol. 440, pp. 2763–2780, May 2014.

[112] R. Fernández and C. Thompson. Stability of a Spherical Accretion Shock with Nuclear Dissociation. *ApJ*, Vol. 697, pp. 1827–1841, June 2009.

[113] A. V. Filippenko. Optical Spectra of Supernovae. *ARA&A*, Vol. 35, pp. 309–355, 1997.

[114] T. Fischer, M. Hempel, I. Sagert, Y. Suwa, and J. Schaffner-Bielich. Symmetry energy impact in simulations of core-collapse supernovae. *European Physical Journal A*, Vol. 50, p. 46, February 2014.

[115] T. Fischer, S. C. Whitehouse, A. Mezzacappa, F.-K. Thielemann, and M. Liebendörfer. Protoneutron star evolution and the neutrino-driven wind in general relativistic neutrino radiation hydrodynamics simulations. *A&A*, Vol. 517, p. A80, July 2010.

[116] J. A. Fleck, Jr. and E. H. Canfield. A random walk procedure for improving the computational efficiency of the implicit Monte Carlo method for nonlinear radiation transport. *Journal of Computational Physics*, Vol. 54, pp. 508–523, June 1984.

[117] J. A. Fleck, Jr. and J. D. Cummings. An implicit Monte Carlo scheme for calculating time and frequency dependent nonlinear radiation transport. *Journal of Computational Physics*, Vol. 8, pp. 313–342, December 1971.

[118] T. Foglizzo. Non-radial instabilities of isothermal Bondi accretion with a shock: Vortical-acoustic cycle vs. post-shock acceleration. *A&A*, Vol. 392, pp. 353–368, September 2002.

[119] T. Foglizzo, P. Galletti, and M. Ruffert. A fresh look at the unstable simulations of Bondi-Hoyle-Lyttleton accretion. *A&A*, Vol. 435, pp. 397–411, May 2005.

[120] T. Foglizzo, R. Kazeroni, J. Guilet, F. Masset, M. González, B. K. Krueger, J. Novak, M. Oertel, J. Margueron, J. Faure, N. Martin, P. Blottiau, B. Peres, and G. Durand. The Explosion Mechanism of Core-Collapse Supernovae: Progress in Supernova Theory and Experiments. *Proc. Astron. Soc. Aust.*, Vol. 32, p. e009, March 2015.

[121] T. Foglizzo, L. Scheck, and H.-T. Janka. Neutrino-driven Convection versus Advection in Core-Collapse Supernovae. *ApJ*, Vol. 652, pp. 1436–1450, December 2006.

[122] C. Freiburghaus, J.-F. Rembges, T. Rauscher, E. Kolbe, F.-K. Thielemann, K.-L. Kratz, B. Pfeiffer, and J. J. Cowan. The Astrophysical r-Process: A Comparison of Calculations following Adiabatic Expansion with Classical Calculations Based on Neutron Densities and Temperatures. *ApJ*, Vol. 516, pp. 381–398, May 1999.

[123] C. Fröhlich, G. Martínez-Pinedo, M. Liebendörfer, F.-K. Thielemann, E. Bravo, W. R. Hix, K. Langanke, and N. T. Zinner. Neutrino-Induced Nucleosynthesis of A¿64 Nuclei: The νp Process. *Physical Review Letters*, Vol. 96, No. 14, p. 142502, April 2006.

[124] C. L. Fryer. Mass Limits For Black Hole Formation. *ApJ*, Vol. 522, pp. 413–418, September 1999.

[125] C. L. Fryer. Compact object formation and the supernova explosion engine. *Classical and Quantum Gravity*, Vol. 30, No. 24, p. 244002, December 2013.

[126] C. L. Fryer, F. Herwig, A. Hungerford, and F. X. Timmes. Supernova Fallback: A Possible Site for the r-Process. *ApJL*, Vol. 646, pp. L131–L134, August 2006.

[127] C. L. Fryer and K. C. B. New. Gravitational Waves from Gravitational Collapse. *Living Reviews in Relativity*, Vol. 14, , January 2011.

[128] C. L. Fryer and M. S. Warren. Modeling Core-Collapse Supernovae in Three Dimensions. *ApJL*, Vol. 574, pp. L65–L68, July 2002.

[129] S.-i. Fujimoto, K. Kotake, M.-a. Hashimoto, M. Ono, and N. Ohnishi. Explosive Nucleosynthesis in the Neutrino-driven Aspherical Supernova Explosion of a Non-rotating 15 M $_{sun}$ Star with Solar Metallicity. *ApJ*, Vol. 738, p. 61, September 2011.

[130] G. M. Fuller, W. A. Fowler, and M. J. Newman. Stellar weak-interaction rates for sd-shell nuclei. I - Nuclear matrix element systematics with application to Al-26 and selected nuclei of importance to the supernova problem. *ApJS*, Vol. 42, pp. 447–473, March 1980.

[131] S. Furusawa, H. Nagakura, K. Sumiyoshi, and S. Yamada. The Influence of Inelastic Neutrino Reactions with Light Nuclei on the Standing Accretion Shock Instability in Core-collapse Supernovae. *ApJ*, Vol. 774, p. 78, September 2013.

[132] S. Furusawa, K. Sumiyoshi, S. Yamada, and H. Suzuki. New Equations of State Based on the Liquid Drop Model of Heavy Nuclei and Quantum Approach to Light Nuclei for Core-collapse Supernova Simulations. *ApJ*, Vol. 772, p. 95, August 2013.

[133] S. Furusawa, S. Yamada, K. Sumiyoshi, and H. Suzuki. A New Baryonic Equation of State at Sub-nuclear Densities for Core-collapse Simulations. *ApJ*, Vol. 738, p. 178, September 2011.

[134] S. Furusawa, S. Yamada, K. Sumiyoshi, and H. Suzuki. A New Baryonic Equation of State at Sub-nuclear Densities for Core-collapse Simulations. *ApJ*, Vol. 738, p. 178, September 2011.

[135] P. Garaud, G. I. Ogilvie, N. Miller, and S. Stellmach. A model of the entropy flux and Reynolds stress in turbulent convection. *MNRAS*, Vol. 407, pp. 2451–2467, October 2010.

[136] M. Gehmeyr and D. Mihalas. Adaptive grid radiation hydrodynamics with TITAN. *Physica D Nonlinear Phenomena*, Vol. 77, pp. 320–341, October 1994.

[137] N. A. Gentile. Implicit Monte Carlo Diffusion-An Acceleration Method for Monte Carlo Time-Dependent Radiative Transfer Simulations. *Journal of Computational Physics*, Vol. 172, pp. 543–571, September 2001.

[138] S. Gezari, L. Dessart, S. Basa, D. C. Martin, J. D. Neill, S. E. Woosley, D. J. Hillier, G. Bazin, K. Forster, P. G. Friedman, J. Le Du, A. Mazure, P. Morrissey, S. G. Neff, D. Schiminovich, and T. K. Wyder. Probing Shock Breakout with Serendipitous GALEX Detections of Two SNLS Type II-P Supernovae. *ApJL*, Vol. 683, pp. L131–L134, August 2008.

[139] C. Gilet, A. S. Almgren, J. B. Bell, A. Nonaka, S. E. Woosley, and M. Zingale. Low Mach Number Modeling of Core Convection in Massive Stars. *ApJ*, Vol. 773, p. 137, August 2013.

[140] N. K. Glendenning. First-order phase transitions with more than one conserved charge: Consequences for neutron stars. *Phys. Rev. D*, Vol. 46, pp. 1274–1287, August 1992.

[141] N. K. Glendenning and J. Schaffner-Bielich. First order kaon condensate. *Phys. Rev. C*, Vol. 60, No. 2, p. 025803, August 1999.

[142] S. M. Gogarten, J. J. Dalcanton, J. W. Murphy, B. F. Williams, K. Gilbert, and A. Dolphin. The NGC 300 Transient: An Alternative Method for Measuring Progenitor Masses. *ApJ*, Vol. 703, pp. 300–310, September 2009.

[143] S. A. Grebenev, A. A. Lutovinov, S. S. Tsygankov, and C. Winkler. Hard-X-ray emission lines from the decay of ^{44}Ti in the remnant of supernova 1987A. *Nature*, Vol. 490, pp. 373–375, October 2012.

[144] J. Guilet and R. Fernández. Angular momentum redistribution by SASI spiral modes and consequences for neutron star spins. *MNRAS*, Vol. 441, pp. 2782–2798, July 2014.

[145] J. Guilet and T. Foglizzo. On the linear growth mechanism driving the standing accretion shock instability. *MNRAS*, Vol. 421, pp. 546–560, March 2012.

[146] A. A. Hakobyan, V. Z. Adibekyan, L. S. Aramyan, A. R. Petrosian, J. M. Gomes, G. A. Mamon, D. Kunth, and M. Turatto. Supernovae and their host galaxies. I. The SDSS DR8 database and statistics. *A&A*, Vol. 544, p. A81, August 2012.

[147] A. A. Hakobyan, A. G. Karapetyan, L. V. Barkhudaryan, G. A. Mamon, D. Kunth, A. R. Petrosian, V. Adibekyan, L. S. Aramyan, and M. Turatto. Supernovae and their host galaxies - III. The impact of bars and bulges on the radial distribution of supernovae in disc galaxies. *ArXiv e-prints*, November 2015.

[148] A. A. Hakobyan, T. A. Nazaryan, V. Z. Adibekyan, A. R. Petrosian, L. S. Aramyan, D. Kunth, G. A. Mamon, V. de Lapparent, E. Bertin, J. M. Gomes, and M. Turatto. Supernovae and their host galaxies - II. The relative frequencies of supernovae types in spirals. *MNRAS*, Vol. 444, pp. 2428–2441, November 2014.

[149] W.-R. Hamann, D. Schoenberner, and U. Heber. Mass loss from extreme helium stars. *A&A*, Vol. 116, pp. 273–285, December 1982.

[150] N. J. Hammer, H.-T. Janka, and E. Müller. Three-dimensional Simulations of Mixing Instabilities in Supernova Explosions. *ApJ*, Vol. 714, pp. 1371–1385, May 2010.

[151] M. Hamuy. Observed and Physical Properties of Core-Collapse Supernovae. *ApJ*, Vol. 582, pp. 905–914, January 2003.

[152] T. Handy, T. Plewa, and A. Odrzywołek. Toward Connecting Core-collapse Supernova Theory with Observations. I. Shock Revival in a 15 M $_{\odot}$ Blue Supergiant Progenitor with SN 1987A Energetics. *ApJ*, Vol. 783, p. 125, March 2014.

[153] F. Hanke, A. Marek, B. Müller, and H.-T. Janka. Is Strong SASI Activity the Key to Successful Neutrino-driven Supernova Explosions? *ApJ*, Vol. 755, p. 138, August 2012.

[154] F. Hanke, B. Müller, A. Wongwathanarat, A. Marek, and H.-T. Janka. SASI Activity in Three-dimensional Neutrino-hydrodynamics Simulations of Supernova Cores. *ApJ*, Vol. 770, p. 66, June 2013.

[155] S. Hannestad and G. Raffelt. Supernova Neutrino Opacity from Nucleon-Nucleon Bremsstrahlung and Related Processes. *ApJ*, Vol. 507, pp. 339–352, November 1998.

[156] T. J. Harries. An algorithm for Monte Carlo time-dependent radiation transfer. *MNRAS*, Vol. 416, pp. 1500–1508, September 2011.

[157] T. J. Harries. Radiation-hydrodynamical simulations of massive star formation using Monte Carlo radiative transfer - I. Algorithms and numerical methods. *MNRAS*, Vol. 448, pp. 3156–3166, April 2015.

[158] M. Hashimoto. Supernova Nucleosynthesis in Massive Stars. *Progress of Theoretical Physics*, Vol. 94, pp. 663–736, November 1995.

[159] J. C. Hayes, M. L. Norman, R. A. Fiedler, J. O. Bordner, P. S. Li, S. E. Clark, A. ud-Doula, and M.-M. Mac Low. Simulating Radiating and Magnetized Flows in Multiple Dimensions with ZEUS-MP. *ApJS*, Vol. 165, pp. 188–228, July 2006.

[160] K. Hebeler, J. M. Lattimer, C. J. Pethick, and A. Schwenk. Constraints on Neutron Star Radii Based on Chiral Effective Field Theory Interactions. *Physical Review Letters*, Vol. 105, No. 16, p. 161102, October 2010.

[161] A. Heger, C. L. Fryer, S. E. Woosley, N. Langer, and D. H. Hartmann. How Massive Single Stars End Their Life. *ApJ*, Vol. 591, pp. 288–300, July 2003.

[162] A. Heger and N. Langer. Stationary hydrodynamic models of Wolf-Rayet stars with optically thick winds. *A&A*, Vol. 315, pp. 421–431, November 1996.

[163] A. Heger, N. Langer, and S. E. Woosley. Presupernova Evolution of Rotating Massive Stars. I. Numerical Method and Evolution of the Internal Stellar Structure. *ApJ*, Vol. 528, pp. 368–396, January 2000.

[164] A. Heger, S. E. Woosley, G. Martínez-Pinedo, and K. Langanke. Presupernova Evolution with Improved Rates for Weak Interactions. *ApJ*, Vol. 560, pp. 307–325, October 2001.

[165] H. Heiselberg, C. J. Pethick, and E. F. Staubo. Quark matter droplets in neutron stars. *Physical Review Letters*, Vol. 70, pp. 1355–1359, March 1993.

[166] M. Hempel, T. Fischer, J. Schaffner-Bielich, and M. Liebendörfer. New Equations of State in Simulations of Core-collapse Supernovae. *ApJ*, Vol. 748, p. 70, March 2012.

[167] M. Hempel and J. Schaffner-Bielich. A statistical model for a complete supernova equation of state. *Nuclear Physics A*, Vol. 837, pp. 210–254, June 2010.

[168] M. Herant, W. Benz, W. R. Hix, C. L. Fryer, and S. A. Colgate. Inside the supernova: A powerful convective engine. *ApJ*, Vol. 435, pp. 339–361, November 1994.

[169] F. Herwig. Evolution and Yields of Extremely Metal-poor Intermediate-Mass Stars. *ApJS*, Vol. 155, pp. 651–666, December 2004.

[170] F. Herwig, B. Freytag, R. M. Hueckstaedt, and F. X. Timmes. Hydrodynamic Simulations of He Shell Flash Convection. *ApJ*, Vol. 642, pp. 1057–1074, May 2006.

[171] W. Hillebrandt, K. Nomoto, and R. G. Wolff. Supernova explosions of massive stars - The mass range 8 to 10 solar masses. *A&A*, Vol. 133, pp. 175–184, April 1984.

[172] D. J. Hillier and L. Dessart. Time-dependent radiative transfer calculations for supernovae. *MNRAS*, Vol. 424, pp. 252–271, July 2012.

[173] D. J. Hillier and L. Dessart. Time-dependent radiative transfer calculations for supernovae. *MNRAS*, Vol. 424, pp. 252–271, July 2012.

[174] D. J. Hillier and T. Lanz. CMFGEN: A non-LTE Line-Blanketed Radiative Transfer Code for Modeling Hot Stars with Stellar Winds. In G. Ferland and D. W. Savin, editors, *Spectroscopic Challenges of Photoionized Plasmas*, Vol. 247 of *Astronomical Society of the Pacific Conference Series*, p. 343, 2001.

[175] K. Hirata, T. Kajita, M. Koshiba, M. Nakahata, and Y. Oyama. Observation of a neutrino burst from the supernova SN1987A. *Physical Review Letters*, Vol. 58, pp. 1490–1493, April 1987.

[176] R. Hirschi, G. Meynet, and A. Maeder. Stellar evolution with rotation. XII. Pre-supernova models. *A&A*, Vol. 425, pp. 649–670, October 2004.

[177] W. R. Hix, O. E. B. Messer, A. Mezzacappa, J. Sampaio, K. Langanke, G. Martínez-Pinedo, M. Liebendörfer, and D. J. Dean. Nuclear electron capture in core collapse supernovae. *Nuclear Physics A*, Vol. 758, pp. 31–34, July 2005.

[178] W. R. Hix and F.-K. Thielemann. Computational methods for nucleosynthesis and nuclear energy generation. *Journal of Computational and Applied Mathematics*, Vol. 109, pp. 321–351, September 1999.

[179] R. D. Hoffman, S. A. Sheets, J. T. Burke, N. D. Scielzo, T. Rauscher, E. B. Norman, S. Tumey, T. A. Brown, P. G. Grant, A. M. Hurst, L. Phair, M. A. Stoyer, T. Wooddy, J. L. Fisker, and D. Bleuel. Reaction Rate Sensitivity of ^{44}Ti Production in Massive Stars and Implications of a Thick Target Yield Measurement of ^{40}Ca(α, γ)^{44}Ti. *ApJ*, Vol. 715, pp. 1383–1399, June 2010.

[180] D. Hollowell and I. Iben, Jr. Neutron production and neutron-capture nucleosynthesis in a low-mass, low-metallicity asymptotic giant branch star. *ApJ*, Vol. 340, pp. 966–984, May 1989.

[181] J. W. Holt, N. Kaiser, and W. Weise. Quasiparticle interaction in nuclear matter with chiral three-nucleon forces. *Nuclear Physics A*, Vol. 876, pp. 61–76, February 2012.

[182] J. W. Holt, N. Kaiser, and W. Weise. Nuclear chiral dynamics and thermodynamics. *Progress in Particle and Nuclear Physics*, Vol. 73, pp. 35–83, November 2013.

[183] S. Horiuchi, K. Nakamura, T. Takiwaki, K. Kotake, and M. Tanaka. The red supergiant and supernova rate problems: implications for core-collapse supernova physics. *MNRAS*, Vol. 445, pp. L99–L103, November 2014.

[184] C. J. Horowitz. Neutrino trapping in a supernova and the screening of weak neutral currents. *Phys. Rev. D*, Vol. 55, pp. 4577–4581, April 1997.

[185] C. J. Horowitz. Weak magnetism for antineutrinos in supernovae. *Phys. Rev. D*, Vol. 65, No. 4, p. 043001, February 2002.

[186] C. J. Horowitz and A. Schwenk. The virial equation of state of low-density neutron matter. *Physics Letters B*, Vol. 638, pp. 153–159, July 2006.

[187] C. J. Horowitz and K. Wehrberger. Neutrino neutral current interactions in nuclear matter. *Nuclear Physics A*, Vol. 531, pp. 665–684, September 1991.

[188] L. Hüdepohl, B. Müller, H.-T. Janka, A. Marek, and G. G. Raffelt. Neutrino Signal of Electron-Capture Supernovae from Core Collapse to Cooling. *Physical Review Letters*, Vol. 104, No. 25, p. 251101, June 2010.

[189] I. Iben, Jr. and A. Renzini. On the formation of carbon star characteristics and the production of neutron-rich isotopes in asymptotic giant branch stars of small core mass. *ApJL*, Vol. 263, pp. L23–L27, December 1982.

[190] I. Iben, Jr. and A. Renzini. The role of semiconvection in bringing carbon to the surface of asymptotic giant branch stars of small core mass. *ApJL*, Vol. 259, pp. L79–L83, August 1982.

[191] S. Ichimaru. Strongly coupled plasmas: high-density classical plasmas and degenerate electron liquids. *Reviews of Modern Physics*, Vol. 54, pp. 1017–1059, October 1982.

[192] C. Ishizuka, A. Ohnishi, K. Tsubakihara, K. Sumiyoshi, and S. Yamada. Tables of hyperonic matter equation of state for core-collapse supernovae. *Journal of Physics G Nuclear Physics*, Vol. 35, No. 8, p. 085201, August 2008.

[193] W. Iwakami, K. Kotake, N. Ohnishi, S. Yamada, and K. Sawada. Three-Dimensional Simulations of Standing Accretion Shock Instability in Core-Collapse Supernovae. *ApJ*, Vol. 678, pp. 1207–1222, May 2008.

[194] W. Iwakami, H. Nagakura, and S. Yamada. Parametric Study of Flow Patterns behind the Standing Accretion Shock Wave for Core-Collapse Supernovae. *ApJ*, Vol. 786, p. 118, May 2014.

[195] H.-T. Janka. Conditions for shock revival by neutrino heating in core-collapse supernovae. *A&A*, Vol. 368, pp. 527–560, March 2001.

[196] H.-T. Janka. Explosion Mechanisms of Core-Collapse Supernovae. *Annual Review of Nuclear and Particle Science*, Vol. 62, pp. 407–451, November 2012.

[197] H.-T. Janka and W. Hillebrandt. Monte Carlo simulations of neutrino transport in type II supernovae. , Vol. 78, pp. 375–397, June 1989.

[198] H.-T. Janka, K. Langanke, A. Marek, G. Martínez-Pinedo, and B. Müller. Theory of core-collapse supernovae. *Phys. Rep.*, Vol. 442, pp. 38–74, April 2007.

[199] H.-T. Janka and E. Mueller. Neutrino heating, convection, and the mechanism of Type-II supernova explosions. *A&A*, Vol. 306, p. 167, February 1996.

[200] A. Jerkstrand, C. Fransson, and C. Kozma. The ^{44}Ti-powered spectrum of SN 1987A. *A&A*, Vol. 530, p. A45, June 2011.

[201] S. Jones, R. Hirschi, M. Pignatari, A. Heger, C. Georgy, N. Nishimura, C. Fryer, and F. Herwig. Code dependencies of pre-supernova evolution and nucleosynthesis in massive stars: evolution to the end of core helium burning. *MNRAS*, Vol. 447, pp. 3115–3129, March 2015.

[202] O. Just, M. Obergaulinger, and H.-T. Janka. A new multidimensional, energy-dependent two-moment transport code for neutrino-hydrodynamics. *MNRAS*, Vol. 453, pp. 3386–3413, November 2015.

[203] T. Kangas, S. Mattila, E. Kankare, J. K. Kotilainen, P. Väisänen, R. Greimel, and A. Takalo. Spatial distributions of core-collapse supernovae in infrared-bright galaxies. *MNRAS*, Vol. 436, pp. 3464–3479, December 2013.

[204] D. Kasen, R. C. Thomas, and P. Nugent. Time-dependent Monte Carlo Radiative Transfer Calculations for Three-dimensional Supernova Spectra, Light Curves, and Polarization. *ApJ*, Vol. 651, pp. 366–380, November 2006.

[205] D. Kasen and S. E. Woosley. Type II Supernovae: Model Light Curves and Standard Candle Relationships. *ApJ*, Vol. 703, pp. 2205–2216, October 2009.

[206] H. Kato and O. M. Phillips. On the penetration of a turbulent layer into stratified fluid. *Journal of Fluid Mechanics*, Vol. 37, pp. 643–655, 1969.

[207] M. T. Keil, G. G. Raffelt, and H.-T. Janka. Monte Carlo Study of Supernova Neutrino Spectra Formation. *ApJ*, Vol. 590, pp. 971–991, June 2003.

[208] W. Keil, H.-T. Janka, and E. Mueller. Ledoux Convection in Protoneutron Stars—A Clue to Supernova Nucleosynthesis? *ApJL*, Vol. 473, p. L111, December 1996.

[209] W. Keil, H.-T. Janka, and G. Raffelt. Reduced neutrino opacities and the SN 1987A signal. *Phys. Rev. D*, Vol. 51, pp. 6635–6646, June 1995.

[210] P. L. Kelly and R. P. Kirshner. Core-collapse Supernovae and Host Galaxy Stellar Populations. *ApJ*, Vol. 759, p. 107, November 2012.

[211] R. C. Kennicutt, Jr. Star Formation in Galaxies Along the Hubble Sequence. *ARA&A*, Vol. 36, pp. 189–232, 1998.

[212] K. Kifonidis and E. Müller. On multigrid solution of the implicit equations of hydrodynamics. Experiments for the compressible Euler equations in general coordinates. *A&A*, Vol. 544, p. A47, August 2012.

[213] K. Kifonidis, T. Plewa, H.-T. Janka, and E. Müller. Non-spherical core collapse supernovae. I. Neutrino-driven convection, Rayleigh-Taylor instabilities, and the formation and propagation of metal clumps. *A&A*, Vol. 408, pp. 621–649, September 2003.

[214] K. Kifonidis, T. Plewa, L. Scheck, H.-T. Janka, and E. Müller. Non-spherical core collapse supernovae. II. The late-time evolution of globally anisotropic neutrino-driven explosions and their implications for SN 1987 A. *A&A*, Vol. 453, pp. 661–678, July 2006.

[215] R. Kippenhahn and A. Weigert. *Stellar Structure and Evolution*. 1990.

[216] F. S. Kitaura, H.-T. Janka, and W. Hillebrandt. Explosions of O-Ne-Mg cores, the Crab supernova, and subluminous type II-P supernovae. *A&A*, Vol. 450, pp. 345–350, April 2006.

[217] K. Kiuchi, Y. Sekiguchi, K. Kyutoku, and M. Shibata. Gravitational waves, neutrino emissions and effects of hyperons in binary neutron star mergers. *Classical and Quantum Gravity*, Vol. 29, No. 12, p. 124003, June 2012.

[218] C. Kobayashi, A. I. Karakas, and H. Umeda. The evolution of isotope ratios in the Milky Way Galaxy. *MNRAS*, Vol. 414, pp. 3231–3250, July 2011.

[219] C. S. Kochanek, J. F. Beacom, M. D. Kistler, J. L. Prieto, K. Z. Stanek, T. A. Thompson, and H. Yüksel. A Survey About Nothing: Monitoring a Million Supergiants for Failed Supernovae. *ApJ*, Vol. 684, pp. 1336–1342, September 2008.

[220] K. Kotake. Multiple physical elements to determine the gravitational-wave signatures of core-collapse supernovae. *Comptes Rendus Physique*, Vol. 14, pp. 318–351, April 2013.

[221] K. Kotake, K. Sato, and K. Takahashi. Explosion mechanism, neutrino burst and gravitational wave in core-collapse supernovae. *Reports on Progress in Physics*, Vol. 69, pp. 971–1143, April 2006.

[222] K. Kotake, K. Sumiyoshi, S. Yamada, T. Takiwaki, T. Kuroda, Y. Suwa, and H. Nagakura. Core-collapse supernovae as supercomputing science: A status report toward six-dimensional simulations with exact Boltzmann neutrino transport in full general relativity. *Progress of Theoretical and Experimental Physics*, Vol. 2012, No. 1, p. 01A301, August 2012.

[223] K. Kotake, T. Takiwaki, Y. Suwa, W. Iwakami Nakano, S. Kawagoe, Y. Masada, and S.-i. Fujimoto. Multimessengers from Core-Collapse Supernovae: Multidimensionality as a Key to Bridge Theory and Observation. *Advances in Astronomy*, Vol. 2012, p. 428757, 2012.

[224] K.-L. Kratz, J.-P. Bitouzet, F.-K. Thielemann, P. Moeller, and B. Pfeiffer. Isotopic r-process abundances and nuclear structure far from stability - Implications for the r-process mechanism. *ApJ*, Vol. 403, pp. 216–238, January 1993.

[225] K.-L. Kratz, K. Farouqi, B. Pfeiffer, J. W. Truran, C. Sneden, and J. J. Cowan. Explorations of the r-Processes: Comparisons between Calculations and Observations of Low-Metallicity Stars. *ApJ*, Vol. 662, pp. 39–52, June 2007.

[226] R. P. Kudritzki, A. Pauldrach, J. Puls, and D. C. Abbott. Radiation-driven winds of hot stars. VI - Analytical solutions for wind models including the finite cone angle effect. *A&A*, Vol. 219, pp. 205–218, July 1989.

[227] R.-P. Kudritzki and J. Puls. Winds from Hot Stars. *ARA&A*, Vol. 38, pp. 613–666, 2000.

[228] M. Kuhlen, W. E. Woosley, and G. A. Glatzmaier. 3D Anelastic Simulations of Convection in Massive Stars. In S. Turcotte, S. C. Keller, and R. M. Cavallo, editors, *3D Stellar Evolution*, Vol. 293 of *Astronomical Society of the Pacific Conference Series*, p. 147, 2003.

[229] T. Kuroda, S. Wanajo, and K. Nomoto. The r-Process in Supersonic Neutrino-driven Winds: The Role of the Wind Termination Shock. *ApJ*, Vol. 672, pp. 1068–1078, January 2008.

[230] G. A. Lalazissis, J. König, and P. Ring. New parametrization for the Lagrangian density of relativistic mean field theory. *Phys. Rev. C*, Vol. 55, pp. 540–543, January 1997.

[231] L. D. Landau and E. M. Lifshits. *Quantum Mechanics. Nonrelativistic theory.* 1974.

[232] K. Langanke and G. Martínez-Pinedo. Nuclear weak-interaction processes in stars. *Reviews of Modern Physics*, Vol. 75, pp. 819–862, June 2003.

[233] K. Langanke, G. Martínez-Pinedo, J. M. Sampaio, D. J. Dean, W. R. Hix, O. E. Messer, A. Mezzacappa, M. Liebendörfer, H.-T. Janka, and M. Rampp. Electron Capture Rates on Nuclei and Implications for Stellar Core Collapse. *Physical Review Letters*, Vol. 90, No. 24, p. 241102, June 2003.

[234] N. Langer. Evolution of massive stars in the Large Magellanic Cloud - Models with semiconvection. *A&A*, Vol. 252, pp. 669–688, December 1991.

[235] N. Langer. Presupernova Evolution of Massive Single and Binary Stars. *ARA&A*, Vol. 50, pp. 107–164, September 2012.

[236] N. Langer and M. F. El Eid. The evolution of very luminous stars. I - Presupernova evolution. *A&A*, Vol. 167, pp. 265–273, October 1986.

[237] N. Langer, M. F. El Eid, and K. J. Fricke. Evolution of massive stars with semiconvective diffusion. *A&A*, Vol. 145, pp. 179–191, April 1985.

[238] N. Langer, M. Kiriakidis, M. F. El Eid, K. J. Fricke, and A. Weiss. The surface temperature of C/O-rich Wolf-Rayet stars. *A&A*, Vol. 192, pp. 177–181, March 1988.

[239] E. W. Larsen and B. Mercier. Analysis of a Monte Carlo method for nonlinear radiative transfer. *Journal of Computational Physics*, Vol. 71, pp. 50–64, July 1987.

[240] J. M. Lattimer. The Nuclear Equation of State and Neutron Star Masses. *Annual Review of Nuclear and Particle Science*, Vol. 62, pp. 485–515, November 2012.

[241] J. M. Lattimer and F. Douglas Swesty. A generalized equation of state for hot, dense matter. *Nuclear Physics A*, Vol. 535, pp. 331–376, December 1991.

[242] J. M. Lattimer, C. J. Pethick, D. G. Ravenhall, and D. Q. Lamb. Physical properties of hot, dense matter: The general case. *Nuclear Physics A*, Vol. 432, pp. 646–742, January 1985.

[243] B. E. Launder and N. D. Sandham. *Closure Strategies for Turbulent and Transitional Flows.* March 2002.

[244] E. J. Lentz, A. Mezzacappa, O. E. B. Messer, W. R. Hix, and S. W. Bruenn. Interplay of Neutrino Opacities in Core-collapse Supernova Simulations. *ApJ*, Vol. 760, p. 94, November 2012.

[245] E. J. Lentz, A. Mezzacappa, O. E. B. Messer, M. Liebendörfer, W. R. Hix, and S. W. Bruenn. On the Requirements for Realistic Modeling of Neutrino Transport in Simulations of Core-collapse Supernovae. *ApJ*, Vol. 747, p. 73, March 2012.

[246] P. Lesaffre, Z. Han, C. A. Tout, P. Podsiadlowski, and R. G. Martin. The C flash and the ignition conditions of Type Ia supernovae. *MNRAS*, Vol. 368, pp. 187–195, May 2006.

[247] W. Li, R. Chornock, J. Leaman, A. V. Filippenko, D. Poznanski, X. Wang, M. Ganeshalingam, and F. Mannucci. Nearby supernova rates from the Lick Observatory Supernova Search - III. The rate-size relation, and the rates as a function of galaxy Hubble type and colour. *MNRAS*, Vol. 412, pp. 1473–1507, April 2011.

[248] M. Liebendörfer, O. E. B. Messer, A. Mezzacappa, S. W. Bruenn, C. Y. Cardall, and F.-K. Thielemann. A Finite Difference Representation of Neutrino Radiation Hydrodynamics in Spherically Symmetric General Relativistic Spacetime. *ApJS*, Vol. 150, pp. 263–316, January 2004.

[249] M. Liebendörfer, M. Rampp, H.-T. Janka, and A. Mezzacappa. Supernova Simulations with Boltzmann Neutrino Transport: A Comparison of Methods. *ApJ*, Vol. 620, pp. 840–860, February 2005.

[250] M. Liebendörfer, S. Rosswog, and F.-K. Thielemann. An Adaptive Grid, Implicit Code for Spherically Symmetric, General Relativistic Hydrodynamics in Comoving Coordinates. *ApJS*, Vol. 141, pp. 229–246, July 2002.

[251] M. Liebendörfer, S. C. Whitehouse, and T. Fischer. The Isotropic Diffusion Source Approximation for Supernova Neutrino Transport. *ApJ*, Vol. 698, pp. 1174–1190, June 2009.

[252] M. Limongi and A. Chieffi. The Nucleosynthesis of ^{26}Al and ^{60}Fe in Solar Metallicity Stars Extending in Mass from 11 to 120 M_{solar}: The Hydrostatic and Explosive Contributions. *ApJ*, Vol. 647, pp. 483–500, August 2006.

[253] M. Limongi and A. Chieffi. Presupernova Evolution and Explosive Nucleosynthesis of Zero Metal Massive Stars. *ApJS*, Vol. 199, p. 38, April 2012.

[254] I. I. Litvinova and D. K. Nadezhin. Hydrodynamical models of type II supernovae. *Ap&SS*, Vol. 89, pp. 89–113, January 1983.

[255] L. B. Lucy. The formation of resonance lines in locally nonmonotonic winds. II - an amplitude diagnostic. *ApJ*, Vol. 274, pp. 372–379, November 1983.

[256] L. B. Lucy. Computing radiative equilibria with Monte Carlo techniques. *A&A*, Vol. 344, pp. 282–288, April 1999.

[257] L. B. Lucy. Monte Carlo transition probabilities. *A&A*, Vol. 384, pp. 725–735, March 2002.

[258] L. B. Lucy. Monte Carlo transition probabilities. II. *A&A*, Vol. 403, pp. 261–275, May 2003.

[259] L. B. Lucy. Monte Carlo techniques for time-dependent radiative transfer in 3-D supernovae. *A&A*, Vol. 429, pp. 19–30, January 2005.

[260] C. Lunardini. Theory and phenomenology of supernova neutrinos. In *American Institute of Physics Conference Series*, Vol. 1666 of *American Institute of Physics Conference Series*, p. 070001, July 2015.

[261] A. Maeder and G. Meynet. Grids of evolutionary models of massive stars with mass loss and overshooting - Properties of Wolf-Rayet stars sensitive to overshooting. *A&A*, Vol. 182, pp. 243–263, August 1987.

[262] A. Maeder and G. Meynet. The Evolution of Rotating Stars. *ARA&A*, Vol. 38, pp. 143–190, 2000.

[263] A. Maeder and J.-P. Zahn. Stellar evolution with rotation. III. Meridional circulation with MU -gradients and non-stationarity. *A&A*, Vol. 334, pp. 1000–1006, June 1998.

[264] G. Magkotsios, F. X. Timmes, A. L. Hungerford, C. L. Fryer, P. A. Young, and M. Wiescher. Trends in ^{44}Ti and ^{56}Ni from Core-collapse Supernovae. *ApJS*, Vol. 191, pp. 66–95, November 2010.

[265] F. Mannucci, M. Della Valle, N. Panagia, E. Cappellaro, G. Cresci, R. Maiolino, A. Petrosian, and M. Turatto. The supernova rate per unit mass. *A&A*, Vol. 433, pp. 807–814, April 2005.

[266] A. Marek and H.-T. Janka. Delayed Neutrino-Driven Supernova Explosions Aided by the Standing Accretion-Shock Instability. *ApJ*, Vol. 694, pp. 664–696, March 2009.

[267] G. Martínez-Pinedo, T. Fischer, and L. Huther. Supernova neutrinos and nucleosynthesis. *Journal of Physics G Nuclear Physics*, Vol. 41, No. 4, p. 044008, April 2014.

[268] F. Martins and A. Palacios. A comparison of evolutionary tracks for single Galactic massive stars. *A&A*, Vol. 560, p. A16, December 2013.

[269] S. Mathis and J.-P. Zahn. Transport and mixing in the radiation zones of rotating stars. I. Hydrodynamical processes. *A&A*, Vol. 425, pp. 229–242, October 2004.

[270] J. R. Maund, M. Fraser, M. Ergon, A. Pastorello, S. J. Smartt, J. Sollerman, S. Benetti, M.-T. Botticella, F. Bufano, I. J. Danziger, R. Kotak, L. Magill, A. W. Stephens, and S. Valenti. The Yellow Supergiant Progenitor of the Type II Supernova 2011dh in M51. *ApJL*, Vol. 739, p. L37, October 2011.

[271] C. A. Meakin and D. Arnett. Anelastic and Compressible Simulations of Stellar Oxygen Burning. *ApJ*, Vol. 665, pp. 690–697, August 2007.

[272] C. A. Meakin and D. Arnett. Anelastic and Compressible Simulations of Stellar Oxygen Burning. *ApJ*, Vol. 665, pp. 690–697, August 2007.

[273] C. A. Meakin and D. Arnett. Turbulent Convection in Stellar Interiors. I. Hydrodynamic Simulation. *ApJ*, Vol. 667, pp. 448–475, September 2007.

[274] C. A. Meakin and W. D. Arnett. Some properties of the kinetic energy flux and dissipation in turbulent stellar convection zones. *Ap&SS*, Vol. 328, pp. 221–225, July 2010.

[275] T. Melson, H.-T. Janka, R. Bollig, F. Hanke, A. Marek, and B. Müller. Neutrino-driven Explosion of a 20 Solar-mass Star in Three Dimensions Enabled by Strange-quark Contributions to Neutrino-Nucleon Scattering. *ApJL*, Vol. 808, p. L42, August 2015.

[276] T. Melson, H.-T. Janka, and A. Marek. Neutrino-driven Supernova of a Low-mass Iron-core Progenitor Boosted by Three-dimensional Turbulent Convection. *ApJL*, Vol. 801, p. L24, March 2015.

[277] O. E. B. Messer, A. Mezzacappa, S. W. Bruenn, and M. W. Guidry. A Comparison of Boltzmann and Multigroup Flux-limited Diffusion Neutrino Transport during the Postbounce Shock Reheating Phase in Core-Collapse Supernovae. *ApJ*, Vol. 507, pp. 353–360, November 1998.

[278] B. S. Meyer and J. S. Brown. Survey of r-Process Models. *ApJS*, Vol. 112, pp. 199–220, September 1997.

[279] G. Meynet, C. Georgy, R. Hirschi, A. Maeder, P. Massey, N. Przybilla, and M.-F. Nieva. Red Supergiants, Luminous Blue Variables and Wolf-Rayet stars: the single massive star perspective. *Bulletin de la Societe Royale des Sciences de Liege*, Vol. 80, pp. 266–278, January 2011.

[280] G. Meynet and A. Maeder. Stellar evolution with rotation. I. The computational method and the inhibiting effect of the μ-gradient. *A&A*, Vol. 321, pp. 465–476, May 1997.

[281] G. Meynet and A. Maeder. Stellar evolution with rotation. X. Wolf-Rayet star populations at solar metallicity. *A&A*, Vol. 404, pp. 975–990, June 2003.

[282] A. Mezzacappa and S. W. Bruenn. Type II supernovae and Boltzmann neutrino transport - The infall phase. *ApJ*, Vol. 405, pp. 637–668, March 1993.

[283] A. Mezzacappa, A. C. Calder, S. W. Bruenn, J. M. Blondin, M. W. Guidry, M. R. Strayer, and A. S. Umar. An Investigation of Neutrino-driven Convection and the Core Collapse Supernova Mechanism Using Multigroup Neutrino Transport. *ApJ*, Vol. 495, pp. 911–926, March 1998.

[284] A. Mezzacappa, M. Liebendörfer, O. E. Messer, W. R. Hix, F.-K. Thielemann, and S. W. Bruenn. Simulation of the Spherically Symmetric Stellar Core Collapse, Bounce, and Postbounce Evolution of a Star of 13 Solar Masses with Boltzmann Neutrino Transport, and Its Implications for the Supernova Mechanism. *Physical Review Letters*, Vol. 86, pp. 1935–1938, March 2001.

[285] D. Mihalas and B. W. Mihalas. *Foundations of radiation hydrodynamics*. 1984.

[286] M. Min, C. P. Dullemond, C. Dominik, A. de Koter, and J. W. Hovenier. Radiative transfer in very optically thick circumstellar disks. *A&A*, Vol. 497, pp. 155–166, April 2009.

[287] M. Mocák, C. A. Meakin, E. Müller, and L. Siess. A New Stellar Mixing Process Operating below Shell Convection Zones Following Off-center Ignition. *ApJ*, Vol. 743, p. 55, December 2011.

[288] B. Müller and H.-T. Janka. Non-radial instabilities and progenitor asphericities in core-collapse supernovae. *MNRAS*, Vol. 448, pp. 2141–2174, April 2015.

[289] B. Müller, H.-T. Janka, and A. Heger. New Two-dimensional Models of Supernova Explosions by the Neutrino-heating Mechanism: Evidence for Different Instability Regimes in Collapsing Stellar Cores. *ApJ*, Vol. 761, p. 72, December 2012.

[290] B. Müller, H.-T. Janka, and A. Heger. New Two-dimensional Models of Supernova Explosions by the Neutrino-heating Mechanism: Evidence for Different Instability Regimes in Collapsing Stellar Cores. *ApJ*, Vol. 761, p. 72, December 2012.

[291] J. W. Murphy and A. Burrows. Criteria for Core-Collapse Supernova Explosions by the Neutrino Mechanism. *ApJ*, Vol. 688, pp. 1159–1175, December 2008.

[292] J. W. Murphy and J. C. Dolence. An Integral Condition for Core-Collapse Supernova Explosions. *ArXiv e-prints*, July 2015.

[293] J. W. Murphy, J. C. Dolence, and A. Burrows. The Dominance of Neutrino-driven Convection in Core-collapse Supernovae. *ApJ*, Vol. 771, p. 52, July 2013.

[294] J. W. Murphy, Z. G. Jennings, B. Williams, J. J. Dalcanton, and A. E. Dolphin. The Progenitor Mass of SN 2011dh from Stellar Population Analysis. *ApJL*, Vol. 742, p. L4, November 2011.

[295] J. W. Murphy and C. Meakin. A Global Turbulence Model for Neutrino-driven Convection in Core-collapse Supernovae. *ApJ*, Vol. 742, p. 74, December 2011.

[296] J. W. Murphy, C. D. Ott, and A. Burrows. A Model for Gravitational Wave Emission from Neutrino-Driven Core-Collapse Supernovae. *ApJ*, Vol. 707, pp. 1173–1190, December 2009.

[297] W. D. Myers and W. J. Świaţecki. The compressibility of finite nuclei. *Nuclear Physics A*, Vol. 587, pp. 92–100, February 1995.

[298] W. D. Myers and W. J. Swiatecki. Nuclear properties according to the Thomas-Fermi model. *Nuclear Physics A*, Vol. 601, pp. 141–167, February 1996.

[299] E. S. Myra and S. A. Bludman. Neutrino transport and the prompt mechanism for type II supernovae. *ApJ*, Vol. 340, pp. 384–395, May 1989.

[300] D. K. Nadyozhin. Explosion energies, nickel masses and distances of Type II plateau supernovae. *MNRAS*, Vol. 346, pp. 97–104, November 2003.

[301] H. Nagakura, H. Ito, K. Kiuchi, and S. Yamada. Jet Propagations, Breakouts, and Photospheric Emissions in Collapsing Massive Progenitors of Long-duration Gamma-ray Bursts. *ApJ*, Vol. 731, p. 80, April 2011.

[302] K. Nakamura, T. Takiwaki, K. Kotake, and N. Nishimura. Revisiting Impacts of Nuclear Burning for Reviving Weak Shocks in Neutrino-driven Supernovae. *ApJ*, Vol. 782, p. 91, February 2014.

[303] K. Nakamura, T. Takiwaki, T. Kuroda, and K. Kotake. Systematic Features of Axisymmetric Neutrino-Driven Core-Collapse Supernova Models in Multiple Progenitors. *ArXiv e-prints*, June 2014.

[304] K. Nakamura, T. Takiwaki, T. Kuroda, and K. Kotake. Systematic features of axisymmetric neutrino-driven core-collapse supernova models in multiple progenitors. *PASJ*, Vol. 67, p. 107, December 2015.

[305] K. Nakazato, S. Furusawa, K. Sumiyoshi, A. Ohnishi, S. Yamada, and H. Suzuki. Hyperon Matter and Black Hole Formation in Failed Supernovae. *ApJ*, Vol. 745, p. 197, February 2012.

[306] K. Nakazato, K. Iida, and K. Oyamatsu. Curvature effect on nuclear "pasta": Is it helpful for gyroid appearance? *Phys. Rev. C*, Vol. 83, No. 6, p. 065811, June 2011.

[307] K. Nakazato, K. Sumiyoshi, H. Suzuki, and S. Yamada. Exploring hadron physics in black hole formations: A new promising target of neutrino astronomy. *Phys. Rev. D*, Vol. 81, No. 8, p. 083009, April 2010.

[308] K. Nakazato, K. Sumiyoshi, and S. Yamada. Astrophysical implications of equation of state for hadron-quark mixed phase: Compact stars and stellar collapses. *Phys. Rev. D*, Vol. 77, No. 10, p. 103006, May 2008.

[309] H. Nieuwenhuijzen and C. de Jager. Parametrization of stellar rates of mass loss as functions of the fundamental stellar parameters M, L, and R. *A&A*, Vol. 231, pp. 134–136, May 1990.

[310] T. Nikšić, D. Vretenar, and P. Ring. Relativistic nuclear energy density functionals: Mean-field and beyond. *Progress in Particle and Nuclear Physics*, Vol. 66, pp. 519–548, July 2011.

[311] U. M. Noebauer, S. A. Sim, M. Kromer, F. K. Röpke, and W. Hillebrandt. Monte Carlo radiation hydrodynamics: methods, tests and application to Type Ia supernova ejecta. *MNRAS*, Vol. 425, pp. 1430–1444, September 2012.

[312] K. Nomoto and M. Hashimoto. Presupernova evolution of massive stars. *Phys. Rep.*, Vol. 163, pp. 13–36, 1988.

[313] K. Nomoto, K. Maeda, M. Tanaka, and T. Suzuki. Gamma-Ray Bursts and magnetar-forming Supernovae. *Ap&SS*, Vol. 336, pp. 129–137, November 2011.

[314] K. Nomoto, N. Tominaga, H. Umeda, C. Kobayashi, and K. Maeda. Nucleosynthesis yields of core-collapse supernovae and hypernovae, and galactic chemical evolution. *Nuclear Physics A*, Vol. 777, pp. 424–458, October 2006.

[315] A. Nonaka, A. S. Almgren, J. B. Bell, M. J. Lijewski, C. M. Malone, and M. Zingale. MAESTRO: An Adaptive Low Mach Number Hydrodynamics Algorithm for Stellar Flows. *ApJS*, Vol. 188, pp. 358–383, June 2010.

[316] A. Nonaka, A. J. Aspden, M. Zingale, A. S. Almgren, J. B. Bell, and S. E. Woosley. High-resolution Simulations of Convection Preceding Ignition in Type Ia Supernovae Using Adaptive Mesh Refinement. *ApJ*, Vol. 745, p. 73, January 2012.

[317] J. Nordhaus, A. Burrows, A. Almgren, and J. Bell. Dimension as a Key to the Neutrino Mechanism of Core-collapse Supernova Explosions. *ApJ*, Vol. 720, pp. 694–703, September 2010.

[318] S. R. Och, L. B. Lucy, and M. R. Rosa. Diffuse radiation in models of photoionized nebulae. *A&A*, Vol. 336, pp. 301–308, August 1998.

[319] E. O'Connor. An Open-source Neutrino Radiation Hydrodynamics Code for Core-collapse Supernovae. *ApJS*, Vol. 219, p. 24, August 2015.

[320] E. O'Connor and C. D. Ott. A new open-source code for spherically symmetric stellar collapse to neutron stars and black holes. *Classical and Quantum Gravity*, Vol. 27, No. 11, p. 114103, June 2010.

[321] E. O'Connor and C. D. Ott. Black Hole Formation in Failing Core-Collapse Supernovae. *ApJ*, Vol. 730, p. 70, April 2011.

[322] E. O'Connor and C. D. Ott. The Progenitor Dependence of the Pre-explosion Neutrino Emission in Core-collapse Supernovae. *ApJ*, Vol. 762, p. 126, January 2013.

[323] M. Oertel, A. F. Fantina, and J. Novak. Extended equation of state for core-collapse simulations. *Phys. Rev. C*, Vol. 85, No. 5, p. 055806, May 2012.

[324] M. Oertel, C. Providência, F. Gulminelli, and A. R. Raduta. Hyperons in neutron star matter within relativistic mean-field models. *Journal of Physics G Nuclear Physics*, Vol. 42, No. 7, p. 075202, July 2015.

[325] N. Ohnishi, K. Kotake, and S. Yamada. Numerical Analysis of Standing Accretion Shock Instability with Neutrino Heating in Supernova Cores. *ApJ*, Vol. 641, pp. 1018–1028, April 2006.

[326] K. Otsuki, H. Tagoshi, T. Kajino, and S.-y. Wanajo. General Relativistic Effects on Neutrino-driven Winds from Young, Hot Neutron Stars and r-Process Nucleosynthesis. *ApJ*, Vol. 533, pp. 424–439, April 2000.

[327] C. D Ott. TOPICAL REVIEW: The gravitational-wave signature of core-collapse supernovae. *Classical and Quantum Gravity*, Vol. 26, No. 6, p. 063001, March 2009.

[328] C. D. Ott, A. Burrows, L. Dessart, and E. Livne. Two-Dimensional Multiangle, Multigroup Neutrino Radiation-Hydrodynamic Simulations of Postbounce Supernova Cores. *ApJ*, Vol. 685, pp. 1069–1088, October 2008.

[329] C. D. Ott, E. P. O'Connor, S. Gossan, E. Abdikamalov, U. C. T. Gamma, and S. Drasco. Core-Collapse Supernovae, Neutrinos, and Gravitational Waves. *Nuclear Physics B Proceedings Supplements*, Vol. 235, pp. 381–387, February 2013.

[330] K. Oyamatsu. Nuclear shapes in the inner crust of a neutron star. *Nuclear Physics A*, Vol. 561, pp. 431–452, August 1993.

[331] K. Oyamatsu and K. Iida. Empirical properties of asymmetric nuclear matter to be obtained from unstable nuclei. *Nuclear Physics A*, Vol. 718, pp. 363–366, May 2003.

[332] D. Page and S. Reddy. Dense Matter in Compact Stars: Theoretical Developments and Observational Constraints. *Annual Review of Nuclear and Particle Science*, Vol. 56, pp. 327–374, November 2006.

[333] A. Palacios. Influence of Rotation on Stellar Evolution. In P. Hennebelle and C. Charbonnel, editors, *EAS Publications Series*, Vol. 62 of *EAS Publications Series*, pp. 227–287, September 2013.

[334] A. Palacios, C. Charbonnel, S. Talon, and L. Siess. Rotational mixing in low-mass stars. II. Self-consistent models of Pop II RGB stars. *A&A*, Vol. 453, pp. 261–278, July 2006.

[335] K.-C. Pan, M. Liebendörfer, M. Hempel, and F.-K. Thielemann. Two-dimensional Core-collapse Supernova Simulations with the Isotropic Diffusion Source Approximation for Neutrino Transport. *ApJ*, Vol. 817, p. 72, January 2016.

[336] I. V. Panov and H.-T. Janka. On the dynamics of proto-neutron star winds and r-process nucleosynthesis. *A&A*, Vol. 494, pp. 829–844, February 2009.

[337] O. Papish, J. Nordhaus, and N. Soker. A call for a paradigm shift from neutrino-driven to jet-driven core-collapse supernova mechanisms. *MNRAS*, Vol. 448, pp. 2362–2367, April 2015.

[338] B. Paxton. EZ to Evolve ZAMS Stars: A Program Derived from Eggleton's Stellar Evolution Code. , Vol. 116, pp. 699–701, July 2004.

[339] B. Paxton, L. Bildsten, A. Dotter, F. Herwig, P. Lesaffre, and F. Timmes. Modules for Experiments in Stellar Astrophysics (MESA). *ApJS*, Vol. 192, p. 3, January 2011.

[340] B. Paxton, M. Cantiello, P. Arras, L. Bildsten, E. F. Brown, A. Dotter, C. Mankovich, M. H. Montgomery, D. Stello, F. X. Timmes, and R. Townsend. Modules for Experiments in Stellar Astrophysics (MESA): Planets, Oscillations, Rotation, and Massive Stars. *ApJS*, Vol. 208, p. 4, September 2013.

[341] B. Paxton, P. Marchant, J. Schwab, E. B. Bauer, L. Bildsten, M. Cantiello, L. Dessart, R. Farmer, H. Hu, N. Langer, R. H. D. Townsend, D. M. Townsley, and F. X. Timmes. Modules for Experiments in Stellar Astrophysics (MESA): Binaries, Pulsations, and Explosions. *ApJS*, Vol. 220, p. 15, September 2015.

[342] O. Pejcha and J. L. Prieto. A Global Model of The Light Curves and Expansion Velocities of Type II-plateau Supernovae. *ApJ*, Vol. 799, p. 215, February 2015.

[343] O. Pejcha and J. L. Prieto. On the Intrinsic Diversity of Type II-Plateau Supernovae. *ApJ*, Vol. 806, p. 225, June 2015.

[344] O. Pejcha and T. A. Thompson. The Physics of the Neutrino Mechanism of Core-collapse Supernovae. *ApJ*, Vol. 746, p. 106, February 2012.

[345] A. Perego, R. Cabezón, and R. Käppeli. An advanced leakage scheme for neutrino treatment in astrophysical simulations. *ArXiv e-prints*, November 2015.

[346] M. H. Pinsonneault, S. D. Kawaler, S. Sofia, and P. Demarque. Evolutionary models of the rotating sun. *ApJ*, Vol. 338, pp. 424–452, March 1989.

[347] P. A. Pinto and R. G. Eastman. The Physics of Type IA Supernova Light Curves. II. Opacity and Diffusion. *ApJ*, Vol. 530, pp. 757–776, February 2000.

[348] P. Podsiadlowski, P. C. Joss, and J. J. L. Hsu. Presupernova evolution in massive interacting binaries. *ApJ*, Vol. 391, pp. 246–264, May 1992.

[349] G. C. Pomraning. *The equations of radiation hydrodynamics*. 1973.

[350] J. A. Pons, J. A. Miralles, and J. M. A. Ibanez.

[351] J. A. Pons, J. A. Miralles, M. Prakash, and J. M. Lattimer. Evolution of Proto-Neutron Stars with Kaon Condensates. *ApJ*, Vol. 553, pp. 382–393, May 2001.

[352] J. A. Pons, A. W. Steiner, M. Prakash, and J. M. Lattimer. Evolution of Proto-Neutron Stars with Quarks. *Physical Review Letters*, Vol. 86, pp. 5223–5226, June 2001.

[353] D. V. Popov. An analytical model for the plateau stage of Type II supernovae. *ApJ*, Vol. 414, pp. 712–716, September 1993.

[354] M. Prakash, I. Bombaci, M. Prakash, P. J. Ellis, J. M. Lattimer, and R. Knorren. Composition and structure of protoneutron stars. *Phys. Rep.*, Vol. 280, pp. 1–77, 1997.

[355] Y.-Z. Qian and G. J. Wasserburg. Where, oh where has the r-process gone? *Phys. Rep.*, Vol. 442, pp. 237–268, April 2007.

[356] Y.-Z. Qian and S. E. Woosley. Nucleosynthesis in Neutrino-driven Winds. I. The Physical Conditions. *ApJ*, Vol. 471, p. 331, November 1996.

[357] G. Raffelt and D. Seckel. Self-consistent approach to neutral-current processes in supernova cores. *Phys. Rev. D*, Vol. 52, pp. 1780–1799, August 1995.

[358] G. Raffelt, D. Seckel, and G. Sigl. Supernova neutrino scattering rates reduced by nucleon spin fluctuations: Perturbative limit. *Phys. Rev. D*, Vol. 54, pp. 2784–2792, August 1996.

[359] M. Rampp and H.-T. Janka. Spherically Symmetric Simulation with Boltzmann Neutrino Transport of Core Collapse and Postbounce Evolution of a 15 M_{solar} Star. *ApJL*, Vol. 539, pp. L33–L36, August 2000.

[360] M. Rampp and H.-T. Janka. Radiation hydrodynamics with neutrinos. Variable Eddington factor method for core-collapse supernova simulations. *A&A*, Vol. 396, pp. 361–392, December 2002.

[361] T. Rauscher, A. Heger, R. D. Hoffman, and S. E. Woosley. Nucleosynthesis in Massive Stars with Improved Nuclear and Stellar Physics. *ApJ*, Vol. 576, pp. 323–348, September 2002.

[362] T. Rauscher and F.-K. Thielemann. Astrophysical Reaction Rates From Statistical Model Calculations. *Atomic Data and Nuclear Data Tables*, Vol. 75, pp. 1–351, May 2000.

[363] D. G. Ravenhall, C. J. Pethick, and J. M. Lattimer. Nuclear interface energy at finite temperatures. *Nuclear Physics A*, Vol. 407, pp. 571–591, October 1983.

[364] S. Reddy, M. Prakash, and J. M. Lattimer. Neutrino interactions in hot and dense matter. *Phys. Rev. D*, Vol. 58, No. 1, p. 013009, July 1998.

[365] S. Richers, D. Kasen, E. O'Connor, R. Fernández, and C. D. Ott. Monte Carlo Neutrino Transport through Remnant Disks from Neutron Star Mergers. *ApJ*, Vol. 813, p. 38, November 2015.

[366] L. F. Roberts. A New Code for Proto-neutron Star Evolution. *ApJ*, Vol. 755, p. 126, August 2012.

[367] T. P. Robitaille. HYPERION: an open-source parallelized three-dimensional dust continuum radiative transfer code. *A&A*, Vol. 536, p. A79, December 2011.

[368] N. Roth and D. Kasen. Monte Carlo Radiation-Hydrodynamics With Implicit Methods. *ApJS*, Vol. 217, p. 9, March 2015.

[369] I. W. Roxburgh. Convection and stellar structure. *A&A*, Vol. 65, pp. 281–285, April 1978.

[370] I. W. Roxburgh. Integral constraints on convective overshooting. *A&A*, Vol. 211, pp. 361–364, March 1989.

[371] B. R. Ryan, J. C. Dolence, and C. F. Gammie. bhlight: General Relativistic Radiation Magnetohydrodynamics with Monte Carlo Transport. *ApJ*, Vol. 807, p. 31, July 2015.

[372] I. Sagert, T. Fischer, M. Hempel, G. Pagliara, J. Schaffner-Bielich, A. Mezzacappa, F.-K. Thielemann, and M. Liebendörfer. Signals of the QCD Phase Transition in Core-Collapse Supernovae. *Physical Review Letters*, Vol. 102, No. 8, p. 081101, February 2009.

[373] F. Sammarruca, B. Chen, L. Coraggio, N. Itaco, and R. Machleidt. Dirac-Brueckner-Hartree-Fock versus chiral effective field theory. *Phys. Rev. C*, Vol. 86, No. 5, p. 054317, November 2012.

[374] H. Sana, S. E. de Mink, A. de Koter, N. Langer, C. J. Evans, M. Gieles, E. Gosset, R. G. Izzard, J.-B. Le Bouquin, and F. R. N. Schneider. Binary Interaction Dominates the Evolution of Massive Stars. *Science*, Vol. 337, p. 444, July 2012.

[375] K. Sato. Supernova explosion and neutral currents of weak interaction. *Progress of Theoretical Physics*, Vol. 54, pp. 1325–1338, November 1975.

[376] R. F. Sawyer. Effects of nuclear forces on neutrino opacities in hot nuclear matter. *Phys. Rev. C*, Vol. 40, pp. 865–874, August 1989.

[377] L. Scheck, H.-T. Janka, T. Foglizzo, and K. Kifonidis. Multidimensional supernova simulations with approximative neutrino transport. II. Convection and the advective-acoustic cycle in the supernova core. *A&A*, Vol. 477, pp. 931–952, January 2008.

[378] L. Scheck, K. Kifonidis, H.-T. Janka, and E. Müller. Multidimensional supernova simulations with approximative neutrino transport. I. Neutron star kicks and the anisotropy of neutrino-driven explosions in two spatial dimensions. *A&A*, Vol. 457, pp. 963–986, October 2006.

[379] P. J. Schinder. Exact expressions and improved approximations for interaction rates of neutrinos with free nucleons in a high-temperature, high-density gas. *ApJS*, Vol. 74, pp. 249–273, September 1990.

[380] K. Scholberg. Supernova Neutrino Detection. *Annual Review of Nuclear and Particle Science*, Vol. 62, pp. 81–103, November 2012.

[381] I. R. Seitenzahl, F. X. Timmes, and G. Magkotsios. The Light Curve of SN 1987A Revisited: Constraining Production Masses of Radioactive Nuclides. *ApJ*, Vol. 792, p. 10, September 2014.

[382] Y. Sekiguchi. Stellar Core Collapse in Full General Relativity with Microphysics – Formulation and Spherical Collapse Test. *Progress of Theoretical Physics*, Vol. 124, pp. 331–379, August 2010.

[383] G. Shen, C. J. Horowitz, and E. O'Connor. Second relativistic mean field and virial equation of state for astrophysical simulations. *Phys. Rev. C*, Vol. 83, No. 6, p. 065808, June 2011.

[384] G. Shen, C. J. Horowitz, and S. Teige. New equation of state for astrophysical simulations. *Phys. Rev. C*, Vol. 83, No. 3, p. 035802, March 2011.

[385] H. Shen, H. Toki, K. Oyamatsu, and K. Sumiyoshi. Relativistic equation of state of nuclear matter for supernova and neutron star. *Nuclear Physics A*, Vol. 637, pp. 435–450, July 1998.

[386] M. Shibata, H. Nagakura, Y. Sekiguchi, and S. Yamada. Conservative form of Boltzmann's equation in general relativity. *Phys. Rev. D*, Vol. 89, No. 8, p. 084073, April 2014.

[387] T. Skyrme. The effective nuclear potential. *Nuclear Physics*, Vol. 9, pp. 615–634, 1959.

[388] S. J. Smartt. Progenitors of Core-Collapse Supernovae. *ARA&A*, Vol. 47, pp. 63–106, September 2009.

[389] S. J. Smartt. Observational Constraints on the Progenitors of Core-Collapse Supernovae: The Case for Missing High-Mass Stars. *Proc. Astron. Soc. Aust.*, Vol. 32, p. e016, April 2015.

[390] S. J. Smartt, J. J. Eldridge, R. M. Crockett, and J. R. Maund. The death of massive stars - I. Observational constraints on the progenitors of Type II-P supernovae. *MNRAS*, Vol. 395, pp. 1409–1437, May 2009.

[391] S. J. Smartt, J. J. Eldridge, R. M. Crockett, and J. R. Maund. The death of massive stars - I. Observational constraints on the progenitors of Type II-P supernovae. *MNRAS*, Vol. 395, pp. 1409–1437, May 2009.

[392] N. Smith. Mass Loss: Its Effect on the Evolution and Fate of High-Mass Stars. *ARA&A*, Vol. 52, pp. 487–528, August 2014.

[393] N. Smith and W. D. Arnett. Preparing for an Explosion: Hydrodynamic Instabilities and Turbulence in Presupernovae. *ApJ*, Vol. 785, p. 82, April 2014.

[394] N. Smith, W. Li, A. V. Filippenko, and R. Chornock. Observed fractions of core-collapse supernova types and initial masses of their single and binary progenitor stars. *MNRAS*, Vol. 412, pp. 1522–1538, April 2011.

[395] C. Sneden, J. J. Cowan, J. E. Lawler, I. I. Ivans, S. Burles, T. C. Beers, F. Primas, V. Hill, J. W. Truran, G. M. Fuller, B. Pfeiffer, and K.-L. Kratz. The Extremely Metal-poor, Neutron Capture-rich Star CS 22892-052: A Comprehensive Abundance Analysis. *ApJ*, Vol. 591, pp. 936–953, July 2003.

[396] A. M. Soderberg, E. Berger, K. L. Page, P. Schady, J. Parrent, D. Pooley, X.-Y. Wang, E. O. Ofek, A. Cucchiara, A. Rau, E. Waxman, J. D. Simon, D. C.-J. Bock, P. A. Milne, M. J. Page, J. C. Barentine, S. D. Barthelmy, A. P. Beardmore, M. F. Bietenholz, P. Brown, A. Burrows, D. N. Burrows, G. Byrngelson, S. B. Cenko, P. Chandra, J. R. Cummings, D. B. Fox, A. Gal-Yam, N. Gehrels, S. Immler, M. Kasliwal, A. K. H. Kong, H. A. Krimm, S. R. Kulkarni, T. J. Maccarone, P. Mészáros, E. Nakar, P. T. O'Brien, R. A. Overzier, M. de Pasquale, J. Racusin, N. Rea, and D. G. York. An extremely luminous X-ray outburst at the birth of a supernova. *Nature*, Vol. 453, pp. 469–474, May 2008.

[397] S. Starrfield, W. M. Sparks, J. W. Truran, and M. C. Wiescher. The Effects of New Nuclear Reaction Rates and Opacities on Hydrodynamic Simulations of the Nova Outburst. *ApJS*, Vol. 127, pp. 485–495, April 2000.

[398] A. W. Steiner and S. Gandolfi. Connecting Neutron Star Observations to Three-Body Forces in Neutron Matter and to the Nuclear Symmetry Energy. *Physical Review Letters*, Vol. 108, No. 8, p. 081102, February 2012.

[399] A. W. Steiner, J. M. Lattimer, and E. F. Brown. The Equation of State from Observed Masses and Radii of Neutron Stars. *ApJ*, Vol. 722, pp. 33–54, October 2010.

[400] A. W. Steiner, J. M. Lattimer, and E. F. Brown. The Neutron Star Mass-Radius Relation and the Equation of State of Dense Matter. *ApJL*, Vol. 765, p. L5, March 2013.

[401] A. W. Steiner, M. Prakash, J. M. Lattimer, and P. J. Ellis. Isospin asymmetry in nuclei and neutron stars [review article]. *Phys. Rep.*, Vol. 411, pp. 325–375, June 2005.

[402] J. M. Stone and M. L. Norman. ZEUS-2D: A radiation magnetohydrodynamics code for astrophysical flows in two space dimensions. I - The hydrodynamic algorithms and tests. *ApJS*, Vol. 80, pp. 753–790, June 1992.

[403] Y. Sugahara and H. Toki. Relativistic mean-field theory for unstable nuclei with non-linear σ and ω terms. *Nuclear Physics A*, Vol. 579, pp. 557–572, October 1994.

[404] D. Sugimoto. On the Numerical Stability of Computations of Stellar Evolution. *ApJ*, Vol. 159, p. 619, February 1970.

[405] D. Sugimoto, K. Nomoto, and Y. Eriguchi. Stable Numerical Method in Computation of Stellar Evolution. *Progress of Theoretical Physics Supplement*, Vol. 70, pp. 115–131, 1981.

[406] T. Sukhbold, T. Ertl, S. E. Woosley, J. M. Brown, and H.-T. Janka. Core-Collapse Supernovae from 9 to 120 Solar Masses Based on Neutrino-powered Explosions. *ArXiv e-prints*, October 2015.

[407] T. Sukhbold and S. E. Woosley. The Compactness of Presupernova Stellar Cores. *ApJ*, Vol. 783, p. 10, March 2014.

[408] K. Sumiyoshi, T. Takiwaki, H. Matsufuru, and S. Yamada. Multi-dimensional Features of Neutrino Transfer in Core-collapse Supernovae. *ApJS*, Vol. 216, p. 5, January 2015.

[409] K. Sumiyoshi and S. Yamada. Neutrino Transfer in Three Dimensions for Core-collapse Supernovae. I. Static Configurations. *ApJS*, Vol. 199, p. 17, March 2012.

[410] K. Sumiyoshi, S. Yamada, H. Suzuki, and S. Chiba. Neutrino Signals from the Formation of a Black Hole: A Probe of the Equation of State of Dense Matter. *Physical Review Letters*, Vol. 97, No. 9, p. 091101, September 2006.

[411] K. Sumiyoshi, S. Yamada, H. Suzuki, H. Shen, S. Chiba, and H. Toki. Postbounce Evolution of Core-Collapse Supernovae: Long-Term Effects of the Equation of State. *ApJ*, Vol. 629, pp. 922–932, August 2005.

[412] Y. Suwa, K. Kotake, T. Takiwaki, S. C. Whitehouse, M. Liebendörfer, and K. Sato. Explosion Geometry of a Rotating $13M_{\odot}$ Star Driven by the SASI-Aided Neutrino-Heating Supernova Mechanism. *PASJ*, Vol. 62, pp. L49–L53, December 2010.

[413] Y. Suwa, T. Takiwaki, K. Kotake, T. Fischer, M. Liebendörfer, and K. Sato. On the Importance of the Equation of State for the Neutrino-driven Supernova Explosion Mechanism. *ApJ*, Vol. 764, p. 99, February 2013.

[414] Y. Suwa, S. Yamada, T. Takiwaki, and K. Kotake. The Criterion of Supernova Explosion Revisited: The Mass Accretion History. *ApJ*, Vol. 816, p. 43, January 2016.

[415] H. Suzuki. Supernova neutrinos - multigroup simulations of neutrinos from protoneutron star. In Y. Suzuki and K. Nakamura, editors, *Frontiers of Neutrino Astrophysics*, pp. 219–226, 1993.

[416] F. D. Swesty. Implicit general relativistic hydrodynamic methods for modeling the late-time explosion mechanism in core collapse supernovae. *ApJ*, Vol. 445, pp. 811–827, June 1995.

[417] F. D. Swesty. Gray models of convection in core-collapse supernovae. In A. Mezzacappa, editor, *Stellar Evolution, Stellar Explosions and Galactic Chemical Evolution*, p. 539, 1998.

[418] F. D. Swesty, J. M. Lattimer, and E. S. Myra. The role of the equation of state in the 'prompt' phase of type II supernovae. *ApJ*, Vol. 425, pp. 195–204, April 1994.

[419] F. D. Swesty and E. S. Myra. Advances in Multi-Dimensional Simulation of Core-Collapse Supernovae. In A. Mezzacappa and G. M. Fuller, editors, *Open Issues in Core Collapse Supernova Theory*, pp. 176–195, December 2005.

[420] F. D. Swesty and E. S. Myra. A Numerical Algorithm for Modeling Multigroup Neutrino-Radiation Hydrodynamics in Two Spatial Dimensions. *ApJS*, Vol. 181, pp. 1–52, March 2009.

[421] M. Takahara and K. Sato. Supernova explosions and the soft equation of state. *ApJ*, Vol. 335, pp. 301–305, December 1988.

[422] K. Takahashi, K. Sato, A. Burrows, and T. A. Thompson. Supernova neutrinos, neutrino oscillations, and the mass of the progenitor star. *Phys. Rev. D*, Vol. 68, No. 11, p. 113009, December 2003.

[423] K. Takahashi, H. Umeda, and T. Yoshida. Stellar Yields of Rotating First Stars. I. Yields of Weak Supernovae and Abundances of Carbon-enhanced Hyper-metal-poor Stars. *ApJ*, Vol. 794, p. 40, October 2014.

[424] K. Takahashi, J. Witti, and H.-T. Janka. Nucleosynthesis in neutrino-driven winds from protoneutron stars II. The r-process. *A&A*, Vol. 286, , June 1994.

[425] K. Takahashi and S. Yamada. Linear Analysis on the Growth of Non-spherical Perturbations in Supersonic Accretion Flows. *ApJ*, Vol. 794, p. 162, October 2014.

[426] T. Takiwaki, K. Kotake, and Y. Suwa. Three-dimensional Hydrodynamic Core-collapse Supernova Simulations for an 11.2 $M_\odot$ Star with Spectral Neutrino Transport. *ApJ*, Vol. 749, p. 98, April 2012.

[427] T. Takiwaki, K. Kotake, and Y. Suwa. A Comparison of Two- and Three-dimensional Neutrino-hydrodynamics Simulations of Core-collapse Supernovae. *ApJ*, Vol. 786, p. 83, May 2014.

[428] G. A. Tammann, W. Loeffler, and A. Schroeder. The Galactic supernova rate. *ApJS*, Vol. 92, pp. 487–493, June 1994.

[429] M. Terasawa, K. Sumiyoshi, S. Yamada, H. Suzuki, and T. Kajino. r-Process Nucleosynthesis in Neutrino-driven Winds from a Typical Neutron Star with M=1.4 M_{solar}. *ApJL*, Vol. 578, pp. L137–L140, October 2002.

[430] L.-S. The, D. D. Clayton, R. Diehl, D. H. Hartmann, A. F. Iyudin, M. D. Leising, B. S. Meyer, Y. Motizuki, and V. Schönfelder. Are ^{44}Ti-producing supernovae exceptional? *A&A*, Vol. 450, pp. 1037–1050, May 2006.

[431] F.-K. Thielemann, A. Arcones, R. Käppeli, M. Liebendörfer, T. Rauscher, C. Winteler, C. Fröhlich, I. Dillmann, T. Fischer, G. Martinez-Pinedo, K. Langanke, K. Farouqi, K.-L. Kratz, I. Panov, and I. K. Korneev. What are the astrophysical sites for the r-process and the production of heavy elements? *Progress in Particle and Nuclear Physics*, Vol. 66, pp. 346–353, April 2011.

[432] T. A. Thompson, A. Burrows, and B. S. Meyer. The Physics of Proto-Neutron Star Winds: Implications for r-Process Nucleosynthesis. *ApJ*, Vol. 562, pp. 887–908, December 2001.

[433] T. A. Thompson, A. Burrows, and P. A. Pinto. Shock Breakout in Core-Collapse Supernovae and Its Neutrino Signature. *ApJ*, Vol. 592, pp. 434–456, July 2003.

[434] T. A. Thompson, E. Quataert, and A. Burrows. Viscosity and Rotation in Core-Collapse Supernovae. *ApJ*, Vol. 620, pp. 861–877, February 2005.

[435] V. Thorsson, M. Prakash, and J. M. Lattimer. Composition, structure and evolution of neutron stars with kaon condensates. *Nuclear Physics A*, Vol. 572, pp. 693–731, May 1994.

[436] F. X. Timmes and D. Arnett. The Accuracy, Consistency, and Speed of Five Equations of State for Stellar Hydrodynamics. *ApJS*, Vol. 125, pp. 277–294, November 1999.

[437] F. X. Timmes, S. E. Woosley, and T. A. Weaver. Galactic chemical evolution: Hydrogen through zinc. *ApJS*, Vol. 98, pp. 617–658, June 1995.

[438] B. G. Todd-Rutel and J. Piekarewicz. Neutron-Rich Nuclei and Neutron Stars: A New Accurately Calibrated Interaction for the Study of Neutron-Rich Matter. *Physical Review Letters*, Vol. 95, No. 12, p. 122501, September 2005.

[439] H. Togashi and M. Takano. Variational study for the equation of state of asymmetric nuclear matter at finite temperatures. *Nuclear Physics A*, Vol. 902, pp. 53–73, March 2013.

[440] H. Togashi, M. Takano, K. Sumiyoshi, and K. Nakazato. Application of the nuclear equation of state obtained by the variational method to core-collapse supernovae. *Progress of Theoretical and Experimental Physics*, Vol. 2014, No. 2, p. 023D05, February 2014.

[441] H. Toki, D. Hirata, Y. Sugahara, K. Sumiyoshi, and I. Tanihata. Relativistic many body approach for unstable nuclei and supernova. *Nuclear Physics A*, Vol. 588, pp. 357–363, February 1995.

[442] M. B. Tsang, J. R. Stone, F. Camera, P. Danielewicz, S. Gandolfi, K. Hebeler, C. J. Horowitz, J. Lee, W. G. Lynch, Z. Kohley, R. Lemmon, P. Möller, T. Murakami, S. Riordan, X. Roca-Maza, F. Sammarruca, A. W. Steiner, I. Vidaña, and S. J. Yennello. Constraints on the symmetry energy and neutron skins from experiments and theory. *Phys. Rev. C*, Vol. 86, No. 1, p. 015803, July 2012.

[443] D. L. Tubbs. Direct-simulation neutrino transport - Aspects of equilibration. *ApJS*, Vol. 37, pp. 287–312, July 1978.

[444] D. L. Tubbs. Conservative scattering, electron scattering, and neutrino thermalization. *ApJ*, Vol. 231, pp. 846–853, August 1979.

[445] C. Tur, A. Heger, and S. M. Austin. On the Sensitivity of Massive Star Nucleosynthesis and Evolution to Solar Abundances and to Uncertainties in Helium-Burning Reaction Rates. *ApJ*, Vol. 671, pp. 821–827, December 2007.

[446] M. Turatto. Classification of Supernovae. In K. Weiler, editor, *Supernovae and Gamma-Ray Bursters*, Vol. 598 of *Lecture Notes in Physics, Berlin Springer Verlag*, pp. 21–36, 2003.

[447] S. Typel, G. Röpke, T. Klähn, D. Blaschke, and H. H. Wolter. Composition and thermodynamics of nuclear matter with light clusters. *Phys. Rev. C*, Vol. 81, No. 1, p. 015803, January 2010.

[448] M. Ugliano, H.-T. Janka, A. Marek, and A. Arcones. Progenitor-explosion Connection and Remnant Birth Masses for Neutrino-driven Supernovae of Iron-core Progenitors. *ApJ*, Vol. 757, p. 69, September 2012.

[449] H. Umeda and K. Nomoto. How Much ^{56}Ni Can Be Produced in Core-Collapse Supernovae? Evolution and Explosions of 30-100 M_{solar} Stars. *ApJ*, Vol. 673, pp. 1014–1022, February 2008.

[450] H. Umeda, T. Yoshida, and K. Takahashi. Massive star evolution and nucleosynthesis: Lower end of Fe-core-collapse supernova progenitors and remnant neutron star mass distribution. *Progress of Theoretical and Experimental Physics*, Vol. 2012, No. 1, p. 01A302, September 2012.

[451] V. P. Utrobin and N. N. Chugai. Progenitor mass of the type IIP supernova 2005cs. *A&A*, Vol. 491, pp. 507–513, November 2008.

[452] K. A. van Riper. Stellar core collapse. II - Inner core bounce and shock propagation. *ApJ*, Vol. 257, pp. 793–820, June 1982.

[453] D. A. VandenBerg, P. A. Bergbusch, and P. D. Dowler. The Victoria-Regina Stellar Models: Evolutionary Tracks and Isochrones for a Wide Range in Mass and Metallicity that Allow for Empirically Constrained Amounts of Convective Core Overshooting. *ApJS*, Vol. 162, pp. 375–387, February 2006.

[454] M. Viallet, I. Baraffe, and R. Walder. Towards a new generation of multi-dimensional stellar evolution models: development of an implicit hydrodynamic code. *A&A*, Vol. 531, p. A86, July 2011.

[455] M. Viallet, I. Baraffe, and R. Walder. Comparison of different nonlinear solvers for 2D time-implicit stellar hydrodynamics. *A&A*, Vol. 555, p. A81, July 2013.

[456] J. S. Vink, A. de Koter, and H. J. G. L. M. Lamers. Mass-loss predictions for O and B stars as a function of metallicity. *A&A*, Vol. 369, pp. 574–588, April 2001.

[457] S. Wanajo. The r-process in Proto-neutron-star Wind Revisited. *ApJL*, Vol. 770, p. L22, June 2013.

[458] S. Wanajo, S. Goriely, M. Samyn, and N. Itoh. The r-Process in Supernovae: Impact of New Microscopic Mass Formulae. *ApJ*, Vol. 606, pp. 1057–1069, May 2004.

[459] S. Wanajo, T. Kajino, G. J. Mathews, and K. Otsuki. The r-Process in Neutrino-driven Winds from Nascent, "Compact" Neutron Stars of Core-Collapse Supernovae. *ApJ*, Vol. 554, pp. 578–586, June 2001.

[460] G. J. Wasserburg, M. Busso, and R. Gallino. Abundances of Actinides and Short-lived Nonactinides in the Interstellar Medium: Diverse Supernova Sources for the r-Processes. *ApJL*, Vol. 466, p. L109, August 1996.

[461] T. A. Weaver, G. B. Zimmerman, and S. E. Woosley. Presupernova evolution of massive stars. *ApJ*, Vol. 225, pp. 1021–1029, November 1978.

[462] A. Weiss and H. Schlattl. GARSTEC-the Garching Stellar Evolution Code. The direct descendant of the legendary Kippenhahn code. *Ap&SS*, Vol. 316, pp. 99–106, August 2008.

[463] S. Weissenborn, I. Sagert, G. Pagliara, M. Hempel, and J. Schaffner-Bielich. Quark Matter in Massive Compact Stars. *ApJL*, Vol. 740, p. L14, October 2011.

[464] C. West, A. Heger, and S. M. Austin. The Impact of Helium-burning Reaction Rates on Massive Star Evolution and Nucleosynthesis. *ApJ*, Vol. 769, p. 2, May 2013.

[465] B. F. Williams, S. Peterson, J. Murphy, K. Gilbert, J. J. Dalcanton, A. E. Dolphin, and Z. G. Jennings. Constraints for the Progenitor Masses of 17 Historic Core-collapse Supernovae. *ApJ*, Vol. 791, p. 105, August 2014.

[466] J. R. Wilson. Supernovae and Post-Collapse Behavior. In J. M. Centrella, J. M. Leblanc, and R. L. Bowers, editors, *Numerical Astrophysics*, p. 422, 1985.

[467] R. B. Wiringa, V. G. J. Stoks, and R. Schiavilla. Accurate nucleon-nucleon potential with charge-independence breaking. *Phys. Rev. C*, Vol. 51, pp. 38–51, January 1995.

[468] A. B. Wollaber. *Advanced Monte Carlo methods for thermal radiation transport*. PhD thesis, University of Michigan, 2008.

[469] A. B. Wollaber and E. W. 2009 Larsen. A hybrid monte carlo-deterministic approach to improve the accuracy and efficiency of monte carlo calculations for thermal radiative transfer. In *International Conference on Mathematics, Computational Methods & Reactor Physics*, 2009.

[470] R. T. Wollaeger and D. R. van Rossum. Radiation Transport for Explosive Outflows: Opacity Regrouping. *ApJS*, Vol. 214, p. 28, October 2014.

[471] R. T. Wollaeger, D. R. van Rossum, C. Graziani, S. M. Couch, G. C. Jordan, IV, D. Q. Lamb, and G. A. Moses. Radiation Transport for Explosive Outflows: A Multigroup Hybrid Monte Carlo Method. *ApJS*, Vol. 209, p. 36, December 2013.

[472] A. Wongwathanarat, H.-T. Janka, and E. Müller. Three-dimensional neutrino-driven supernovae: Neutron star kicks, spins, and asymmetric ejection of nucleosynthesis products. *A&A*, Vol. 552, p. A126, April 2013.

[473] S. E. Woosley and A. Heger. Nucleosynthesis and remnants in massive stars of solar metallicity. *Phys. Rep.*, Vol. 442, pp. 269–283, April 2007.

[474] S. E. Woosley, A. Heger, and T. A. Weaver. The evolution and explosion of massive stars. *Reviews of Modern Physics*, Vol. 74, pp. 1015–1071, November 2002.

[475] S. E. Woosley and T. A. Weaver. Presupernova models: sensitivity to convective algorithm and Coulomb corrections. *Phys. Rep.*, Vol. 163, pp. 79–94, 1988.

[476] S. E. Woosley and T. A. Weaver. The Evolution and Explosion of Massive Stars. II. Explosive Hydrodynamics and Nucleosynthesis. *ApJS*, Vol. 101, p. 181, November 1995.

[477] S. E. Woosley, J. R. Wilson, G. J. Mathews, R. D. Hoffman, and B. S. Meyer. The r-process and neutrino-heated supernova ejecta. *ApJ*, Vol. 433, pp. 229–246, September 1994.

[478] A. Yahil. Self-similar stellar collapse. *ApJ*, Vol. 265, pp. 1047–1055, February 1983.

[479] S. Yamada. An Implicit Lagrangian Code for Spherically Symmetric General Relativistic Hydrodynamics with an Approximate Riemann Solver. *ApJ*, Vol. 475, pp. 720–739, February 1997.

[480] S. Yamada, H.-T. Janka, and H. Suzuki. Neutrino transport in type II supernovae: Boltzmann solver vs. Monte Carlo method. *A&A*, Vol. 344, pp. 533–550, April 1999.

[481] T. Yamasaki and S. Yamada. Effects of Rotation on the Revival of a Stalled Shock in Supernova Explosions. *ApJ*, Vol. 623, pp. 1000–1010, April 2005.

[482] T. Yamasaki and S. Yamada. Standing Accretion Shocks in the Supernova Core: Effects of Convection and Realistic Equations of State. *ApJ*, Vol. 650, pp. 291–298, October 2006.

[483] T. Yamasaki and S. Yamada. Stability of Accretion Flows with Stalled Shocks in Core-Collapse Supernovae. *ApJ*, Vol. 656, pp. 1019–1037, February 2007.

[484] N. Yasutake, T. Maruyama, and T. Tatsumi. Amorphous state in the mixed phase of hadron-quark phase transition in protoneutron stars. *Phys. Rev. D*, Vol. 86, No. 10, p. 101302, November 2012.

[485] S.-C. Yoon and N. Langer. On the evolution of rapidly rotating massive white dwarfs towards supernovae or collapses. *A&A*, Vol. 435, pp. 967–985, June 2005.

[486] T. Yoshida, M. Terasawa, T. Kajino, and K. Sumiyoshi. Nucleosynthesis of Light Elements and Heavy r-Process Elements through the ν-Process in Supernova Explosions. *ApJ*, Vol. 600, pp. 204–213, January 2004.

[487] T. Yoshida and H. Umeda. A progenitor for the extremely luminous Type Ic supernova 2007bi. *MNRAS*, Vol. 412, pp. L78–L82, March 2011.

[488] P. A. Young and D. Arnett. Observational Tests and Predictive Stellar Evolution. II. Nonstandard Models. *ApJ*, Vol. 618, pp. 908–918, January 2005.

[489] P. A. Young and C. L. Fryer. Uncertainties in Supernova Yields. I. One-dimensional Explosions. *ApJ*, Vol. 664, pp. 1033–1044, August 2007.

[490] P. A. Young, C. L. Fryer, A. Hungerford, D. Arnett, G. Rockefeller, F. X. Timmes, B. Voit, C. Meakin, and K. A. Eriksen. Constraints on the Progenitor of Cassiopeia A. *ApJ*, Vol. 640, pp. 891–900, April 2006.

[491] J.-P. Zahn. Circulation and turbulence in rotating stars. *A&A*, Vol. 265, pp. 115–132, November 1992.

[492] L. Zampieri, A. Pastorello, M. Turatto, E. Cappellaro, S. Benetti, G. Altavilla, P. Mazzali, and M. Hamuy. Peculiar, low-luminosity Type II supernovae: low-energy explosions in massive progenitors? *MNRAS*, Vol. 338, pp. 711–716, January 2003.

[493] M. Zingale, A. S. Almgren, J. B. Bell, C. M. Malone, and A. Nonaka. Astrophysical applications of the MAESTRO code. *Journal of Physics Conference Series*, Vol. 125, No. 1, p. 012013, July 2008.

早稲田大学　博士（理学）　学位申請　研究業績書

氏 名　　山本　佑　　印

（2016　年　3 月　現在）

種 類 別	題名、　発表・発行掲載誌名、　発表・発行年月、　連名者（申請者含む）
論文	1. ○“Systematic studies of the post-shock revival and subsequent evolutions in core collapse supernovae with parametric progenitor models”, Yu Yamamoto and Shoichi Yamada, Astrophysical Journal,　818, 165 (2016) 2. ○“A systematic theoretical study of explosion energies in Core Collapse Supernovae” Yu Yamamoto and Shoichi Yamada, Proceeding of Science, XIII International Symposium on Nuclei in the Cosmos, 3. ○“Post-shock-revival evolutions in the neutrino-heating mechanism of core-collapse supernovae”, Yu Yamamoto , Shin-ichiro Fujimoto, Hiroki Nagakura and Shoichi Yamada, Astrophysical Journal, 771, 27 (2013) 4. “Semi-dynamical approach to the shock revival in core-collapse supernovae”, Hiroki Nagakura, Yu Yamamoto and Shoichi Yamada Astrophysical Journal, 765, 123 (2013)
講演	・”Systematic Studies of the Post-Shock-Revival Evolutions in Core Collapse Supernovae with Parametric Progenitor Models”, Yu Yamamoto, “Numazu Workshop 2015: Challenges of modeling supernovae with nuclear data”, Numazu, 1-4, Sept. 2015 ・ “A Systematic Theoretical Study of Explosion energies in Core Collapse Supernovae” Yu Yamamoto & Shoichi Yamada “F.O.E. Fifty-One Erg: An international workshop on the physics and observations of supernovae and supernova remnants” North Carolina State University, Raleigh, 1-5, June 2015 ・“A systematic theoretical study of explosion energies in core collapse supernovae” Yu Yamamoto, Shoichi Yamada XIII International Symposium on Nuclear in Cosmos , July, 2014

早稲田大学　博士（理学）　学位申請　研究業績書

種 類 別	題名、　発表・発行掲載誌名、　発表・発行年月、　連名者（申請者含む）
講演	・ “A systematic theoretical study of explosion energies in CCSNe” Yu Yamamoto , Shoichi Yamada, Ko Nakamura, Tomoya Takiwaki, Takami, Kuroda, Kei Kotake, Masomi Tanaka RIKEN Astrophysical Big Bang Seminars, April, 2014 ・ ” Post-shock-revival evolutions in the neutrino-heating mechanism of core-collapse supernovae” 山本佑、山田章一 日本天文学会、東北大学、2013 年 9 月 ・“The estimation of explosion energies of the neutrino heating mechanism in core-collapse supernovae” Yu Yamamoto, Shoichi Yamada, Workshop “Formations of Compact Objects: from the cradle to the grave” Waseda University ,Japan, March, 2012 ・”ニュートリノ加熱機構における超新星爆発エネルギー” 山本佑、山田章一 セミナー、国立天文台、2010 年 3 月 ・”超新星の爆発エネルギー” 山本佑、山田章一 基盤Ｓ研究会　超新星の爆発機構とガンマ線バースト源エンジンの統一的解明、 国立天文台、2010 年 1 月 ・ “ニュートリノ加熱機構における超新星爆発エネルギーの評価” 山本佑、山田章一 日本天文学会、山口大学、2009 年 9 月